

NOTICE: When government or other drawings, specifications or other data are used for any purpose other than in connection with a definitely related government procurement operation, the U. S. Government thereby incurs no responsibility, nor any obligation whatsoever; and the fact that the Government may have formulated, furnished, or in any way supplied the said drawings, specifications, or other data is not to be regarded by implication or otherwise as in any manner licensing the holder or any other person or corporation, or conveying any rights or permission to manufacture, use or sell any patented invention that may in any way be related thereto.

AFML-TR-64-363

466662

INVESTIGATION OF THE EFFECT OF SURFACE CONDITION
ON THE RADIANT PROPERTIES OF METALS

R. E. Rolling
A. I. Funai
J. R. Grammer

Lockheed Missiles & Space Company

TECHNICAL REPORT NO. AFML-TR-64-363

November 1964

Air Force Materials Laboratory
Research and Technology Division
Air Force Systems Command
Wright-Patterson Air Force Base, Ohio

NOTICES

When Government drawings, specifications, or other data are used for any purpose other than in connection with a definitely related Government procurement operation, the United States Government thereby incurs no responsibility nor any obligation whatsoever; and the fact that the Government may have formulated, furnished, or in any way supplied the said drawings, specifications, or other data is not to be regarded by implication or otherwise as in any manner licensing the holder or any other person or corporation, or conveying any rights or permission to manufacture, use, or sell any patented invention that may in any way be related thereto.

Qualified requesters may obtain copies of this report from the Defense Documentation Center (DDC), (formerly ASTIA), Cameron Station, Bldg 5, 5010 Duke Street, Alexandria, Virginia, 22314.

DDC release to CFSTI not authorized. The distribution of this report is limited because the report contains technology identifiable with items on the strategic embargo lists excluded from export or re-export under U.S. Export Control Act of 1949 (63 STAT. 7), as amended (50 U.S.C. App. 2020.2031), as implemented by AFR 400-10.

Copies of this report should not be returned to the Research and Technology Division unless return is required by security considerations, contractual obligations, or notice on a specific document.

FOREWORD

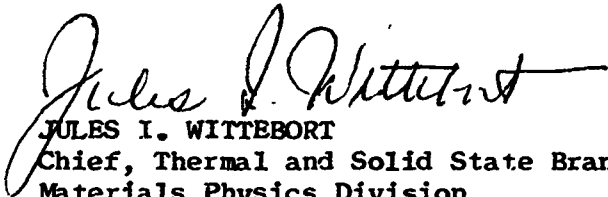
This report was prepared by the Thermophysics Section of the Aerospace Sciences Laboratory, Lockheed Missiles and Space Company under Air Force Contract AF 33(657)-11281. The contract was initiated under Project No. 7360, "The Chemistry and Physics of Materials," Task No. 736001, "Thermodynamics and Heat Transfer." The work was administered under the direction of the AF Materials Laboratory, Research and Technology Division, with Mr. R.J. Prezecki as project engineer.

This report describes work conducted from 1 July 1963 to 31 August 1964. The principal investigators were R.E. Rolling, A.I. Funai, and J. R. Grammer. Consultation and assistance on the theory of reflectance from rough surfaces were provided by Dr. C.L. Tien, Associate Professor of Mechanical Engineering, University of California at Berkeley.

Acknowledgments for special assistance and services during the program are due to the following persons: A. Gleason, metallography; J. Stelmokas, profilometry; C.A. Jernberg, equipment modifications and maintenance; A.R. Tolman, sample instrumentation; and P. Rauen, data reduction.

Manuscript released by authors October 1964 for publication as an AFML Technical Report.

This technical report has been reviewed and is approved.


JULES I. WITTEBORT
Chief, Thermal and Solid State Branch
Materials Physics Division
AF Materials Laboratory

ABSTRACT

Results are presented on the optical and radiant properties of copper, platinum, and tungsten. Optical constants n and k are presented as a function of temperature and wavelength, and the method for their determination is described. Radiant properties reported include the total and spectral emittance as a function of emission angle, polarization, temperature, and surface roughness.

Methods are described for the evaluation of surface geometry, and results obtained on all test samples are presented. Profilometry, metallographic inspection, x-ray diffraction, and spark spectroscopy were employed for evaluation of surface condition and are discussed in terms of their utility for this program.

Theories of the scattering of electromagnetic waves from a rough surface are briefly reviewed and necessary extensions of present theories to an emitting surface are indicated.

CONTENTS

Section		Page
1	INTRODUCTION	1
2	NOMENCLATURE	3
3	RADIANT PROPERTIES OF SURFACES	5
	3.1 Smooth Surfaces	5
	3.2 Rough Surfaces	9
4	SAMPLE PREPARATION PROCEDURES	18
	4.1 Selection of Samples	18
	4.2 Surface Finishing Methods	19
	4.3 Test Sample Preparation	22
5	SURFACE CHARACTERIZATION METHODS	24
	5.1 Profilometry Apparatus and Methods	24
	5.2 Microscope Methods	27
	5.3 Chemical Analyses	28
6	EXPERIMENTAL APPARATUS	30
	6.1 Vacuum Chamber	30
	6.2 Rotating Sample Mount	30
	6.3 Radiation Detection System	30
7	EXPERIMENTAL PROCEDURES	35
	7.1 Measurement of Spectral Directional and Normal Emittance	35
	7.2 Measurement of Total Directional and Normal Emittance	37
	7.3 Optical Constant Determinations	38
	7.4 Test Procedure	42
8	RESULTS	43
	8.1 Surface Characteristics	43
	8.2 Optical Constants	48
	8.3 Emittance Characteristics	50
	8.4 Discussion	61
9	CONCLUSIONS AND RECOMMENDATIONS	64
10	EXPERIMENTAL DATA	65
	10.1 Copper Sample 1	66
	10.2 Copper Sample 3	72
	10.3 Copper Sample 5	78
	10.4 Copper Sample 7	84
	10.5 Copper Sample 8	90
	10.6 Tungsten Sample 1	96
	10.7 Tungsten Sample 2	104
	10.8 Tungsten Sample 3	112
	10.9 Platinum Sample 1	120
	10.10 Platinum Sample 3	128
	10.11 Platinum Sample 6	136
11	REFERENCES	143
Appendix	REFLECTANCE OF A RANDOM ROUGH SURFACE OF FINITE CONDUCTIVITY FROM EXACT THEORY	147

TABLES

Table		Page
1	Surface Finishing Methods Used to Prepare Emittance Test Samples	23
2	Surface Roughness Parameters (Determined From Proficorder Traces) for Samples Before and After Emittance Tests	44
3	Peak-to-Valley Depths as Indicated by the Proficorder and by Sample Photomicrographs	46
4	Optical Constants of Tungsten for Four Wavelengths	48
5	Measured and Calculated Spectral Normal Emittance Values of Tungsten for Three Wavelengths	49
6	Optical Constants of Platinum for Five Wavelengths	49
7	Measured and Calculated Spectral Normal Emittance Values for Platinum at Two Wavelengths	50
8	Total and Spectral Normal Emittance Ratios for Rough Samples Relative to Polished Samples	57
9	Hemispherical to Normal Emittance Ratios for Copper	58
10	Hemispherical to Normal Emittance Ratios for Platinum	59
11	Hemispherical to Normal Emittance Ratios for Tungsten	60
12	Absolute Emittance Data for Copper Sample 1	68
13	Absolute Emittance Data for Copper Sample 3	74
14	Absolute Emittance Data for Copper Sample 5	80
15	Absolute Emittance Data for Copper Sample 7	86
16	Absolute Emittance Data for Copper Sample 8	92
17	Absolute Emittance Data for Tungsten Sample 1	98
18	Absolute Emittance Data for Tungsten Sample 2	106
19	Absolute Emittance Data for Tungsten Sample 3	114
20	Absolute Emittance Data for Platinum Sample 1	122
21	Absolute Emittance Data for Platinum Sample 3	130
22	Absolute Emittance Data for Platinum Sample 6	138

ILLUSTRATIONS

Figure		Page
1	Reflection and Refraction Angles at a Surface	5
2	Polarized Components of Directional Emission From a Plane	6
3	Relative Directional Emittance for Various n and k	10
4	Spectral Directional Emittance Components for Tungsten Determined from n and k	11
5	Relative Total Specular Reflectance for Rough Surfaces	15
6	Representation of a Rough Surface Profile	25
7	Taper Section Mount	29
8	Illustrations for Interpretation of Taper Section Photomicrographs	29
9	Directional Emittance Apparatus	31
10	Schematic Layout of Directional Emittance Apparatus	32
11	Rotating Sample Mount	33
12	Relative Total Directional Intensity Data for Smooth Tungsten	39
13	Optical Constants of Tungsten from Relative Spectral Directional Emittance Data	40
14	Relative Spectral Directional Emittance Data for Tungsten	41
15	Relative Spectral Directional Emittance of Copper	52
16	Relative Total Directional Emittance of Copper	53
17	Relative Spectral Directional Emittance Distribution for Copper	54
18	Relative Spectral Directional Emittance Distribution for Platinum	55
19	Relative Spectral Directional Emittance Distribution for Tungsten	56
20	Surface Interference Photomicrographs of Copper Sample 1 Before and After Emittance Tests	67
21	Typical Profile Traces for Copper Sample 1 Before and After Emittance Tests	67
22	Taper Section Photomicrographs of Copper Sample 1 Before and After Emittance Tests	69
23	Relative Total Directional Emittance, Copper Sample 1	70
24	Relative Spectral Directional Emittance, Copper Sample 1	71
25	Surface Photomicrographs of Copper Sample 3 Before and After Emittance Tests	73
26	Typical Profile Traces for Copper Sample 3 Before and After Emittance Tests	73
27	Cross and Taper Section Photomicrographs Indicating the Surface Condition of Copper Sample 3 Before Emittance Tests	75
28	Relative Total Directional Emittance, Copper Sample 3	76
29	Relative Spectral Directional Emittance, Copper Sample 3	77
30	Surface Photomicrographs of Copper Sample 5 Before and After Emittance Tests	79
31	Typical Profile Traces for Copper Sample 5 Before and After Emittance Tests	79
32	Taper Section Photomicrographs of Copper Sample 5 Before and After Emittance Tests	81
33	Relative Total Directional Emittance, Copper Sample 5	82
34	Relative Spectral Directional Emittance, $\lambda = 2 \mu$, Copper Sample 5	83
35	Relative Spectral Directional Emittance, $\lambda = 4 \mu$, Copper Sample 5	83
36	Surface Photomicrographs of Copper Sample 7 Before and After Emittance Tests	85

ILLUSTRATIONS

Figure		Page
37	Typical Profile Traces for Copper Sample 7 Before and After Emittance Tests	85
38	Cross and Taper Section Photomicrographs Indicating the Surface Condition of Copper Sample 7 Before Emittance Tests	87
39	Relative Total Directional Emittance, Copper Sample 7	88
40	Relative Spectral Directional Emittance, Copper Sample 7	89
41	Surface Photomicrographs of Copper Sample 8 Before and After Emittance Tests	91
42	Typical Profile Traces for Copper Sample 8 Before and After Emittance Tests	91
43	Taper Section Photomicrographs of Copper Sample 8 Before and After Emittance Tests	93
44	Relative Total Directional Emittance, Copper Sample 8	94
45	Relative Spectral Directional Emittance, $\lambda = 2 \mu$, Copper Sample 8	95
46	Relative Spectral Directional Emittance, $\lambda = 4 \mu$, Copper Sample 8	95
47	Surface and Surface Interference Photomicrographs of Tungsten Sample 1 Before and After Emittance Tests	97
48	Typical Profile Traces for Tungsten Sample 1 Before and After Emittance Tests	97
49	Cross and Taper Section Photomicrographs of Tungsten Sample 1 Before and After Emittance Tests	99
50	Relative Total Directional Emittance, Tungsten Sample 1	100
51	Relative Spectral Directional Emittance, $\lambda = 2 \mu$, Tungsten Sample 1	101
52	Relative Spectral Directional Emittance, $\lambda = 1.5 \mu$, Tungsten Sample 1	102
53	Relative Spectral Directional Emittance, $\lambda = 4 \mu$, Tungsten Sample 1	103
54	Surface Photomicrographs of Tungsten Sample 2 Before and After Emittance Tests	105
55	Typical Profile Traces for Tungsten Sample 2 Before and After Emittance Tests	105
56	Cross and Taper Section Photomicrographs of Tungsten Sample 2 After Emittance Tests	107
57	Relative Total Directional Emittance, Tungsten Sample 2	108
58	Relative Spectral Directional Emittance, $\lambda = 2 \mu$, Tungsten Sample 2	108
59	Relative Spectral Directional Emittance, $\lambda = 4 \mu$, Tungsten Sample 2	109
60	Relative Spectral Directional Emittance, $\lambda = 8 \mu$, Tungsten Sample 2	110
61	Relative Spectral Directional Emittance, $\lambda = 6 \mu$, Tungsten Sample 2	111
62	Surface Photomicrographs of Tungsten Sample 3 Before and After Emittance Tests	113
63	Typical Profile Traces for Tungsten Sample 3 Before and After Emittance Tests	113
64	Cross and Taper Section Photomicrographs of Tungsten Sample 3 Before and After Emittance Tests	115

ILLUSTRATIONS

Figure		Page
65	Relative Total Directional Emittance, Tungsten Sample 3	116
66	Relative Spectral Directional Emittance, $\lambda = 2 \mu$, Tungsten Sample 3	117
67	Relative Spectral Directional Emittance, $\lambda = 4 \mu$, Tungsten Sample 3	118
68	Relative Spectral Directional Emittance, $\lambda = 6 \mu$, Tungsten Sample 3	119
69	Relative Spectral Directional Emittance, $\lambda = 8 \mu$, Tungsten Sample 3	119
70	Surface and Surface Interference Photomicrographs of Platinum Sample 1 Before and After Emittance Tests	121
71	Typical Profile Traces for Platinum Sample 1 Before and After Emittance Tests	121
72	Cross and Taper Section Photomicrographs of Platinum Sample 1 Before and After Emittance Tests	123
73	Relative Total Directional Emittance, Platinum Sample 1	124
74	Relative Spectral Directional Emittance, $\lambda = 2 \mu$, Platinum Sample 1	124
75	Relative Spectral Directional Emittance, $\lambda = 1 \mu$, Platinum Sample 1	125
76	Relative Spectral Directional Emittance, $\lambda = 4 \mu$, Platinum Sample 1	125
77	Relative Spectral Directional Emittance, $\lambda = 6 \mu$, Platinum Sample 1	126
78	Relative Spectral Directional Emittance, $\lambda = 1.5 \mu$, Platinum Sample 1	127
79	Surface Photomicrographs of Platinum Sample 3 Before and After Emittance Tests	129
80	Typical Profile Traces of Platinum Sample 3 Before and After Emittance Tests	129
81	Cross and Taper Section Photomicrographs of Platinum Sample 3 After Emittance Tests	131
82	Relative Total Directional Emittance, Platinum Sample 3	132
83	Relative Spectral Directional Emittance, $\lambda = 1.5 \mu$, Platinum Sample 3	133
84	Relative Spectral Directional Emittance, $\lambda = 2 \mu$, Platinum Sample 3	133
85	Relative Spectral Directional Emittance, $\lambda = 4 \mu$, Platinum Sample 3	134
86	Relative Spectral Directional Emittance, $\lambda = 6 \mu$, Platinum Sample 3	135
87	Surface Photomicrographs of Platinum Sample 6 Before and After Emittance Tests	137
88	Typical Profile Traces of Platinum Sample 6 Before and After Emittance Tests	137
89	Cross and Taper Section Photomicrographs of Platinum Sample 6 Before and After Emittance Tests	139
90	Relative Total Directional Emittance, Platinum Sample 6	140
91	Relative Spectral Directional Emittance, $\lambda = 1.5 \mu$, Platinum Sample 6	141

ILLUSTRATIONS

Figure		Page
92	Relative Spectral Directional Emittance, $\lambda = 2 \mu$, Platinum Sample 6	141
93	Relative Spectral Directional Emittance, $\lambda = 4 \mu$, Platinum Sample 6	142
94	Relative Spectral Directional Emittance, $\lambda = 6 \mu$, Platinum Sample 6	142

The exact and approximate theories for reflectance of electromagnetic energy from a randomly rough surface were examined. Results from the exact theory were used to verify the roughness dependence which was previously predicted on the basis of diffraction theory. The examination indicates that additional information about the effects of shadowing and multiple reflections may be obtained if the series solution of the exact approach can be evaluated through the third term.

This report presents the methods used, the general results, and conclusions in Sections 2 through 9. Specific data obtained on each sample are presented in Section 10. This format was selected because of the extent of data obtained on each sample and because it appeared desirable to include as much of this original matter as possible for use by the recipients of the report.

Section 1

INTRODUCTION

The thermal radiative properties of metallic surfaces have been studied by many investigators because of the wide range of practical applications and because of the relative ease of preparing these surfaces. Many data have been published on the reflectance, emittance, and optical constants of metals; however, variations which are greater than can be explained on the basis of difference in experimental method are observed in the reported values. In most cases the data from different investigators cannot be objectively compared or correlated because of insufficient information about the physical, chemical, and geometrical nature of the test specimen surfaces. It is still not possible to predict quantitative values for the radiative properties of a specifically prepared surface without experimental verification.

The thermal radiative properties of a surface determine the interaction between the surface and that part of the electromagnetic spectrum important to radiant heat transfer. The wavelength limits for the thermal spectrum are normally between 0.25 and 30 μ ; however, for specialized material applications at extremely high or low temperatures, it is necessary to consider an even broader spectrum. Surface properties which are important in establishing radiant behavior are surface roughness, surface chemistry, and the physical state of the surface layer of material. The effects of these parameters on the radiative properties of a surface are generally a function of the wavelength of the emitted or reflected energy. Thus, while a surface condition may affect the radiant properties of a material in one region of the spectrum e. g. the ultraviolet or visible, the same condition may leave the remainder of the spectrum, i. e., the near and far infrared, unaffected.

The object of this program was to determine experimentally and analytically the influence of surface condition on the thermal radiation properties of three pure metals. Experimental techniques were developed for the measurement of emittance properties on carefully prepared samples of copper, tungsten, and platinum. The surface geometry and physical condition of the samples were carefully evaluated by profilometric and photomicrographic methods. Extensive studies of the surface chemistry of the samples could not be made; however, considerable care was taken to maintain surface purity. The problem of maintaining high surface purity while, at the same time, achieving a wide range of roughness values was not solved with complete satisfaction.

Experimental determinations of the absolute total and spectral normal emittance for each sample were made at several temperatures between 500 and 1650°K and at wavelengths between 0.25 and 2 μ . At each test temperature, the relative total directional emittance of the sample was measured at angles out to ± 87 deg from the normal to the sample surface. Similarly, at each wavelength the relative spectral directional emittance for the parallel and perpendicular polarized components was measured over the same angular range, as energy permitted. Analytical methods were then used to obtain the optical constants for each metal from the experimental data for the smooth samples.

Section 2

NOMENCLATURE

The following definitions for thermal radiation properties of materials and surfaces will be used throughout this report and are in accordance with the terminology advocated by Worthing (Reference 1) and accepted for use by the National Bureau of Standards (Reference 2). Words ending in "ivity" are reserved for intrinsic properties of the bulk material; words ending in "ance" denote properties of the specimen surface; and words ending in "ion" describe acts or processes. Therefore, emission is the process by which energy is emitted by a surface or body by virtue of its temperature; emittance is a property of the surface measured relative to the same property for a blackbody; and emissivity is an intrinsic property of the pure material.

The symbols used in this report are defined in the following list.

A	area
c_1	first radiation constant
c_2	second radiation constant
$E = \sigma T^4$	total emissive power of a blackbody per unit area
F	function describing the efficiency of the optical system
h	responsivity (of a detector)
i	$\sqrt{-1}$
I	current
J	spectral radiant intensity ($\text{W}/\text{cm}^3\text{-sr}$)
k	imaginary part of complex index of refraction (absorption index)
k_0	extinction coefficient
n	real part of complex index of refraction
\bar{n}	complex index of refraction of a material
n_0	index of refraction of surrounding medium
T	absolute temperature ($^{\circ}\text{K}$)
v	detector response
V	voltage
α	absorptance
ϵ	emittance
ϵ_{∞}	emissivity (emittance of a pure, smooth, polished sample)
ξ	surface plane of a sample
θ	angle of emission
λ	wavelength
ρ	reflectance
σ	Stefan-Boltzmann constant

σ_m	root-mean-square surface roughness
τ	transmittance
ϕ	complex angle of refraction in a metal
χ	plane of emission
ψ	angle of incidence relative to the normal of the mean surface plane
Ω	solid angle
K	a dimensionless group term, defined on page 13

Subscripts

∞	change from a surface characteristic to an intrinsic property of the material (e.g., ϵ and ϵ_∞)
s	property of the sample
e	property of the environment
w	property of the window
b	property of the blackbody
\parallel	electric vector vibrating in plane of emission
\perp	electric vector vibrating perpendicular to plane of emission
N	direction normal to the surface
c	chamber
a	ambient

Parentheses

(θ, λ, T)	spectral directional
(θ_N, λ, T)	spectral normal
(λ, T)	spectral hemispherical
(θ, T)	total directional
(θ_N, T)	total normal
(T)	total hemispherical
$\frac{(\theta, \lambda, T)}{(\theta_N, \lambda, T)}$	relative spectral directional
$\frac{(\theta, T)}{(\theta_N, T)}$	relative total directional

Section 3

RADIANT PROPERTIES OF SURFACES

3.1 SMOOTH SURFACES

In the interior of an opaque material of uniform temperature, at distances from the surface which yield complete absorption for entering radiation, blackbody conditions are fulfilled. Therefore, radiant energy generated within the bulk of an opaque material is blackbody energy. Part of the internally generated radiant energy is transmitted, or is refracted into hemispherical space above the surface plane; the remainder is internally reflected and re-absorbed.

In Figure 1 the surface plane of the material is represented by ξ ; \bar{n} is the index of refraction of the material and n_o is the index of refraction of the surrounding medium. Internal radiant energy incident on the surface at angle ϕ is either internally reflected at angle ϕ' or is transmitted and refracted into the surrounding medium at angle θ . Similarly for the reflectance case, external energy incident on the surface at angle ψ is either externally reflected at angle θ or is refracted into the material at angle ϕ' .

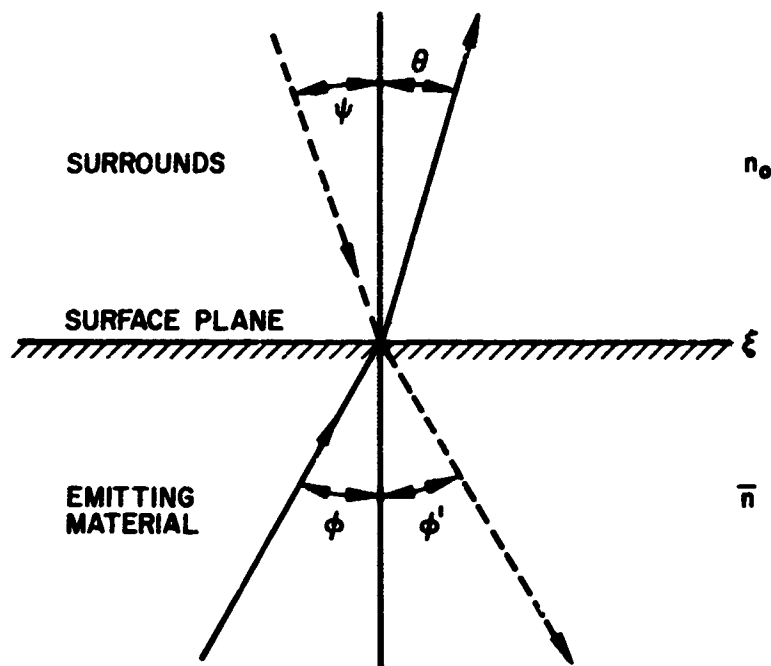


Figure 1 Reflection and Refraction Angles at a Surface

In Figure 2 the plane of emission, χ , is defined as a horizontal plane perpendicular to the surface plane ξ . The angle of emission, θ , defines the direction of radiant emission in the plane of emission, and is measured from the normal to the sample plane.

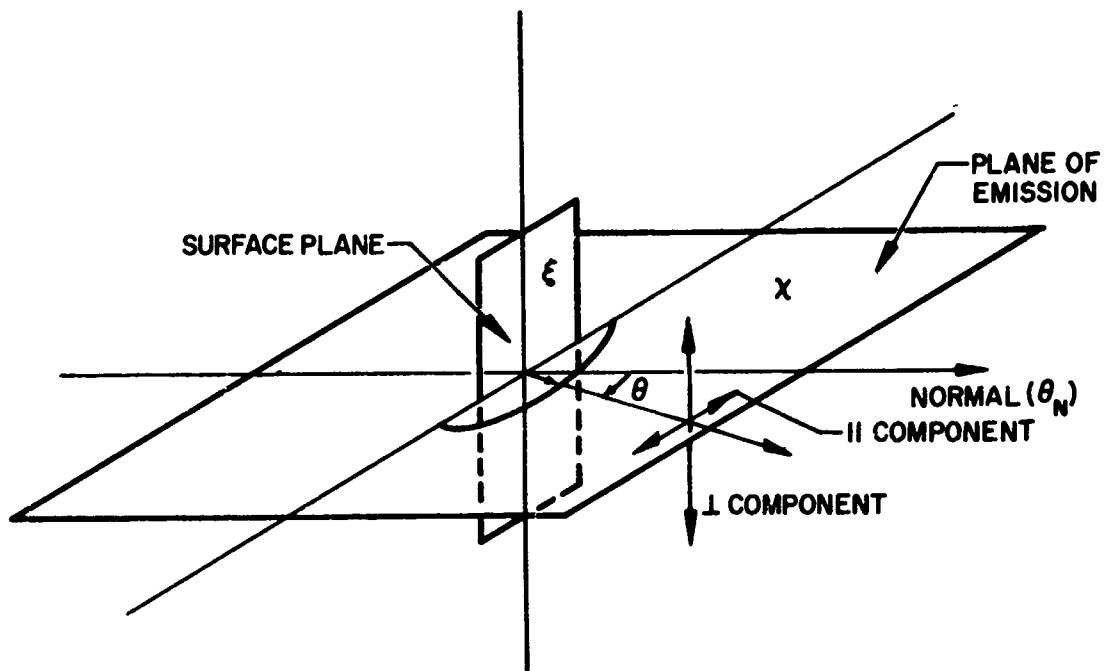


Figure 2 Polarized Components of Directional Emission From a Plane

The intensity of internally generated blackbody energy transmitted by the material surface and refracted into the surrounding space in the direction θ is given by

$$J(\theta, \lambda, T) = \tau(\phi, \lambda, T) J_b(\phi, \lambda, T) \quad (1)$$

where

$$J_b(\phi, \lambda, T) = \frac{c_1 \lambda^{-5}}{\pi \left(e^{\frac{c_2}{\lambda T}} - 1 \right)} \quad (2)$$

which is Planck's radiation law for the spectral intensity of a blackbody.

The spectral directional emittance is defined as

$$\epsilon(\theta, \lambda, T) = J(\theta, \lambda, T) / J_b(\theta, \lambda, T) \quad (3)$$

Thus,

$$\epsilon(\theta, \lambda, T) = \tau(\phi, \lambda, T) \quad (4)$$

for an optically opaque material, since for blackbody energy $J_b(\phi, \lambda, T) = J_b(\theta, \lambda, T)$.

For an opaque material, Kirchoff's law holds and

$$\epsilon(\theta, \lambda, T) = 1 - \rho(\theta, \lambda, T) \quad (5)$$

The spectral directional reflectance $\rho(\theta, \lambda, T)$ may be expressed in terms of the polarized spectral directional reflectance components by

$$\rho(\theta, \lambda, T) = \frac{1}{2} [\rho_{\parallel}(\theta, \lambda, T) + \rho_{\perp}(\theta, \lambda, T)] \quad (6)$$

where ρ_{\parallel} and ρ_{\perp} are, respectively, the polarized reflectances with the electric vector vibrating in and perpendicular to the plane of emission. The two polarized components are expressed in terms of the incident and refracted angles by the Fresnel equations (Reference 3)

$$\rho_{\perp}(\theta, \lambda, T) = \frac{\sin^2(\phi - \theta)}{\sin^2(\phi + \theta)}$$

and

$$\rho_{\parallel}(\theta, \lambda, T) = \frac{\tan^2(\phi - \theta)}{\tan^2(\phi + \theta)} \quad (7)$$

Thus the spectral directional emittance may be written as

$$\epsilon(\theta, \lambda, T) = 1 - \frac{1}{2} \left[\frac{\sin^2(\phi - \theta)}{\sin^2(\phi + \theta)} + \frac{\tan^2(\phi - \theta)}{\tan^2(\phi + \theta)} \right] \quad (8)$$

The spectral directional emittance of the material is now expressed in terms of the angle of incidence ϕ , and the angle of refraction or emission θ as

$$\epsilon(\theta, \lambda, T) = f(\phi, \theta, \lambda, T) \quad (9)$$

The angle of incidence at the surface for internally generated radiation is related to the angle of emission by Snell's law,

$$n_0 \sin \theta = \bar{n} \sin \phi \quad (10)$$

In a dispersive absorbing medium, the index of refraction is complex and is written as

$$\bar{n} = n - ik = n(1 - ik_0) \quad (11)$$

Therefore, the angle of incidence, for an absorbing medium in vacuum ($n_0 = 1$), is also complex and is defined by

$$\bar{n} \cos \phi = (\bar{n}^2 - \sin^2 \theta)^{1/2} = a - ib \quad (12)$$

The expressions for a and b in terms of n, k , and θ are obtained by substitution of Equations 10 and 11 into Equation 12:

$$a^2 = \frac{1}{2} \left\{ [(n^2 - k^2 - \sin^2 \theta)^2 + 4n^2 k^2]^{1/2} + (n^2 - k^2 - \sin^2 \theta) \right\} \quad (13)$$

$$b^2 = \frac{1}{2} \left\{ [(n^2 - k^2 - \sin^2 \theta)^2 + 4n^2 k^2]^{1/2} - (n^2 - k^2 - \sin^2 \theta) \right\} \quad (14)$$

The complex angle of incidence ϕ may be eliminated from Equations 7 by the use of Equations 10, 11, and 12. The polarized spectral directional reflectance components will then be expressed in terms of the quantities a, b , and θ :

$$\rho_{\perp}(\theta, \lambda, T) = \frac{a^2 + b^2 - 2a \cos \theta + \cos^2 \theta}{a^2 + b^2 + 2a \cos \theta + \cos^2 \theta} \quad (15)$$

$$\rho_{\parallel}(\theta, \lambda, T) = \rho_{\perp}(\theta, \lambda, T) \frac{a^2 + b^2 - 2a \sin \theta \tan \theta + \sin^2 \theta \tan^2 \theta}{a^2 + b^2 + 2a \sin \theta \tan \theta + \sin^2 \theta \tan^2 \theta} \quad (16)$$

From Equation 5 the directional components of emittance may be expressed as

$$\epsilon_{\perp}(\theta, \lambda, T) = 1 - \rho_{\perp}(\theta, \lambda, T) = \frac{4a \cos \theta}{a^2 + b^2 + 2a \cos \theta + \cos^2 \theta} \quad (17)$$

$$\epsilon_{\parallel}(\theta, \lambda, T) = 1 - \rho_{\parallel}(\theta, \lambda, T) = \frac{\epsilon_{\perp}(\theta, \lambda, T)}{\cos^2 \theta} \frac{a^2 + b^2 + \sin^2 \theta}{a^2 + b^2 + 2a \sin \theta \tan \theta + \sin^2 \theta \tan^2 \theta} \quad (18)$$

The emittance is given by half the sum of the components. Therefore, combining Equations 17 and 18 gives

$$\epsilon(\theta, \lambda, T) = \frac{1}{2} \epsilon_{\perp}(\theta, \lambda, T) \left[1 + \frac{a^2 + b^2 + \sin^2 \theta}{\cos^2 \theta (a^2 + b^2 + 2a \sin \theta \tan \theta + \sin^2 \theta \tan^2 \theta)} \right] \quad (19)$$

Since a and b from Equations 13 and 14 are functions of n, k , and θ , the spectral directional emittance of the material as a function of the angle of emission is now expressed in terms of n, k , and θ :

$$\epsilon(\theta, \lambda, T) = f(\theta, n, k) = \epsilon(\theta, n, k) \quad (20)$$

The spectral normal emittance of the surface may be determined from Equations 13, 14, and 19 for $\theta = 0$:

$$\epsilon(\theta_N, \lambda, T) = \frac{4n}{(n+1)^2 + k^2} \quad (21)$$

The spectral directional emittance at an angle θ may be normalized to that at $\theta = 0$:

$$\frac{\epsilon(\theta, \lambda, T)}{\epsilon(\theta_N, \lambda, T)} = f(\theta, \lambda, T) \quad (22)$$

This is called the normalized spectral directional emittance. The normalized emittance components are then

$$\frac{\epsilon_{\perp}(\theta, \lambda, T)}{\epsilon_{\perp}(\theta_N, \lambda, T)} = \frac{(n+1)^2 + k^2}{4n} \frac{4a \cos \theta}{a^2 + b^2 + 2a \cos \theta + \cos^2 \theta} \quad (23)$$

$$\frac{\epsilon_{\parallel}(\theta, \lambda, T)}{\epsilon_{\parallel}(\theta_N, \lambda, T)} = \frac{\epsilon_{\perp}(\theta, \lambda, T)}{\epsilon_{\perp}(\theta_N, \lambda, T)} \frac{a^2 + b^2 + \sin^2 \theta}{\cos^2 \theta (a^2 + b^2 + 2a \sin \theta \tan \theta + \sin^2 \theta \tan^2 \theta)} \quad (24)$$

The normalized spectral emittance becomes

$$\frac{\epsilon(\theta, \lambda, T)}{\epsilon(\theta_N, \lambda, T)} = \frac{1}{2} \frac{\epsilon_{\perp}(\theta, \lambda, T)}{\epsilon_{\perp}(\theta_N, \lambda, T)} \left[1 + \frac{a^2 + b^2 + \sin^2 \theta}{\cos^2 \theta (a^2 + b^2 + 2a \sin \theta \tan \theta + \sin^2 \theta \tan^2 \theta)} \right] \quad (25)$$

Values of the normalized relative directional emittance, $\epsilon(\theta, \lambda, T)/\epsilon(\theta_N, \lambda, T)$, evaluated from Equation 25 for various combinations of n and k , are shown in Figure 3 of Reference 4.

Values of the normalized spectral directional emittance components $\epsilon_{\perp}(\theta, \lambda, T)/\epsilon_{\perp}(\theta_N, \lambda, T)$ and $\epsilon_{\parallel}(\theta, \lambda, T)/\epsilon_{\parallel}(\theta_N, \lambda, T)$ which are evaluated from Equations 23 and 24 respectively for $n = 3.38$ and $k = 2.32$ (data from Reference 5, on tungsten for $\lambda = 2\mu$ and $T = 1100^\circ\text{K}$) are shown in Figure 4. The spectral direction emittance, $\epsilon(\theta, \lambda, T)/\epsilon(\theta_N, \lambda, T)$, derived from Equation 25 is also shown.

3.2 ROUGH SURFACES

The previous subsection presented the relationship between optical constants and radiant properties for a material at fixed wavelength and temperature. The treatment is based upon classical optics and is applicable to the very special circumstances where a smooth, optically polished surface is realized. Unfortunately, such surfaces are not normally encountered in engineering practice. Most real situations also require consideration of surface geometry, surface chemistry, and physical state, since these effects on radiant properties may often equal or exceed the influence of

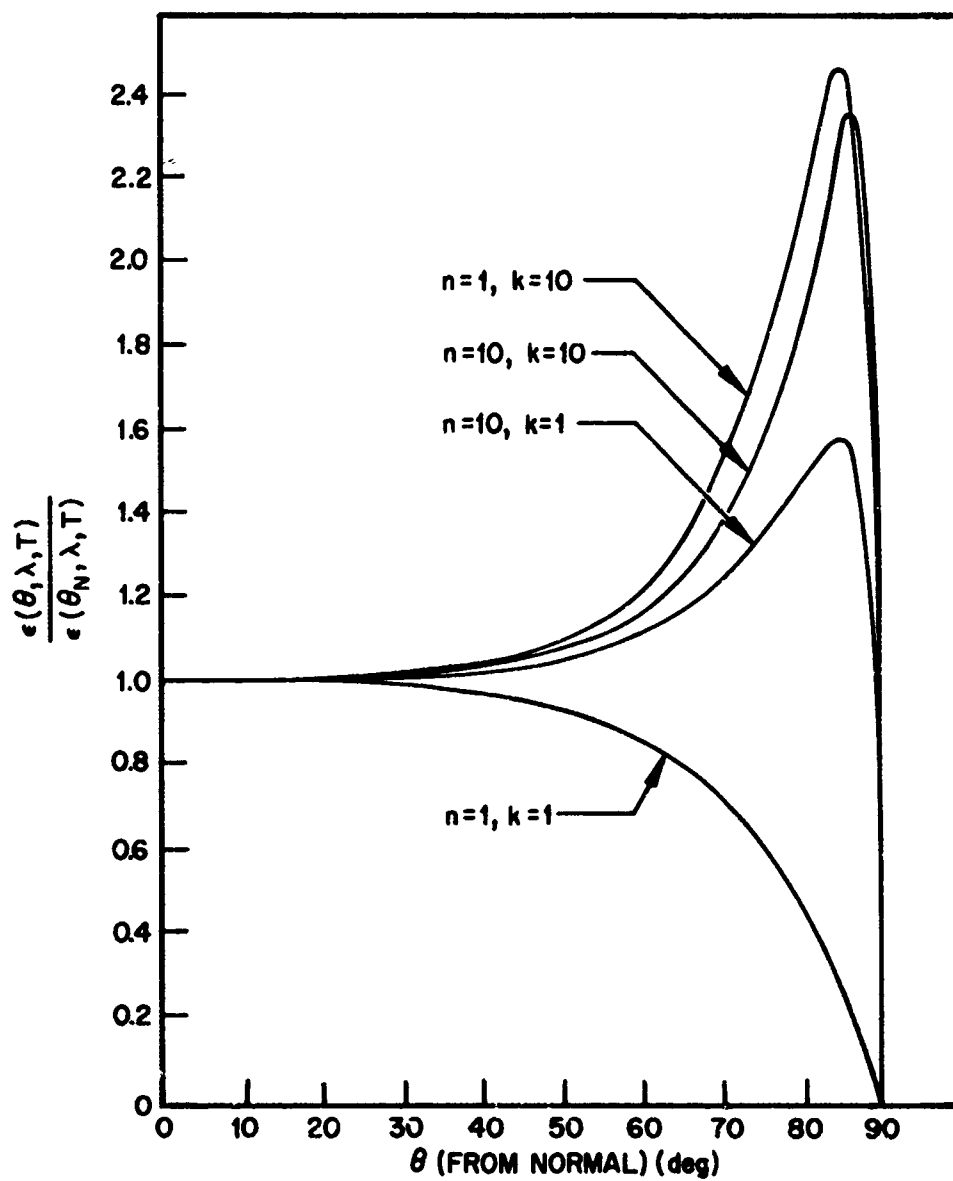


Figure 3 Relative Directional Emittance for Various n and k

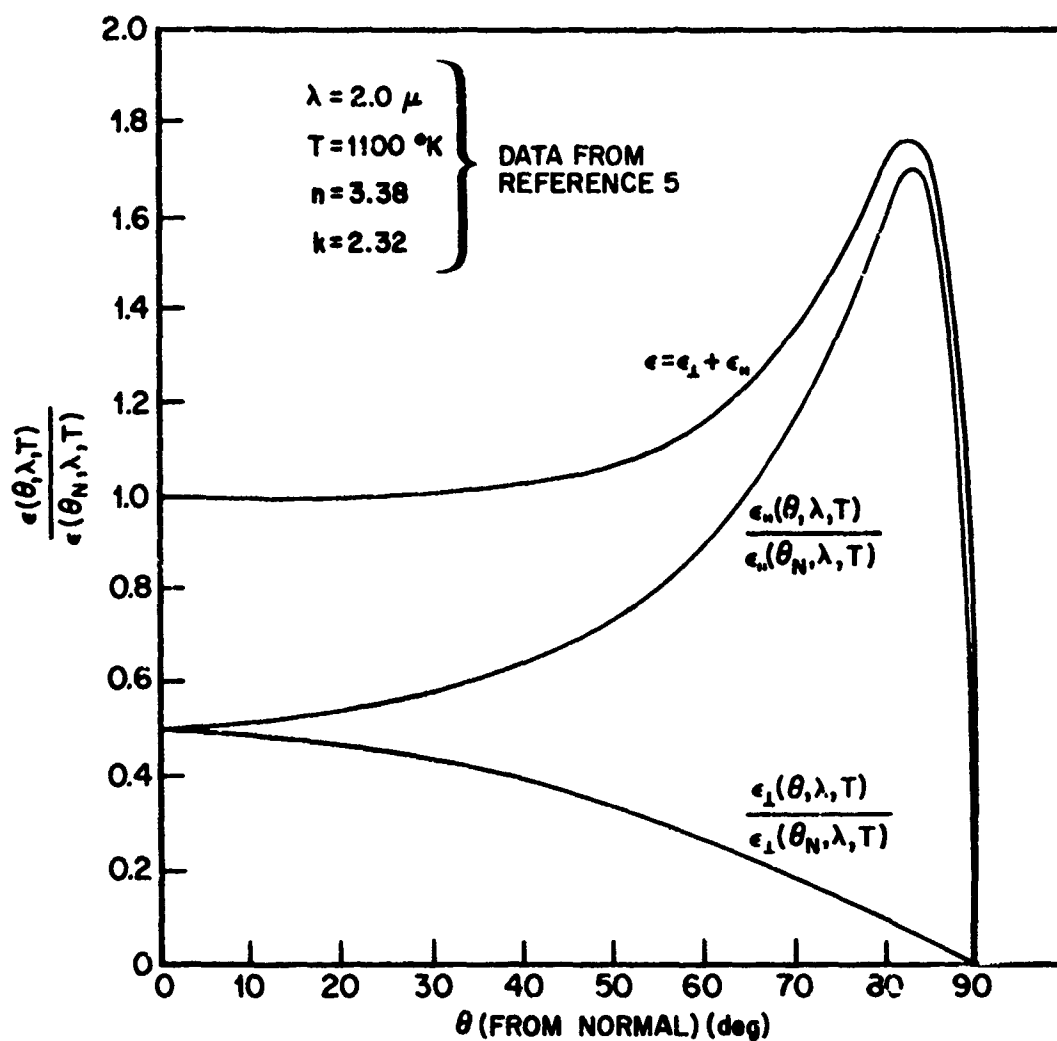


Figure 4 Spectral Directional Emittance Components for Tungsten Determined from n and k

the optical properties of the pure material. To predict the overall radiant behavior of a rough oxidized surface at elevated temperatures would require a detailed characterization of the surface in terms of its physical and chemical state in conjunction with a sufficient theoretical understanding for analysis of the combined effects. At present, such prediction is not possible because of both the absence of adequate theories and the formidable task of adequate characterization. Nonetheless, some theoretical understanding of the role of surface roughness in establishing radiant properties has been attained and will be considered in this subsection.

Theoretical treatments have concentrated upon reflection of energy from either a well-defined or arbitrary rough surface having infinite electrical conductivity. Two basic analytical approaches have been used. The first involves the application of Fresnel and Rayleigh diffraction theories to a stochastic rough surface. The work of Davies (Reference 6) clearly demonstrates this method, although other investigators have treated the problem from a slightly different viewpoint (Reference 7). The second and more rigorous approach requires the solution of Maxwell's equations with the complex boundary conditions involved. This analytical technique was first presented by Rice (Reference 8) for random surfaces. Here, owing to the mathematical complexity of the solution, only a first-order approximation was obtained. However, the method has the inherent advantage of accounting for finite electrical conductivity and shadowing, whereas the diffraction theories require significant modifications to include approximation of these effects. A detailed treatment of the analytical approaches used by many investigators has been prepared as a text by Beckmann and Spizzichino and is presently available (Reference 9). This publication presents an excellent review of the subject with emphasis on diffraction theory approaches.

Davies (Reference 6) has determined that the specular component of energy reflected from a rough surface will depend upon the angle of incidence ψ , wavelength λ , and root-mean-square roughness σ_m . For a rough reflector Davies found that the ratio of energy contained in the coherent reflected beam to that incident upon the reflecting surface is $\exp [-(4\pi\sigma_m \cos \theta/\lambda)^2]$. The assumptions made in arriving at this result were: the surface is a perfect reflector; the surface is only slightly rough, $\sigma_m/\lambda \ll 1$; peak-to-peak spacing is large so that no interreflections occur; and the roughness has Gaussian distribution. The solution has been extended to a finite conductor under the same assumptions by including the surface reflectivity. The specular reflectance of a slightly rough surface is then given by

$$\rho(\theta, \lambda, T) = \rho_\infty(\theta, \lambda, T) \exp [-(4\pi\sigma_m \cos \theta/\lambda)^2] \quad (26)$$

The validity of this result has been established experimentally by Bennett and Porteus (Reference 9) through very careful measurements on aluminized ground glass. For the range of roughness used ($0.15 \mu < \sigma_m < 1 \mu$), good correlation was found between theory and measurement. Additional work by Bennett (Reference 10) reports the effectiveness of ground glass scatter plates and further justifies the use of Equation 26 where the surface meets the theoretical criteria. Porteus (Reference 11) has extended the theory to include the behaviour expected when non-Gaussian surfaces (surfaces referred to as "abnormal") are encountered.

Birkebak, Sparrow, Eckert, and Ramsey (Reference 12) have reported measurements of the specular reflectance of blackbody energy from roughened nickel surfaces

relative to polished surfaces of the same material. Since the blackbody temperatures were characteristic of long wavelengths ($325^\circ\text{K} \leq T \leq 633^\circ\text{K}$) and the surfaces only slightly rough ($0.14\mu \leq \sigma_m \leq 0.86\mu$), it is of interest to attempt correlation with the theoretical relationship in Equation 26. To accomplish this requires an expression for the reflectance which includes the entire blackbody spectrum.

The total specular reflectance is defined as

$$\rho(\theta, T) = \frac{1}{\sigma T^4} \int_0^\infty \rho(\theta, \lambda, T) E_{b\lambda} d\lambda \quad (27)$$

where σ is the Stefan-Boltzmann constant, T the absolute temperature of the incident beam of radiation, and $E_{b\lambda}$ the spectral emissive power of a blackbody at temperature T . Substitution of the Planck distribution law for $E_{b\lambda}$ and Equation 26 for $\rho(\theta, \lambda, T)$ gives

$$\rho(\theta, T) = \frac{c_1}{\sigma T^4} \int_0^\infty \frac{\rho_\infty(\theta, \lambda, T) \lambda^{-5} \exp(-16\pi^2 \sigma_m^2 \cos^2 \theta / \lambda^2) d\lambda}{\exp(c_2/\lambda T) - 1} \quad (28)$$

where c_1 and c_2 are the first and second radiation constants in the Planck distribution law, $c_1 = 3.741 \times 10^{-12} \text{ W-cm}^2$ and $c_2 = 1.439 \text{ cm}^\circ\text{K}$. At long wavelengths, say $\lambda > 1\mu$, the spectral reflectance of the smooth surface is relatively insensitive to variation of wavelength (Reference 13). As an approximation, Equation 28 can be rearranged as

$$\frac{\rho(\theta, T)}{\rho_\infty(\theta, T)} = \frac{c_1}{\sigma T^4} \int_0^\infty \frac{\lambda^{-5} \exp(-16\pi^2 \sigma_m^2 \cos^2 \theta / \lambda^2)}{\exp(c_2/\lambda T) - 1} d\lambda \quad (29)$$

The integral in Equation 29 can be integrated directly by first introducing the new variable $t \equiv (1/\lambda)$ and expanding the exponential term in the numerator into series form. The result is

$$\frac{\rho(\theta, T)}{\rho_\infty(\theta, T)} = 1 + \frac{1}{6} \sum_{n=1}^{\infty} (-1)^n \xi(4+2n) \Gamma(4+2n) (4\pi K)^{2n} \quad (30)$$

where $\xi(n)$ and $\Gamma(n)$ represent the zeta and gamma functions, respectively, and $K = (\sigma_m T \cos \theta / c_2)$ is a dimensionless group.

The series given in Equation 30, though exact, is an oscillating one and converges very slowly for values of K on the order of 10^{-2} or larger. Unfortunately, such values represent most actual systems of physical interest. However, a more convenient though approximate expression is feasible. The approximate result is obtained by use of the Wien distribution law for blackbody spectral energy. The Wien distribution gives excellent agreement with the Planck distribution except in the range $\lambda T > 0.3 \text{ cm}^\circ\text{K}$ (Reference 13), where the absolute intensity is very

small and normally insignificant in engineering calculations. From Equation 27, the total specular reflectance $\rho(\theta, T)$, based on the Wien distribution law, becomes

$$\frac{\rho(\theta, T)}{\rho_{\infty}(\theta, T)} = \frac{c_1}{\sigma T^4} \int_0^{\infty} \lambda^{-5} \exp \left[- \left(\frac{c_2}{\lambda T} + \frac{16\pi^2 \sigma_m^2 \cos^2 \theta}{\lambda^2} \right) \right] d\lambda \quad (31)$$

A change of the integration variable from λ to t ($t \equiv 1/\lambda$) yields

$$\frac{\rho(\theta, T)}{\rho_{\infty}(\theta, T)} = \frac{c_1}{\sigma T^4} \int_0^{\infty} t^3 \exp \left[- \left(\frac{c_2 t}{T} + 16\pi^2 \sigma_m^2 t^2 \cos^2 \theta \right) \right] dt \quad (32)$$

which is of a form easily treated by a Laplace transformation. Appropriate manipulations through a Laplace transform give the following result:

$$\frac{\rho(\theta, T)}{\rho_{\infty}(\theta, T)} = \frac{4}{3} \left(\frac{1}{8\pi K} \right)^4 \left(1 + \frac{1}{64\pi^2 K^2} \right) - \frac{4\sqrt{\pi}}{3} \left(\frac{1}{8\pi K} \right)^5 \left(\frac{3}{2} + \frac{1}{64\pi^2 K^2} \right) \exp \left(\frac{1}{64\pi^2 K^2} \right) \operatorname{erfc} \left(\frac{1}{8\pi K} \right) \quad (33)$$

With the asymptotic expressions of $\operatorname{erfc}(\chi)$ for $\chi \gg 1$,

$$\operatorname{erfc}(\chi) = \frac{1}{\chi\sqrt{\pi}} e^{-\chi^2} \left[1 - \frac{1}{2\chi^2} + \frac{3}{(2\chi^2)^2} - \dots \right] \quad (34)$$

and for $\chi \ll 1$,

$$\operatorname{erfc}(\chi) = 1 - \frac{2}{\sqrt{\pi}} \chi + \frac{2}{\sqrt{\pi}} \frac{\chi^3}{3} - \dots \quad (35)$$

it can be shown that for $8\pi K \gg 1$

$$\frac{\rho(\theta, T)}{\rho_{\infty}(\theta, T)} = \frac{4}{3} \left(\frac{1}{8\pi K} \right)^4 \left(1 - \frac{3\sqrt{\pi}}{16\pi K} \right) \quad (36)$$

and for $8\pi K \ll 1$

$$\frac{\rho(\theta, T)}{\rho_{\infty}(\theta, T)} = 1 - 5(8\pi K)^2 \quad (37)$$

Figure 5 presents the results obtained from integration of Equation 28 and also shows experimental data from (Reference 12). The exact solution was obtained by numerical integration of Equation 29 using a digital computer. The dashed line shows the approximate solution of Equation 33, while the asymptotic expression for $8\pi K \ll 1$ is plotted as a broken line. The results show the approximate expression to agree

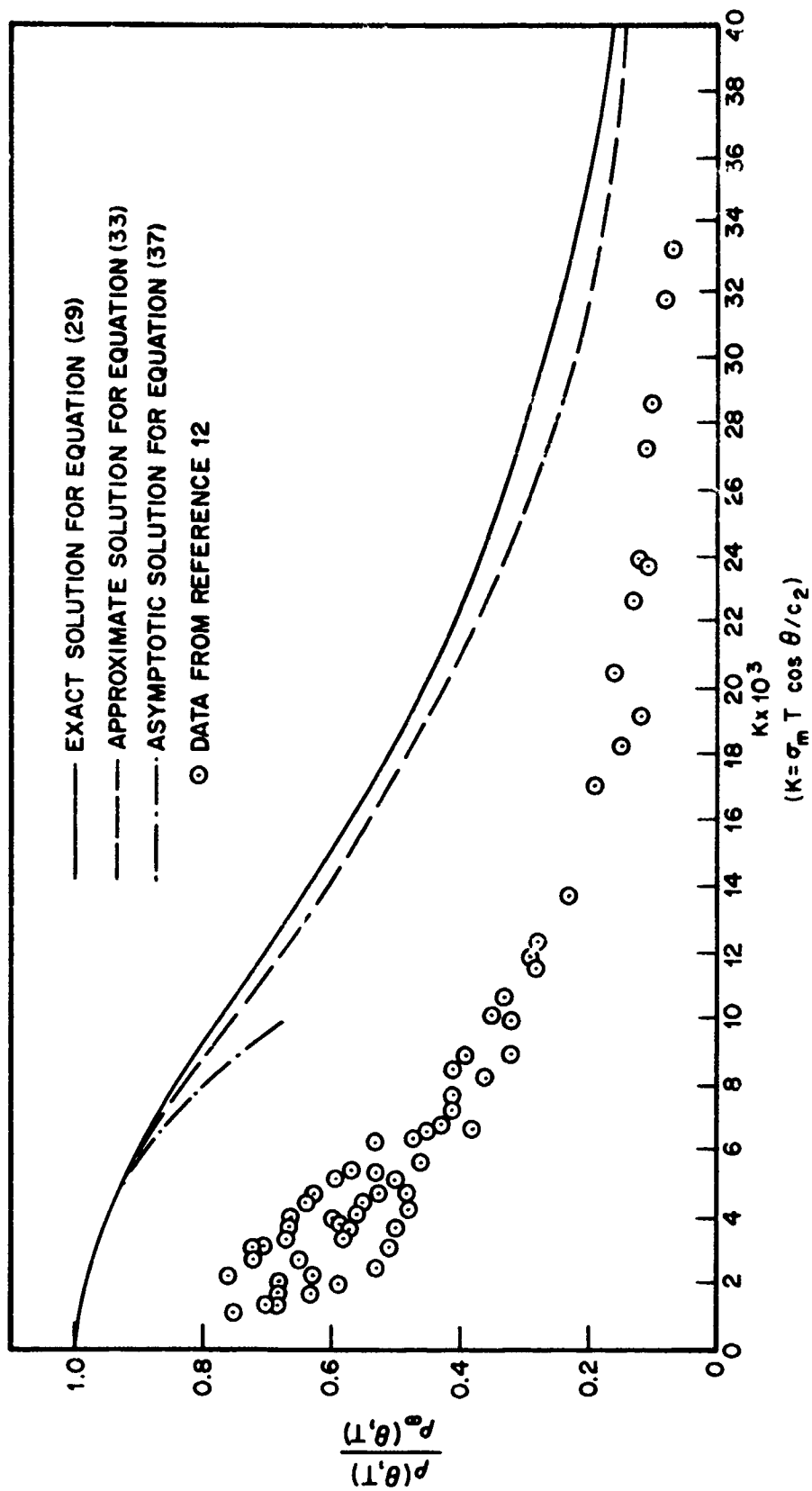


Figure 5 Relative Total Specular Reflectance for Rough Surfaces

very well with the exact result, while the asymptotic expression is inadequate except for extremely low values of K . The asymptotic expression of Equation 36 for $8\pi K \gg 1$ is not shown, since it compares favorably only for values of $K > 200$.

The difference between experimental and theoretical results is large, although the trend with increasing K is clearly obtained. A number of reasons may be postulated for the low magnitude of measured values. One of these is that the reported surface roughness was determined with a stylus profilometer. Roughness measurements with this type of instrument are liable to error, with values being low by as much as 100%. (See Reference 9 and Section 8 of this report.) A second and equally significant source of error is that the samples were not annealed after grinding prior to the reflectance determinations. Surface strain will cause a significant decrease in the inherent reflectance properties. Later work reported by Birkebak and Eckert (Reference 14) shows the same effect on the specular spectral reflectance of ground nickel surfaces. Reference 14 reports the relative spectral reflectance for both aluminized ground glass and ground nickel samples having the same order of roughness. Relative reflectance values for the nickel samples were observed to be considerably lower than those for an equally rough aluminized sample. However, the distribution of energy about the normal was found to be approximately the same. For this reason, it is assumed that surface strain played a strong role in establishing the absolute reflectance of the nickel specimens.

The above theoretical criteria were established using the approximate diffraction theory approach and are limited to cases where interreflections and shadowing do not exist. An exact approach, wherein solutions are sought to Maxwell's equations (Rayleigh method), has been suggested by Rice (Reference 8) and is presented in detail in the Appendix. The method in its general form could demonstrate the effects of shadowing, multiple reflections, and finite electrical conductivity. However, the solution is obtained in series form and is so unwieldy that only the second-order result, which applies to a slightly rough surface, is reported. The result obtained from the second-order solution is

$$\frac{\rho(\theta, \lambda, T)}{\rho_{\infty}(\theta, \lambda, T)} = 1 - 16\pi^2 \sigma_m^2 / \lambda^2 \quad (38)$$

for the specular reflectance of a horizontally polarized wave. It is interesting to note that this form is identical to that obtained from the diffraction theory up to the second-order term. Therefore, no additional information is obtained concerning shadowing or multiple reflections. However, the calculation is incomplete in that it does not include either the vertically polarized wave or the diffuse component. These should be included in the second-order solution as they may clarify the problem of depolarization and provide information on absorptance. An even more valuable result would be that obtained by extending the solution to include the third-order terms, as these may contain the variables which demonstrate the effects of shadowing and multiple reflections. This extension is planned as future program activity.

The diffraction theory solutions have the inherent disadvantage of being unable to account for finite conductivity, shadowing, or multiple reflections without departing from the basic formulation involved. This limitation results in a prediction of the spatial distribution of energy without an indication of changes in absolute values. The predicted hemispherical reflectance for a rough surface is identical to that for a smooth surface when using the diffraction theory. An extension of diffraction theory to include finite conductivity on periodic surfaces has been proposed by Lysanov (Reference 15),

and the technique could probably be extended to random surfaces. Fok (Reference 16) has suggested a shadowing effect which may further extend the diffraction theory approach to prediction of changes in absolute reflectance. It is apparent that present reflectance theories are not yet well enough developed to permit predictions of the reflective behavior of rough surfaces in terms of both distribution and magnitude.

Theories for the emissive behavior of a rough surface are even less well developed than those for reflective behavior. Limitations in the diffraction theory are such that the predicted spectral hemispherical emittance of a rough surface will be identical to that of a smooth one. Where slight roughness exists, preventing the occurrence of multiple reflections, this is a proper result. However, in rougher surfaces the hemispherical emittance will increase and multiple reflections must be accounted for. Further, the reflectance theories result in formulation for the distribution of reflected energy, while for the emitting surface the distribution of absorbed energy is required. At present, it appears that analysis for emissive behavior will require an extension of the exact approach proposed by Rice wherein the method inherently accounts for the effects that lead to an increase in emissive power.

Section 4

SAMPLE PREPARATION PROCEDURES

4.1 SELECTION OF SAMPLES

Copper, tungsten, and platinum were selected to be studied in this program because they are representative of monovalent, transition, and noble metals. In addition, previous workers have investigated tungsten and platinum in detail, thus furnishing a good deal of comparative data. Preliminary investigations of roughening techniques disclosed that the roughest producible surface finish for these materials, while still maintaining other necessary sample features, was on the order of 300 to 400 μ in. The principal restriction to obtaining greater roughness was the necessarily thin strip size of 2 in. by 8 in. by 0.010 in. This sample geometry was required for installation in the angular emittance device and also for attainment of the following:

- Sufficiently high temperatures with resistive heating to supply the required energy for directional total, spectral, and polarized spectral measurements as a function of wavelength between 1 and 15 μ and angle out to ± 87 deg from the normal
- A uniform high-temperature region up to 1600°K over the center 5/8-in. portion of the strip

In addition to the sample size requirements as related to temperature uniformity and electrical resistance, it was necessary or desirable to achieve the following sample characteristics:

- High purity
- Uniform and reproducible roughness characteristics over the entire surface area
- Roughness characteristics which were arbitrary in nature with near Gaussian distribution of profile

A discussion of the sample finishing methods investigated for possible use during this study is contained in subsection 4.2. A description of the methods finally used for roughening the emittance samples is given in subsection 4.3.

Copper samples were prepared from 2 in. by 8 in. by 0.015 in. strips of OFHC cold-rolled copper having a purity specification of 99.9+ % copper. Typical chemical analyses for OFHC copper are reported in Reference 17. An independent spectrographic analysis of the as-received copper was made during this program and confirmed the absence of any significant metallic impurities. Roll marks were apparent on the copper surface, parallel to the long (8 in.) dimension of the strips. A Proficorder trace transverse to the roll marks indicated a peak-to-peak spacing of about 6000 μ in., an average peak-to-valley height of 12 μ in., and a rms roughness of 6 μ in.

The tungsten sample strips were 2 in. by 8 in. by 0.010 in. These were obtained from the General Electric Company, Cleveland, Ohio, along with the following analysis of the powder lot used in forming the sheet:

<u>Element</u>	<u>Ingot 6115D Concentration (ppm)</u>
Mo	29
Fe, Si, Cu, Al, Mn, Sn	<7
Ca, Cr, Ni, Mg, Co, Zr	<3

An independent spectrographic analysis of the as-received tungsten confirmed the absence of any significant metallic impurities in the sheet. The as-received strips appeared bright and smooth, with faintly visible roll marks. A Proficorder trace transverse to the long dimension of the strips indicated the presence of peaks and valleys with an average peak-to-peak spacing of 1260 $\mu\text{in.}$, and a calculated rms roughness of 1.5 $\mu\text{in.}$

The platinum samples were 2 in. by 8 in. by 0.008 in. strips obtained from the Western Gold and Platinum Company, Belmont, California. These samples were certified to have a purity of 99.9+% and were especially rolled with Wesgo's high-quality rollers. The as-received strips appeared bright and smooth with no noticeable roll marks. A Proficorder trace taken transverse to the length of the strip was flat, indicating no measurable roughness; however, an interference photomicrograph of the surface indicated the presence of ridges and valleys with peak-to-peak spacings of approximately 500 $\mu\text{in.}$ and peak-to-valley depths between 5 and 20 $\mu\text{in.}$ (see Section 8).

4.2 SURFACE FINISHING METHODS

Several techniques for preparation of the emittance samples were investigated with no single technique found satisfactory for obtaining controlled and uniform roughness characteristics over the entire range of roughness values desired (5 to 1000 $\mu\text{in.}$). Electropolishing techniques were investigated for preparation of pure polished surfaces and appeared to smooth and brighten the as-rolled copper samples. This procedure had no apparent effect on the tungsten samples. It was found that grit and Glas-Shot blasting techniques were most useful in preparation of the rough samples. A review of the various surface finishing methods investigated follows.

4.2.1 Machining

Preliminary investigations of the applicability of machining rough surfaces were made on copper-disk samples (1-in. diameter by 1/8-in. thick) with lathe and milled finishes having rms roughness values between 32 and 500 $\mu\text{in.}$ However, the difficulties associated with machining long thin strips with uniform surface finish over their 2 in. by 8 in. surface area, as well as the directional nature of these machined surfaces, were considered as undesirable features for this program. For these reasons, no serious effort was made to roughen the strip samples by these methods. However, it should be mentioned that machined surface finishes would be expected to be of interest for experimentally checking predictions of angular energy distributions based upon the theories of multiple reflections in grooves. These theories would be expected to apply to thermal radiation from surfaces whose roughness exceeds a few microns.

4.2.2 Grinding

"Double-disk" surface grinding was investigated as a possible technique for preparing roughened samples, since it is particularly useful for grinding and finishing thin, flat samples. The sample is mounted and held between two counter-rotating

disks which can be charged with various abrasives, depending upon the surface finish desired. Thus, a uniform sample thickness can be maintained to much closer tolerances than by conventional grinding of one side only. The method appeared to be useful for obtaining surface finishes with roughness values between 2 and 100 $\mu\text{in.}$ on samples of copper and tungsten. Efforts to obtain rougher surfaces were found to be unsatisfactory due to contamination of the sample surfaces by grit from the grinding wheels. Since alternate and more straightforward methods were available for obtaining this range of surface roughness, the double-disk grinding method was not used for preparation of the final test samples.

4.2.3 Electrodischarge Machining

An investigation of the electrodischarge machining (EDM) method was made with particular emphasis on roughening tungsten samples. This technique is used to cut, mill, or drill small or irregularly shaped metal parts which are not amenable to conventional machining processes. The piece to be processed is rigidly mounted to an electrode and immersed in a circulating dielectric liquid such as oil. A second, movable, electrode is lowered to a point above the sample where an electric discharge occurs, depending upon the electrode shape and the applied voltage. The amount of material removed by the discharge is controlled to some extent by the voltage. This technique was only partially successful in roughening copper. Small, randomly located craters up to 300 $\mu\text{in.}$ deep were produced; however, the craters were coated with a dark residue which could not be entirely removed without considerable modification of the surface profile. The results on tungsten samples were unsatisfactory because the discharge tended to delaminate the sample surface before any significant cratering was achieved. Tungsten flakes jumped up to the upper electrode, causing an electrical short and stopping the machining process. From these results it was concluded that the EDM technique was not suitable for preparing the emittance samples.

4.2.4 Photoetch Method

Standard photoetching techniques were investigated for application to test surfaces. The surface pattern obtained may be of any desired form the common usage being for the manufacture of fine screens and microelectronic circuits. For this study, standard lithographic screens with line spacings of 120 and 200 lines per inch were used. Various etch depths were produced for each spacing by varying the process etching time. Evenly spaced peak-to-valley depths of up to 800 $\mu\text{in.}$ were obtained on copper samples by etching in ferric chloride for 20 min. Inquiries to local firms doing this type of work indicated that the photoetch technique may also be applied to tungsten surfaces but not to platinum because of its resistance to etching processes. The emittance tests of copper samples prepared by etching have not yet been completed and are not included in this report.

4.2.5 Grit and Glas-Shot Blasting

Grit blasting was considered early in this study and appeared highly desirable because of the random surface profiles obtained; however, the technique contaminates the surface with materials (alumina, silicon carbide, etc.) which, by their nature, are almost impossible to remove by physical or chemical means without seriously modifying the surface profile. The use of Glas-Shot, small round microbeads of crown glass, in place of the commonly used grit materials, appears to reduce the surface contamination problem. With Glas-Shot the surface receives a peening treatment as opposed to the gouging action of sharp angular types of grit.

Two sizes of Glas-Shot were available: MS-XL, 0.0005 to 0.0021 in. diameter, and MS-ML, 0.0021 to 0.0041 in. diameter. The blast facilities of the Dri-Honing Service Company, Belmont, California, were used because their blast cabinets are equipped with filter and circulation systems which remove fractured bead material, thereby further reducing the possibility of contamination. Regulated air blast pressures from 10 to 80 psi were used, while the standoff distance (nozzle-to-sample distance) was manually controlled by the operator. Glas-Shot blasted surfaces with rms roughness values between 30 and 200 μ in. were obtained on copper and platinum samples. The maximum roughness was obtained with the larger beads at a pressure of 80 psi and standoff distance of 4 in. Attempts to obtain greater roughness by increasing the pressure were unsuccessful, resulting in severe deformation of the sample and in a higher fraction of shattered beads. Glas-Shot treatment of tungsten samples was ineffective as it produced a polished surface appearance instead of a roughened surface.

Efforts were made to obtain roughened tungsten surfaces using a No. 50 mesh steel shot with the intent of removing embedded steel through solution in hydrochloric acid without appreciably affecting the tungsten. This procedure was found to be unsatisfactory since the shot removed large tungsten platelets from the surface and delaminated the sheet. A copper sample was successfully prepared with steel shot to an rms roughness of 350 μ in.; however, the sample was badly warped in the process.

Samples of tungsten with rms roughness values from 20 to 100 μ in. were finally obtained using 5- μ alumina dust and No. 20 mesh silicon carbide grit at a pressure of 80 psi. This procedure led to contamination by grit entrapment but was found to be the only satisfactory method for preparation of the tungsten strips.

A summary of the procedures used to prepare each of the emittance samples is contained in subsection 4.3.

4.2.6 Electropolishing

Electropolishing techniques were investigated as a means of polishing the as-rolled copper and tungsten samples to provide smooth emittance samples for use as polished reference surfaces. No attempt was made to improve the finish on the platinum samples because of its inherent resistance to oxidation and the high quality of its as-rolled surface.

The following procedure was followed for copper:

- Step 1. Preclean in MacDermid L513 (1:1) for 1 min. Rinse and dry.
- Step 2. Electropolish for 30 min in a water-cooled bath of
 - 82.5% vol of 85% H_3PO_4
 - 17.5% vol of distilled water
 - Cathodes - copper
 - Current Density - 0.5 A/in.²
 - Bath Temperature - 60 to 70° F
- Step 3. Hot and cold water rinse
- Step 4. Passivate by dipping in HBF_4 (1:2)
- Step 5. Cold-water rinse
- Step 6. Alcohol rinse

Proficorder traces taken before and after electropolishing indicated that the process did not significantly smooth the surface profile; however, the surface brightness was much improved and was found to be considerably more tarnish-resistant during subsequent storage.

The following procedure was followed for tungsten:

- Step 1. Electropolish for 5 min in water-cooled bath of
 - 100 gm NaOH
 - 1000 ml distilled water
 - 1000 ml glycerineCathodes - Tungsten
Current Density - Varied; potential difference maintained at 30 V
Bath Temperature - 60 to 65° F
- Step 2. Cold-water rinse
- Step 3. Alcohol rinse

This process was found to improve the surface of tungsten sheet with a dull matte finish but did not noticeably improve the finish on the as-rolled GE tungsten; consequently, the as-rolled strip was used as the smooth, emittance sample.

4.3 TEST SAMPLE PREPARATION

A summary of the surface finishing methods used to prepare the final test samples is contained in Table 1. Additional information on the surface characteristics of these samples is presented in Sections 8 and 10.

All samples were cleaned after roughening by immersion in an ultrasonic bath of trichlorethylene for 15 min and then stored in a desiccated bell jar. In addition to the above treatment, copper sample 8 was immersed for 5 min in a 50% hydrochloric acid bath to etch out any embedded steel grit.

The roughened samples were noticeably warped by the blasting process, with the exception of the tungsten samples and copper sample 3. Copper samples 5 and 7 were straightened just prior to the emittance tests by heating in vacuum to 800° K for 1/2 hr and readjusting the longitudinal tension on the sample. The platinum samples and copper sample 8 were straightened by annealing at 800° K for 2 min followed by a gentle rolling between a flat steel bar and 6-in. tubing. This procedure flattened the strips without noticeably affecting the rough surface texture.

Microscope inspections of the roughened sample surfaces failed to reveal the presence of grit or Glas-Shot contamination. Similar negative results were obtained from x-ray diffraction patterns of roughened copper and platinum samples. Diffraction patterns from tungsten samples 1 (polished) and 2 were identical; however, three additional, weak, "d-lines" were detected in the pattern from tungsten sample 3, suggesting that some silicon carbide contamination had occurred. Spark spectrographic analyses were made at the conclusion of the emission studies and indicated that all of the roughened samples were contaminated to some extent by the material used for roughening them. (See Section 8.)

Before taking emittance data, all the copper samples were preheated to 600° K or higher, in vacuum, for removal of surface contamination caused by exposure to ambient conditions. This procedure has been reported to be effective by Roberts

(Reference 18) and appeared to work successfully in this case. Copper surfaces were visually observed to clean up as the temperature rose above 500° K with the center 4-in. portion of the sample appearing bright and clean at the conclusion of the preheat cycle.

Table 1
SURFACE FINISHING METHODS USED
TO PREPARE EMITTANCE TEST SAMPLES

Sample Designation	Surface Finishing Method ^(a)	Roughness ^(b) rms (μ in.)
Copper Sample 1	Electropolished by method described in sub-section 4.2.6	5.2
Copper Sample 3	Glas-Shot blasted, size MS-XL beads, 20 psi, 4 in.	76
Copper Sample 5	Glas-Shot blasted, size MS-XL beads, 80 psi, 4 in.	121
Copper Sample 7	Glas-Shot blasted, size MS-ML beads, 80 psi, 4 in.	176
Copper Sample 8	Steel shot blasted, No. 50 mesh, 50 psi, 6 in.	348
Tungsten Sample 1	None (tested as received)	1.5
Tungsten Sample 2	Grit blasted, 5- μ alumina, 80 psi, 2 in.	17
Tungsten Sample 3	Grit blasted, No. 20 mesh silicon carbide, 80 psi, 4 in.	110
Platinum Sample 1	None (tested as received)	< 1
Platinum Sample 3	Glas-Shot blasted, size MS-ML beads, 60 psi, 6 in.	169
Platinum Sample 6	Glas-Shot blasted, size MS-XL beads, 40 psi, 6 in.	91

(a) For the Glas-Shot and grit blasted samples, the air pressure supplied to the nozzle of the blasting gun and the distance between the nozzle and the sample are given. In all cases, the blast direction was normal to the sample surface.

(b) The rms roughness values are those obtained from Proficorder traces taken before the emittance tests.

Section 5

SURFACE CHARACTERIZATION METHODS

Considerable effort was devoted to the preparation and study of the sample surfaces to establish the relationship between the radiative characteristics of metals and their surface characteristics. Studies of the geometrical and physical aspects of the surface were emphasized, since these features appeared to be more amenable to quantitative measurement and the easiest to control in a systematic manner. To minimize surface chemistry effects, considerable care was taken to use uniform handling and processing methods for each sample and to minimize the possibility of surface contamination. As discussed earlier, however, the problem of obtaining rough surfaces without contamination was not solved with complete satisfaction. Furthermore, it is doubtful if the 10^{-5} Torr vacuum environment for the emittance tests was sufficiently low to rule out the possibility of significant effects due to surface-gas reactions, particularly in the case of tungsten.

Several different methods were used to ascertain the geometry and physical condition of the sample surfaces. Surface profiles were obtained with a Proficorder and were also examined using interferometric microscopy on the smooth samples and by metallographic inspections of cross-section and taper-section mounts of the roughened samples. The latter photomicrographs also supplied information on the physical condition of the sample substrate before and after the emittance tests. Additional information about the texture and condition of the sample surfaces was obtained from simple microscopic examinations.

Qualitative indications of the surface purity of the samples were obtained from x-ray diffraction and spark spectrographic analyses. Evidence of the absence of any gross contamination of the surfaces was obtained from the section photomicrographs and surface inspections through the microscope.

5.1 PROFILOMETRY APPARATUS AND METHODS

5.1.1 Surface Roughness Parameters

Figure 6 represents a surface profile trace which would be obtained by amplifying and recording the movement of a fine stylus over a rough surface. In general, the vertical scale of a profile trace is highly magnified relative to the horizontal scale. The degree to which the profile trace represents the "true" surface profile of the sample depends upon the resolution and accuracy of the tracing instrument and the hardness of the sample material. The depth of a valley will not be accurately represented if the stylus is too large relative to the width of the valley; and the height of the peaks will not be accurately represented if the surface material is too soft to resist scratching by the stylus.

Surface-roughness parameters are defined in terms of the true surface profile but in practice are measured or calculated from a recorded profile in accordance with standard methods. Descriptions of some of the common parameters used to describe a surface and methods for their computation are contained in References 19, 20, and 21. Many of these parameters are measured with reference to a centerline, as shown in Figure 6. In this study, the following roughness parameters were determined:

- Centerline (or mean line) - A line parallel to the general direction of the profile and so located that the areas enclosed between it and the profile above and below it are equal.

5.1.2 The Proficorder

Recorded traces of the surface profile of each sample were obtained with the Proficorder, a stylus instrument made by the Micrometrical Manufacturing Company, Ann Arbor, Michigan. Unless otherwise noted, all the quantitative values for sample roughness parameters were calculated from these traces. The Proficorder consists of three basic components:

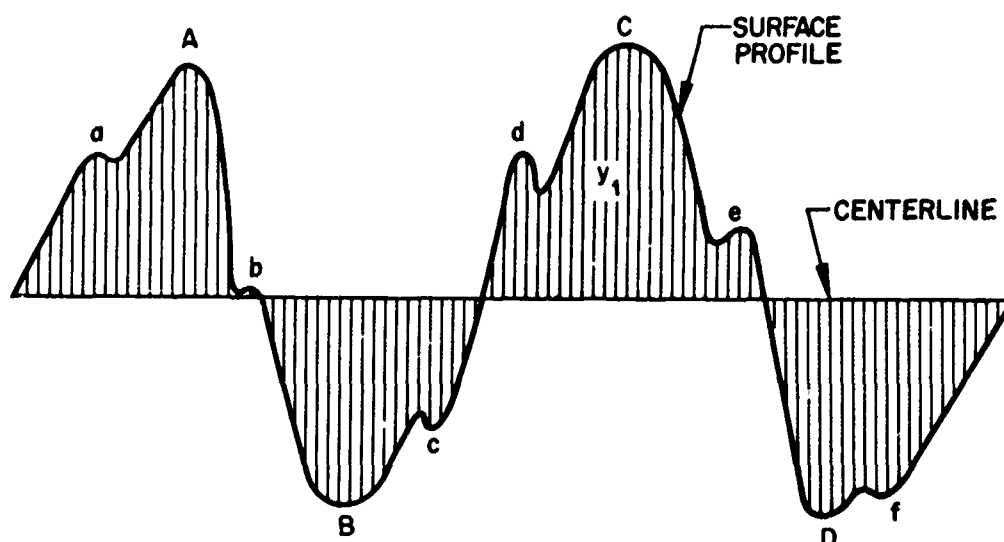
- A tracer, which contains the stylus and is mechanically moved along the desired path across the sample. The stylus is a diamond point with a radius of 500 μ in. which exerts a nominal pressure of 0.3 g on the sample. The up and down motion of the stylus is transformed into an output voltage by a differential transformer.
- A piloter, which supports the tracer and moves it along the desired path, with reference to an optical flat.
- An ampliforder, which contains the electronic circuitry and controls for amplifying and recording the voltage signals from the tracer.

The tracing speed of the stylus is 0.005 in./sec, and the chart drive speed can be varied to give seven different horizontal sensitivities from 0.001 to 0.100 in. per 1/2-in. chart division. Vertical sensitivities of 5, 25, 100, 250, and 1000 μ in. per 1/4-in. chart division may be selected. Electronic filters may be utilized to record the roughness profile only, the waviness profile only, or the total (combined) profile of the surface. The roughness width cutoff is 0.030 in. The Proficorder used in this study is located in a temperature- and humidity-controlled room of the Primary Standards Laboratory and is periodically checked by tracing over various roughness standards, thus assuring maximum instrument accuracy and performance.

5.1.3 Procedure

Proficorder traces were obtained before and after the emittance test of each sample. Graphic representations of these traces are shown in Section 10 with the horizontal scale magnification reduced slightly from that of the actual trace in order to show a longer section of the trace. All the traces were made using the maximum horizontal sensitivity (0.001 in. per 1/2-in. chart division). Vertical sensitivity was adjusted to keep the highest peaks and lowest valleys on the chart. A horizontal traverse of 1/8 to 1/4 in. across the sample was recorded by each trace. Since each trace represents the profile of a very narrow section of the surface, two transverse and two longitudinal traces were made at each examination to assure that the profiles were representative of the surface. These four traces were usually very similar to each other, and for calculating the roughness parameters a section of one of the traces which appeared representative of the overall surface was selected. AA and rms roughness values were calculated from 90 profile height readings uniformly spaced 500 μ in. apart. The accuracy of the centerline position for this portion of the trace was checked by measuring the appropriate areas above and below the centerline with a planimeter and relocating its position when necessary. Peak-to-peak spacings, peak heights, and valley depths were calculated on the basis of the predominant peaks and valleys occurring in the same section of the trace. The determination of whether a peak or valley was predominant or secondary was somewhat arbitrary and was based upon whether its spacing agreed with the regularity of the overall trace pattern.

Additional information about the surface geometry of the sample was obtained from cross-section and taper-section mounts of the samples and from interference photomicrographs of the smooth sample surfaces.



PREDOMINANT PEAKS AND VALLEYS-A,B,C,AND D
SECONDARY PEAKS AND VALLEYS-a,b,c,d,e, AND f

Figure 6 Representation of a Rough Surface Profile

- Root-mean-square (rms) roughness – The mean-squared deviations of the profile from the centerline. Calculated as follows:

$$\sigma_m = \left[\frac{1}{n} \sum_{i=1}^n y_i^2 \right]^{1/2}$$

- Arithmetic average (AA) roughness – The average deviation of the profile from the centerline. Calculated from

$$AA = \frac{1}{n} \sum_{i=1}^n |y_i|$$

- Average peak-to-peak spacing – The average horizontal spacing of the predominant peaks on the profile. Decreases in significance as the randomness of the profile increases because of the arbitrary judgement required to differentiate between predominant and secondary roughness peaks.
- Average peak height – The average vertical distance from the centerline to the tops of the predominant peaks.
- Average valley depth – The average vertical distance from the centerline to the valley bottoms between the predominant peaks.
- Average peak-to-valley distance – The sum of the average peak height and valley depth.
- Average profile slope – The angle whose tangent is obtained by dividing the average peak-to-valley distance by half the average peak-to-peak spacing. Represents the slope of a symmetrical, saw-toothed surface with no secondary roughness between the peaks and valleys.

5.2 MICROSCOPE METHODS

5.2.1 Surface Examinations

Preliminary examinations and photomicrographs of each sample surface were made to inspect the roughened samples for embedded grit and to obtain comparative photographs of the surface textures. These examinations were made using a Bausch and Lomb model DMTR metallurgical microscope equipped with a vertical illuminator, graduated mechanical stage, and graduated fine-focus adjustment. To obtain the photomicrographs, the microscope was used in conjunction with a model L camera. Typical photomicrographs of the surface texture of each sample before and after the emittance tests are shown in Section 10.

Additional information about the surface geometry of the smooth samples was obtained from interference micrographs of their surfaces. These micrographs were taken using the Bausch and Lomb interference objective attachment to the microscope and a blue-green filter for the vertical illuminator with a narrowband transmission peak at 4870 Å. Photomicrographs of 3 in. by 3-3/4 in. size at a magnification of 200 were obtained using the 20% reflectance test plate with the interference fringes superimposed upon the corresponding surface area of the sample. With ideal surface conditions, the horizontal limit of resolution of two parallel adjacent scratches on a flat surface is about 500 μ in. When a flat surface is viewed, the interference fringes appear as equally spaced parallel black bands. The number of fringes depends upon and can be varied by the angle which the reference test plate makes with the sample surface. If linear imperfections are present on the surface, the band or bands will deviate to one side across a valley or to the other side across a ridge. If the imperfection consists of small rounded hills or craters, closed circular fringes are formed, their spacing depending upon the slope of the imperfection and their number depending upon the height or depth of the imperfection. Fringe deviations of n fringe spacings indicate nominal vertical deviations of $10n$ μ in. on the sample surface. Interference micrograph techniques and interpretations are discussed in References 20 and 22, and with particular application to the determination of surface roughness in References 23 and 24.

Interference micrographs of the three smooth samples in this study, before and after their emittance tests, are shown in Section 10. Comparisons of the roughness values indicated by the micrographs with those obtained from the Proficorder traces are discussed in Section 8. Attempts to obtain meaningful interference micrographs of the slightly rough samples in this study were unsuccessful.

5.2.2 Section Examinations

Photomicrographs of cross- and taper-section mounts of the samples were taken to indicate the physical condition of the sample surface and to obtain additional information about the surface geometry. Typical photomicrographs of each sample are discussed in Section 8 and are shown in Section 10. Specimens for the section mounts were obtained from the hot center area of each strip to indicate the "after-test" condition of the sample, and from the cool end area of the strip to indicate the "before test" condition. Before being mounted, the copper and tungsten specimens were plated with a thin layer of nickel (about 0.0005 in.) and the platinum specimens with about the same thickness of copper. The purpose of the plating layer was to preserve the surface edge of the specimens as they were polished. After being plated, the specimens were mounted in bakelite, polished, examined, and photographed by the Research Metallurgy Laboratory.

Descriptions of the taper-sectioning technique along with illustrations of its application to the study of metal surfaces are contained in References 25 and 26. Figures 7 and 8 illustrate how the taper-section mounts were prepared for this study and how the photomicrographs of these mounts are interpreted. To prepare the mount, the plated surface of the specimen to be examined is placed face down on a supporting wedge and covered with the desired amount of mounting material. After the mount has solidified, the face of it is ground and polished in a conventional manner until a suitable edge is obtained for examination. In this manner the surface features of the specimen are geometrically magnified in depth by the cosecant of the taper angle, while the horizontal spacing of the surface features remains unchanged, as in a standard cross-section mount.

Steel and aluminum wedges 1/2 in. wide by 3/4 in. long and with a taper angle of $5 \text{ deg } 45 \text{ min} \pm 15 \text{ min}$ were used in this study. The magnification obtained at this angle was therefore about 10 ± 0.4 . The taper-section mount shown in Figure 7 was sectioned to check that the taper angle did not change during the mounting and polishing processes. In this particular mount, a thin strip of brass shim stock was placed on top of the specimen to aid in positioning. Photomicrographs at magnifications of 100 and 500 were obtained from these mounts; consequently, the total magnification of the surface features in the direction of the wedge was approximately 1000 and 5000, respectively.

5.3 CHEMICAL ANALYSES

Qualitative indications of the surface purity of each samples were obtained from microscope examinations of the surface and the section mounts. X-ray diffraction patterns were also obtained from the roughened samples (using a General Electric XRD-5 diffraction unit) and were compared with the patterns from the smooth samples to determine the presence of any gross surface contamination. After the emittance tests, spark spectrographic analyses of the copper and tungsten samples were made using a 3.4-m Jarrell-Ash spectrograph. The results of these analyses are discussed in Section 8.

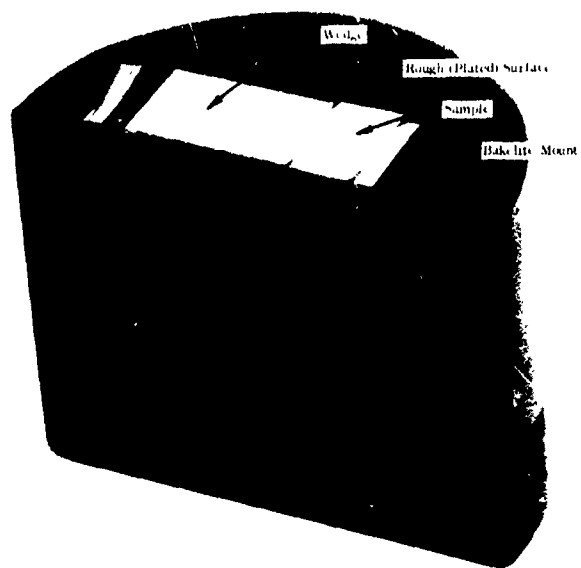


Figure 7 Taper Section Mount

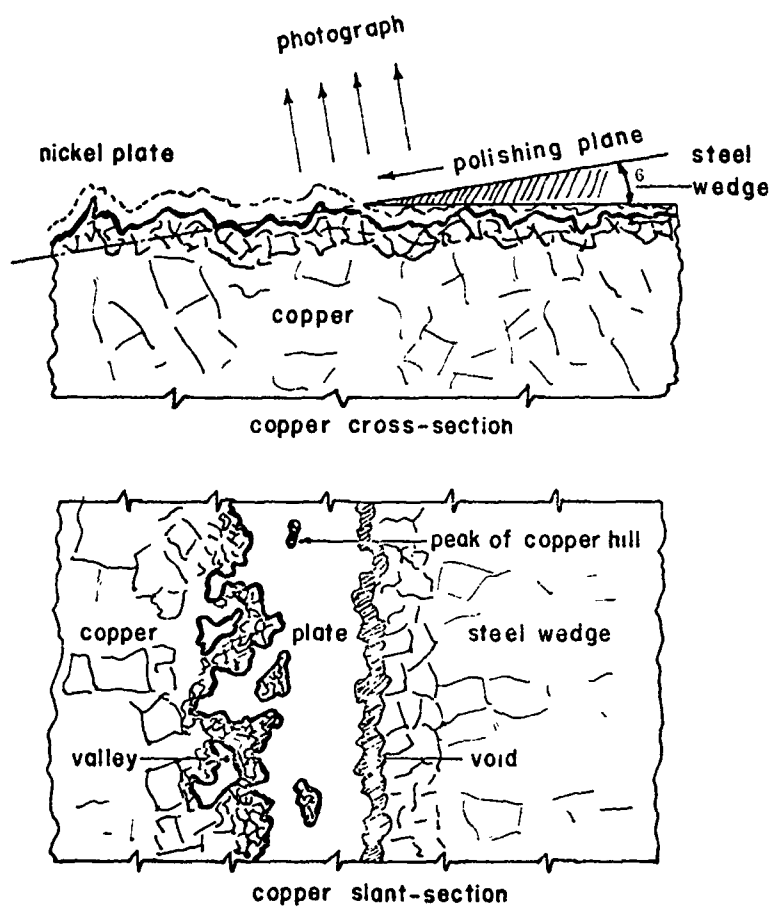


Figure 8 Illustrations for Interpretation of Taper Section Photomicrographs

Section 6

EXPERIMENTAL APPARATUS

The experimental apparatus used for measurement of the radiant emission characteristics of metal surfaces is shown in Figures 9 and 10. The apparatus consists of a water-cooled evacuated chamber which contains a resistive, electrically heated sample. The sample may be rotated in azimuth while it is viewed by an external optical transfer system. The optical system focuses an image of a portion of the sample on a vacuum thermocouple detector or on the entrance slit of a monochromator.

6.1 VACUUM CHAMBER

The vacuum chamber consists of a water-cooled stainless steel bell jar which is 12 in. in diameter and 14 in. high. The cylindrical chamber rests on a 1-in.-thick stainless steel base plate. Thermal transfer from the chamber to the cooling coils around the chamber is aided by the application of Thermon, a high-conductance cement, over the external surface of the chamber and cooling coils. The inner surface of the bell jar is coated with a low-reflectance, flat black paint, which minimizes reflection internal to the chamber. A potassium bromide window provides for transmission of emitted energy from the sample through the external optics to the radiation detectors. A quartz window is provided for visual observation of the sample and optical pyrometer temperature measurements.

Pressures on the order of 10^{-5} Torr are maintained within the chamber during each elevated temperature run. Vacuum is maintained by a 2-in. diffusion pump and a 5 cu ft/min. mechanical pump. A liquid nitrogen cold trap and a water-cooled baffle are mounted between the diffusion pump and the chamber to minimize back-streaming of oil into the chamber. Removable vacuum feedthroughs are mounted on the base plate for passage of thermocouple leads.

6.2 ROTATING SAMPLE MOUNT

The sample mount is shown in Figure 11. The sample is clamped between two water-cooled electrodes which pass through a freely rotating flange. The flange is mounted on the base plate and may be rotated through 184 deg on an O-ring seal. Angular rotation of the sample is indicated by a pointer attached to the actuator arm. The indication is given by an angular scale which has an 8.5-in. radius giving readings to 0.5 deg. Tension is applied to the sample by an external spring adjustment to compensate for linear expansion of the sample.

Electrical power for heating the sample is supplied by a variac-controlled 10-kVA stepdown transformer with a rated output of 1000 A at 10 V. The current is monitored with a 0 to 5 A current transformer. The amount of current is determined by measuring the voltage drop across a standard resistor (shunt) placed in series with the samples. Voltage drops across the sample and the standard resistors are measured with a Hewlett-Packard Model 400 D vacuum-tube voltmeter.

6.3 RADIATION DETECTION SYSTEM

The collecting and focusing optics are shown schematically in Figure 10. All reflecting surfaces are front-surface aluminized mirrors. The radiant energy emitted by the sample passes through the KBr window in the chamber wall at (3) and is chopped at 13 cps by the chopper (5).

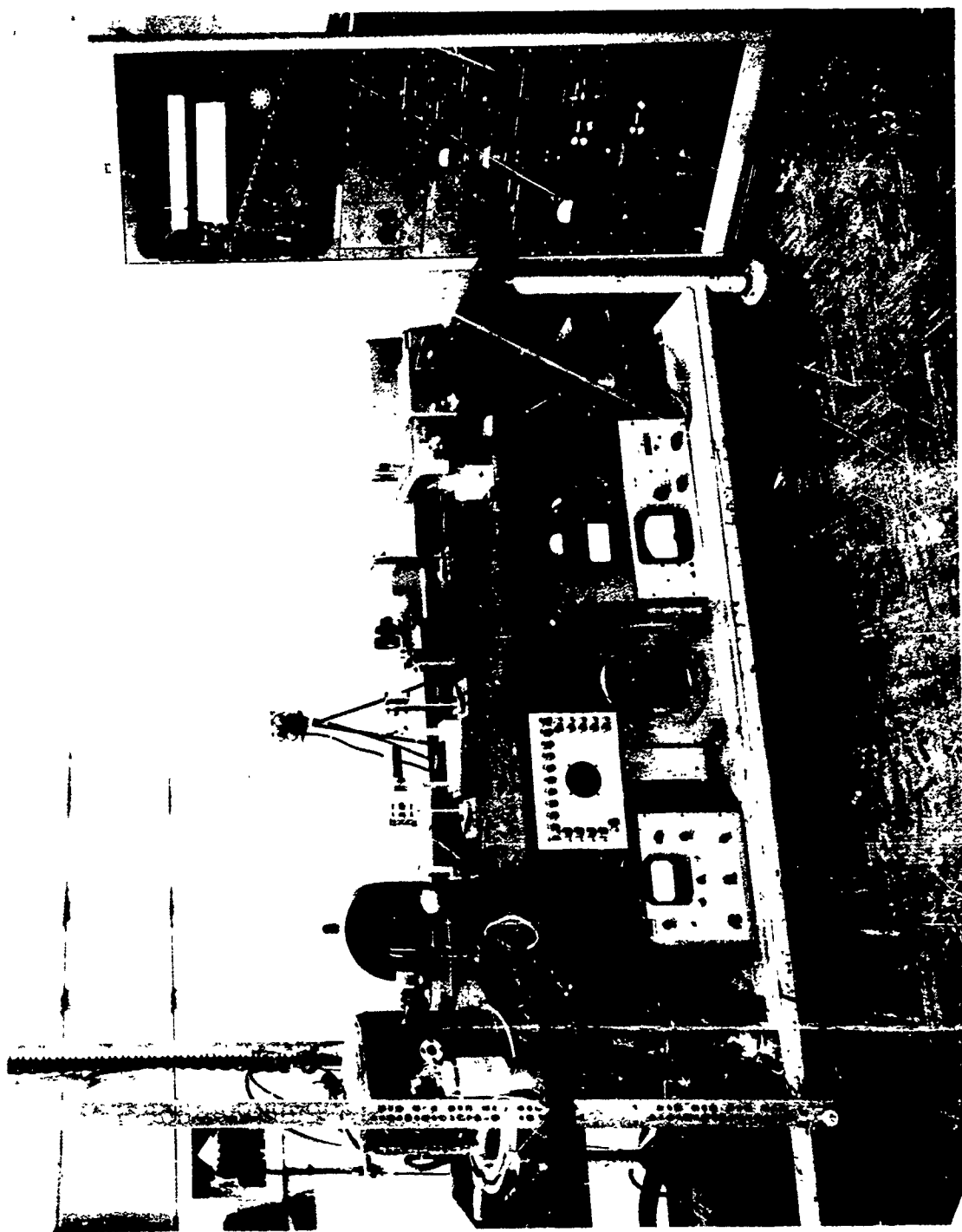
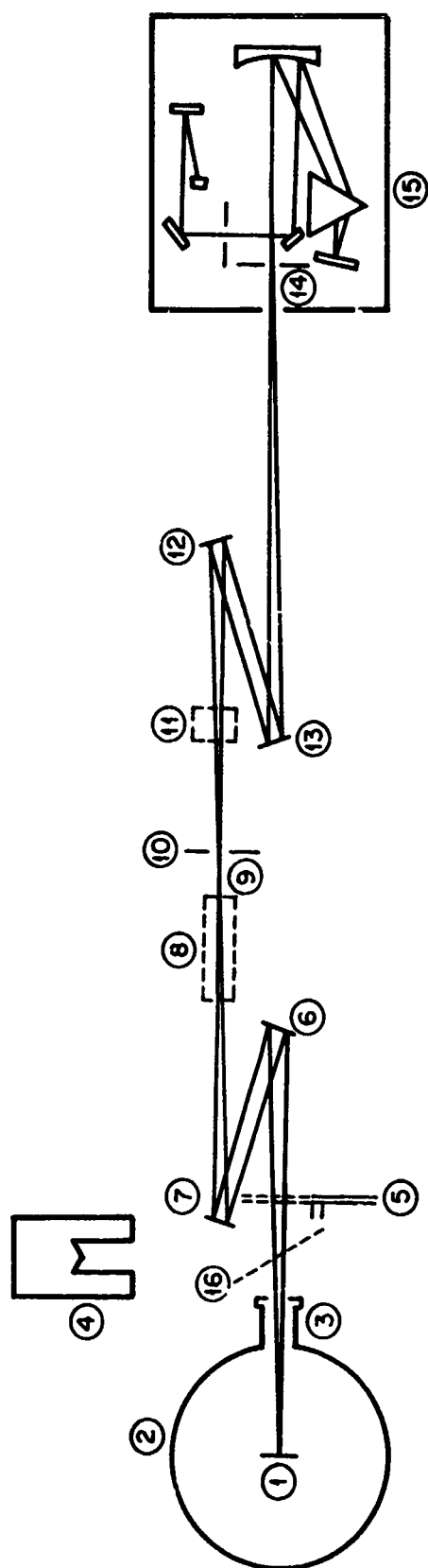


Figure 9 Directional Emittance Apparatus



- | | |
|---|--|
| 1. Rotating sample | 9. Sample image point |
| 2. Vacuum chamber | 10. Adjustable slit |
| 3. KBr window | 11. Vacuum thermocouple detector |
| 4. External blackbody | 12. Front surface mirror |
| 5. Chopper | 13. 14-in. focal length front surface mirror |
| 6. 14-in. focal length front surface mirror | 14. Monochromator inlet slit |
| 7. Front surface plain mirror | 15. P.E. 13U monochromator |
| 8. Polarizer | 16. Blackbody mirror |

Figure 10 Schematic Layout of Directional Emittance Apparatus

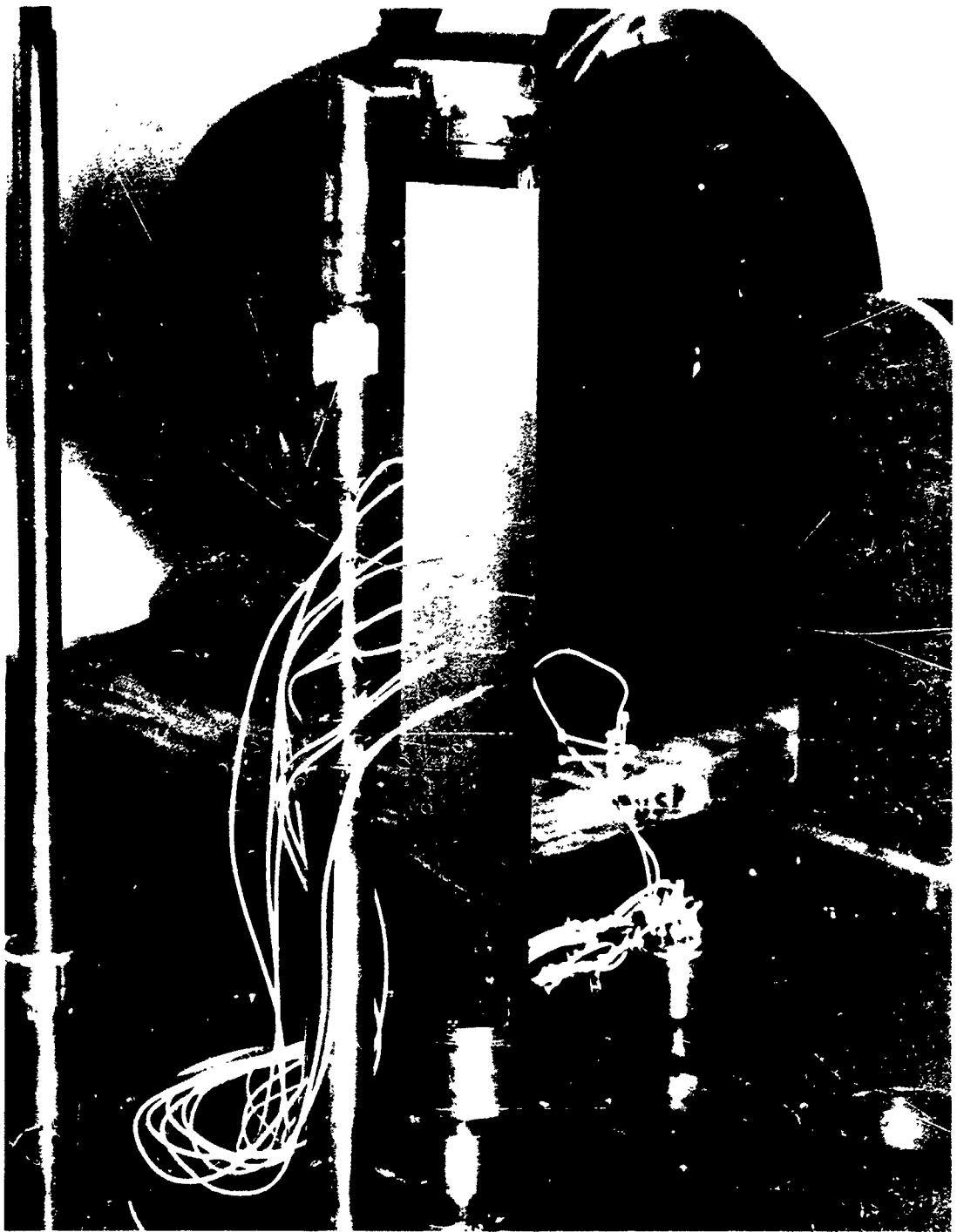


Figure 11 Rotating Sample Mount

Chopped radiant energy is collected by the spherical mirror (6), which is masked to limit the collecting angle to 1.2 circular deg (3.4×10^{-4} sr). The energy collected by the spherical mirror (6) is directed by the plane mirror (7) to a variable aperture slit at (10). At this position, a real image is formed of the sample with a magnification of unity and the slit adjusted so that it is completely filled for viewing angles up to 87 deg from the normal. This condition was obtained for a slit width of 0.035 in. After passing through the adjustable slit (10), the energy is focused either on a vacuum thermocouple total radiation detector (11) or by mirrors (12) and (13) on the entrance slit of a Model 13U Perkin-Elmer single-pass monochromator (14) equipped with a NaCl prism and a vacuum thermocouple detector.

Two types of sensors were tested for use as the total radiation detector. The first was a thermistor bolometer with a KRS-5 window which was located just behind the aperture slit. The second was a Perkin-Elmer vacuum thermocouple with a KBr window and spherical collection mirror for focusing the energy on the thermocouple. The latter detector was located approximately half way between the aperture slit and mirror. (See Figure 10.) Greater sensitivity and improved linearity were obtained with the vacuum thermocouple; consequently, it was selected.

The spectral radiation detector was also a Perkin-Elmer vacuum thermocouple. The linearity of both detectors was checked using known energy levels from a standard blackbody. The same chopper, preamplifier, amplifier, and recorder were used with both detectors.

An Infra-Red Industries Model IR-101 blackbody was used for calibration and initial checking of the system response and as a reference standard for all emittance determinations. The radiant energy from the blackbody was reflected by a plane mirror (16) into the same optical path as the radiant energy from the sample.

An infrared polarizer was constructed to permit polarization measurements. The polarizer consisted of ten 0.010-in.-thick silver chloride plates inclined at a polarizing angle of 75 deg. The characteristics of this polarizer have been described in detail by Newman and Halford (Reference 27).

During operation the entire optical system shown in Figure 9 was covered with an optically black enclosure to eliminate collection of scattered room energy.

Section 7

EXPERIMENTAL PROCEDURES

7.1 MEASUREMENT OF SPECTRAL DIRECTIONAL AND NORMAL EMITTANCE

For the arrangement shown in Figure 10, the voltage response of the spectrometer detector is proportional to the difference in spectral radiant flux received by the detector from the sample and that received from the chopper. The response of the system with the normal to the sample plane at an angle θ to the optical axis may be expressed as

$$V_s(\theta) = [\epsilon_s(\theta, \lambda, T)E_s(\lambda, T)\tau_w + \epsilon_s(\theta, \lambda, T)E_s(\lambda, T)\rho_c\rho_s\tau_w + \epsilon_c E_c(\lambda, T)\rho_s\tau_w + \epsilon_w E_w(\lambda, T) + \rho_w E_a(\lambda, T) - E_a(\lambda, T)]hF_s \quad (39)$$

where F_s is a function which describes the efficiency of the optical transfer system; h is the detector responsivity; and $\epsilon_s(\theta, \lambda, T)E_s(\lambda, T)\rho_c\rho_s\tau_w$ is an approximate term representing energy reflected by the chamber walls which is then directed by the sample into the optical path. At $\theta = 0$, the sample plane is normal to the optical axis and the voltage response becomes

$$V_s(\theta_N) = [\epsilon_s(\theta_N, \lambda, T)E_s(\lambda, T)\tau_w + \epsilon_s(\theta_N, \lambda, T)E_s(\lambda, T)\rho_c\rho_s\tau_w + \epsilon_c E_c(\lambda, T)\rho_s\tau_w + \epsilon_w E_w(\lambda, T) + \rho_w E_a(\lambda, T) - E_a(\lambda, T)]hF_s \quad (40)$$

Since the temperatures of window, chamber, and ambient environments are very nearly the same, it may be assumed that

$$E_w(\lambda, T) = E_c(\lambda, T) = E_a(\lambda, T)$$

It is also true that $\rho_c \ll 1$, and $\epsilon_c \cong 1$ for reflected and emitted energy from the chamber walls. Since $\rho_w + \alpha_w + \tau_w = 1$ for the window at any given wavelength λ , and $\rho + \alpha = 1$ for an opaque sample, Equations 39 and 40 become

$$V_s(\theta) = \epsilon_s(\theta, \lambda, T)\tau_w [E_s(\lambda, T) - E_a(\lambda, T)]hF_s \quad (41)$$

$$V_s(\theta_N) = \epsilon_s(\theta_N, \lambda, T)\tau_w [E_s(\lambda, T) - E_a(\lambda, T)]hF_s \quad (42)$$

The voltage response of the detector when observing the blackbody reference is given by

$$V_b = [E_b(\lambda, T) - E_a(\lambda, T)]hF_s \quad (43)$$

The spectral normal emittance $\epsilon(\theta_N, \lambda, T)$ may then be determined from the ratio of signals as

$$\frac{V_s(\theta_N)}{V_b} = \frac{\epsilon_s(\theta_N, \lambda, T) \tau_w [E_s(\lambda, T) - E_a(\lambda, T)] h F_s}{[E_b(\lambda, T) - E_a(\lambda, T)] h F_s} \quad (44)$$

and thus

$$\epsilon_s(\theta_N, \lambda, T) = \frac{1}{\tau_w} \frac{V_s(\theta_N)}{V_b} \left[\frac{E_b(\lambda, T) - E_a(\lambda, T)}{E_s(\lambda, T) - E_a(\lambda, T)} \right] \quad (45)$$

For equal blackbody and sample temperatures,

$$E_s(\lambda, T) = E_b(\lambda, T)$$

which reduces Equation 45 to

$$\epsilon_s(\theta_N, \lambda, T) = \frac{1}{\tau_w} \frac{V_s(\theta_N)}{V_b} \quad (46)$$

The spectral transmission τ_w of the KBr window was measured after each sample run, and the measured transmissions were used in the reduction of data.

The normalized relative spectral directional emittance is determined from the ratio of Equations 41 and 42:

$$\frac{V_s(\theta)}{V_s(\theta_N)} = \frac{\epsilon_s(\theta, \lambda, T) \tau_w [E_s(\lambda, T) - E_a(\lambda, T)] h F_s}{\epsilon_s(\theta_N, \lambda, T) \tau_w [E_s(\lambda, T) - E_a(\lambda, T)] h F_s} \quad (47)$$

Since a constant sample temperature is maintained,

$$\frac{\epsilon_s(\theta, \lambda, T)}{\epsilon_s(\theta_N, \lambda, T)} = \frac{V_s(\theta)}{V_s(\theta_N)} \quad (48)$$

In prism spectrometers the refracting and reflecting surfaces are vertical, causing polarization in the horizontal plane. The degree of polarization for a Perkin-Elmer Model 12-B is approximately 30% as measured by Simon (Reference 28). In view of the highly polarized state of directional emission from metals, as shown by Figure 4, careful measurement procedures must be employed to eliminate the effects of apparatus polarization. The relative directional emittance cannot be measured directly without knowledge of the absolute polarization characteristics of the detecting instrument.

The difficulty of determining the absolute polarization characteristics of a given detection system may be circumvented by measurements of the relative polarized components $\epsilon_{\perp}(\theta, \lambda, T)/\epsilon_{\perp}(\theta_N, \lambda, T)$ and $\epsilon_{\parallel}(\theta, \lambda, T)/\epsilon_{\parallel}(\theta_N, \lambda, T)$. Energy

emitted at the normal viewing angle $\theta_N(\theta=0)$ is by symmetry circularly polarized, permitting determination of absolute values of emittance at that angle. The relative results may then be converted to absolute values through use of the absolute values for normal viewing. This procedure was used in establishing all absolute values given in Section 8.

7.2 MEASUREMENT OF TOTAL DIRECTIONAL AND NORMAL EMITTANCE

The total directional and normal emittance was determined by placing a vacuum thermocouple detector with a KBr window at position (11) in Figure 10. The detector response is again proportional to the difference between energy received from the sample and that received from the chopper. Performing an analysis similar to that given in subsection 7.1 yields

$$\epsilon_s(\theta, T) = \frac{1}{\tau_w} \frac{V_s(\theta)}{V_b} \left[\frac{E_b(\lambda, T) - E_a(\lambda, T)}{E_s(\lambda, T) - E_a(\lambda, T)} \right] \quad (49)$$

For equal blackbody and sample temperatures

$$\epsilon_s(\theta, T) = \frac{1}{\tau_w} \frac{V_s(\theta)}{V_h} \quad (50)$$

The window transmission used here is that value obtained for transmitted blackbody energy at the temperature of the samples. The measured values of the transmission showed the window transmission to be spectrally flat from 1 to 12 μ .

Relative values of directional emittance are again obtained from the ratio of signal levels as

$$\frac{\epsilon_s(\theta, T)}{\epsilon_s(\theta_N, T)} = \frac{V_s(\theta)}{V_s(\theta_N)} \quad (51)$$

The relative total directional emittance was determined by rotation of the samples 0 to ± 87 deg at a fixed temperature, with absolute values of emittance established only at the normal. Polarization of emitted energy is not a source of difficulty in these measurements since the collecting and detecting system is insensitive to the state of polarization. Polarized components were not determined for total emittance measurements owing to the nongrey transmission characteristics of the polarizers. The total energy emitted in each component is best obtained by integration of the spectral results.

Values of the spectral hemispherical emittance, $\epsilon(\lambda, T)$, are obtained by integration of the directional results through the relation

$$\epsilon(\lambda, T) = \frac{\int_0^{\pi/2} \epsilon(\theta_N, \lambda, T) f(\theta) J_b(\lambda, T) 2\pi \sin \theta \cos \theta dA d\theta}{\int_0^{\pi/2} J_b(\lambda, T) 2\pi \sin \theta \cos \theta dA d\theta} \quad (52)$$

where symmetry in the azimuth about the surface normal has been assumed for $\epsilon(\theta, \lambda, T)$ and

$$J_b(\lambda, T) = \text{spectral intensity of a blackbody}$$

$$f(\theta) = \epsilon(\theta, \lambda, T) / \epsilon(\theta_N, \lambda, T)$$

$$2\pi \sin \theta d\theta = \text{differential solid angle}$$

Integration yields

$$\frac{\epsilon(\lambda, T)}{\epsilon(\theta_N, \lambda, T)} = 2 \int_0^{\pi/2} f(\theta) \sin \theta \cos \theta d\theta = 2 \int_0^1 f(\theta) \cos \theta d(\cos \theta) \quad (53)$$

This form was used for numerical integration of data such as that shown in Figure 12 to obtain the hemispherical results presented in Section 8

7.3 OPTICAL CONSTANT DETERMINATIONS

The optical constants of a polished surface may be determined from directional emission measurements using a method similar to those reported by Simon (Reference 28), Martin (Reference 4), and Blau (Reference 29). As shown in Section 3 of this report, the normalized directional emittance at a particular temperature and wavelength is related to the independent variables θ , n , and k by Equations 20 and 22:

$$\frac{\epsilon(\theta, n, k)}{\epsilon(\theta_N, n, k)} = f(\theta, n, k) \quad (54)$$

For two different angles of emission, θ_1 , and θ_2 , the measured $\epsilon(\theta, n, k) / \epsilon(\theta_N, n, k)$ provide two separate values of $f(\theta, n, k)$, thus permitting determination of a unique solution for the quantities n and k .

Solutions to Equation 54 were determined on a digital computer and tabulated to provide values of $f(\theta, n, k)$ for θ in 5-deg increments between 50 and 80 deg and values of n and k appropriate to the materials of interest. For any measured $f(\theta, n, k)$ at angle θ , the appropriate values of n and k are plotted as shown in Figure 13. This procedure is followed for a number of viewing angles to determine an intersection of all curves which then represents the required solution. The accuracy of the determination is strongly influenced by the accuracy of the angular measurements. Errors of 1 deg in angular measurements can cause the intersections of the curves to vary significantly and in some cases may result in no intersections.

Figure 14 shows the angular data for tungsten at 1200° and 1370° K used to obtain the values of n and k shown in Figure 13. Inspection of these figures demonstrates the shift of n and k values for small differences in angular distribution.

Subsection 8.2 presents the results obtained for all samples using this technique.

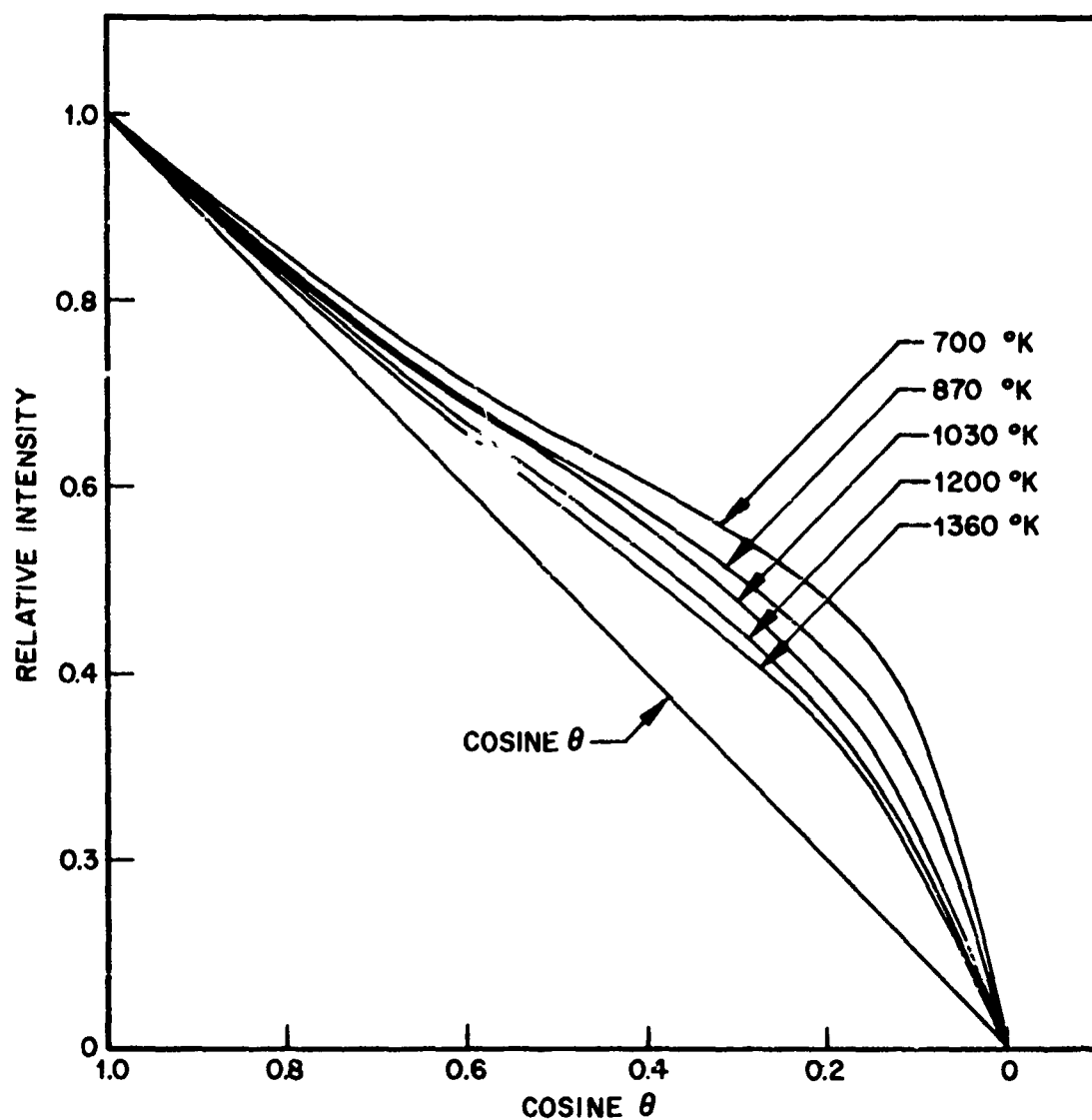


Figure 12 Relative Total Directional Intensity Data for Smooth Tungsten

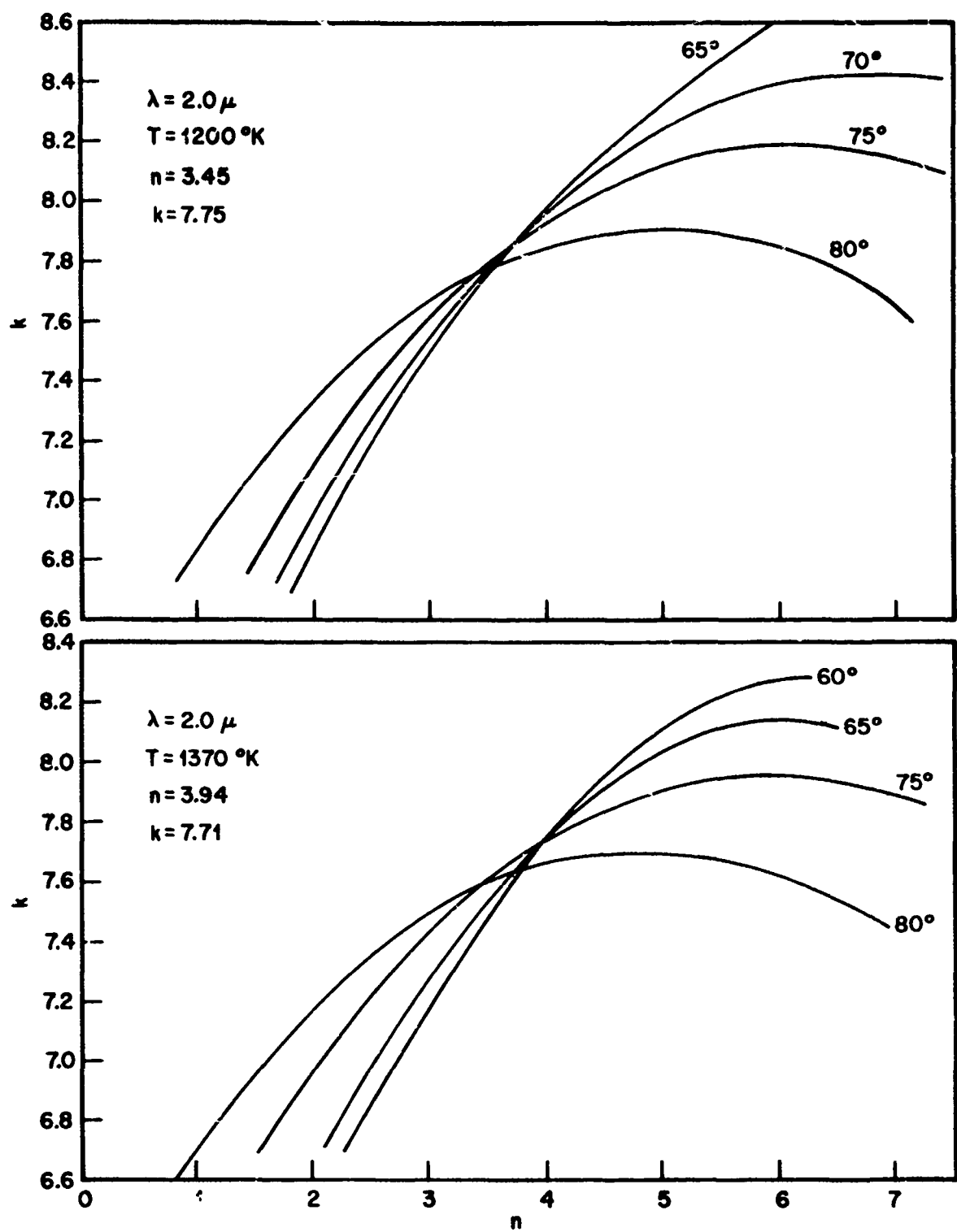


Figure 13 Optical Constants of Tungsten from Relative Spectral Directional Emittance Data

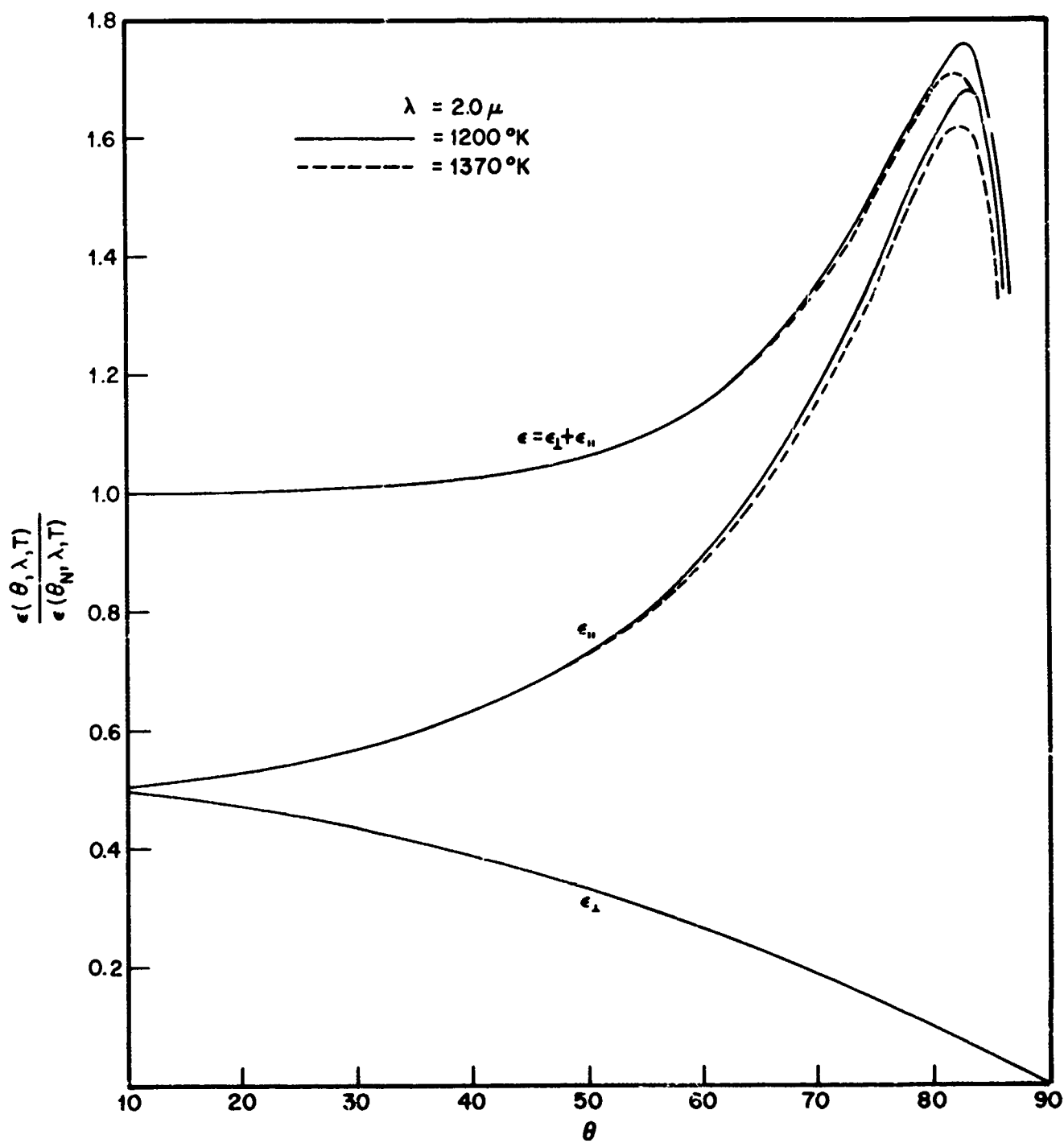


Figure 14 Relative Spectral Directional Emittance Data for Tungsten

7.4 TEST PROCEDURE

7.4.1 Sample Instrumentation

Each test sample was instrumented with five Pt/Pt-13% Rh thermocouples attached to the back surface of the strip, as shown in Figure 11. Forty-gage thermocouple wire was used to minimize the thermal conduction loss from the sample through the wires and at the same time provide mechanical and electrical stability at high temperatures. The thermocouple junctions were located approximately 1/2 in. from one edge of the strip and at vertical positions 0, $\pm 1/2$, ± 1 in. from the mid line of the strip. In this manner a good measure of the temperature distribution over the center portion of the strip was obtained, and anomalous temperature readings caused by poor thermocouple attachment or short circuits were easily detected. The individual thermocouple wires were attached to the tungsten and platinum samples by spot welding. Care was taken to attach the wires of each junction at identical vertical positions on the strip to avoid pickup of an a-c voltage gradient. Attachment to the copper samples was accomplished by first drilling 0.013-in. -diameter holes into the back face of the sample, about 3/4 of the way through the strip. The thermocouple junctions were then inserted into the holes, and the adjacent copper was lightly peened over the junctions until they were firmly attached. The thermocouple leads were insulated with fiberglass sleeving to about 3/4 in. from the junction to prevent short circuits. The leads passed through vacuum-tight feed throughs in the base plate and terminated in a reference junction ice bath. Sample temperatures were determined from measurements of the thermocouple emf's with a Leeds and Northrup potentiometer.

7.4.2 Emittance Test Procedure

After being instrumented, the samples were mounted in the angular emittance device, the thermocouple wires attached to the vacuum feed through leads, and the test chamber evacuated to a pressure of 10^{-5} Torr. Before taking emittance data, the samples were preheated for periods of time which ranged from 1/2 to 3 hr in vacuum. This preheat cycle served to clean up any volatile material on the sample surface and also annealed out the surface strain in the roughened samples. Annealing temperatures and times are recorded in Section 10, in the test procedure for each sample. Complete sets of emittance data were taken at each test temperature as sample energy permitted, starting at the lowest temperature and working up. After analyzing the data from several of the roughened samples, it was found that their absolute emittance values changed when their temperatures were raised above the initial, annealing temperature. Consequently, it was necessary to retest several of the samples after holding them at their maximum test temperature until their emittance appeared to be stable. Final data were then obtained at the lower test temperatures.

To insure reliable sample temperature data, the five thermocouple junction temperatures were plotted graphically against their vertical position and a smooth curve fitted through the measured points. In this manner, the temperature of the center 5/8 in. portion of the sample was obtained with an accuracy of better than $\pm 1\%$. The absence of any significant horizontal temperature gradients across the width of the samples was verified by optical pyrometer readings at the higher temperatures.

Section 8

RESULTS

8.1 SURFACE CHARACTERISTICS

8.1.1 Roughness

Roughness parameters determined from the Proficorder traces of each sample before and after the emittance tests are shown in Table 2. Unless otherwise noted, the roughness parameter values used in the analyses of the sample emittance data in Subsection 8.3 are taken from this table. Typical sections of the profiles used for determining these parameters are shown with the sample data in Section 10.

The data for the initially smooth samples indicate their roughness increased slightly during the tests. This increase in roughness is attributed to the annealing of residual surface strain and recrystallization of the samples. Evidence of recrystallization is clearly shown in the photomicrographs of these samples obtained after the emittance tests and was visually evident on the surfaces of the copper and platinum samples. The effect of surface recrystallization on the total normal emittance of the smooth copper and platinum samples appeared to be very small.

In contrast to the sharply defined grain boundaries observed on the surface of the smooth copper and platinum samples, the face of the smooth tungsten sample appeared to be thermally etched after the emittance tests. This characteristic gave the tungsten a hazy appearance, in contrast with the initially bright appearance of the surface. The reason for this change is not known; however, surface attack by residual oxygen or water vapor in the vacuum chamber is suspected. Examination of the surface through the microscope indicated the attack to be on preferred areas of the surface in the vicinity of the grain boundaries (Figure 47).*

As a check on the accuracy of the Proficorder traces for the smooth samples, interference photomicrographs of these samples were obtained before and after the emittance tests. The photomicrographs are shown with the data for these samples in Section 10. The interference patterns from copper sample 1 (Figure 20) indicate peak-to-valley depths of 3 or 4 fringe spacings (30 to 40 $\mu\text{in.}$) on the surface of this sample. This agrees well with the maximum peak-to-valley depth indicated by the Proficorder traces from the sample. The irregular nature of the fringe patterns indicates the surface of the electropolished copper to be covered with randomly spaced hills and craters rather than long parallel roll marks which were predominant on the as-received surface. The patterns are typical of those obtained from electropolished surfaces by Strang and Ogburn (Reference 23).

The interference patterns from tungsten sample 1 (Figure 47) indicate a definite lay to the roughness, parallel to the long dimension of the strip. This type of pattern is typical of rolled metal surfaces. Comparison of the patterns indicates the roughness of the sample did not change significantly during the emittance tests; however, the clarity of the fringes over the thermally etched areas of the tested surface is poor. An average peak-to-peak spacing of 750 $\mu\text{in.}$ was determined from these patterns, which is about one-half the spacing determined from the Proficorder traces. The difference is attributed to the fact that not all of the peaks on the Proficorder trace were counted as predominant peaks when the traces were evaluated. From the

*The figures with numbers greater than 19 are to be found in Section 10.

Table 2

SURFACE ROUGHNESS PARAMETERS FOR SAMPLES BEFORE AND AFTER EMITTANCE TESTS

Sample	Average Peak-to-Peak Spacing (a) ($\mu\text{in.}$)	Peak Height		Valley Depth			Average Profile Slope (\pm deg)	AA Roughness ($\mu\text{in.}$)	RMS Roughness ($\mu\text{in.}$)
		Maximum ($\mu\text{in.}$)	Minimum ($\mu\text{in.}$) (c)	Average ($\mu\text{in.}$)	Maximum ($\mu\text{in.}$)	Minimum ($\mu\text{in.}$) (c)			
Copper 1 Before	5,670	17	0	5.9	12	0	1/4	4.1	5.2
Copper 1 After	7,720	11	1	6.8	13	0	1/4	4.7	5.7
Copper 3 Before	1,420	194	-53	81	180	-48	11-3/4	63	76
Copper 3 After	1,760	96	-28	31	83	-33	4	27	33
Copper 5 Before	1,630	280	-50	124	310	-100	15-1/2	98	121
Copper 5 After	1,370	115	-30	60	165	-37	8-1/4	46	56
Copper 7 Before	2,185	525	-80	191	460	-90	17-1/4	144	176
Copper 7 After	2,680	275	0	123	220	-20	9-1/2	92	114
Copper 8 Before	2,900	770	-200	368	820	-420	24-3/4	286	348
Copper 8 After	3,650	464	-86	221	616	-294	11-1/4	156	204
Tungsten 1 Before	1,260	5.2	-0.8	1.5	3.8	0	1/4	1.1	1.5
Tungsten 1 After	1,470	6.0	-0.5	2.1	8.0	1.0	1/2	1.8	2.4
Tungsten 2 Before	1,630	38	0	18.4	44	-18	2-1/4	13	17
Tungsten 2 After	1,595	63	-10	19.3	60	-24	2-3/4	16	21
Tungsten 3 Before	1,760	260	25	127	345	-30	14-1/2	86	110
Tungsten 3 After	1,280	110	-37	42	112	-48	6-1/2	31	38
Platinum 1 Before			Not Determined						
Platinum 1 After	10,500	16	-1	6.6	12	-2	<1/4	3.6	4.7
Platinum 3 Before	1,935	440	-20	225	450	-140	19-1/4	133	69
Platinum 3 After	2,270	125	-65	73	175	-3	7-3/4	66	79
Platinum 6 Before	1,555	175	0	90	220	-60	13-1/4	74	91
Platinum 6 After	1,465	90	-20	33	81	-15	5-1/2	31	38

(a) For predominant peaks appearing on the profile.

(b) For predominant valleys appearing on the profile.

(c) Negative values denote peaks and valleys which were below or above the centerline, respectively.

profile traces shown in Figure 48 it is seen that by counting all of the peaks, a peak-to-peak spacing is obtained which agrees closely to the value determined from the interference pattern. Peak-to-valley depths appear to range between one-fourth and one-half fringe spacing (2.5 to 10 $\mu\text{in.}$), which also agrees fairly well with the values obtained from the Proficorder traces.

The interference patterns from the smooth platinum sample (Figure 70) show a noticeable change in surface texture before and after the emittance tests. Roll marks on the as-received surface are spaced about 500 $\mu\text{in.}$ apart and the peak-to-valley depth ranges from about one-half to two fringe spacings (5 to 20 $\mu\text{in.}$). Neither of these features were detected by the Proficorder which indicates the stylus did not "see" the narrowly spaced valleys, but instead rode over the peak tops. The true rms roughness of the as-received platinum is therefore estimated to be between 5 and 10 $\mu\text{in.}$ The interference pattern obtained after the emittance tests shows the peak-to-peak spacing increased to about 1000 $\mu\text{in.}$ and became more irregular. The peak-to-valley depth remained about the same. These latter characteristics agree fairly well with those indicated by the Proficorder traces of the annealed surface.

The most notable feature of the roughness data in Table 2 is the significant drop in the roughness values for the grit and shot-blasted samples after their emittance tests; the only exception being tungsten sample 2. This change in surface roughness provides an explanation for the drop in the total and spectral normal emittance values from these samples which was observed whenever the sample temperature was raised above previous level. The reason for the lower roughness value is attributed to thermal relief of the surface strain created by the shot-blast treatment; and subsequent recrystallization and grain growth.

To check the accuracy of the Proficorder traces from the rough samples, cross section and taper section mounts of several of the samples were prepared for metallographic examination. Photomicrographs of these sections are included with the sample data in Section 10. Unfortunately, the preservation of the surface profile in several of the taper-section mounts was poor because too thin a layer of plated metal was applied to the surface of these specimens. As a consequence, the surface profile in these sections did not always survive the metallographic grinding and polishing processes sufficiently to permit accurate measurements of the roughness parameters. Estimates of the average peak-to-valley depths were obtained from most of the sections, however, and are compared with the peak-to-valley depth values obtained from the Proficorder traces in Table 3. These comparisons indicate the Proficorder values to be significantly lower than the values indicated by measurements from the section photomicrographs except for copper sample 3 and tungsten sample 2. This finding casts serious doubt upon the validity of the rms, AA, and peak-to-valley roughness parameters listed in Table 2 for the copper and platinum samples. It appears possible that the magnitude of these parameters may actually be from 1-1/2 to 3 times larger than was determined from the Proficorder traces for these samples. However, the evaluation of roughness by microscopic techniques is also subject to possible error since only a small area of the surface is examined, and the specimens tend to be difficult to analyse.

Interpretation of the taper-section photomicrographs is difficult due to the random nature of the surfaces and the varied appearance of the surface plane caused by the particular polishing and etching procedures used. Dark occluded areas appear beneath the surface in several of the taper section photomicrographs of the rough copper samples. These areas are due to the presence of pits or valleys below the

Table 3

PEAK-TO-VALLEY DEPTHS AS INDICATED BY THE PROFICORDER
AND BY SAMPLE PHOTOMICROGRAPHS

Sample ^(a)	Average Peak-to-Valley Depth (μ in.)			
	Proficorder	Interference Photomicrographs	Taper Section	Cross Section
Copper 1 (A)	14	20	20	140
Copper 3 (B)	149		150	
Copper 5 (B)	224		400	750
Copper 5 (A)	98		300	
Copper 7 (B)	340		700	
Copper 8 (B)	668		800	
Copper 8 (A)	365		600	
Tungsten 1 (B)	2.8	5		
Tungsten 1 (A)	5.5	7	20	
Tungsten 2 (A)	38		30	
Tungsten 3 (B)	228		360	200
Tungsten 3 (A)	72		160	120
Platinum 1 (B)	0	15		
Platinum 1 (A)	12	15	20	
Platinum 3 (A)	153		500	500
Platinum 6 (B)	184			300
Platinum 5 (A)	70		200	200

(a) (A) denotes after emittance test (annealed); (B) denotes before emittance test (unannealed).

mean surface plane of the sample. Similarly, the occluded areas of copper in the nickel-plate layer represent surface peaks above the mean surface plane. If the polishing process was continued, the surface boundary would appear to advance in the direction of the wedge; the occluded copper areas (peaks) would be seen to attach to and become part of the copper surface, while the occluded voids and disturbed areas (valleys) beneath the surface would diminish in size and finally disappear. The dark appearance of these areas is attributed to the different polishing and etching characteristics of the disturbed surface metal. Similar, but well defined, occlusions of nickel and copper plate material were found in the taper sections of the tungsten and platinum samples, respectively. Before more accurate measures of the roughness parameters can be obtained from taper-section mounts, improvements are needed in the mounting technique to obtain clearer edge definition and more than one area should be sampled.

8.1.2 Surface Contamination

X-ray diffraction and spark spectrographic analyses of the as-received metals used in this study confirmed the absence of any significant impurities. The diffraction pattern from the smooth platinum sample, which was obtained after the emittance tests, consisted of only two d-lines, indicating that the surface of this sample was strongly oriented with the (200) and (220) crystal faces exposed.

X-ray diffraction patterns from the roughened copper and platinum samples also failed to detect any contamination. The patterns from the roughened platinum samples were more complete, indicating that the roughening process tended to destroy the preferred orientation of the surface. The degree of crystal randomization of the platinum surface correlated with the roughness; the d-line intensities from sample 3 corresponding to those reported by Swanson and Tatge (Reference 30), the intensities for sample 6 being intermediate to those for samples 1 and 3. The diffraction pattern for tungsten sample 2 was identical to that for sample 1, but three faint, additional lines were detected in the pattern from sample 3. Positive identification of the lines was not obtained, but they presumably were due to contamination from the silicon carbide grit used to roughen the sample.

Spark spectrographic analyses indicated all of the roughened copper and tungsten samples to be contaminated to some extent by the material used for roughening. Traces of silicon were detected in the copper samples, indicating glass contamination. Iron was detected in the spectrum from copper sample 8, indicating that the 5-min etch in hydrochloric acid was not successful in removing all of the embedded steel-shot contamination. Traces of aluminum and silicon were also detected in the spectra from tungsten samples 2 and 3. No attempt was made to obtain a quantitative analysis of these contaminants. Spectrographic analyses of the roughened platinum samples were not made but it is assumed that contamination similar to that found in the copper samples was likely.

No evidence of surface contamination was obtained from the microscopic examinations of the roughened surfaces. Similarly, no signs of embedded shot or grit were found in any of the cross and taper section mounts of the samples, with the exception of copper sample 7. In the cross section mount of this sample, several areas showing embedded glass fragments were found. A photomicrograph of one of these areas is shown in Figure 38.

From these analyses and examinations it is concluded that contamination of all of the roughened sample surfaces occurred. Although no quantitative analyses were made, the inability to detect embedded grit by microscope examinations of the surfaces and its absence in most of the metallographic sections indicates that the degree of contamination was small. Neither the x-ray diffraction nor the spectrographic technique was suitable for detecting the presence of thin ($< 1000 \text{ \AA}$) oxide layers on these surfaces. The best indication of the absence of any significant surface film was the bright, clean visual appearance of the sample surfaces after being heated in vacuum.

8.1.3 Substrate Damage

Evidence of considerable damage to the surface substrate layers of the roughened copper samples was revealed in the photomicrographs of the etched, taper-section mounts of these samples. A relatively deep layer of small crystallites which evidently were fractured during the shot-blast treatment of the surface is clearly evident at the surfaces of copper samples 3, 5, 7, and 8, before testing. The depth of the layer, determined from measurements on the photomicrographs, is shown below:

Sample	Depth of Substrate Damage	
	(μ in.)	(μ)
Copper 3	400	10
Copper 5	1100	28
Copper 7	1600	40
Copper 8	1500	38

Photomicrographs of the samples after their emittance tests indicate that the damaged layer disappeared after the sample annealed and recrystallized.

From the photomicrographs of the tungsten samples, no evidence of substrate damage is apparent in the fibrous grain structure of this metal. No attempt was made to determine the damage to the roughened platinum samples because no suitable etchant for the platinum was found which did not first remove the copper-plate layer from the section mount.

8.2 OPTICAL CONSTANTS

Optical constants for tungsten and platinum were computed by the method described in subsection 7.3, from data similar to that shown in Figures 13 and 14. Values were not obtained for copper due to insufficient energy from the polished specimen at temperatures below its softening point.

Values of optical constants obtained from measurements on tungsten sample 1 are presented in Table 4. The table also includes values interpolated from those presented by Roberts (Reference 5), and Martin (Reference 4). Very good agreement is obtained for values of k but only fair agreement for values of n . Figure 13 shows that this may be expected since values of n obtained from intersections of the characteristic curves are much more sensitive to uniqueness of the intersections.

Table 4

OPTICAL CONSTANTS OF TUNGSTEN FOR FOUR WAVELENGTHS

Temperature (°K)	Source	Optical Constants							
		1.0 μ		1.5 μ		2.0 μ		4.0 μ	
		n	k	n	k	n	k	n	k
300	Reference 5	3.18	3.95	2.83	5.32	1.52	7.92		
1100	Reference 5	3.66	4.11	3.51	5.87	3.38	7.84		
1200	Reference 5			3.60	5.90	3.60	7.70		
	Data			3.10	5.70	3.50	7.80	3.70	13.0
1370	Reference 5			3.80	6.00	3.90	7.60		
	Data			3.00	5.70	3.90	7.70		
1600	Reference 5	4.03	4.21	4.13	6.02	4.18	7.76		
2200	Reference 4	4.40	4.00	4.30	5.40	4.70	7.00	7.60	12.5

The slope of relative directional spectral emittance curves is a strong function of wavelength, as can be seen by inspection of these curves presented in Section 10. At long wavelengths the slope becomes increasingly steep at the larger angles. Therefore small errors in θ produce large errors in the measurement of

normalized relative emittance and as the wavelength increases a higher degree of accuracy is required in the measurements of θ where values of n and k are desired. It was found that at wavelengths of $4\ \mu$ and higher, this source of error increased considerably so that a reliable determination of n and k beyond this wavelength was not possible.

The absolute spectral normal emittance may be computed from the optical constants by use of Equation 21. This computation was performed as a check on the validity of results. Table 5 presents a comparison between calculated and measured values of spectral normal emittance. Very good agreement was found at 1200°K , but larger differences occurred at 1370°K . The agreement obtained shows that optical constant measurements made on this sample are of sufficient accuracy for computing thermal radiative behaviour. The comparison verifies the measurement techniques used since the optical constant results are derived from angular measurements and the absolute emittance values from temperature measurements. Therefore, the errors in each case are due to different influences.

Table 5
MEASURED AND CALCULATED SPECTRAL NORMAL
EMITTANCE VALUES OF TUNGSTEN
FOR THREE WAVELENGTHS

Temperature (°K)	Type of Value	Normal Emittance		
		1.5 μ	2.0 μ	4.0 μ
1200	Measured	0.270	0.170	0.093
	Calculated	0.257	0.173	
1370	Measured	0.220	0.140	0.110
	Calculated	0.250	0.187	

Optical constants obtained for platinum sample 1 are presented in Table 6 and compared to those reported by Eaton and Conn (Reference 31) at lower temperatures. No published values were found at higher temperatures for this material. Difficulty was encountered with the platinum samples due to flexing and warping under tension at elevated temperatures. This affected the accuracy of angular determinations, especially at the larger grazing angles. The measured angles were corrected by

Table 6
OPTICAL CONSTANTS OF PLATINUM FOR FIVE WAVELENGTHS

Temperature (°K)	Source	Optical Constants									
		1.0 μ		1.5 μ		2.0 μ		3.0 μ		4.0 μ	
		n	k	n	k	n	k	n	k	n	k
300	Reference 31	3.4	6.2	4.5	3.2	5.7	9.7	7.7	12.3	9.7	14.1
860	Data					5.6	9.6				
1030	Data					5.8	9.4				
1200	Data			5.4	7.8	6.1	9.1				
1360	Data			5.2	7.8						

assuming symmetry of the relative emittance peaks on either side of the normal. Optical constants were then computed from the corrected directional emittance measurements. The spectral normal emittance was calculated from Equation 21 in the same manner as for tungsten. The results are compared with the measured values in Table 7. Very good agreement was obtained between calculated and measured values with the largest deviation on the order of 8% of the measured absolute value.

Table 7
MEASURED AND CALCULATED SPECTRAL
NORMAL EMITTANCE VALUES
FOR PLATINUM AT TWO WAVELENGTHS

Temperature (°K)	Type of Values	Normal Emittance	
		1.5 μ	2.0 μ
860	Measured	0.220	0.163
	Calculated		0.165
1030	Measured	0.225	0.178
	Calculated		0.173
1200	Measured	0.230	0.187
	Calculated	0.212	0.183
1370	Measured	0.225	0.193
	Calculated	0.212	

8.3 EMITTANCE CHARACTERISTICS

Spectral and total directional emittance data were obtained for all test samples as a function of wavelength, temperature, and polarization. These data are presented in Section 10 in both graphical and tabular form. The temperature and wavelength range achieved for each sample was established on the basis of available radiant energy, high temperature properties of test materials, and power supply limitations. Since the analytical methods for evaluating the effect of roughness on the emittance of a surface involves knowing the emittance of both the rough and the smooth surfaces of the material, a considerable amount of the rough sample data could not be analyzed because of the lack of comparable data from the smooth samples. In the case of copper sample 1, measurable spectral energy was only obtained at wavelengths of 2 μ and 4 μ and then only after raising the sample temperature to 1030°K. In the case of the tungsten samples, significant changes in the surface condition and the emittance at temperatures above 1600°K indicated that reliable analyses could only be made with the lower temperature data from these samples.

The results on copper, tungsten, and platinum all indicated that the emitted energy for surfaces with rms roughness as high as 205 μ in. was still significantly polarized. The degree of polarization and the distribution of emitted energy are wavelength and temperature dependent and are partially established by the properties of the pure material. However, the test results yield no obvious correlation which would establish a relationship between surface roughness and changes in directional emittance or which would permit prediction of directional properties for rough surfaces from known properties for the polished surface.

A comparison of the spectral directional emittance for the rough samples at a given temperature and wavelength shows a reduction in specularity with increasing roughness. Figure 15 for copper at $4\ \mu$ is typical of such results for all samples tested. It is observed that roughness tends to reduce maximum values of $\epsilon(\theta, \lambda, T)/\epsilon(\theta_N, \lambda, T)$ at grazing angles and increase this ratio between 0 and 60 deg from the normal. Similar plots for the copper samples at other temperatures and wavelengths, indicate the same general result. The same characteristics are also indicated for the three platinum samples tested.

Figure 16 shows some typical total directional properties of the copper samples. The changes in the angular distribution of emitted energy throughout the spectrum are similar to those shown for copper at $4\ \mu$. Results for platinum were similar to those for copper.

The effect of roughness on angular distribution of emitted energy is clearly demonstrated by Figures 15 and 16. Present theories indicate that the energy distribution should be dependent upon the ratio of roughness to emitted wavelength, σ_m/λ , and upon the optical properties of the pure material. This dependence is expected where $(\sigma_m/\lambda) < 1$. Variations in the angular distribution of energy as a function of σ_m/λ are shown in Figures 17, 18, and 19. In these figures, the distribution of emitted monochromatic energy for a rough sample is shown relative to the distribution for a polished specimen at the same temperature and wavelength. A constant value of unity is equivalent to the pure polished surface while a purely diffuse emitter would give values of less than unity at all angles greater than zero.

For copper the distribution of emitted energy becomes uniformly more diffuse for increasing values of σ_m/λ . The line referred to as a cosine surface represents a purely diffuse emitter relative to the polished specimen and indicates the limit expected for an extremely rough sample. The copper data indicate the possibility of a correlation between σ_m/λ and the energy distribution. However, as shown by Figure 18, the energy distribution from the platinum samples fails to exhibit uniform change with σ_m/λ for the same range of roughness values as for the copper.

The data on copper and platinum show that changes in energy distribution with increasing σ_m/λ are not continuous as this roughness parameter varies over the range, $0 < (\sigma_m/\lambda) < 5$. Figures 17 and 18 show that as the value of σ_m/λ increases from 0 to approximately 0.35 the relative energy increases at angles between 0 and 80 deg and decreases at the higher grazing angles. As σ_m/λ is increased beyond this value, the distribution then becomes increasingly diffuse. Such behaviour would not be anticipated on the basis of presently available diffraction theories. However, it is not surprising that present analyses do not clarify the observed results since in all cases the absolute emittance of the rough samples also changed indicating an influence due to inter-reflections at the sample surface.

Relative energy distributions for tungsten are shown in Figure 19. It is clear that the tungsten samples did not produce results similar to platinum and copper as σ_m/λ was increased. These samples exhibited nearly diffuse behaviour at values of σ_m/λ as low as 0.13. This must be attributed to surface effects other than roughness on the tungsten since roughness alone could not have given a diffuse surface at such low values of σ_m/λ . Evidence of changes in the surface character of the tungsten samples was visually evident after removal from the test

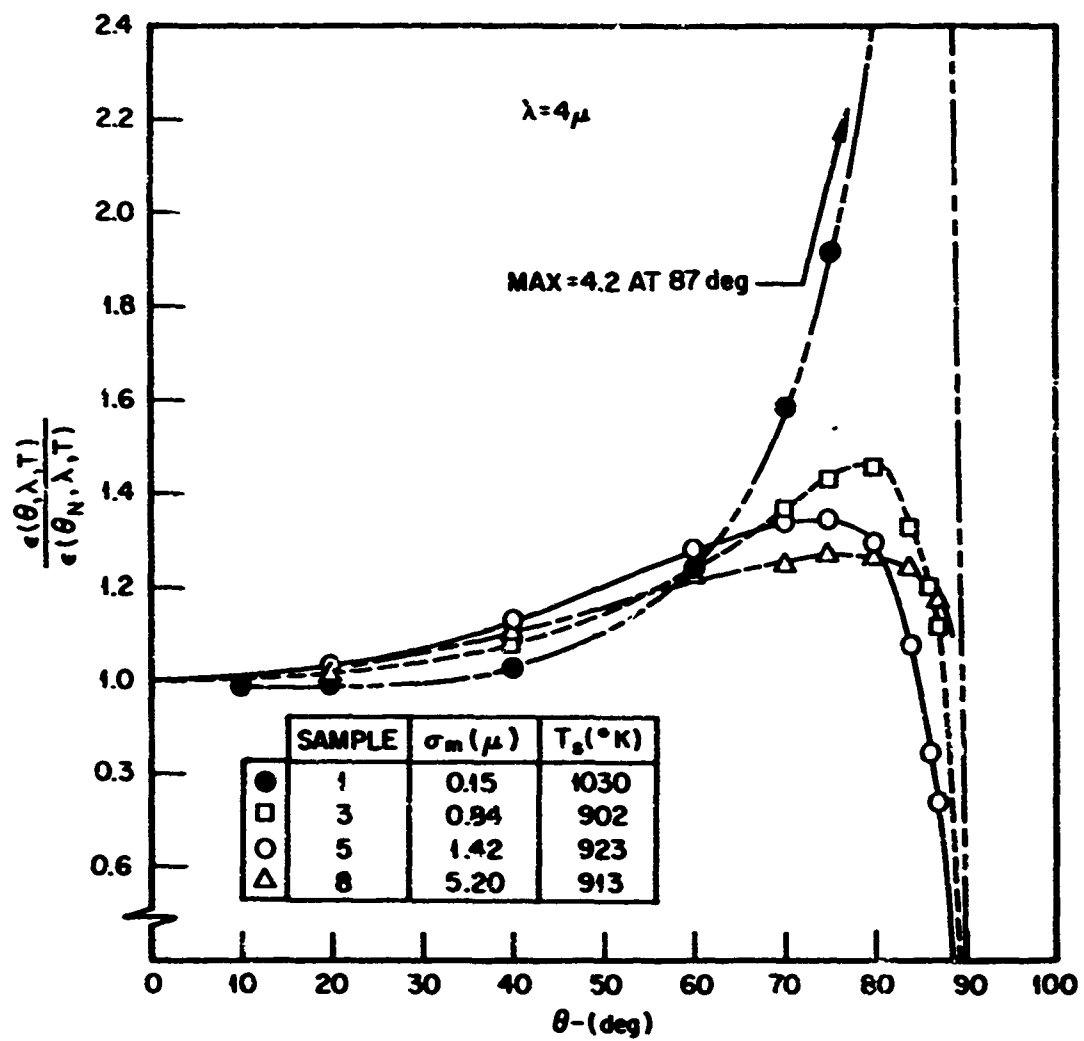


Figure 15 Relative Spectral Directional Emittance of Copper

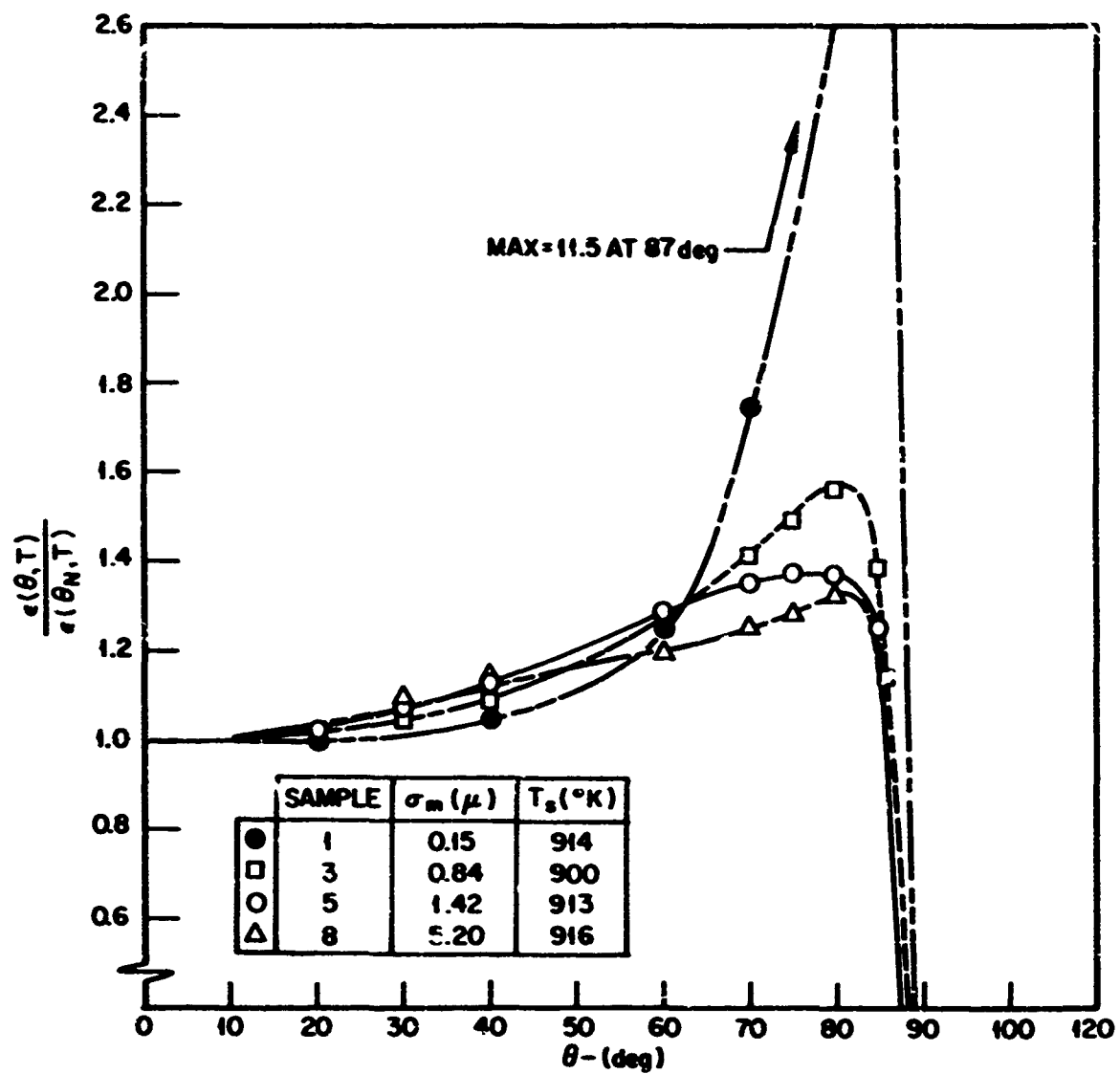


Figure 16 Relative Total Directional Emittance of Copper

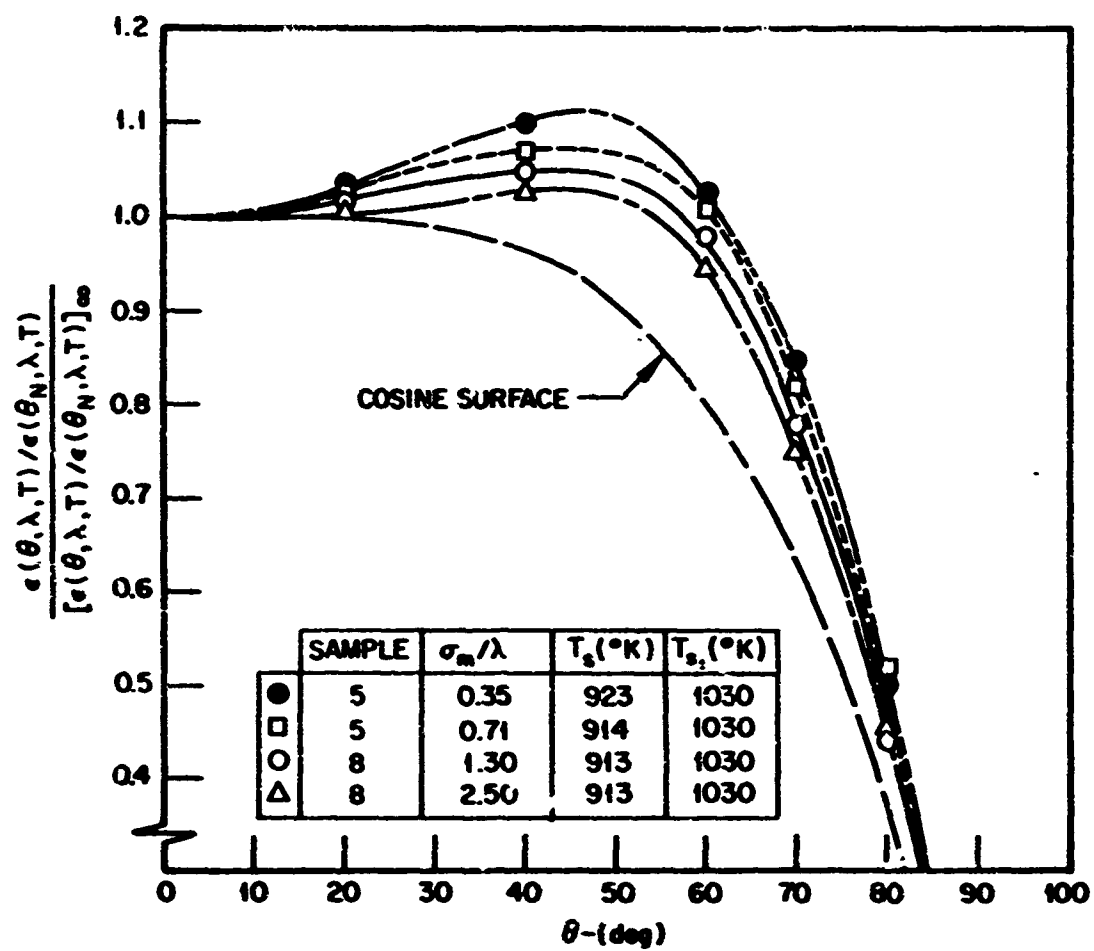


Figure 17 Relative Spectral Directional Emittance Distribution for Copper

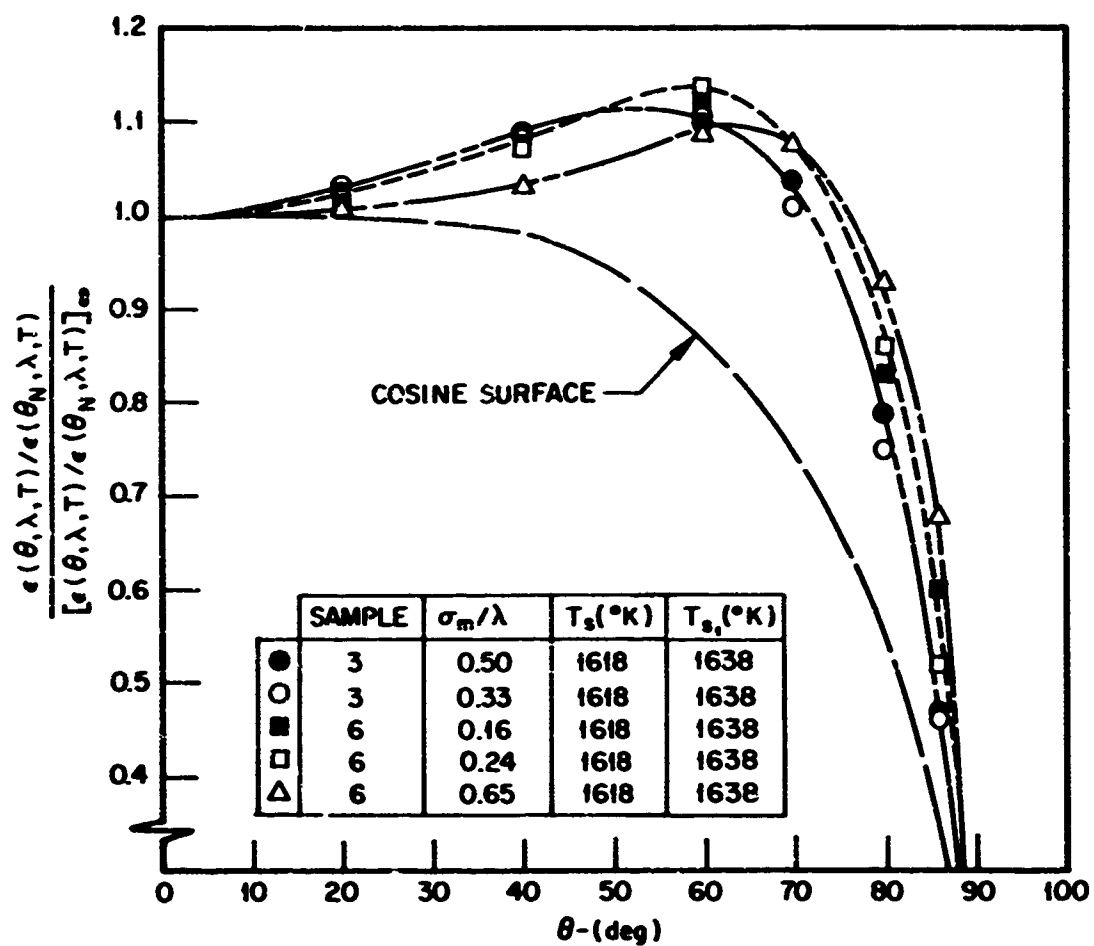


Figure 18 Relative Spectral Directional Emittance Distribution for Platinum

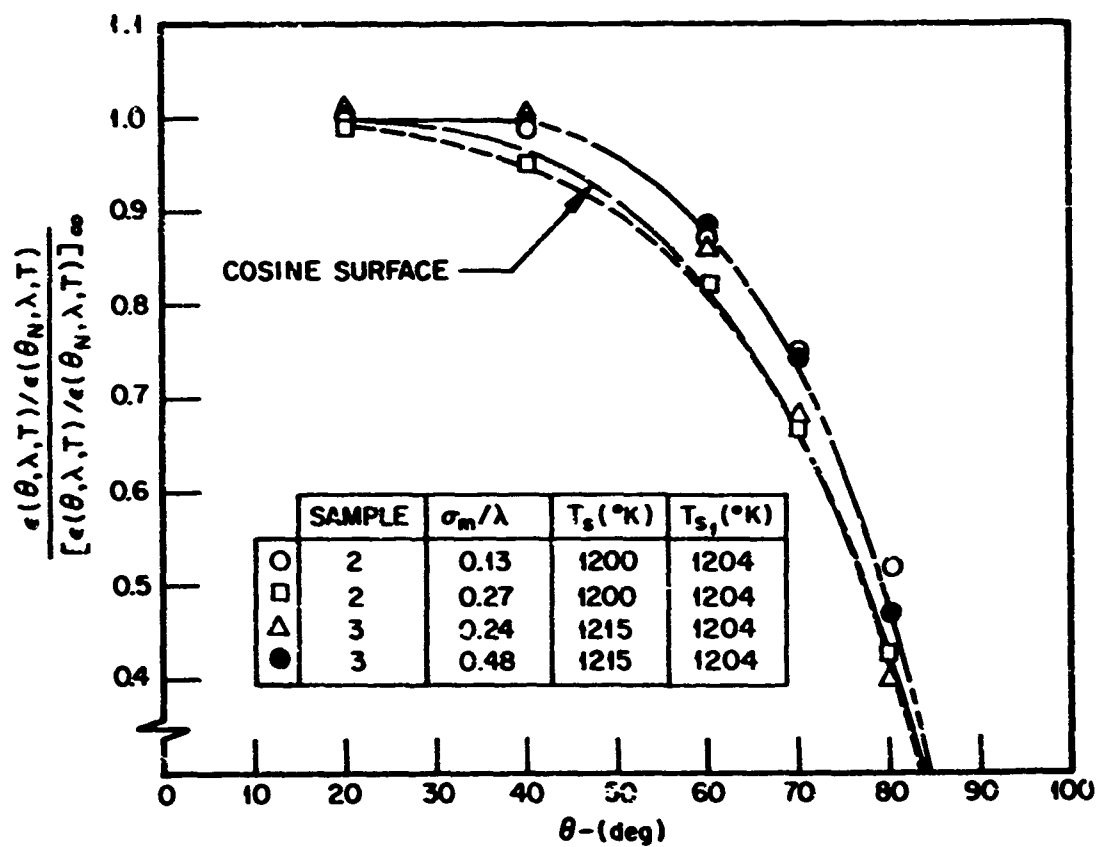


Figure 19 Relative Spectral Directional Emittance Distribution for Tungsten

chamber. However, it is not specifically known at what temperature these changes became significant in terms of radiant properties.

Absolute values of spectral normal and total normal emittance were determined as a function of temperature and are tabulated in Section 10 for each sample. No clear relationship between roughness and increase in emittance is apparent from inspection of the data. Table 8 shows the ratio of normal values for a rough surface to those of a polished surface for copper, platinum, and tungsten as surface roughness was increased. In each case, sample 1 is considered as the polished surface although each had measurable roughness at the conclusion of the high-temperature exposure.

Table 8
TOTAL AND SPECTRAL NORMAL EMITTANCE RATIOS
FOR ROUGH SAMPLES RELATIVE TO POLISHED SAMPLES

Sample	σ_m (μ)	Temperature (°K)	$\frac{\epsilon(\theta_N, T)}{[\epsilon(\theta_N, T)]_\infty}$	$\epsilon(\theta_N, \lambda, T)/[\epsilon(\theta_N, \lambda, T)]_\infty$			
				2 μ	4 μ	6 μ	8 μ
Copper	1	0.15	915	1	1	1	1
	3	0.84	901	2.5	2.9	2.4	2.9
	5	1.42	913	2.7	3.3	2.5	2.2
	7	2.90	923	3.5	4.0	3.3	3.2
	8	5.2	913	6.7	8.9	6.7	5.4
Platinum	1	0.12	1639	1	1	1	1
	6	0.97	1618	1.33	1.12	1.05	1.04
	3	2.00	1618	1.40	1.19	1.13	1.08
Tungsten	1	0.025	1039	1	1	1	1
	2	0.53	1033	2.9	2.9	3.3	2.7
	3	0.96	1040	3.9	2.6	5.1	5.8

The results presented in Table 8 represent only a small part of the available data. However, the comparison between smooth and rough samples is typical of all results obtained. The total and spectral normal emittance of the samples was observed to increase with increasing roughness for all three materials. There is also a trend toward a lesser increase in $\epsilon(\theta_N, \lambda, T)$ for longer wavelengths. Comparison of all data, however, shows no clear relationship between $\epsilon(\theta_N, \lambda, T)/[\epsilon(\theta_N, \lambda, T)]_\infty$ and σ_m . The largest increase in emittance was observed for the first step in increasing roughness with lesser changes taking place as higher values of σ_m were achieved.

The results shown in Table 8 for copper sample 8 must be considered in terms of the surface characteristics of this sample. This sample was significantly damaged by the roughening process and had trace contaminants of iron when examined after the high-temperature runs. Therefore, the significantly higher value for copper sample 8 may not be entirely due to roughness.

The emittance of all the tungsten samples was observed to become unstable during high-temperature exposure and for this reason the correlation with increasing roughness is subject to interpretation. This is particularly true for tungsten

Sample 3 which showed increasing values of normal emittance ratios for increasing wavelengths. This behaviour cannot be attributed to roughness alone and must be due to the surface condition of the samples.

The ratio of hemispherical to normal emittance was computed by the method described in Section 7 for each sample from the relative directional data presented in Section 10. This ratio furnishes an indication of sample specularity and is expected to decrease relative to the polished surface as roughness increases. The results obtained for copper, platinum, and tungsten are presented in Tables 9, 10, and 11.

Table 9

HEMISPHERICAL TO NORMAL EMITTANCE RATIOS FOR COPPER

Temperature (°K)	Sample	$\frac{\epsilon(T)}{\epsilon(\theta_N, T)}$	$\epsilon(\lambda, T)/\epsilon(\theta_N, \lambda, T)$	
			2 μ	4 μ
541	1			
561	3			
564	5	1.280		
	7	1.226		
	8	1.216		
656	1			
660	3	1.207		
645	5	1.198		
	7	1.223		
	8			
757	1	1.376		
741	3	1.187		
750	5	1.191		
747	7	1.219		
761	8	1.113		
866	1	1.353		
854	3	1.233		1.066
863	5	1.154	1.126	1.146
869	7	1.198	1.176	1.180
863	8	1.167	1.105	1.143
914	1	1.353		
902	3	1.141	1.106	1.123
914	5	1.164	1.111	1.147
897	7	1.206	1.156	1.146
913	8		1.088	1.128
1033	1	1.304	1.296	1.263

Table 10

HEMISPHERICAL TO NORMAL EMITTANCE RATIOS FOR PLATINUM

Temperature (°K)	Sample	$\frac{\epsilon(T)}{\epsilon(\theta_N, T)}$	$\epsilon(\lambda, T)/\epsilon(\theta_N, \lambda, T)$				
			1.0 μ	1.5 μ	2.0 μ	4.0 μ	6.0 μ
696	1	1.225					
703	3	1.211					
861	1	1.196			1.147	1.175	
863	6	1.222			1.207	1.227	
866	3	1.203			1.161	1.214	
1032	1	1.190			1.132	1.175	
1025	6	1.227			1.200	1.220	
1034	3	1.190			1.183	1.209	
1196	1	1.177		1.123	1.138	1.188	1.194
1194	6	1.206		1.168	1.202	1.208	1.192
1202	3	1.175		1.155	1.178	1.203	1.197
1369	1	1.162		1.119	1.147	1.180	1.195
1369	6	1.208		1.171	1.204	1.210	1.200
1373	3	1.076		1.136	1.155	1.181	1.187
1639	1	1.139	1.082		1.143	1.174	1.180
1615	6	1.090		1.176	1.205	1.231	1.218
1618	3			1.162	1.185	1.197	1.193

Table 11

HEMISPHERICAL TO NORMAL EMITTANCE RATIOS FOR TUNGSTEN

Temperature (°K)	Sample	$\frac{\epsilon(T)}{\epsilon(\theta_N, T)}$	$\epsilon(\lambda, T)/\epsilon(\theta_N, \lambda, T)$					
			1.0 μ	1.5 μ	2.0 μ	4.0 μ	6.0 μ	8.0 μ
706	1	1.280						
693	2	1.087						
692	3	1.030						
870	1	1.220						
862	2	1.025			0.953	1.056	1.100	
863	3	1.024			1.010	1.024	1.027	
1039	1	1.200			1.152	1.248		
1029	2	1.061			0.958	1.031	1.046	1.084
1040	3	1.022		0.995	1.010	1.022	1.022	1.031
1200	1	1.160		1.078	1.130	1.200		
1200	2	0.993		0.935	0.952	1.041	1.089	1.137
1215	3	1.020		0.998	1.003	1.021	1.024	1.030
1380	1	1.140	1.021	1.078	1.116	1.168	1.187	1.213
1385	2	0.996	0.957		0.960	1.072	1.115	1.200
1391	3	1.012	0.990	1.007	1.018	1.028	1.025	1.023
1603	1		1.039	1.660	1.075	1.125	1.155	1.181
1607	2	1.001	0.974		0.965	1.082	1.120	1.157

The results for copper samples indicate that the ratio $\epsilon(T)/\epsilon(\theta_N, T)$ does in general decrease as the roughness increases relative to a smooth surface, but that this change is not uniform. Inspection of the data presented in Section 10 shows that the directional emittance from the copper surfaces was non-uniform about the normal. This would produce irregular results for hemispherical emittance. The non-uniform distribution of emitted energy for the rough copper samples was verified through repeated measurement on each sample, with the sample mounted end to end in the apparatus. Identical results were obtained during the second measurement confirming the initial observation. It is presently assumed that the non-uniformity was caused by the sample surface geometry although the profilometer and micrographic inspections failed to produce results which clearly justify this assumption.

The platinum hemispherical to normal emittance ratio was observed to increase with increasing roughness for temperatures between 700 and 1370°K and decrease at 1600°K. The reason for this trend is apparent from inspection of Figure 18 which shows the distribution change for the 1618°K temperature. While the energy at grazing angles decreases there is an increase of energy between 0 and 80 deg. integration of the distribution curve between 0 and 90 deg gives a higher result of $\epsilon(T)/\epsilon(\theta_N, T)$ for the rough sample. More data are required on samples having roughness from 0 to 150 μ in. to clarify the manner in which energy is re-distributed due to changes in surface roughness.

8.4 DISCUSSION

The results obtained during this program show the changes expected in surface emittance due to considerable surface roughness. The directional emission of the rougher surfaces indicates that assumptions of cosine law distribution must be applied with considerable caution when dealing with surfaces of the types studied. Significant polarization and specularity are still present for roughnesses as high as 200 μ in. at a wavelength of 8 μ . The degree of specularity is, of course, dependent upon the optical properties (n and k) of the bulk material at the temperature and wavelength of interest.

Changes in distribution of energy, relative to a smooth surface, were observed to occur most rapidly for surface rms roughness values between 5 and 50 μ in. with more gradual modification occurring as roughness was increased beyond 50 μ in. The corresponding range in roughness to wavelength ratio was $0 < \sigma_m/\lambda < 1$. More data should be obtained in this range to define the exact nature of the rapid changes which occur upon introduction of small roughness.

Existing theories for predicting distribution of reflected energy have been reviewed to show the nature of the results obtained and the assumptions used. It was shown that results from the exact approach, up to the first order terms, are identical to those from the approximate solutions for the simple case of $\sigma_m/\lambda \ll 1$. This verifies the approximate solution for this special case. However, the utility of the approximate solution is very limited for use in prediction of emissive behaviour since the results are based upon assumptions of a perfectly conducting surface and no shadowing or multiple reflections. With these assumptions it is possible to obtain solutions for the distribution of reflected energy; however, the hemispherical reflectance remains identical to that for a polished surface.

To aid in the prediction of emissive behaviour it is essential to establish solutions which include effects of polarization, shadowing, and multiple reflections.

The exact approach accounts for these effects in its most general form. The complexity involved in accomplishing a general solution and the slowly converging nature of the series are discussed in the appendix. Nonetheless, it is obvious that efforts must be expended toward obtaining a solution which includes effects of multiple reflections and scattering. The exact approach may yield information on the nature of these effects when it is extended to the second order terms. Such a solution is essential for correlation of data where roughening is observed to increase the absolute hemispherical emittance of a pure metal.

The data obtained on copper, platinum and tungsten for various values of roughness show that increasing roughness will produce increasingly diffuse surfaces with higher normal and hemispherical emittance values. However, no correlation was found between surface roughness and the observed changes in emissive behaviour. Comparisons between sample types disclose a different nature to the changes which occur for nearly identical values of roughness. Copper was observed to have a significant increase in normal emittance relative to the polished surface as rms roughness was increased to 33 $\mu\text{in.}$ (0.84 μ). The platinum surfaces exhibited less of an increase in relative values while tungsten increased in relative values in the same manner as copper. However, the distribution of energy for slightly roughened tungsten was found to be nearly diffuse while emission from both copper and platinum continued to remain highly directional as rms roughness was increased to 200 $\mu\text{in.}$ Such differences in sample emissive behaviour cannot be attributed to surface geometry only, but must also be due to chemical contamination and/or changes in the physical state of the surface layers.

Differences in relative behavior have also been reported by Birkebak (Reference 14) where measurements were made of the directional reflectance from slightly rough samples of vapor deposited aluminum and ground nickel. It was found that the relative hemispherical reflectance of aluminum surfaces was reduced to a lesser degree than for nickel surfaces having the same value of roughness. These observations confirm the existence of dissimilar changes in surface condition due to the roughening process and show further the difficulties involved in observing effects of surface roughness without other factors influencing the results.

Bennett and Porteus (Reference 9) have suggested the use of bidirectional reflectance measurements on polished and roughened surfaces as a means for determination of an optical rms roughness (σ_0) in lieu of profilometer results for σ_m . This procedure was followed by Birkebak on the nickel and aluminum surfaces and compared to profilometer readings. Once again the results obtained were apparently influenced by surface characteristics other than roughness with the ratio σ_0/σ_m being much higher for nickel than for aluminum.

The above reports point out the difficulties involved in separating the effect of surface roughness from effects caused by other surface characteristics. Under these circumstances, two samples of different material which are prepared using identical procedures to obtain equal roughness are likely to produce significantly different ratios of $\epsilon(\theta, \lambda, T)/[\epsilon(\theta, \lambda, T)]_\infty$. Elevating surfaces to temperatures near the softening point compounds the problem of producing identical surface optical constants from one sample to another. Inspection of the photomicrographs presented for copper samples demonstrates the variety of surface conditions found on samples used in this program and demonstrates the difficulty in obtaining reproducible chemical and physical conditions at the radiating surface.

It is apparent that studies performed solely for determining effects of surface roughness require elimination or positive control of all other influences. It is possible that vacuum deposition on roughened substrates may provide the required surface purity. However, such procedures will require development since deposition rates, chamber cleanliness, and film thickness are factors which affect surface optical properties. Until such procedures are available it is apparent that only highly stable materials should be used such that chemical effects are minimized. Further studies are planned to investigate these possibilities.

Section 9

CONCLUSIONS AND RECOMMENDATIONS

The following conclusions and recommendations are based upon the experience gained during this research.

1. Pure metal surfaces retain directional emittance properties with increasing rms roughness up to 204 $\mu\text{in.}$ The greatest modification to the distribution of emitted energy relative to a smooth sample occurs between 0 and 50 $\mu\text{in.}$ for the temperatures and wavelengths observed in this program. This range of roughness requires further study to clarify the emissive behaviour of slightly rough surfaces.
2. Present theoretical treatments of the interaction of electromagnetic energy with rough surfaces are inadequate for predicting the emissive behaviour of such surfaces. Present theories must be extended to include the effects of shadowing, multiple reflections, and finite conductivity for application to prediction of the distribution and magnitude of emitted energy. An extension of the exact approach suggested by Rice appears best suited for including these real surface effects.
3. Very rough surfaces ($\sigma_m > 100 \mu\text{in.}$) prepared by grinding or blasting techniques will invariably suffer partial contamination from the grit or compound used. Cleaning solutions and etchants are ineffective for removing all trapped material without destroying the surface itself. Vacuum deposition over a previously roughened substrate appears promising for the preparation of very rough pure metal surfaces.
4. Surface profilometry gives results which are in significant disagreement with metallographic examination, with profilometry generally indicating lesser roughness values. Further studies should be accomplished to determine whether a usable relationship exists between the true surface profile and that given by a profilometer trace. Such a study would necessarily be statistical in nature and require improvement of present metallographic inspection techniques as applied to the determination of surface roughness.
5. X-ray diffraction and conventional spectrographic analysis yield little useful information concerning the nature or existence of surface oxides or contaminant films. Techniques should be developed for determination of the thickness and chemical nature of such films so that an evaluation of their effects on radiant behaviour may be accomplished. Electron diffraction and electron microscopy are promising analytical tools for this evaluation.

Section 10

EXPERIMENTAL DATA

Photomicrographs, profile traces, emittance data, and sample history are presented for each of the test samples in this section. The following information is also presented:

- RMS roughness values
- Emittance test procedure and temperatures
- Index to location of emittance-data tables and figures
- Remarks regarding the stability or changes of the sample characteristics

Absolute total and spectral normal emittance values are shown in tabular form, relative total and spectral directional emittance data are shown in graphical form. The ordinate scale chosen to present relative emittance ratios for each sample was varied to best illustrate the temperature effect on directional emittance. Total directional emittance values were normalized to a value of 1 at $\theta = 0$ deg.; whereas the spectral directional emittance values for the parallel and perpendicular polarized components were normalized to a value of 0.5 at $\theta = 0$ deg. Thus, to obtain the complete relative spectral directional values, the relative values for the parallel and perpendicular components at each respective angle must be added together. In general, the relative directional emittance curves were comparatively flat in the region $-20 \text{ deg} \leq \theta \leq 20 \text{ deg}$. Therefore, the abscissa has been compressed in this region to aid in presenting the data.

The directional emittance has been plotted as measured, with no angular correction applied to compensate for possible sample misalignment or warpage. The aperture slit width (Sections 6 and 7) was set to a value such that the sample image filled the slit out to viewing angles of ± 87 deg. In those cases where sample alignment was modified by warpage the sample edge was imaged at somewhat smaller viewing angles for one direction of rotation about the axis and correspondingly larger angles for the other. Allowance was made for possible misalignment by making observations out to angles of ± 92 deg from the normal, or until it was obvious that the aperture slit was no longer completely filled by the sample. Interpretation of the graphical results must be made in terms of the above procedure.

10.1 COPPER SAMPLE 1

1. Sample – Copper Sample 1.
2. Preparation – Electropolished by the method described in subsection 4.2.6.
3. RMS roughness – Before emittance tests, $5.2 \mu\text{in.}$; after, $5.7 \mu\text{in.}$
4. Test procedure – Sample was heated to 550°K for $1/2$ hr in vacuum before obtaining emittance data after which absolute and relative directional emittance data were obtained at five temperatures between 545 and 1035°K . Total and spectral normal emittance values at 755 and 865°K were rechecked to determine the effect of surface recrystallization on the emittance of the sample. Vacuum throughout the test was maintained between 1 and 5×10^{-5} Torr. Total elapsed time at T_{max} was 3 hr.
5. Emittance data – Absolute total and spectral normal emittance values are shown in Table 12. Relative total directional emittance data are shown in Figure 23. Relative spectral directional emittance data at 2 and 4μ are shown in Figure 24.
6. Remarks – Due to the low emittance of this sample, it was necessary to raise the sample temperature to 1035°K to obtain sufficient energy for spectral directional emittance measurements at 2 and 4μ .

Clearly defined grain boundaries were visible on the sample surface after being tested at 1035°K . (See Figure 20). The substrate grain structure before and after the emittance test is shown in the taper section photomicrographs in Figure 22. Rechecks of the absolute emittance at lower temperatures indicated recrystallization did not significantly affect the emittance. Comparison of the interference photomicrographs (Figure 20) indicates the predominant surface profile did not change significantly but the secondary roughness smoothed out somewhat resulting in clearer interference fringes. These findings were also indicated by the Proficorder traces.

X-ray diffraction and spark spectrographic analyses of the sample, after testing, indicated the sample purity to be $99.9+\%$.

A high uncertainty in the accuracy of the absolute emittance values at the lower temperature exists, and is inherent in the method for low emittance samples. Since the sample to blackbody signal ratio was between 0.5 and 2.5% , a small reading error in either the zero or sample signal levels results in a large relative error in the emittance value.

Dis-symmetry in the angular position of the relative directional emittance peaks in Figures 23 and 24 indicates the sample may have been misaligned 1 or 2 deg.



Before



After

Figure 20 Surface Interference Photomicrographs of Copper Sample 1 Before and After Emittance Tests

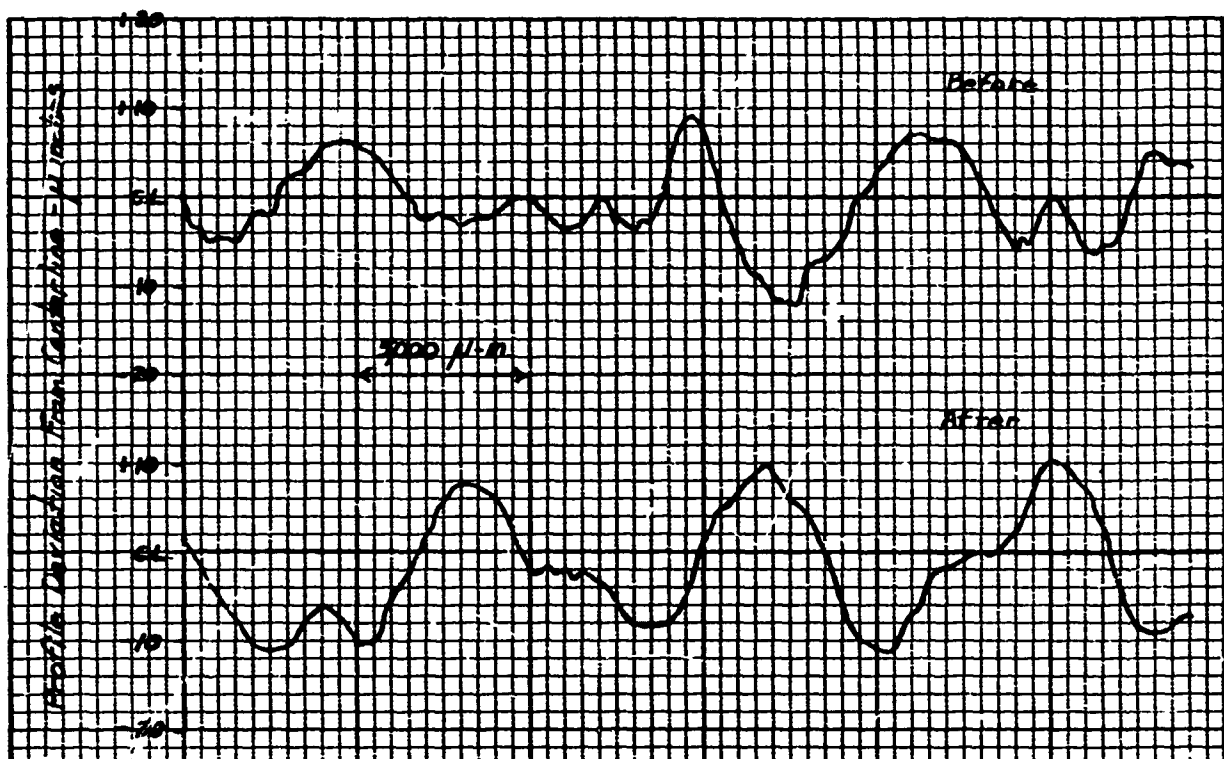
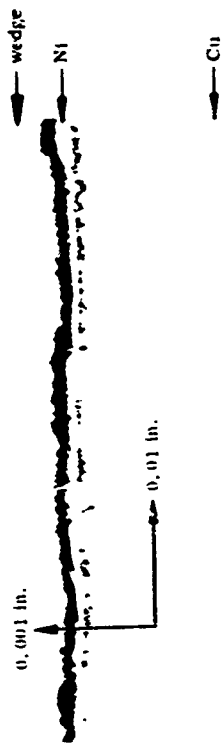


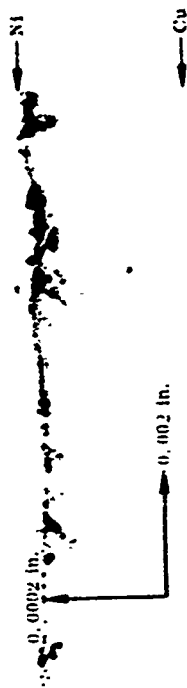
Figure 21 Typical Profile Traces for Copper Sample 1 Before and After Emittance Tests

Table 12
ABSOLUTE EMITTANCE DATA FOR COPPER SAMPLE 1

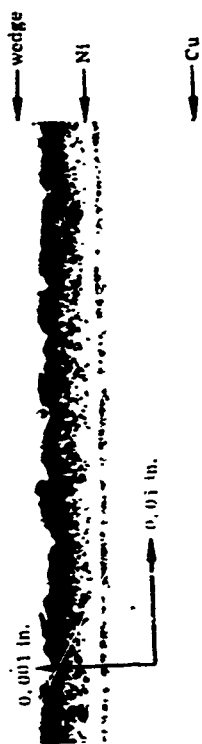
Temperature (°K)	Test	$\epsilon(\theta_N, T)$	$\epsilon(\theta_N, \lambda, T)$					
			1.5 μ	2 μ	4 μ	6 μ	8 μ	10 μ
545 755 865 915 1035	2	0.004	First Temperature Cycle					
	4, 5	0.015						
	8, 9	0.020						
	12, 13	0.023						
	15, 16	0.025						
Second Temperature Cycle, After Recrystallization								
755	22, 23	0.016	0.027	0.020	0.019	0.016	0.014	0.016
865	25, 26	0.019	0.023	0.023	0.022	0.019	0.017	0.013



Taper Section After



Taper Section After



Taper Section Before



Taper Section Before

Figure 22 Taper Section Photomicrographs of Copper Sample 1 Before and After Emittance Tests

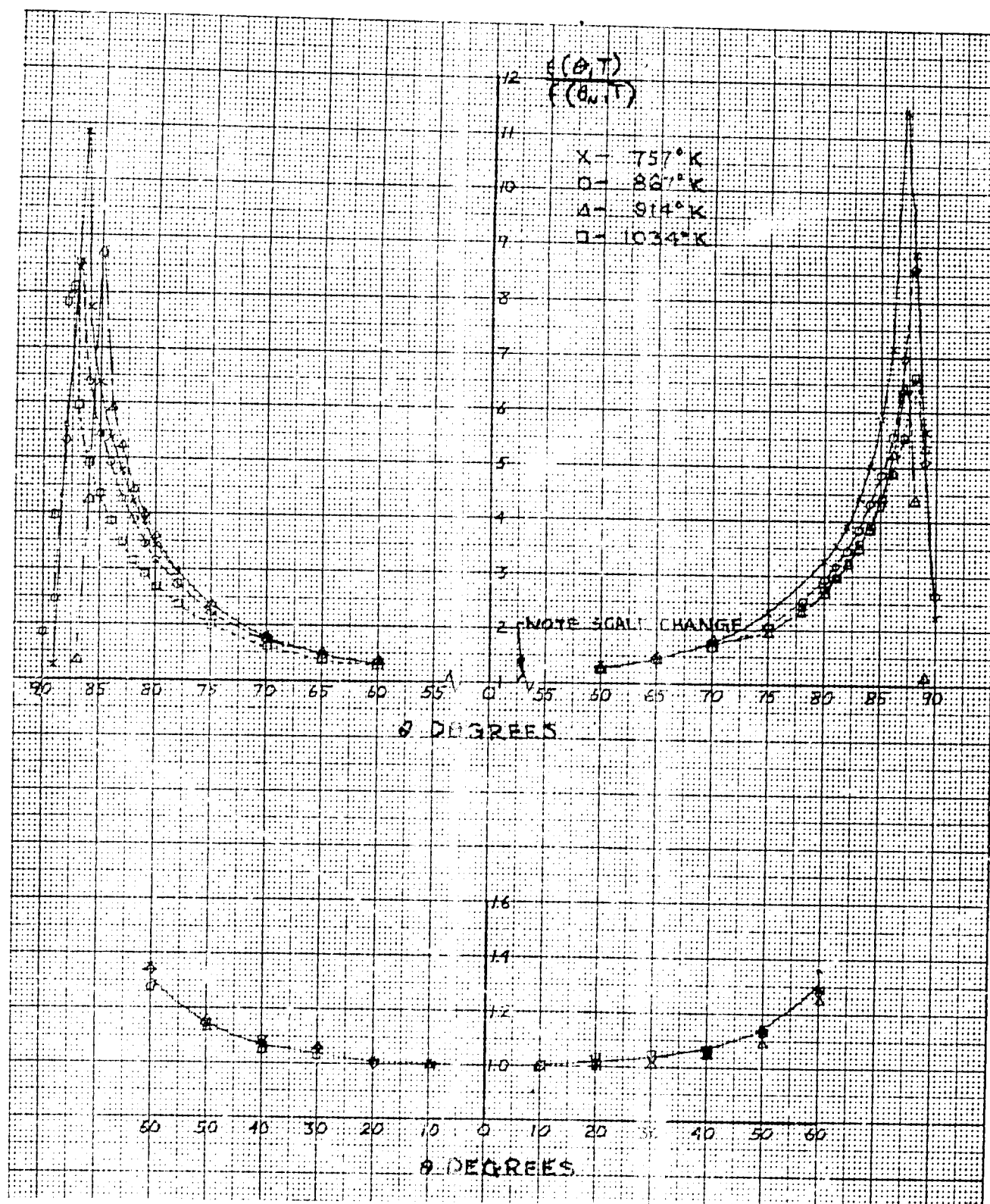


Figure 23 Relative Total Directional Emittance, Copper Sample 1

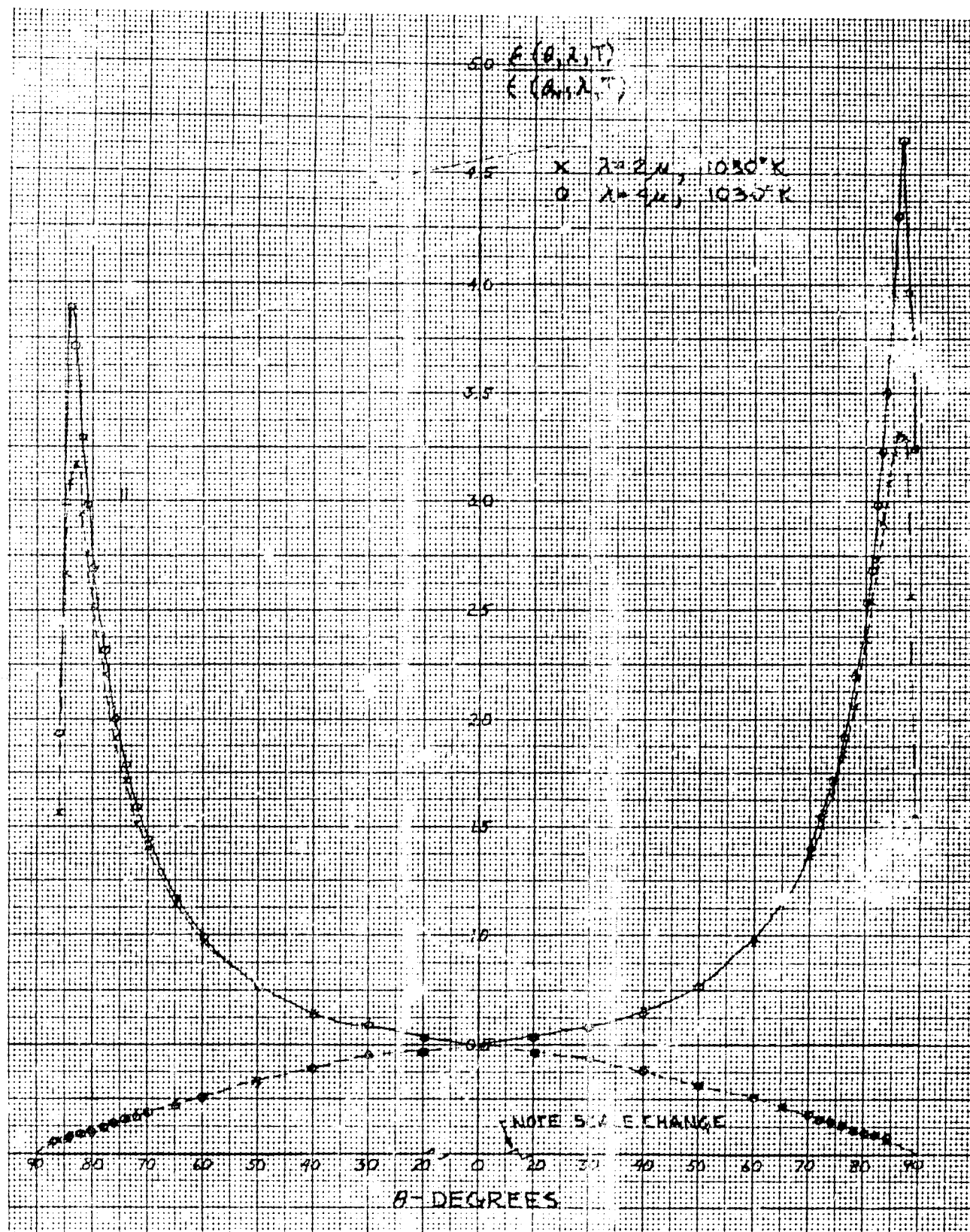


Figure 24 Relative Spectral Directional Emittance, Copper Sample 1

10.2 COPPER SAMPLE 3

1. Sample - Copper Sample 3.
2. Preparation - Glas-Shot Blasted, Size MS-XL Beads 20 psi at 4 in.
3. RMS roughness - Before emittance tests, 76 $\mu\text{in.}$; after, 33 $\mu\text{in.}$
4. Test procedure - Sample was heated to 800°K for 1/2 hr in vacuum before obtaining emittance data after which absolute and relative directional emittance data were obtained at temperatures between 557 and 928°K. (Tests 1 through 31.) Sample was retested (Tests 32 through 52), after "stabilizing" the sample of 900°K for 3/4 hr. Vacuum was maintained between 1 and 4×10^{-5} Torr throughout the tests. Total time at T_{max} was 7 hr.
5. Emittance Data - Absolute total and spectral normal emittance values are shown in Table 13.

Relative total directional emittance data are shown in Figure 28.

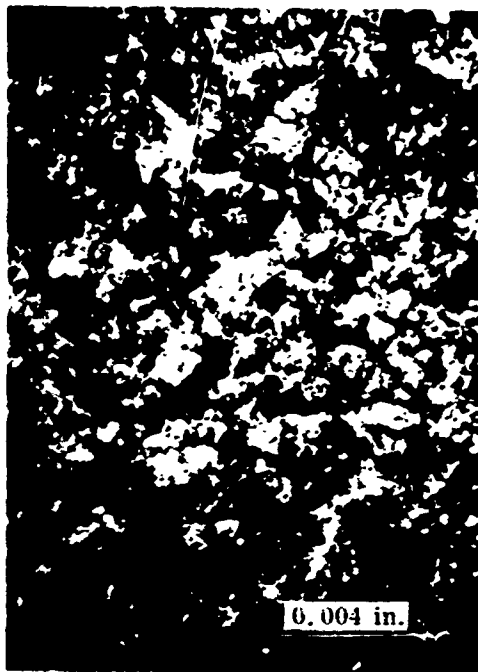
Relative spectral directional emittance data at 2 and 4 μ are shown in Figure 29.

6. Remarks - Because of instability of the absolute emittance data from this sample during the first test, the sample was retested after its emittance had stabilized at 900°K. The relative directional emittance data shown in Figures 28 and 29 were obtained during the latter test cycle. The change in sample emittance during the first test is attributed to relief of surface strain and a significant change in surface roughness.

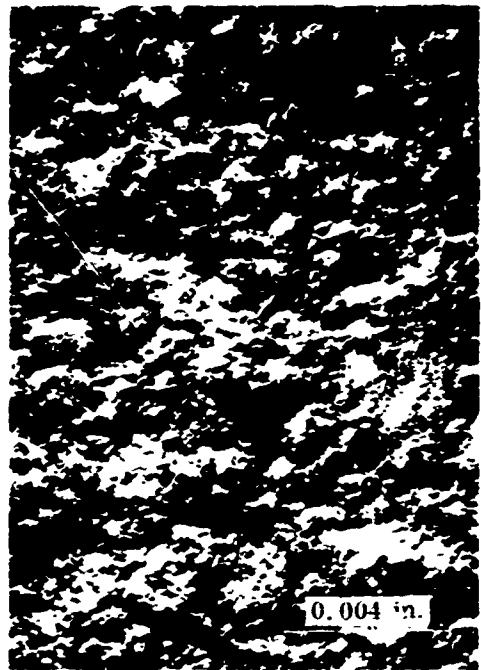
Figure 27 shows cross section and taper section photomicrographs of a disk sample which was roughened along with copper sample 3 to indicate the before-test condition of this surface. The Glas-Shot process appears to fracture the surface layer grains to a depth of about 400 $\mu\text{in.}$ (10 μ). After-test sections of this sample were not prepared, but would presumably be similar to those shown in Figure 32 for copper sample 5.

The x-ray diffraction pattern from this sample was identical to the pattern from copper sample 1, indicating no detectable impurities. The spectrographic analysis detected the presence of silicon, however, indicating that some Glas-Shot contamination of the surface occurred. No traces of glass were found during the microscopic examinations of the surface and section mounts.

Dis-symmetry in the angular position of the relative directional emittance peaks in Figure 28 indicates that the sample may have been misaligned approximately 1 deg.



Before



After

Dark Field Illumination

Figure 25 Surface Photomicrographs of Copper Sample 3 Before and After Emittance Tests

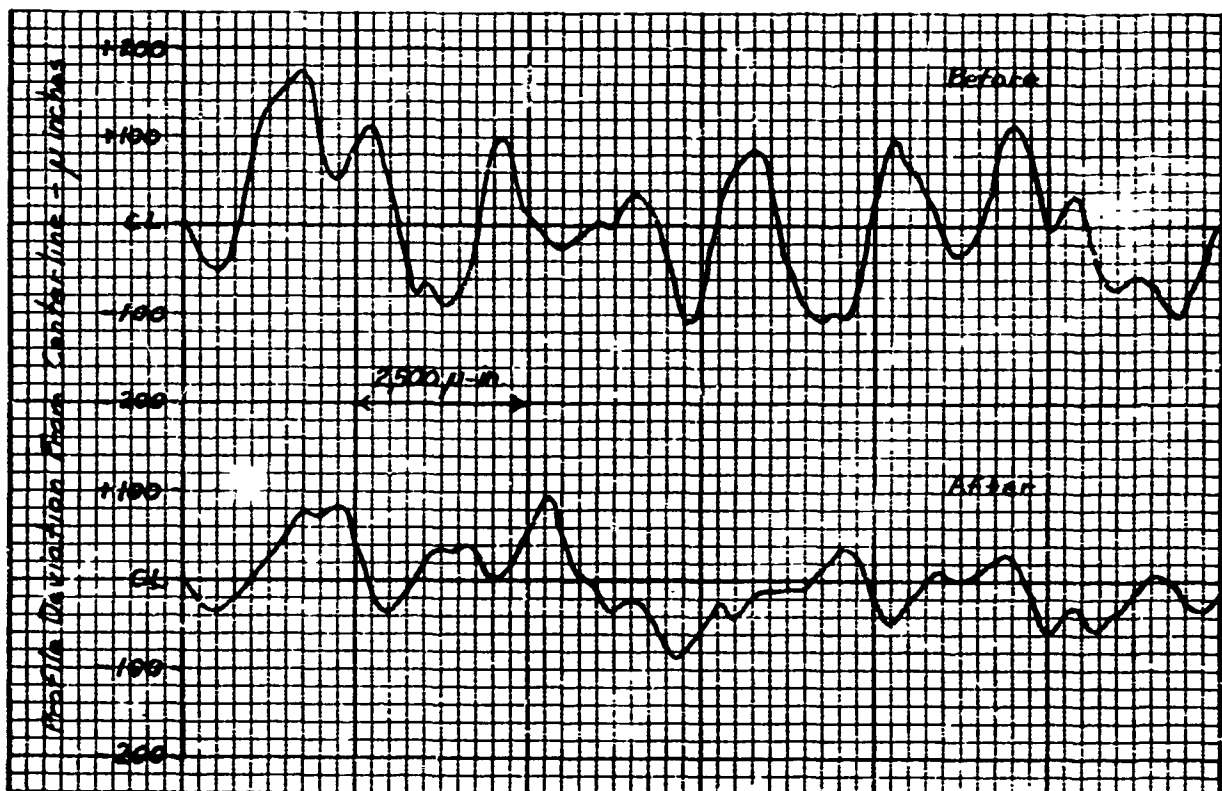


Figure 26 Typical Profile Traces for Copper Sample 3 Before and After Emittance Tests

Table 13
ABSOLUTE EMITTANCE DATA FOR COPPER SAMPLE 3

Temperature (°K)	Test	$\epsilon(\theta_N, T)$	$\epsilon(\theta_N, \lambda, T)$						
			1.5 μ	2 μ	4 μ	6 μ	8 μ	10 μ	
			First Temperature Cycle						
557	1	0.057							
653	4	0.055							
763	9, 10	0.063	0.070	0.063	0.059	0.060	0.060	0.063	
873	17, 18	0.057	0.104	0.076	0.053	0.047	0.040	0.047	
907	20, 21	0.056	0.104	0.081	0.053	0.042	0.037	0.051	
928	26	0.056							
883	27	0.052							
770	28	0.046							
636	29, 30	0.036		0.063	0.039	0.031	0.026		
			Second Temperature Cycle, After "Stabilizing" at 900°K						
901	32, 34	0.058	0.093	0.075	0.057	0.054		0.059	
957	42, 44	0.056	0.092	0.071	0.051	0.044	0.050		
748	47, 49	0.049	0.097	0.063	0.050	0.042	0.051		
656	50	0.041							
545	52	0.033							

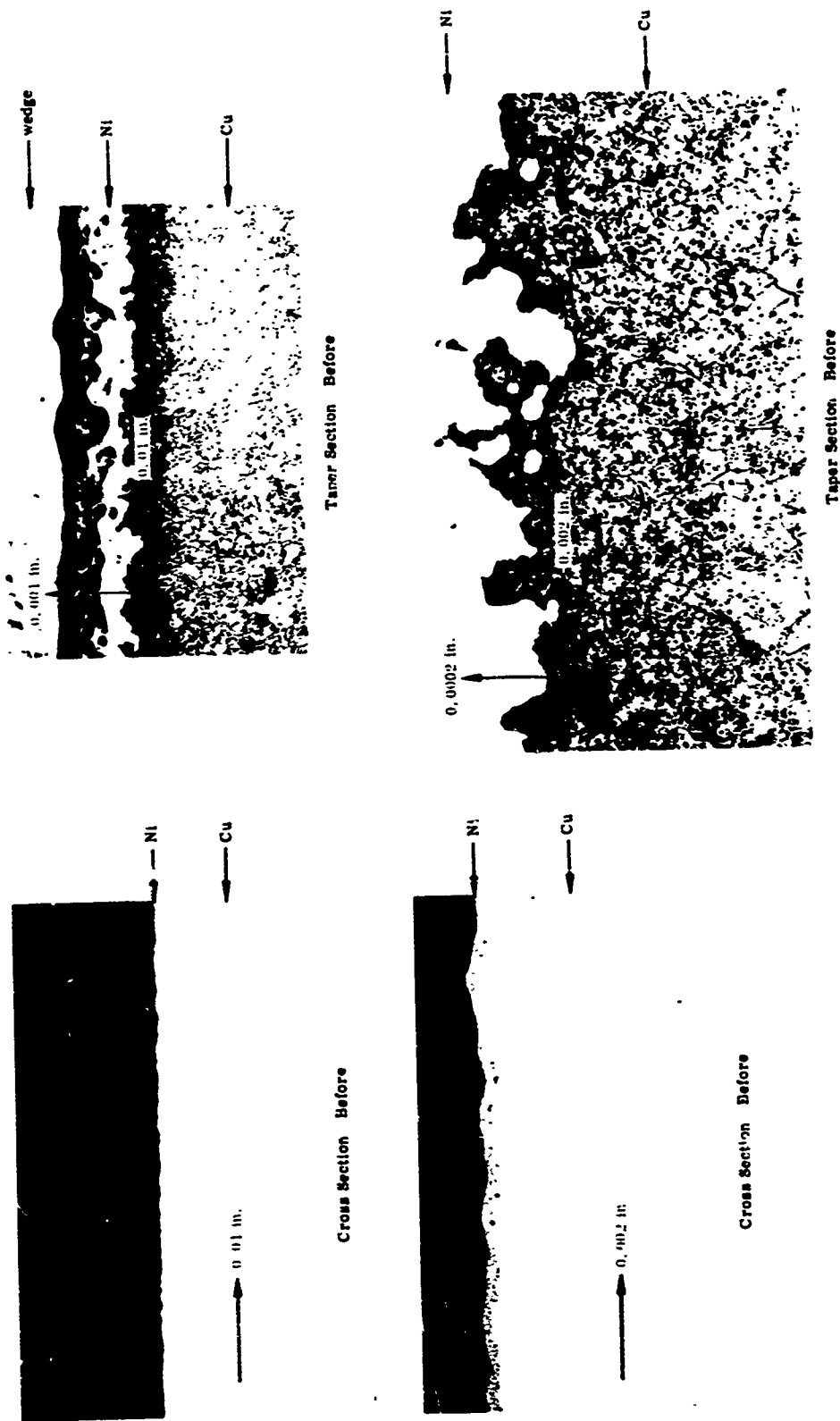


Figure 27 Cross and Taper Section Photomicrographs Indicating the Surface Condition of Copper Sample 3 Before Emittance Tests

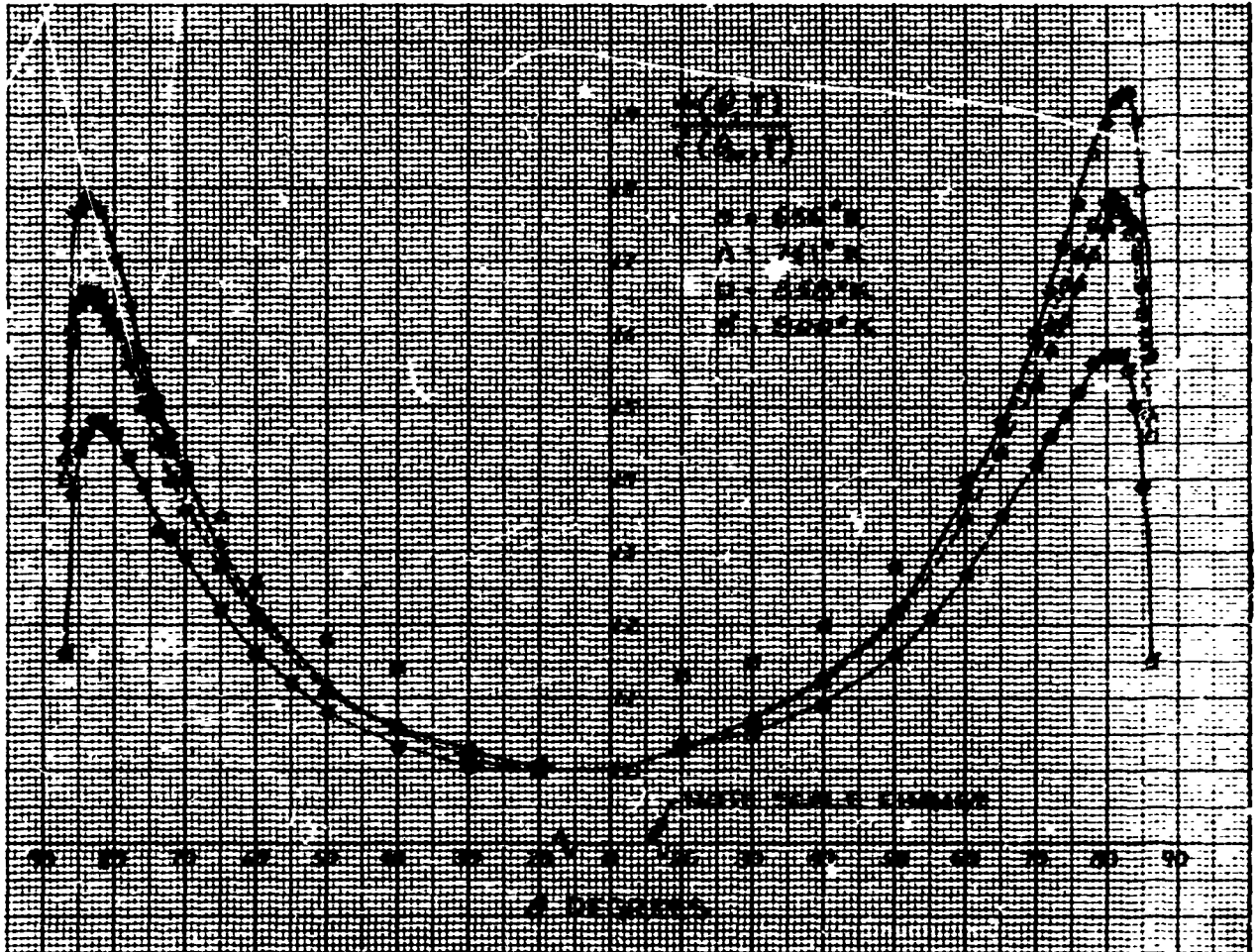


Figure 28 Relative Total Directional Emittance, Copper Sample 3

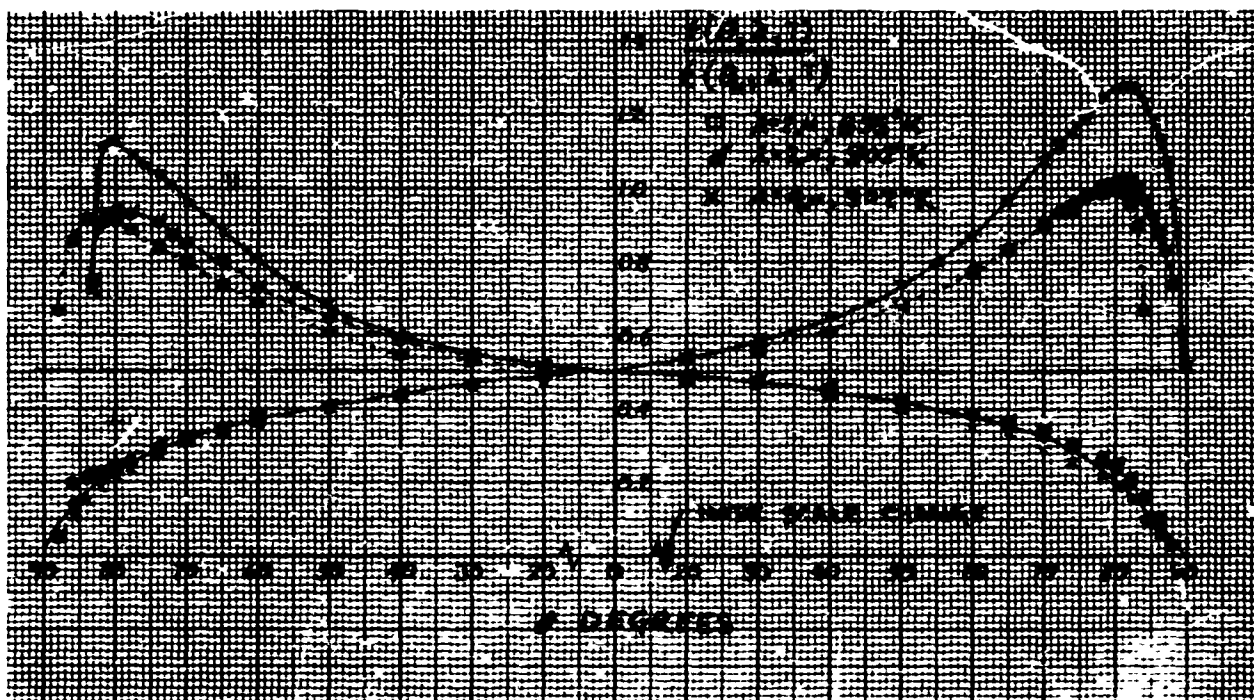


Figure 29 Relative Spectral Directional Emittance, Copper Sample 3

10.3 COPPER SAMPLE 5

1. Sample - Copper Sample 5.
2. Preparation - Glas-Shot blasted, size MS-XL beads, 80 psi at 4 in.
3. RMS roughness - Before emittance tests, 121 μ in. ; after, 56 μ in.
4. Test procedure - Sample was heated to 800° K in vacuum before obtaining emittance data after which absolute emittance data were obtained at temperatures from 552 to 858° K. (Tests 1 through 15.) The sample was aged at 913° K for 2-1/2 hr until the total normal emittance appeared to stabilize. Absolute and relative directional emittance data were remeasured at five temperatures from 913 to 541° K (Test 16 through 38). Vacuum was maintained between 1 and 5×10^{-5} Torr throughout the test. Total time at T_{\max} was 4-1/2 hr.

5. Emittance Data - Absolute total and spectral normal emittance values are shown in Table 14.

Relative total directional emittance data is shown in Figure 33.

Relative spectral directional emittance data at 2 and 4 μ are shown in Figures 34 and 35.

6. Remarks -- Absolute emittance values were observed to decrease with time at the higher test temperatures, similar to the initial data from copper Sample 3, but remained stable after aging the sample at 913° K. The change in emittance is attributed to relief of surface strain and a significant change in surface roughness, as indicated by the Proficorder traces.

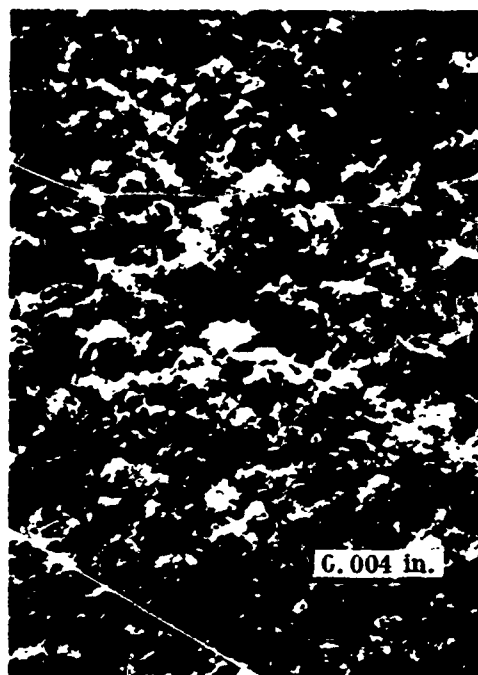
Figure 32 shows taper section photomicrographs which indicate the condition of the sample surface before and after the emittance test. The depth of the disturbed layer of fractured crystals caused by the Glas-Shot blast is about 1100 μ in. (28 μ). Recrystallization is clearly evident in the after-test sections. Surface profile definition was poor in these sections because of insufficient thickness of nickel plate.

X-ray diffraction and spark spectrographic results were the same as for copper sample 3, indicating the surface to be slightly contaminated with glass. No glass was detected by the microscopic examinations.

Symmetry of the relative directional peaks in Figures 33, 34 and 35 indicates that the sample was properly aligned. The cause for the difference in peak heights on either side of normal in Figure 33 is not known.



Before



After

Dark Field Illumination

Figure 30 Surface Photomicrographs of Copper Sample 5 Before and After Emittance Tests

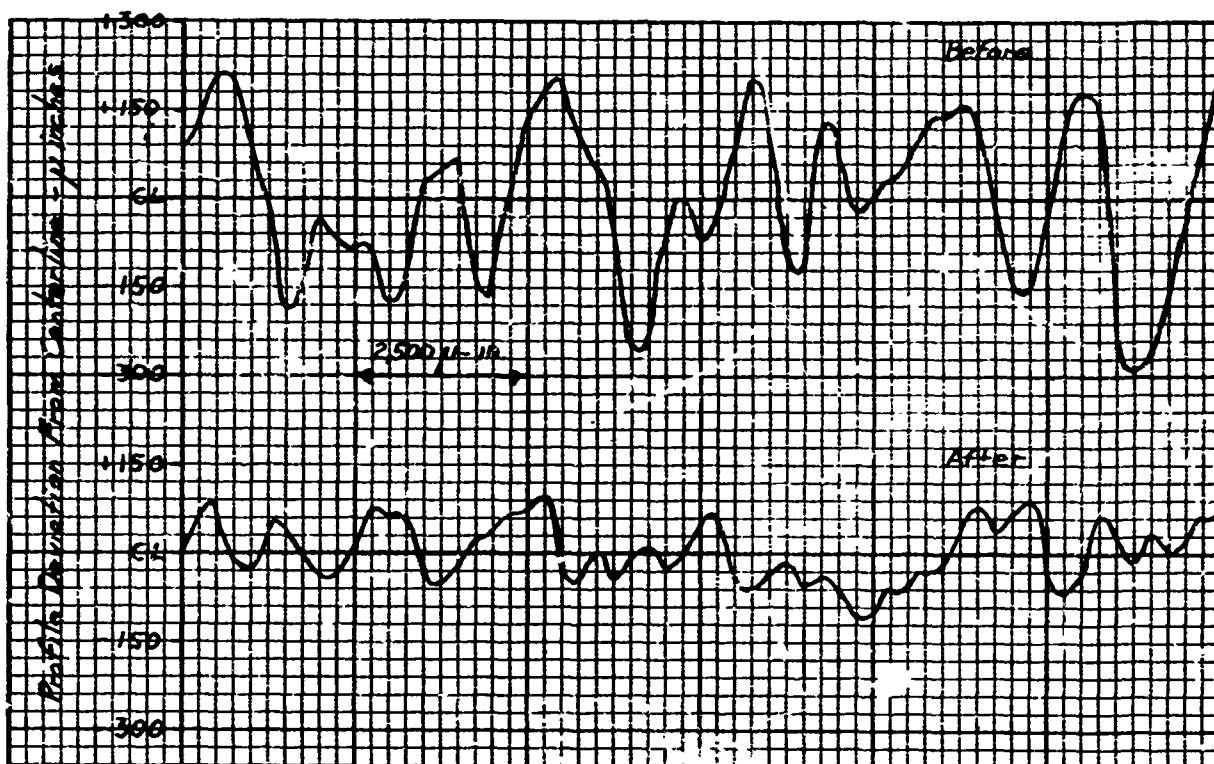


Figure 31 Typical Profile Traces for Copper Sample 5 Before and After Emittance Tests

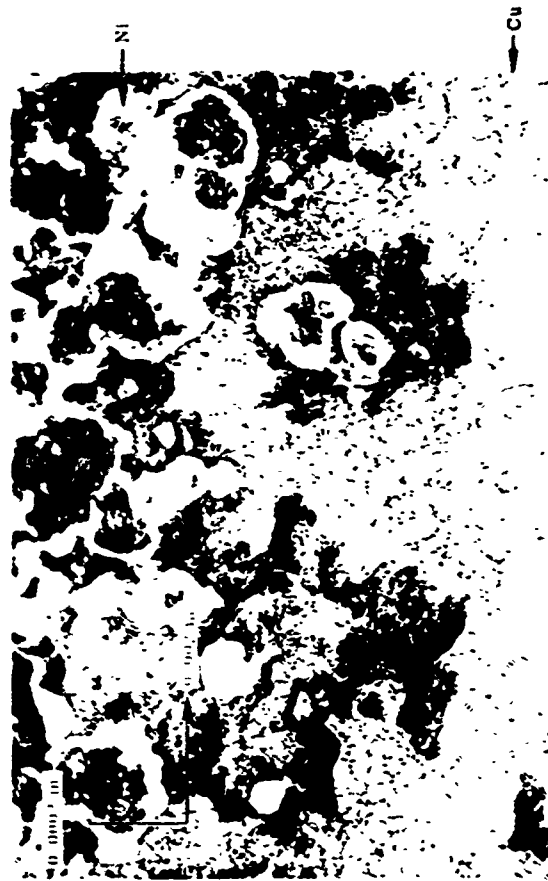
Table 14
ABSOLUTE EMITTANCE DATA FOR COPPER SAMPLE 5

Temperature (°K)	Test	$\epsilon(\theta_N, T)$	$\epsilon(\theta_N, \lambda, T)$					
			1.5 μ	2 μ	4 μ	6 μ	8 μ	10 μ
			First Temperature Cycle					
552	2	0.072						
660	3	0.086						
748	5, 6	0.093	0.104	0.091	0.090	0.091	0.087	0.084
858	8, 9	0.075	0.109	0.093	0.085	0.077	0.076	0.082
866	14	0.057						
574	15	0.046						
			Second Temperature Cycle, After Stabilizing at 913°K					
913	16, 18	0.063	0.109	0.085	0.059	0.050	0.046	0.058
865	24, 26	0.059	0.087	0.074	0.052	0.047	0.046	0.059
749	31, 33	0.050	0.092	0.073	0.049	0.046	0.041	0.058
546	34	0.032						
660	36	0.044						
902	38	0.062						



→ Cu

Taper Section Before

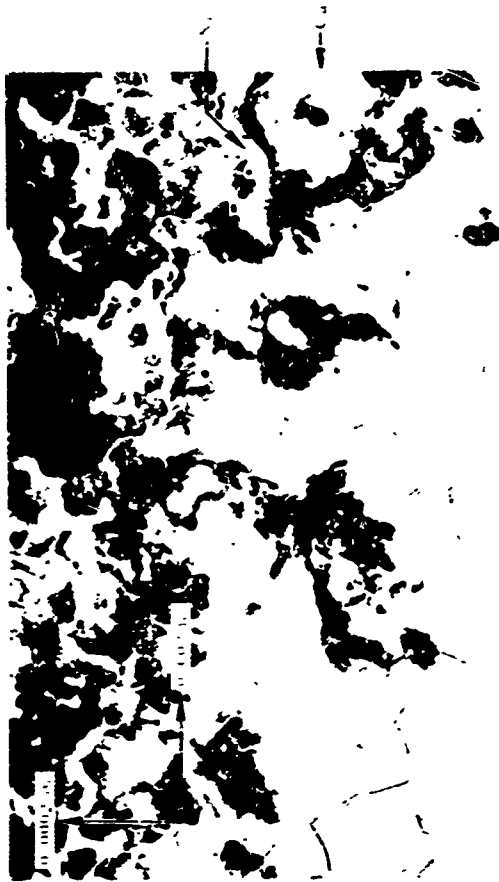


Taper Section Before



→ Cu

Taper Section After



Taper Section After

Figure 12 Taper Section Photomicrographs of Copper Sample 5 Before and After Emittance Tests

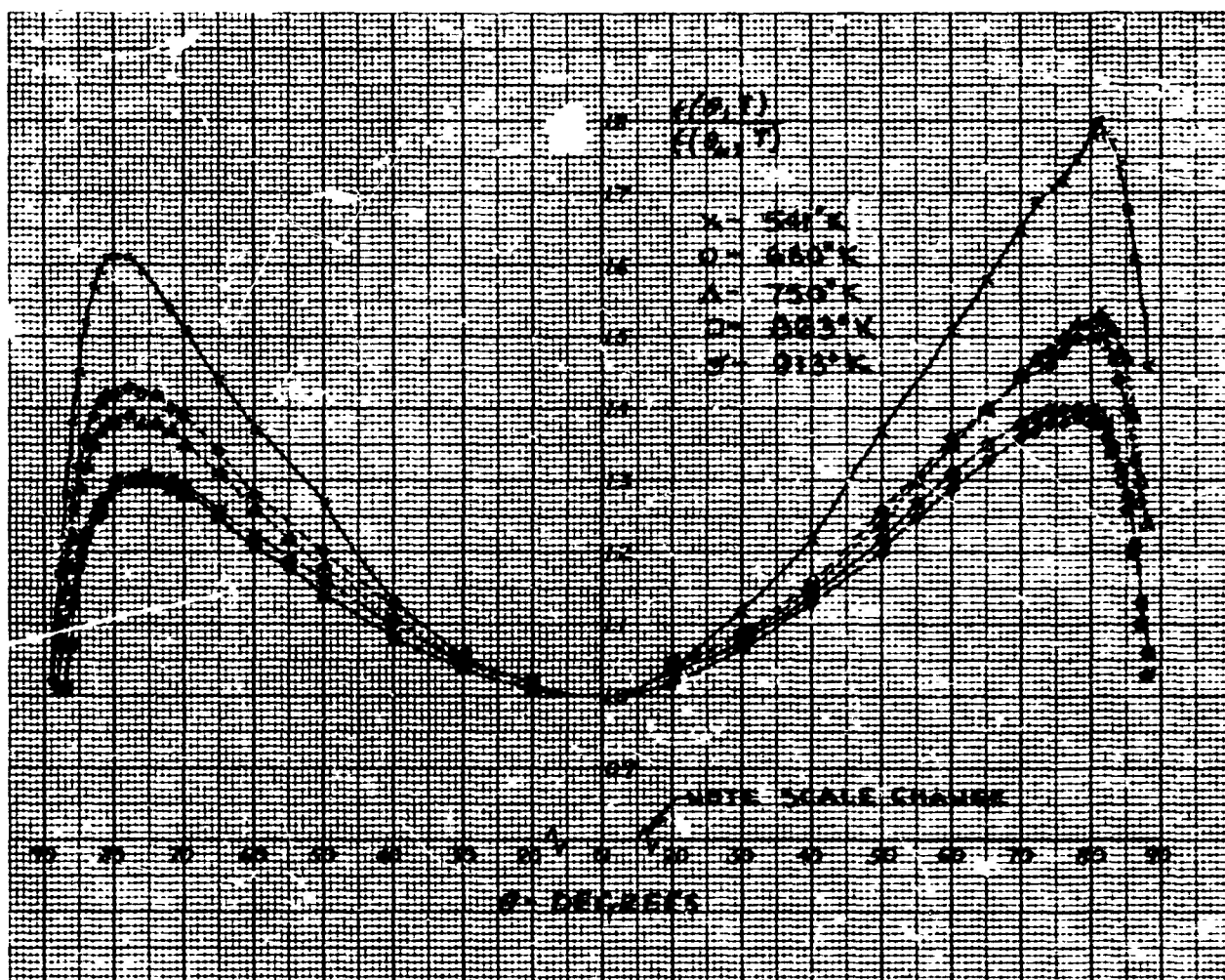


Figure 33 Relative Total Directional Emittance, Copper Sample 5

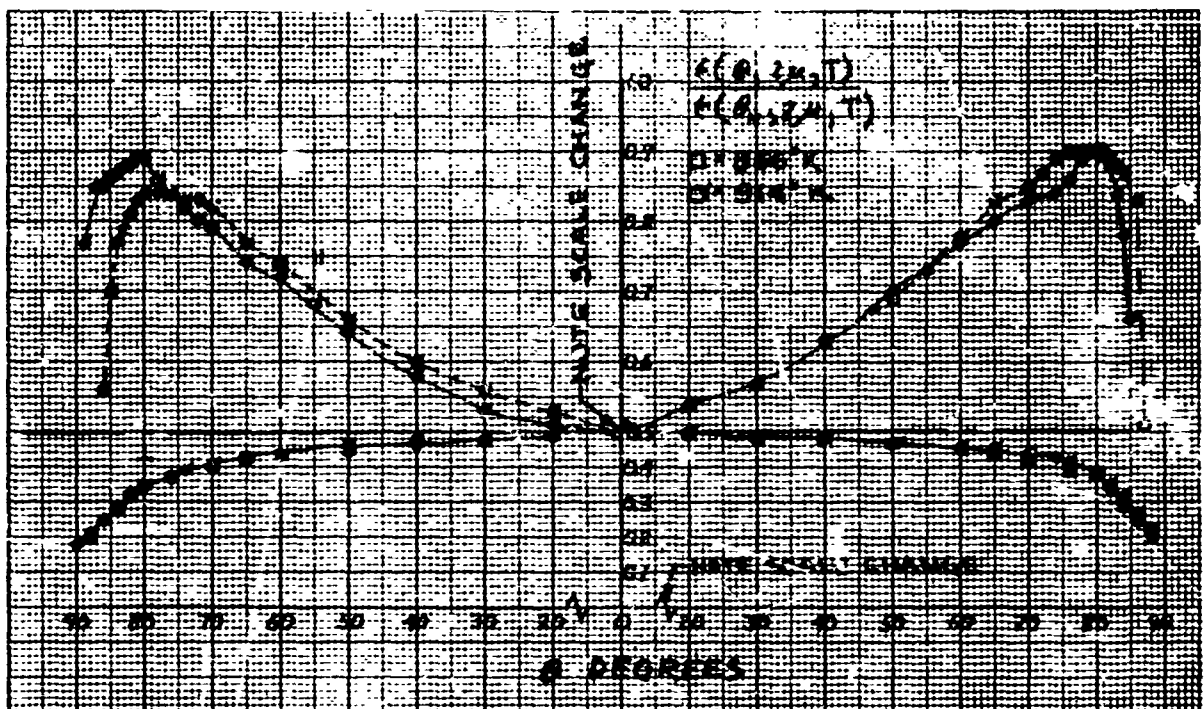


Figure 34 Relative Spectral Directional Emittance, $\lambda = 2 \mu$, Copper Sample 5

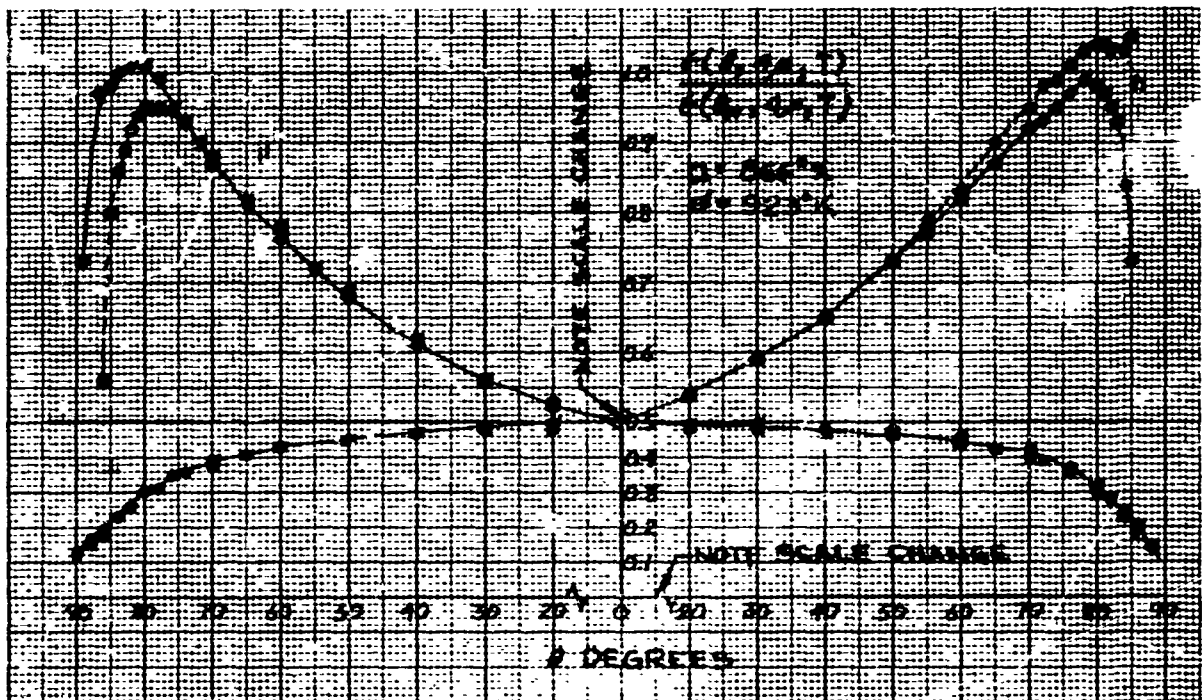


Figure 35 Relative Spectral Directional Emittance, $\lambda = 4 \mu$, Copper Sample 5

10.4 COPPER SAMPLE 7

1. Sample - Copper Sample 7
2. Preparation - Glas-Shot blasted, size MS-M.L beads, 80 psi at 4 in.
3. RMS roughness - Before emittance tests, 176 $\mu\text{in.}$; after, 114 $\mu\text{in.}$
4. Test procedure - Because this sample was noticeably warped by the Glas-Shot blast process, it was initially annealed (in vacuum) at 800°K for ~3 min, then cooled and straightened. This was done by gently bending the strip and adjusting the sample tension until it appeared flat relative to a reference straight edge. Sample was reheated to 800°K for 1/2 hr in vacuum. Absolute emittance data were obtained at 555°K and 741°K before stabilizing the sample emittance at 921°K (2-1/2 hr) after which absolute and relative directional emittance data were obtained at five temperatures from 923 to 561°K. Vacuum throughout the tests was maintained between 1 and 5×10^{-5} Torr. Total time at T_{max} was 4-1/2 hr.

5. Emittance Data - Absolute total and spectral normal emittance values are shown in Table 15.

Relative total directional emittance data are shown in Figure 39.

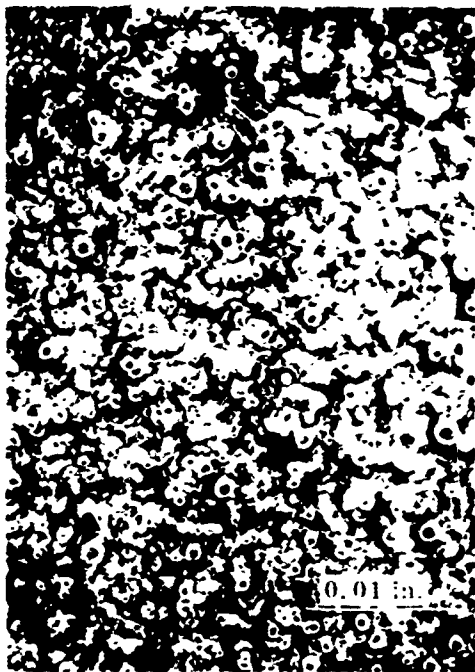
Relative spectral directional emittance data at 2 and 4 microns are shown in Figure 40.

6. Remarks - Absolute total and spectral normal emittance values were observed to decrease with time at the higher test temperatures, similar to the initial emittance data from copper samples 3 and 5. The drop in emittance is attributed to the relief of surface strain and a decrease in surface roughness which was detected by the Proficorder. The relative directional emittance data in Figures 39 and 40 were obtained after the emittance had stabilized at 923°K.

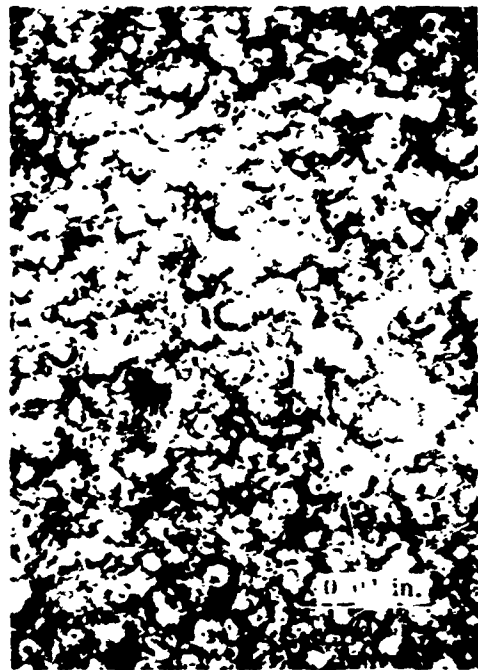
The photomicrographs in Figure 38 were taken from a disk sample which was roughened along with copper sample 7 to illustrate the before test condition of the sample surface. The dark spots at the surface and beneath the valleys in the cross section photos did not appear to be foreign matter but rather to be small voids caused by the non-uniform polishing characteristics of the disturbed surface metal. The same spots are seen in the taper section photomicrographs and are considerably more pronounced after etching the section. The depth of the disturbed surface layer appears to be about 2600 $\mu\text{in.}$ (65 μ) on this sample. As with the other Glas-Shot blasted samples, no sign of contamination was detected by the surface inspection through the microscope - however, a few areas of embedded glass fragments were found in the cross section mount. A high magnification photograph of one of these areas is shown at the bottom of Figure 38.

X-ray diffraction and spark spectrographic results were the same as for copper samples 3 and 5, indicating some glass contamination of the surface.

The anomalous shape of the relative total directional emittance data in Figure 39 is believed caused by a warp which developed in the sample during the tests. This may also be the cause for the anomalous distribution of the perpendicularly polarized components of radiation at 2 and 4 μ .



Before



After

Dark Field Illumination

Figure 36 Surface Photomicrographs of Copper Sample 7 Before and After Emittance Tests

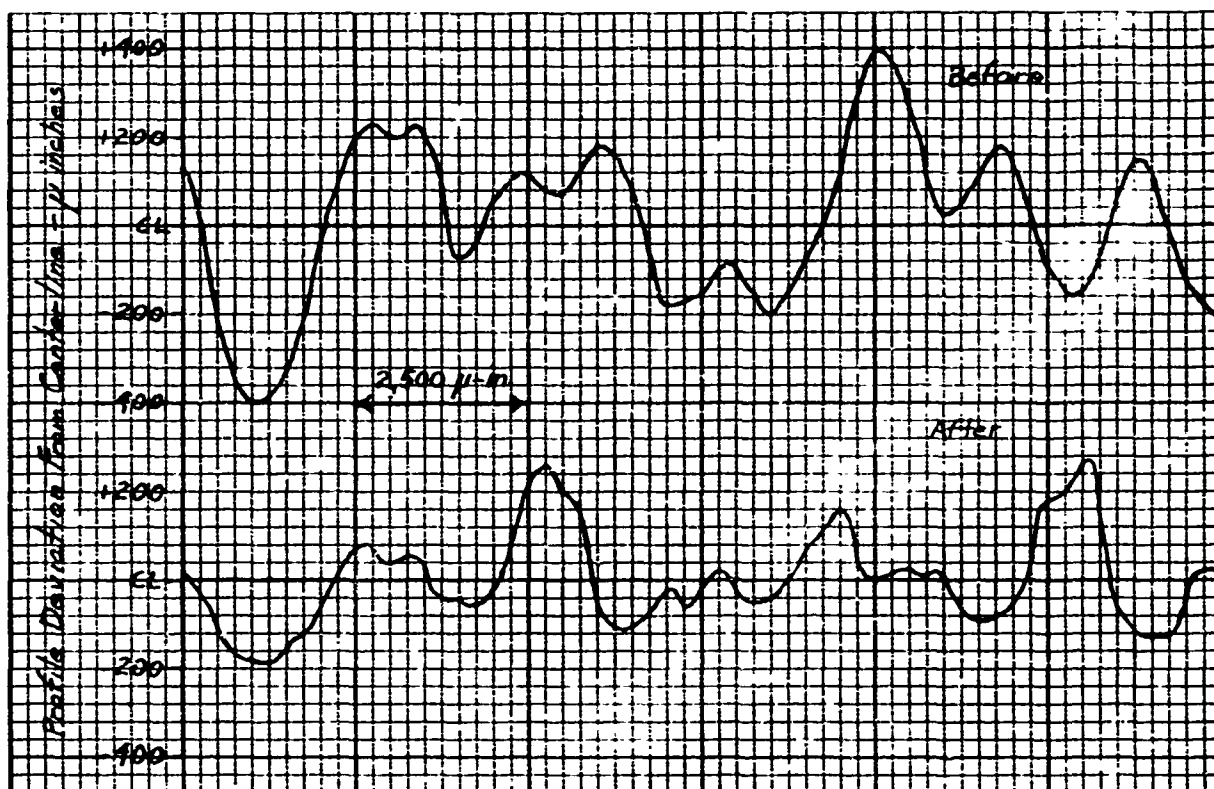


Figure 37 Typical Profile Traces for Copper Sample 7 Before and After Emittance Tests

Table 15
ABSOLUTE EMITTANCE DATA FOR COPPER SAMPLE 7

Temperature (°K)	Test	$\epsilon(\theta_N, T)$	$\epsilon(\theta_N, \lambda, T)$					
			1.5 μ	2 μ	4 μ	6 μ	8 μ	10 μ
			First Temperature Cycle					
555	1	0.068						
741	3, 4	0.079	0.097	0.089	0.084	0.082	0.079	0.077
921	5	0.084						
			Second Temperature Cycle, After Stabilizing at 923°K					
923	7	0.082						
891	9, 11	0.081	0.112	0.094	0.083	0.072	0.070	0.077
868	16, 18	0.075	0.126	0.102	0.088	0.083	0.068	0.077
750	23, 24	0.067	0.097	0.082	0.070	0.069	0.069	0.070
645	26	0.061						
561	28	0.054						
923	30, 31	0.080	0.106	0.104	0.080	0.073	0.075	0.082



Cross Section Before



Cross Section Before



Glass-Sheet Contamination



Taper Section Before (Unetched)



Taper Section Before (Etched)

Figure 36 Cross and Taper Section Photomicrographs Indicating the Surface Condition of Copper Sample 1 Before Emittance Tests

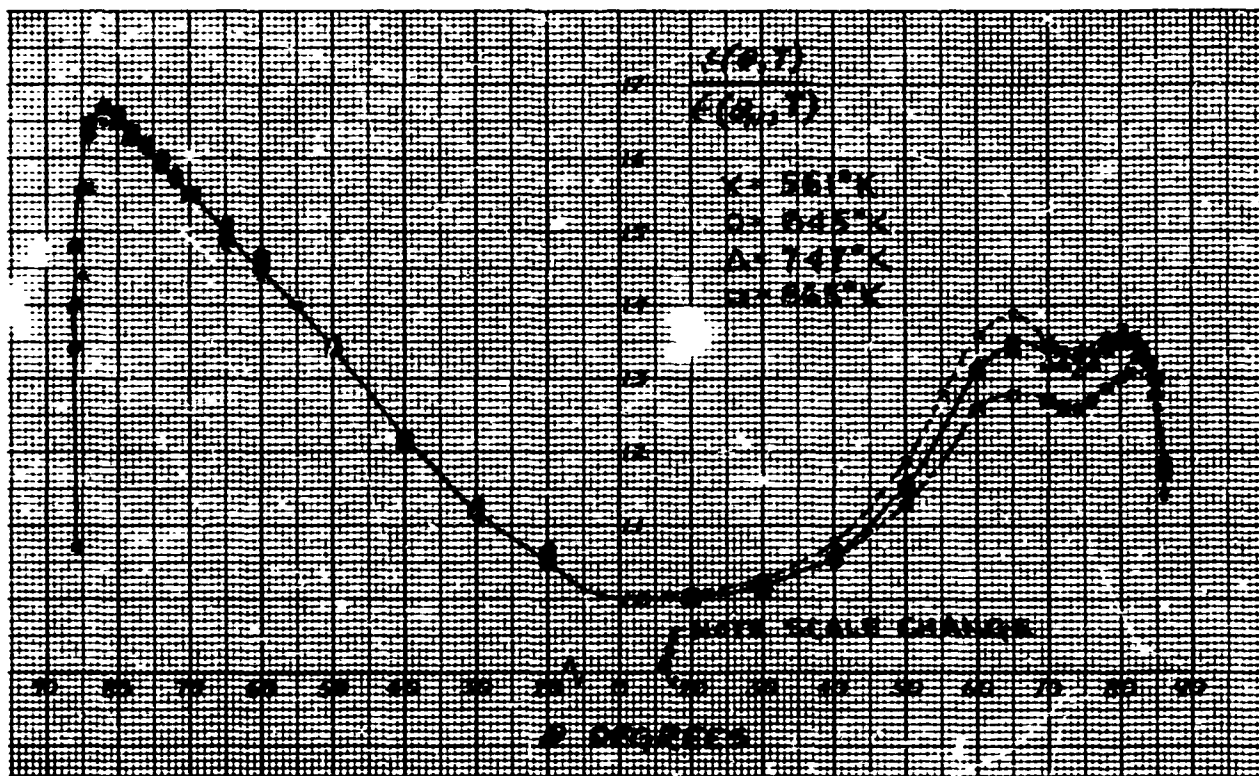


Figure 39 Relative Total Directional Emittance, Copper Sample 7

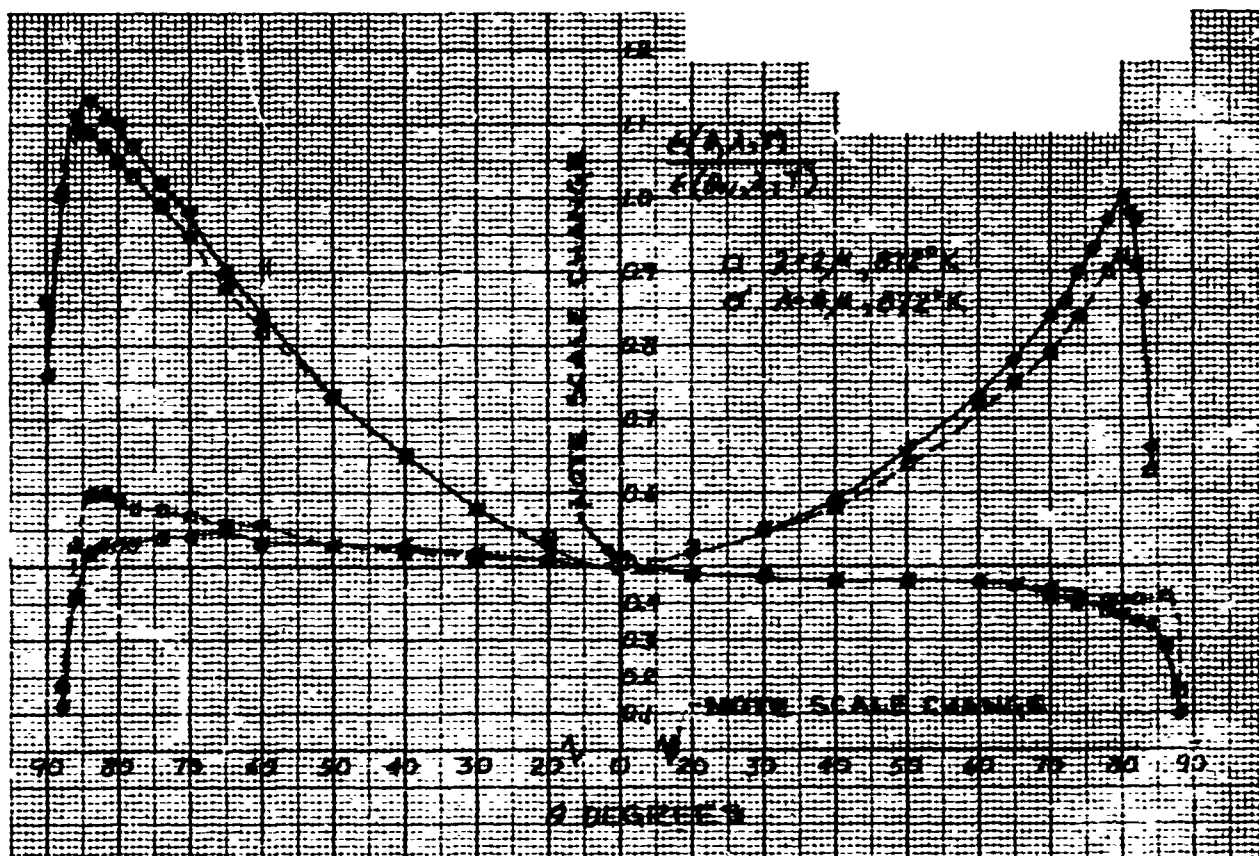


Figure 40 Relative Spectral Directional Emittance, Copper Sample 7

10.5 COPPER SAMPLE 8

1. Sample - Copper Sample 8.
2. Preparation - Steel shot blasted, No. 50 mesh shot, 50 psi at 6 in.
3. RMS roughness - Before emittance tests, 348 $\mu\text{in.}$; after, 204 $\mu\text{in.}$
4. Test procedure - Because this sample was severely warped by the blasting process, it was initially heated in air to 800°K for 2 min to anneal the surface, and then was gently rolled flat with a 6-in. diameter section of tubing. Prior to obtaining emittance data, the sample was heated to 1000°K for 5 min in vacuum to clean up the surface oxide which formed during that first heat treatment. At the conclusion of this treatment, the surface appeared bright and clean. Absolute and relative directional emittance data was then obtained at five temperatures from 564 to 913°K. Vacuum throughout the tests was maintained between 1 and 6×10^{-5} Torr.
5. Emittance Data - Absolute total and spectral normal emittance values are shown in Table 16.

Relative total directional emittance data are shown in Figure 44.

Relative spectral directional emittance data at 2 and 4 μ are shown in Figures 45 and 46.

6. Remarks - The absolute emittance of this sample remained stable with temperature throughout the test, indicating that the sample roughness and emittance had stabilized during the 5-min preheat treatment at 1000°K. As with the other rough copper samples, the roughness of this sample was found to be significantly lower after the emittance tests.

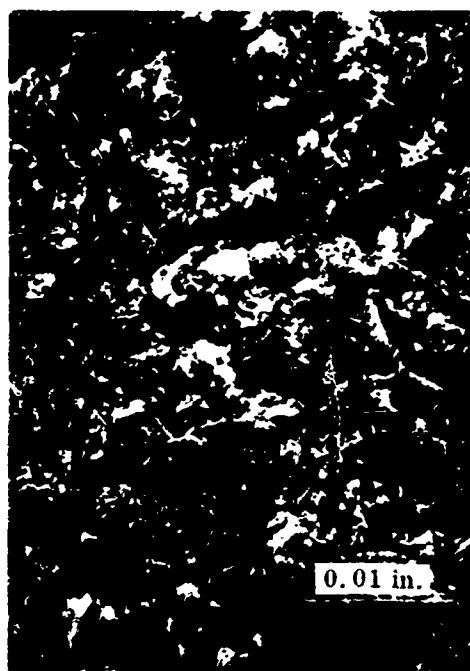
Taper section photomicrographs indicating the before- and after-test condition of the surface of this sample are shown in Figure 43. Unfortunately, the nickel plate layer on these sections was too thin. As a consequence, the surface edge was not preserved during the polishing and appears void in the photomicrographs. From the before-test section, the depth of the disturbed surface layer of copper appears to be about 2000 $\mu\text{in.}$ (50 μ). The after-test section shows the grain growth at the surface was inhibited relative to the deeper, undisturbed substrate.

The x-ray diffraction pattern from copper sample 8 was the same as from the other copper samples (no detectable impurities). The spectrographic analysis, however, detected a significant amount of iron, indicating the surface had been contaminated by the steel shot and that the contamination was not removed by the 5-min etch in HCl. No sign of embedded steel was detected by the microscopic examinations of the surface and taper sections.

The cause for the anomalous shape of the relative direction emittance curves is not known. Although the sample was badly warped by the shot-blast treatment, it appeared to remain flat after being annealed and rolled, as described above. Dissymmetry of the angular location of the peaks indicates that the sample alignment was off by about 2 deg.



Before



After

Dark Field Illumination

Figure 41 Surface Photomicrographs of Copper Sample 8 Before and After Emittance Tests

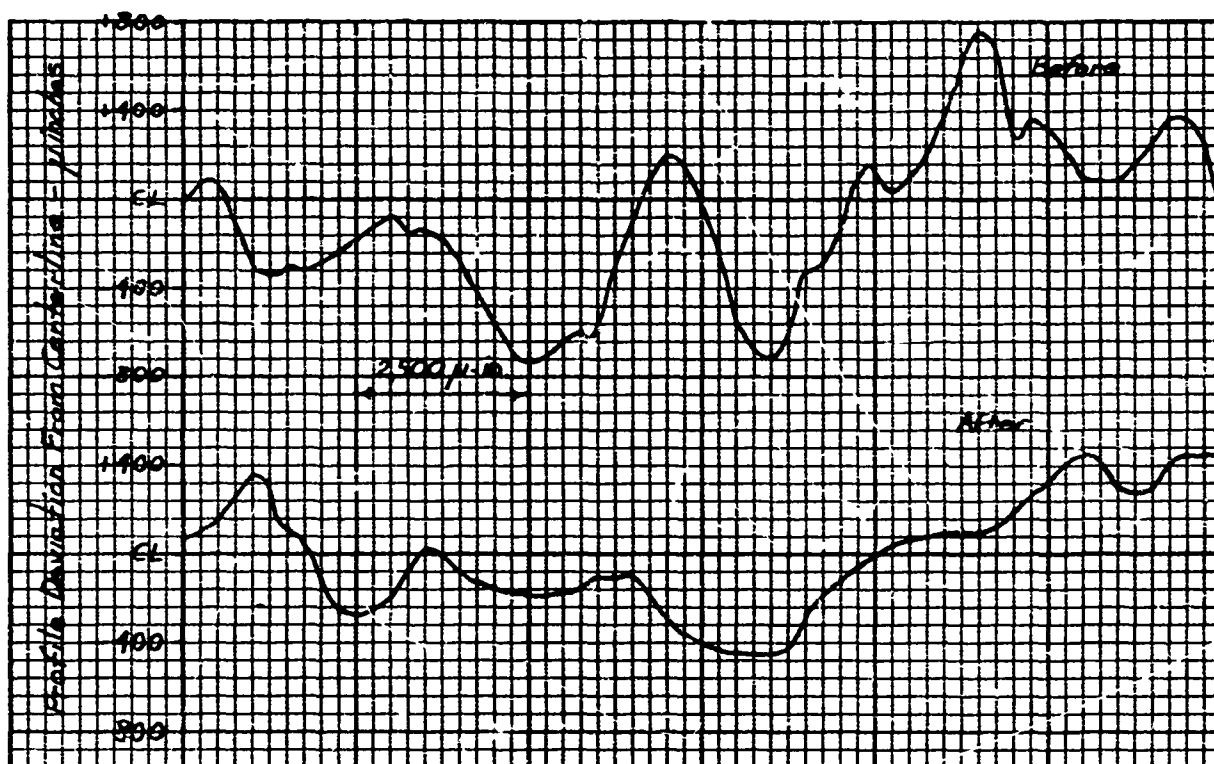
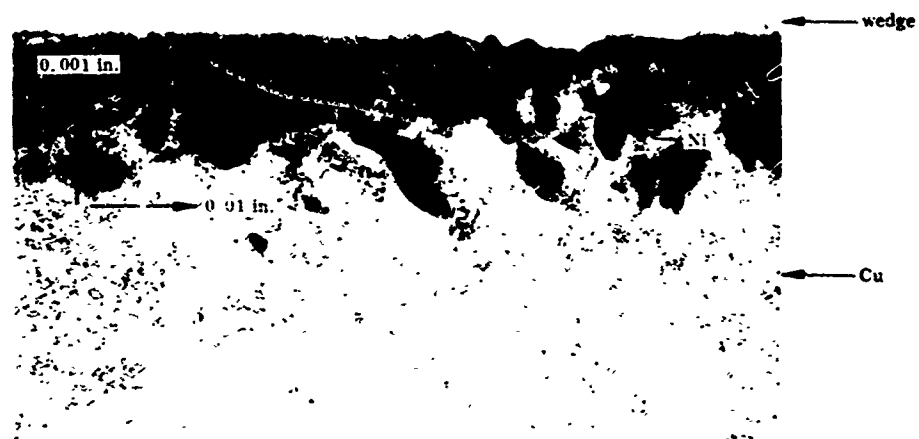


Figure 42 Typical Profile Traces for Copper Sample 8 Before and After Emittance Tests

Table 16
ABSOLUTE EMITTANCE DATA FOR COPPER SAMPLE 8

Temperature (°K)	Test	$\epsilon(\theta_N, T)$	$\epsilon(\theta_N, \lambda, T)$					
			1.5 μ	2 μ	4 μ	6 μ	8 μ	10 μ
564	2	0.101						
757	4, 5	0.130	0.262	0.214	0.146	0.111	0.095	0.097
807	7, 8	0.149	0.280	0.229	0.154	0.119	0.106	0.108
913	14, 15	0.155	0.277	0.231	0.160	0.124	0.111	0.109
913	21	0.156						
565	22	0.107						
652	24, 25	0.117		0.228	0.145	0.102	0.088	0.080



Before



After

Figure 43 Taper Section Photomicrographs of Copper Sample 6 Before and After Emittance Tests

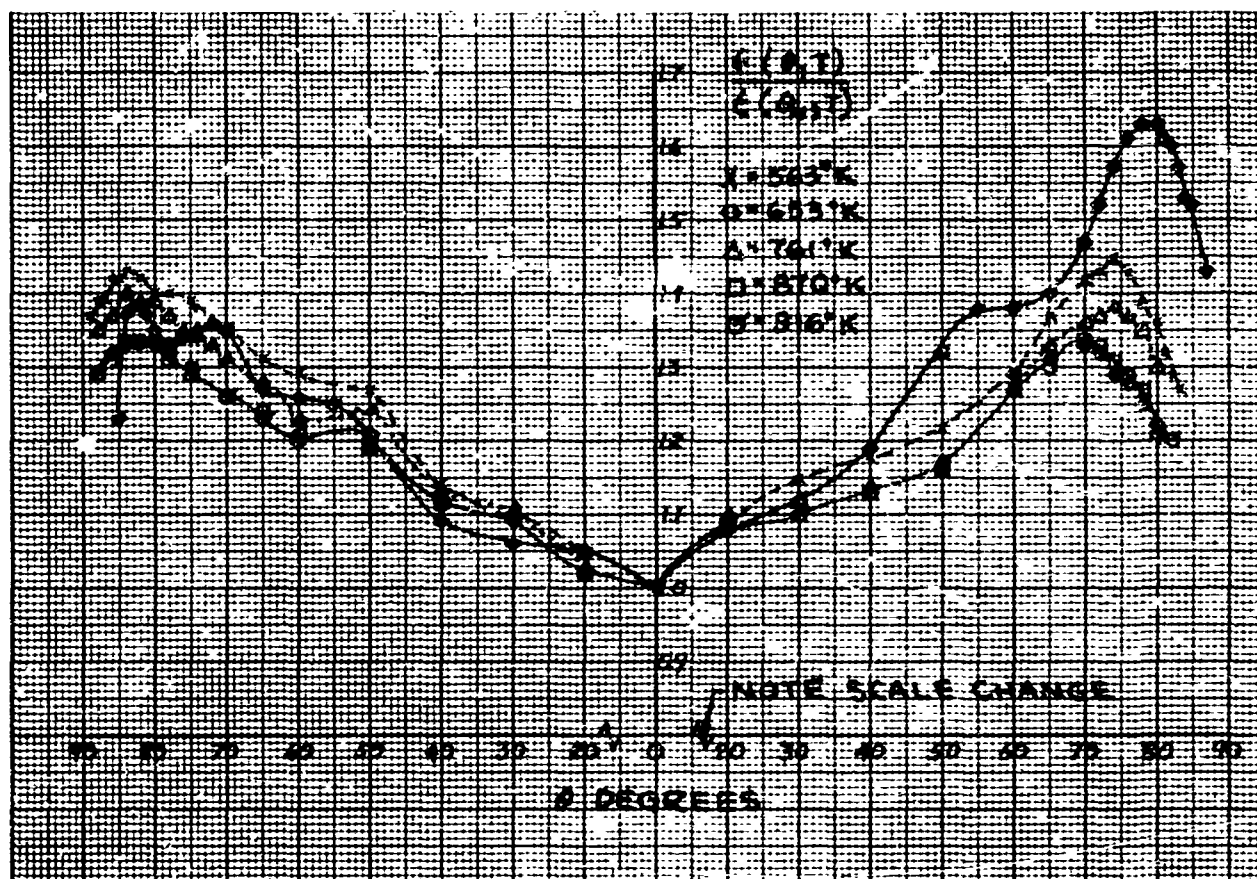


Figure 44 Relative Total Directional Emittance, Copper Sample 8

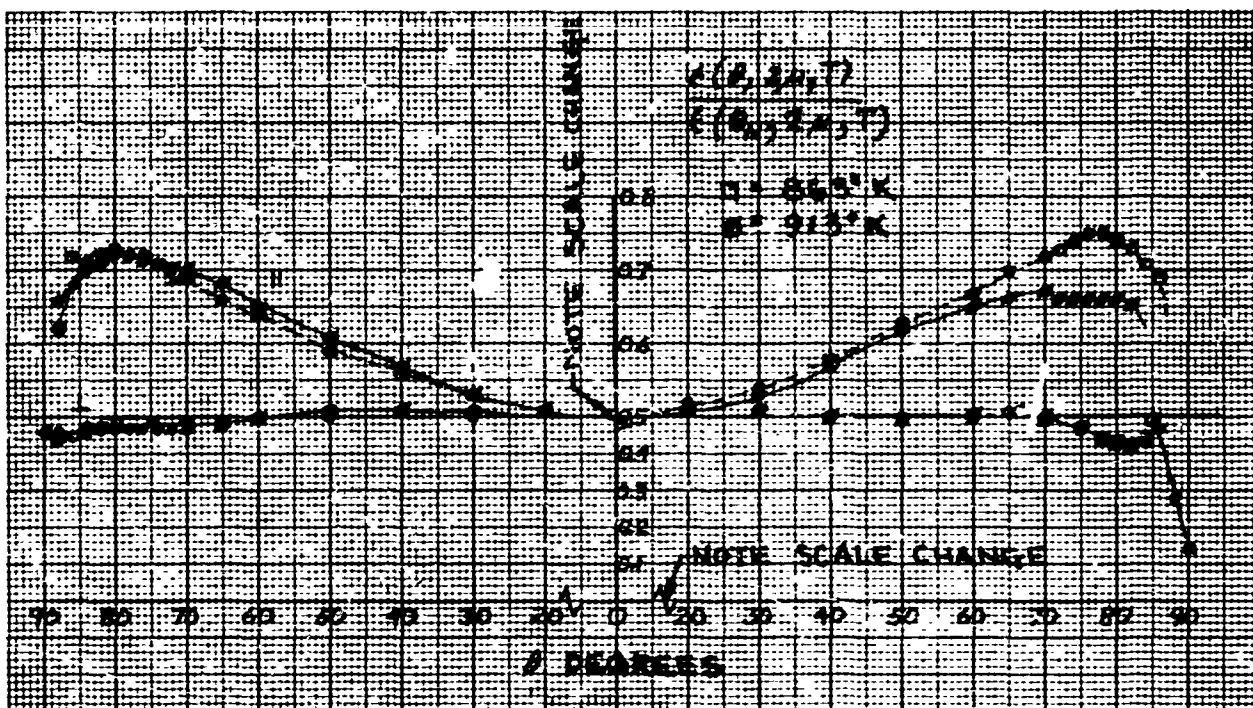


Figure 45 Relative Spectral Directional Emittance, $\lambda = 2 \mu$, Copper Sample 8

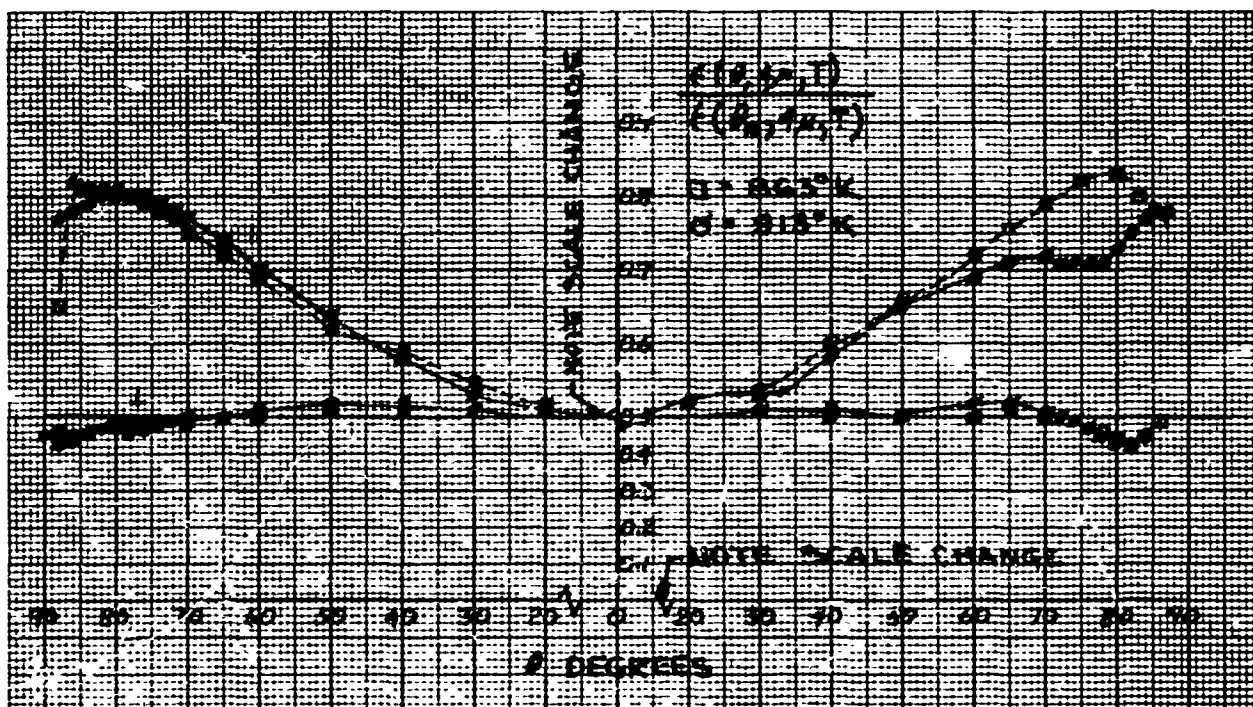


Figure 46 Relative Spectral Directional Emittance, $\lambda = 4 \mu$, Copper Sample 8

10.6 TUNGSTEN SAMPLE 1

1. Sample - Tungsten Sample 1.
2. Preparation - None (tested as received)
3. RMS roughness - Before emittance tests, 1.5 μ in. ; after, 2.4 μ in.
4. Test procedure - Sample was heated to 900°K for 2 hr in vacuum before taking emittance data after which absolute and relative directional emittance data were obtained at seven temperatures from 544 to 1603°K. Total normal emittance was rechecked at 873°K to indicate the effect of the test cycle on sample emittance. Vacuum was maintained between 2 and 7×10^{-5} Torr throughout the test. Total time at T_{\max} was 2-1/2 hr.
5. Emittance Data - Absolute total and spectral normal emittance values are shown in Table 17.

Relative total directional emittance data are shown in Figure 50.

Relative spectral directional emittance data at 2, 1.5, and 4 μ are shown in Figures 51, 52, and 53.

6. Remarks - Absolute emittance of this sample appeared to be unstable at temperatures above 1300°K, presumably because of changes in the surface characteristics. Recheck of the total normal emittance at 870°K indicated it had risen from an initial value of 0.080 to 0.24. An inspection of the sample surface showed it to have a hazy appearance which, under the microscope, appeared to be caused by intergranular etching. The reason for this change in surface character was not determined; however, attack of the surface by residual oxygen and/or water vapor in the vacuum chamber is suspected. Chamber pressures throughout the tests were maintained between 2 and 7×10^{-5} Torr.

Photomicrographs of the surface of this sample, before and after the emittance tests, are shown in Figure 47. The nature of the intergranular etching which occurred is shown in the after-test photo. The interference photomicrographs indicate the same general roughness characteristics as were determined from the Proficorder traces (see subsection 8.1.1). Before and after photomicrographs of cross- and taper-section mounts prepared from the sample are shown in Figure 49. The after-test photos indicate a marked change in the grain structure of the recrystallized tungsten.

X-ray diffraction and spark spectrographic analyses of the tested sample indicated no significant impurities.

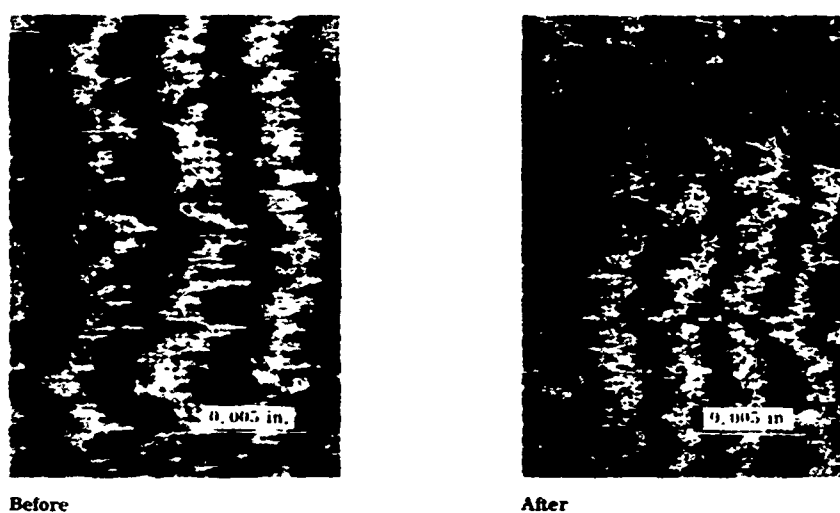
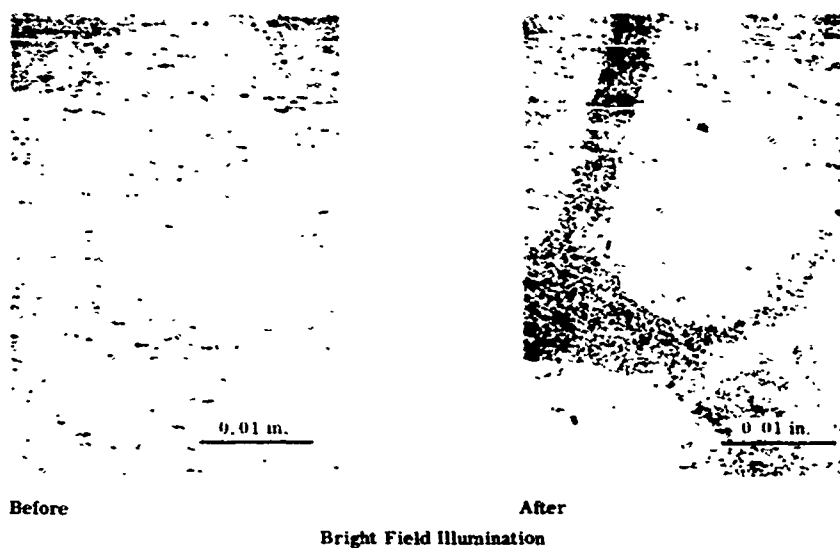


Figure 47 Surface and Surface Interference Photomicrographs of Tungsten Sample 1 Before and After Emittance Tests

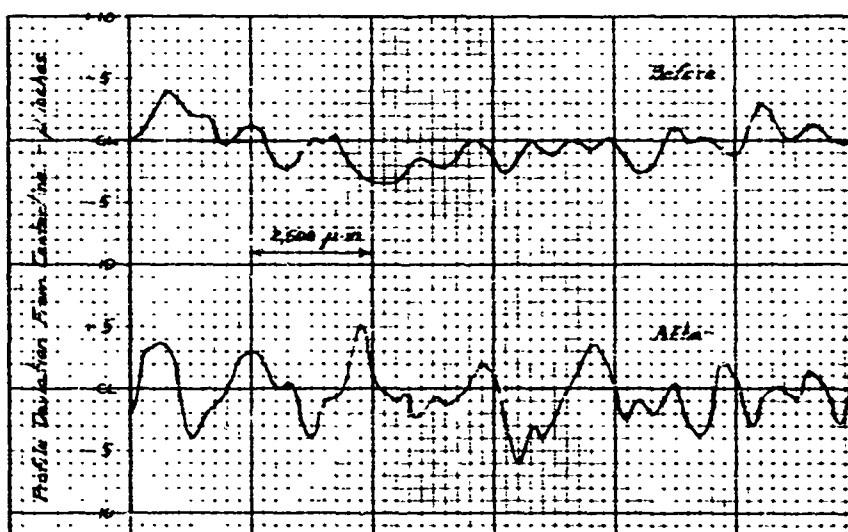


Figure 48 Typical Profile traces for Tungsten Sample 1 Before and After Emittance Tests

Table 17
ABSOLUTE EMITTANCE DATA FOR TUNGSTEN SAMPLE 1

Temperature (°K)	Test	$\epsilon(\lambda_N, T)$	$\epsilon(\theta_N, \lambda, T)$									
			0.65 μ (a)	1 μ	1.5 μ	2 μ	4 μ	6 μ	8 μ	10 μ	12 μ	
544	2	0.025										
702	4, 5	0.054			0.24	0.13	0.060	0.046	0.035	0.026		
870	7, 8	0.080			0.26	0.15	0.074	0.056	0.048	0.044		
1039	13, 15	0.114			0.32	0.18	0.088	0.069	0.057	0.055	0.050	
1208	23, 25	0.177	0.54	0.46	0.27	0.17	0.093	0.077	0.068	0.072	0.058	
1378	33a, 33b	0.164	0.46		0.22	0.14	0.11					
1603	44a, 44b	0.27	0.52		0.29	0.21	0.18					
873	59a	0.24										

(a) Spectral emittance at 0.65 μ determined with optical pyrometer.

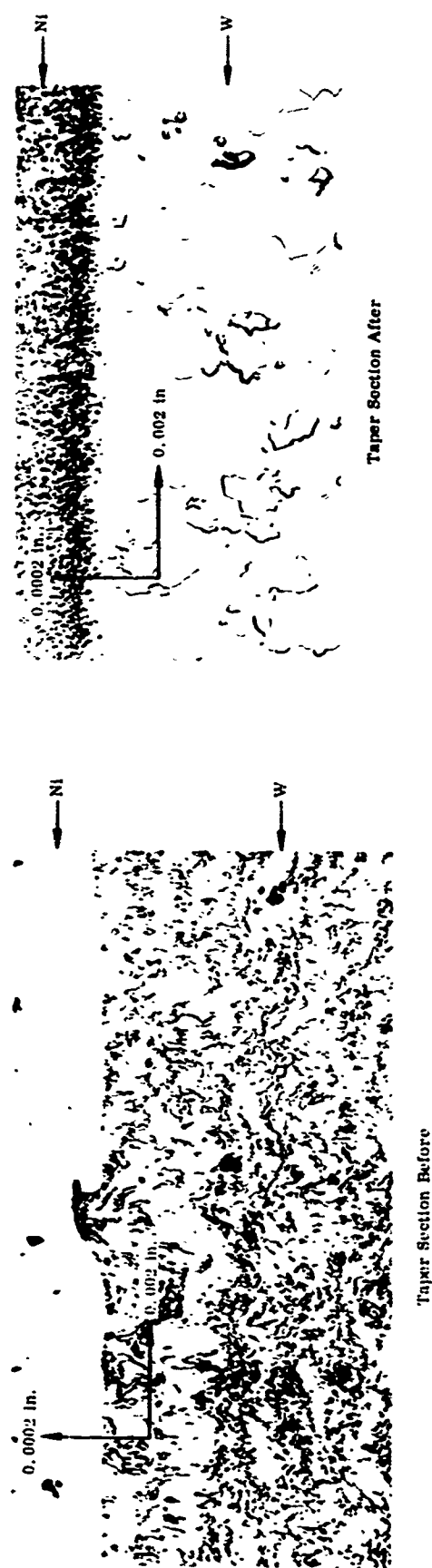
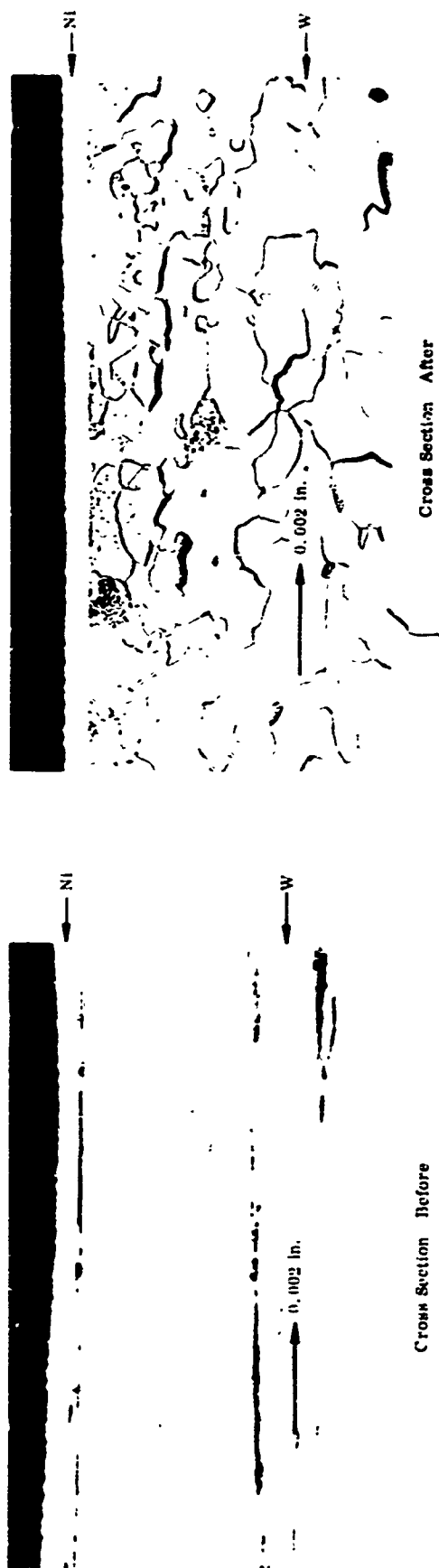


Fig. 49 Cross and Taper Section Photomicrographs of Tungsten Sample 1 Before and After Emittance Tests

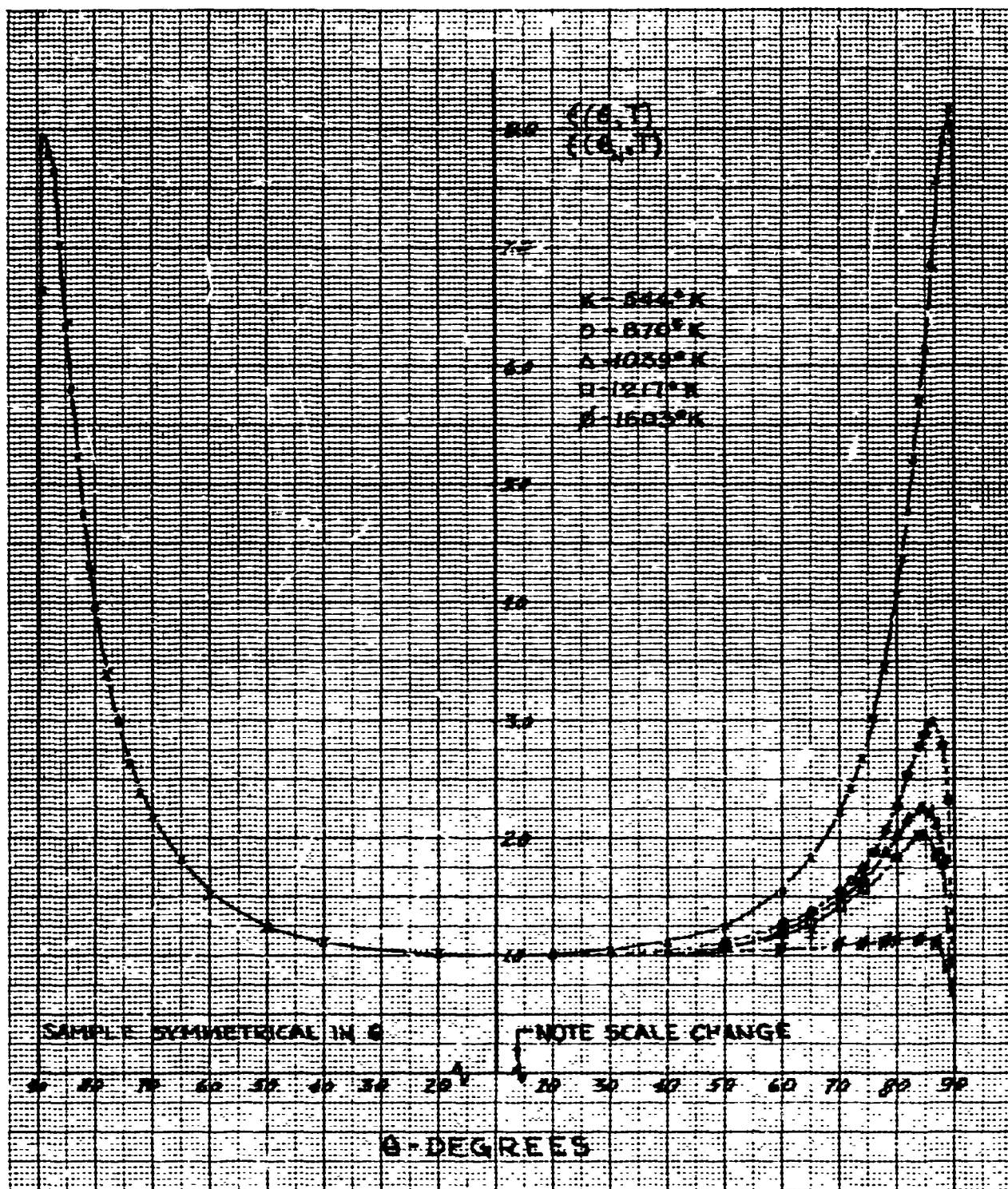


Figure 50 Relative Total Directional Emittance, Tungsten Sample 1

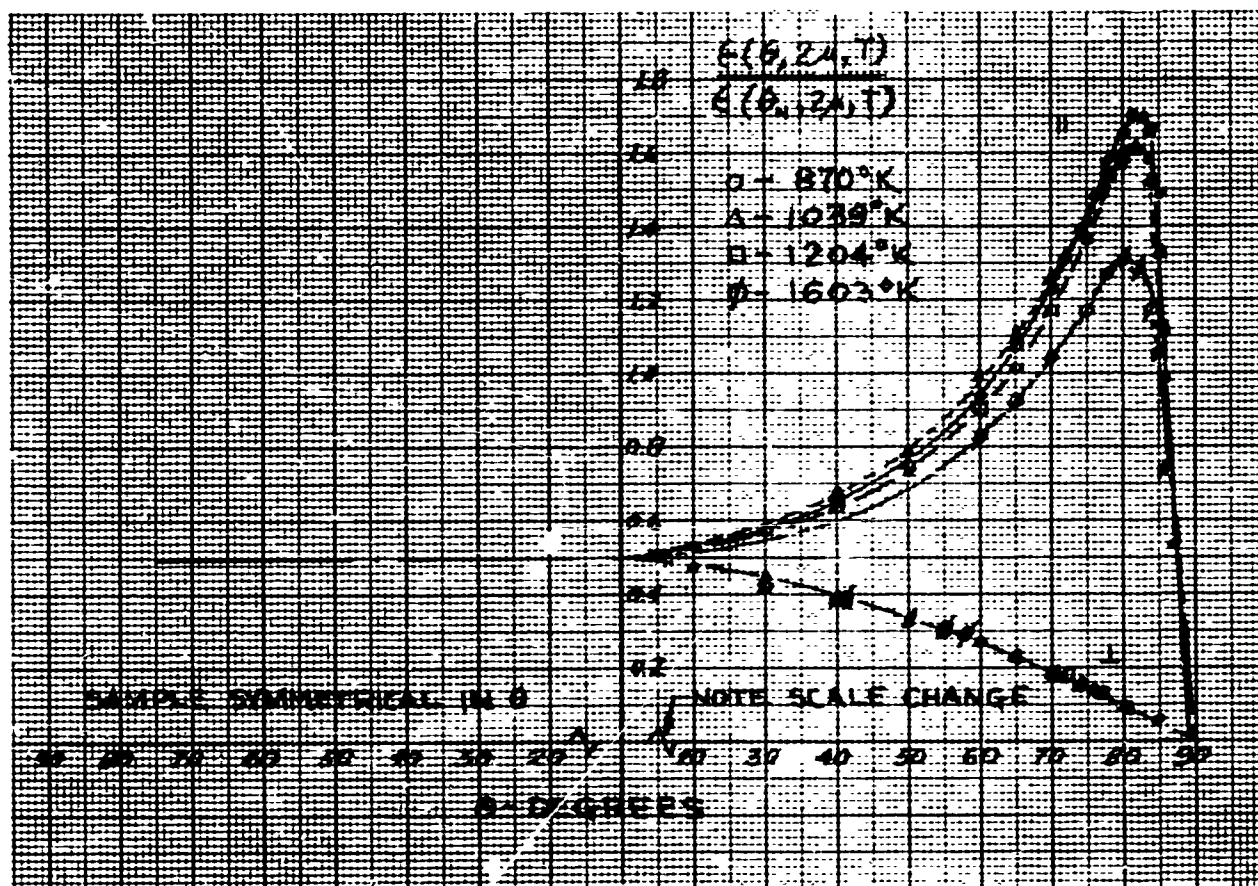


Figure 51 Relative Spectral Directional Emittance, $\lambda = 2\mu$, Tungsten Sample 1

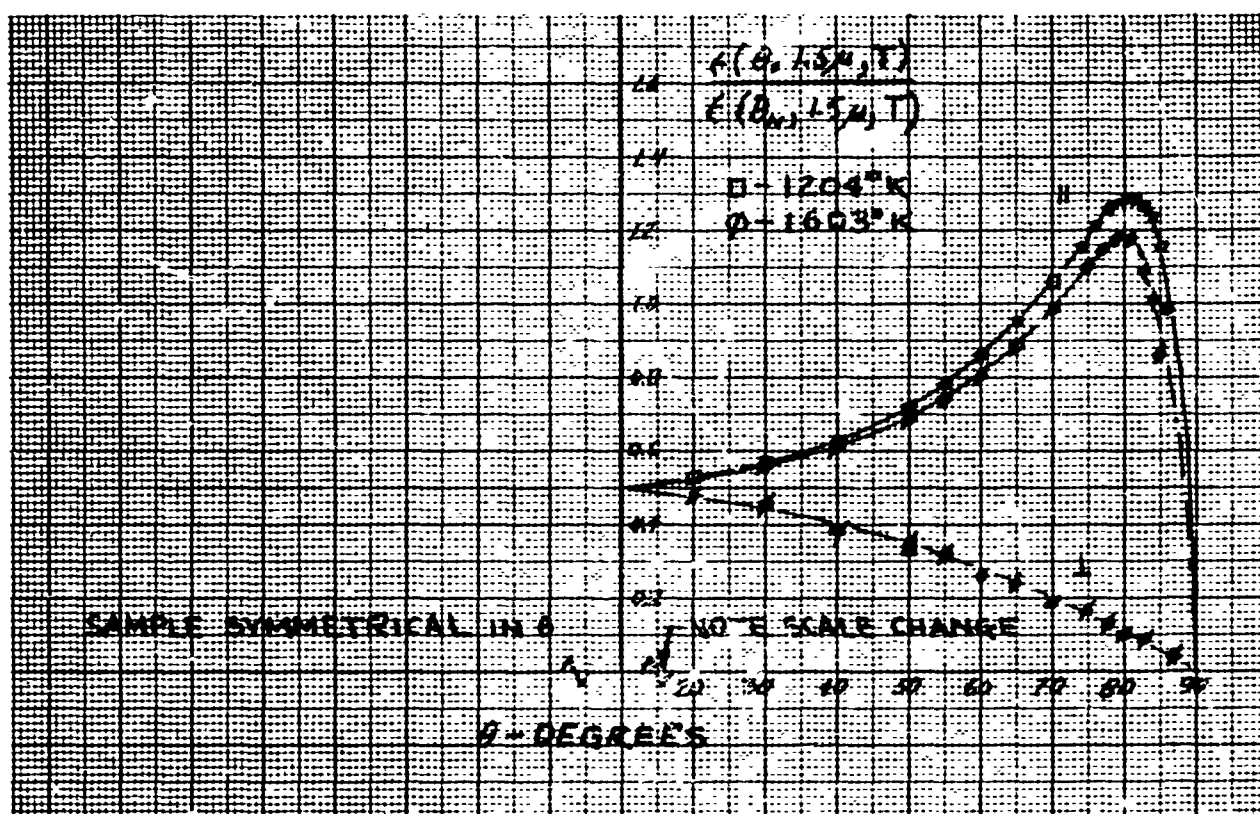


Figure 52 Relative Spectral Directional Emittance, $\lambda = 1.5 \mu$, Tungsten Sample 1

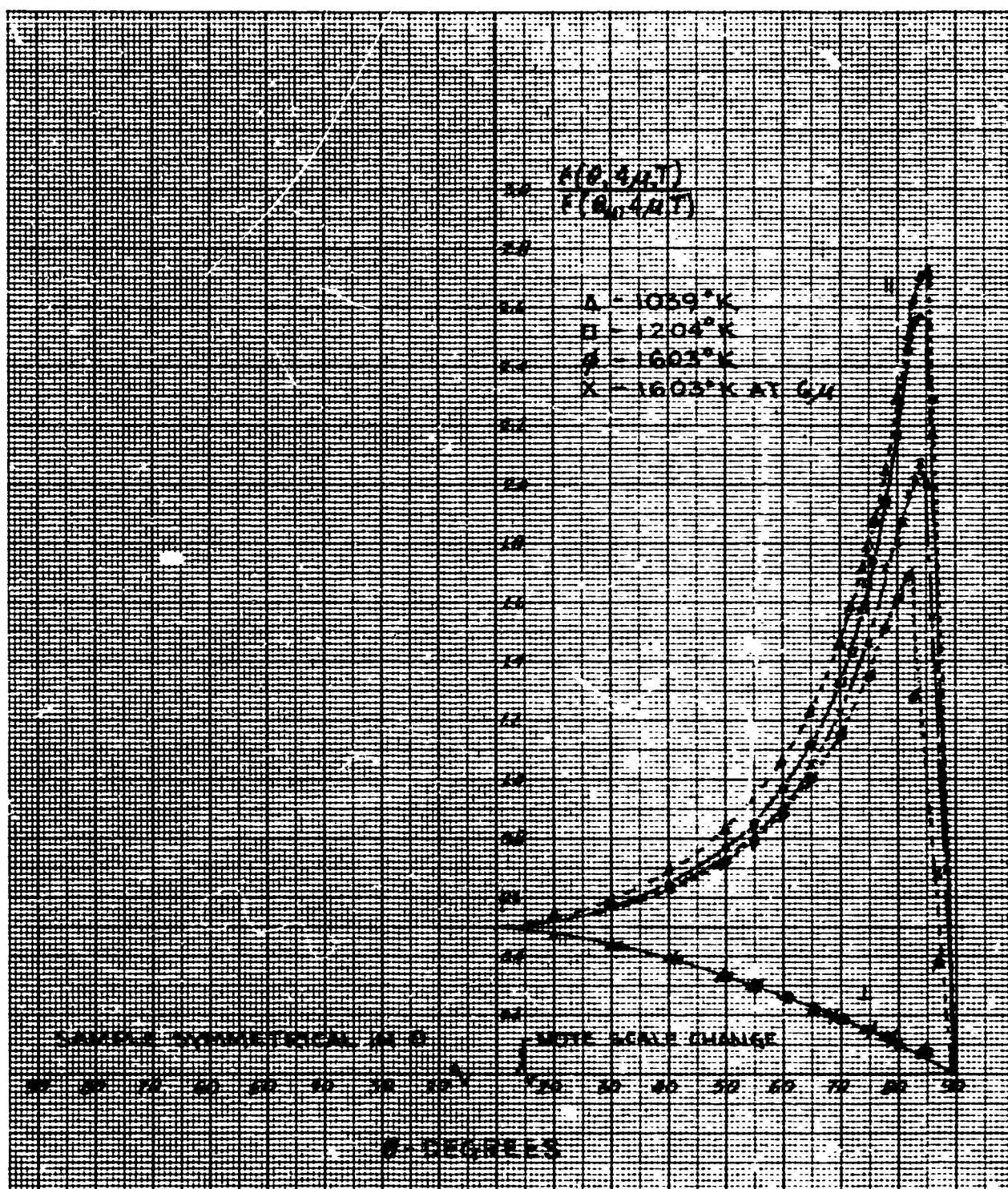


Figure 53 Relative Spectral Directional Emittance, $\lambda = 4 \mu$, Tungsten Sample 1

10.7 TUNGSTEN SAMPLE 2

1. Sample - Tungsten Sample 2.
2. Preparation - Grit Blasted, 5- μ alumina, 80 psi at 2 in.
3. RMS roughness - Before emittance tests, 17 μ in. ; after, 21 μ in.
4. Test procedure - Sample was heated to 1000°K for 1/2 hr in vacuum before taking emittance data, after which absolute and relative directional emittance data were obtained at seven temperatures between 536 and 1603°K. Total and spectral normal emittance data were rechecked at six temperatures between 536 and 1378°K. Vacuum throughout the tests was maintained between 1 and 8×10^{-5} Torr. Total time at T_{\max} (1603°K) was 2 hr.
5. Emittance Data - Absolute total and spectral normal emittance values are shown in Table 18.

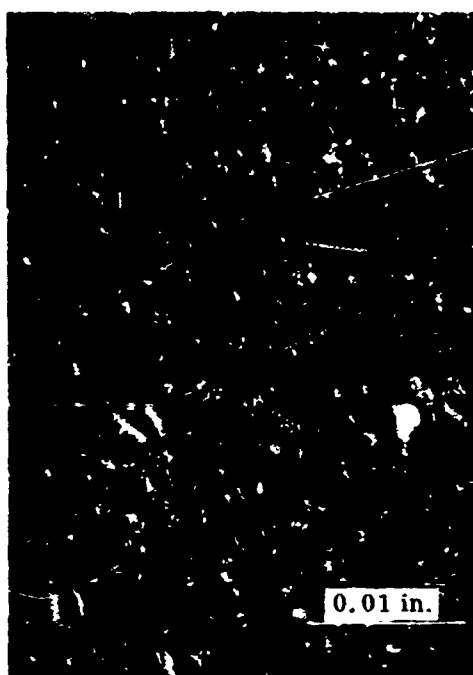
Relative total directional emittance data are shown in Figure 57.

Relative spectral directional emittance data at 2, 4, 6 and 8 μ are shown in Figures 58 through 61.

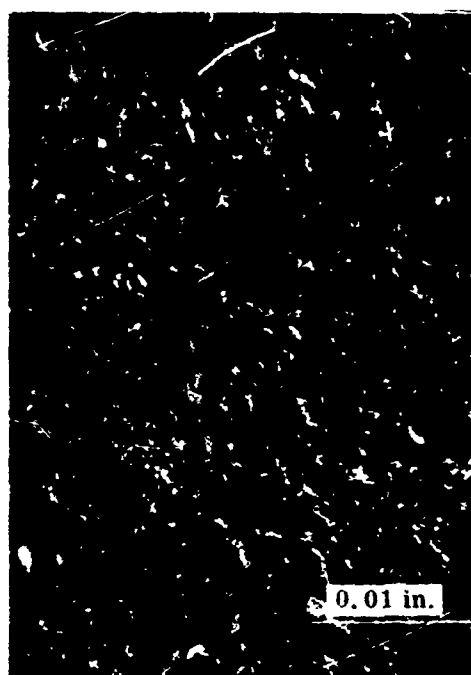
6. Remarks - The absolute total and spectral normal emittance values of this sample were observed to decrease significantly as the temperature was raised above 1300°K. Subsequent redeterminations of the sample emittance values indicated they had dropped at all wavelengths and temperatures. The relative directional emittance data shown in Figures 57 through 61 were obtained during the first temperature cycle. The drop in sample emittance is attributed to sample annealing and recrystallization effects; however, no significant change in the roughness characteristics of the sample were detected.

Photomicrographs of the sample surface before and after the emittance tests are shown in Figure 54. No visual change in the appearance of this sample was noted. Cross- and taper-section photomicrographs of the sample after the emittance tests are shown in Figure 56.

The x-ray diffraction pattern obtained from this sample was identical to the pattern obtained from tungsten sample 1, indicating no detectable impurities. The presence of aluminum was detected however in the spark spectrographic analysis, indicating some surface contamination occurred during the alumina-blast treatment. No evidence of embedded alumina was detected in the microscopic examinations of the surface or in the section mounts of the sample.



Before



After

Oblique Illumination

Figure 54 Surface Photomicrographs of Tungsten Sample 2 Before and After Emittance Tests

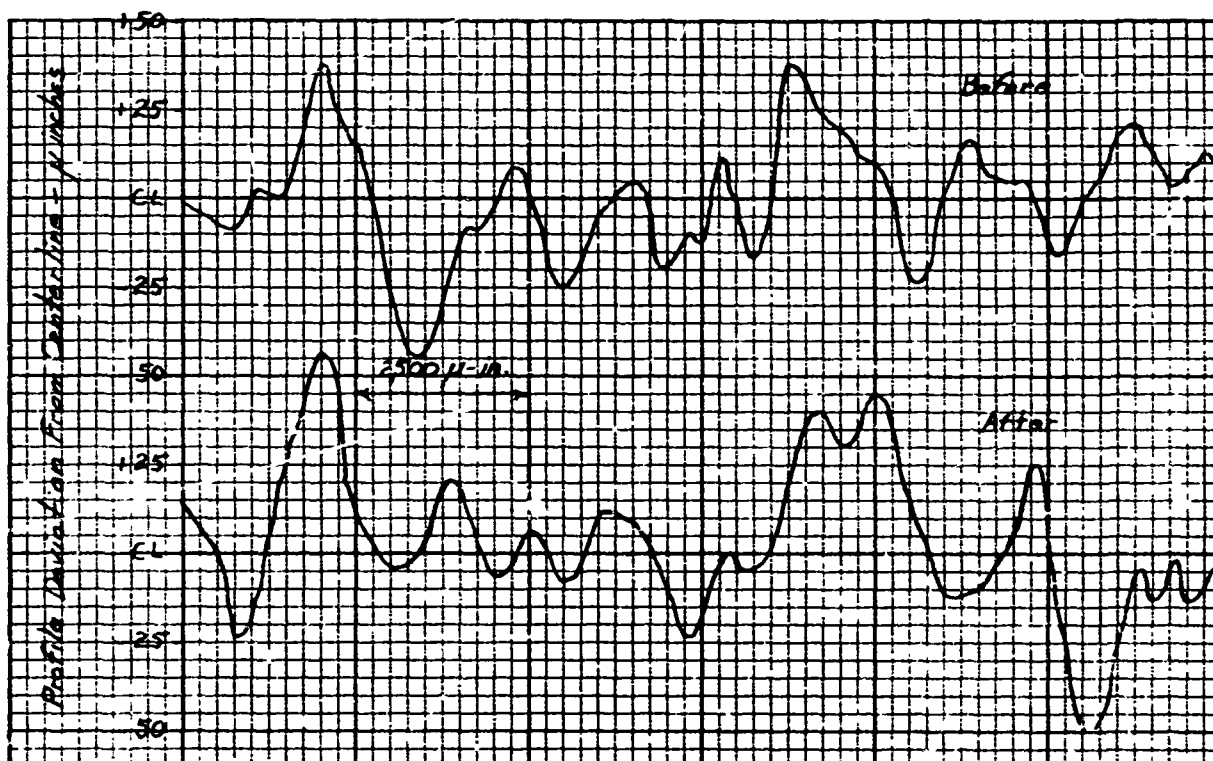


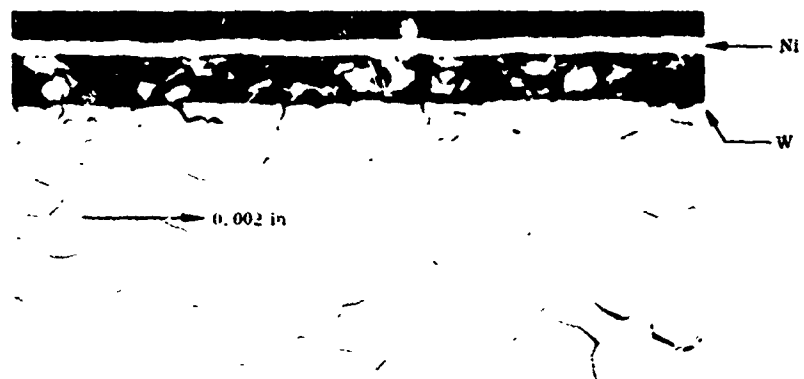
Figure 55 Typical Profile Traces for Tungsten Sample 2 Before and After Emittance Tests

Table 18

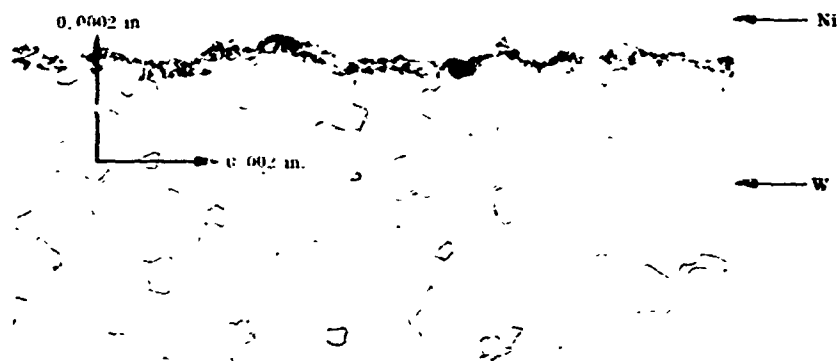
ABSOLUTE EMITTANCE DATA FOR TUNGSTEN SAMPLE 2

Temperature (°K)	Test	$\epsilon(\theta_N, T)$	$\epsilon(\theta_N, \lambda, T)$									
			$\epsilon(\theta_N, \lambda, T)$									
			0.65 μ (a)	1 μ	1.5 μ	2 μ	4 μ	6 μ	8 μ	10 μ	12 μ	
First Temperature Cycle												
536	2	0.159				0.57	0.54	0.28	0.165	0.118	0.088	
693	4, 5	0.224				0.64	0.52	0.29	0.181	0.130	0.107	
860	7, 8	0.288							0.188	0.140	0.118	0.085
1033	16, 17	0.334	0.66	0.73	0.62	0.52	0.29	0.29	0.185	0.143	0.119	0.104
1200	28a, 29	0.390	0.67	0.73	0.61	0.52	0.29	0.29	0.141	0.119	0.090	0.103
1373	40a, 42	0.330	0.57	0.65	0.50	0.39	0.21	0.21				0.096
1603	53a, 53b	0.280	0.58		0.38	0.28	0.18					
Second Temperature Cycle												
536	65	0.037				0.36	0.21	0.032	0.057	0.043	0.034	
698	67, 68	0.073				0.41	0.25	0.100	0.071	0.059	0.050	
860	70, 71	0.108							0.081	0.067	0.058	0.051
1029	73, 74	0.156		0.55	0.40	0.25	0.110	0.129	0.095	0.080	0.070	0.063
1196	75a, 77	0.230		0.62	0.42	0.29	0.129					
1378	78a, 78b	0.240			0.32	0.25	0.16					

(a) Spectral emittance values at 0.65 μ were determined from optical pyrometer readings.



Cross Section After
(Note: Nickel Layer Separated From Sample During Mounting)



Taper Section After

Figure 56 Cross and Taper Section Photomicrographs of Tungsten Sample 2 After Emittance Tests

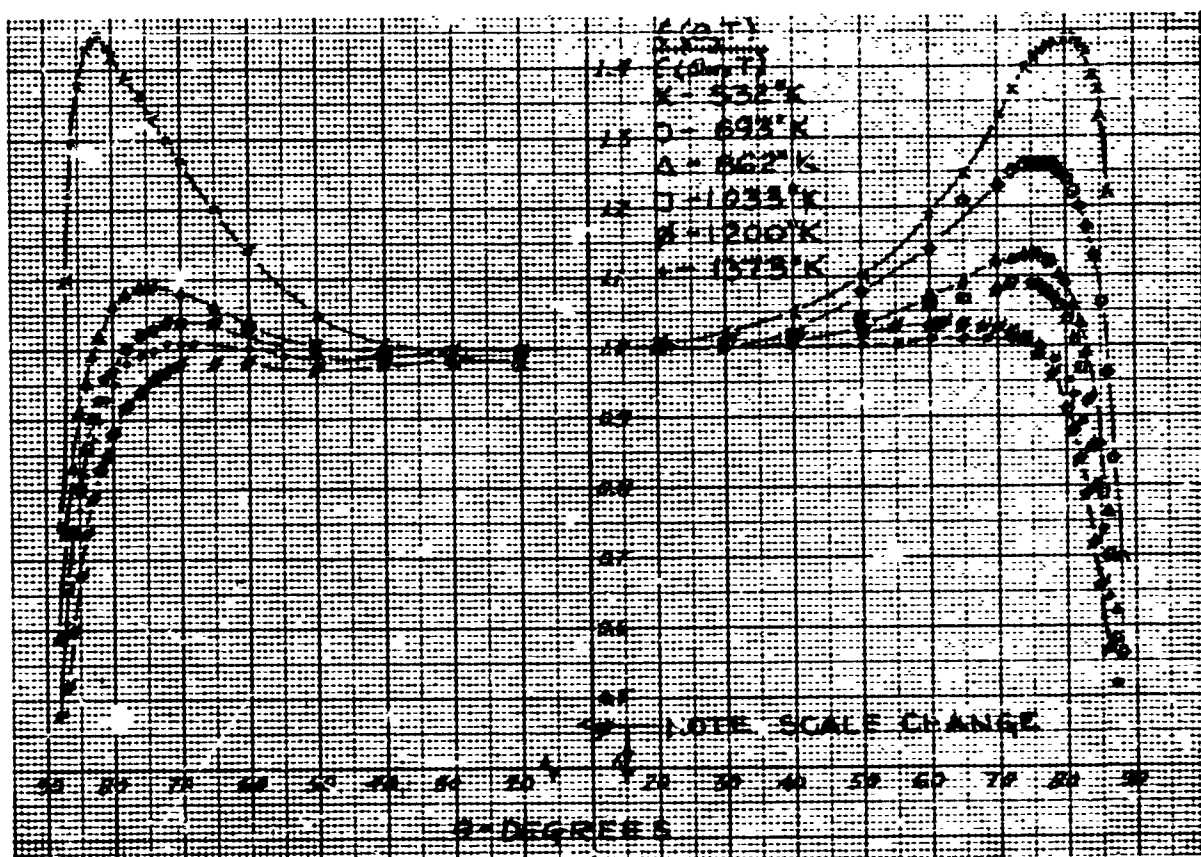


Figure 57 Relative Total Directional Emittance, Tungsten Sample 2

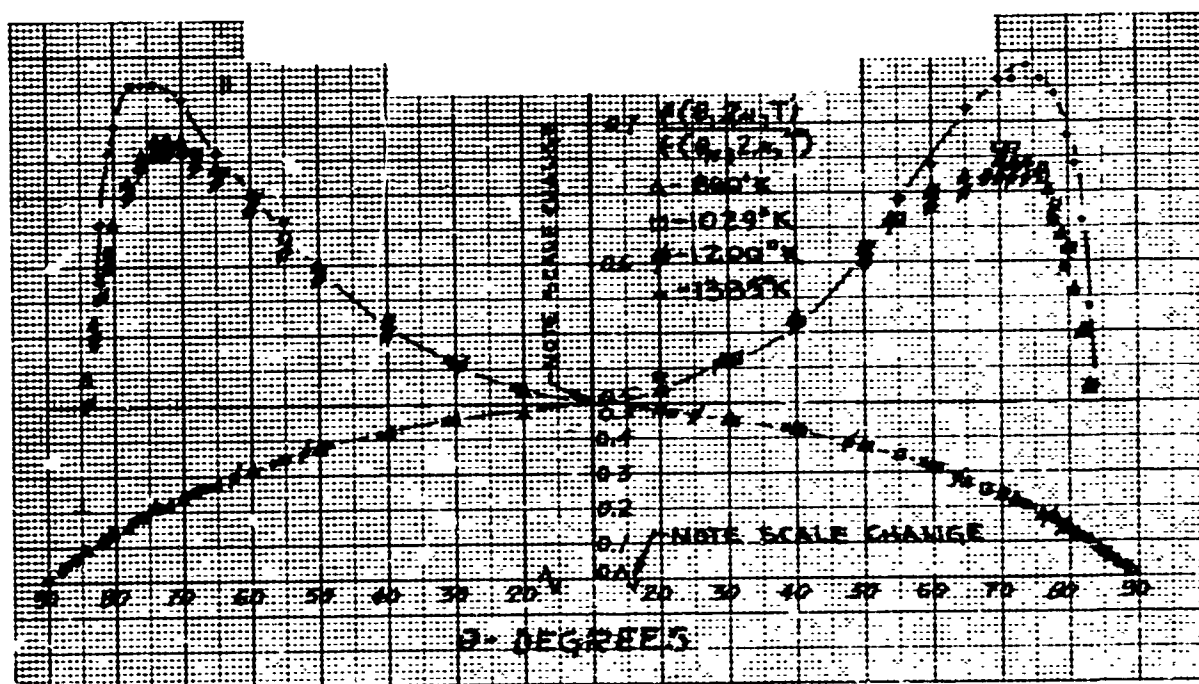


Figure 58 Relative Spectral Directional Emittance, $\lambda = 2 \mu$, Tungsten Sample 2

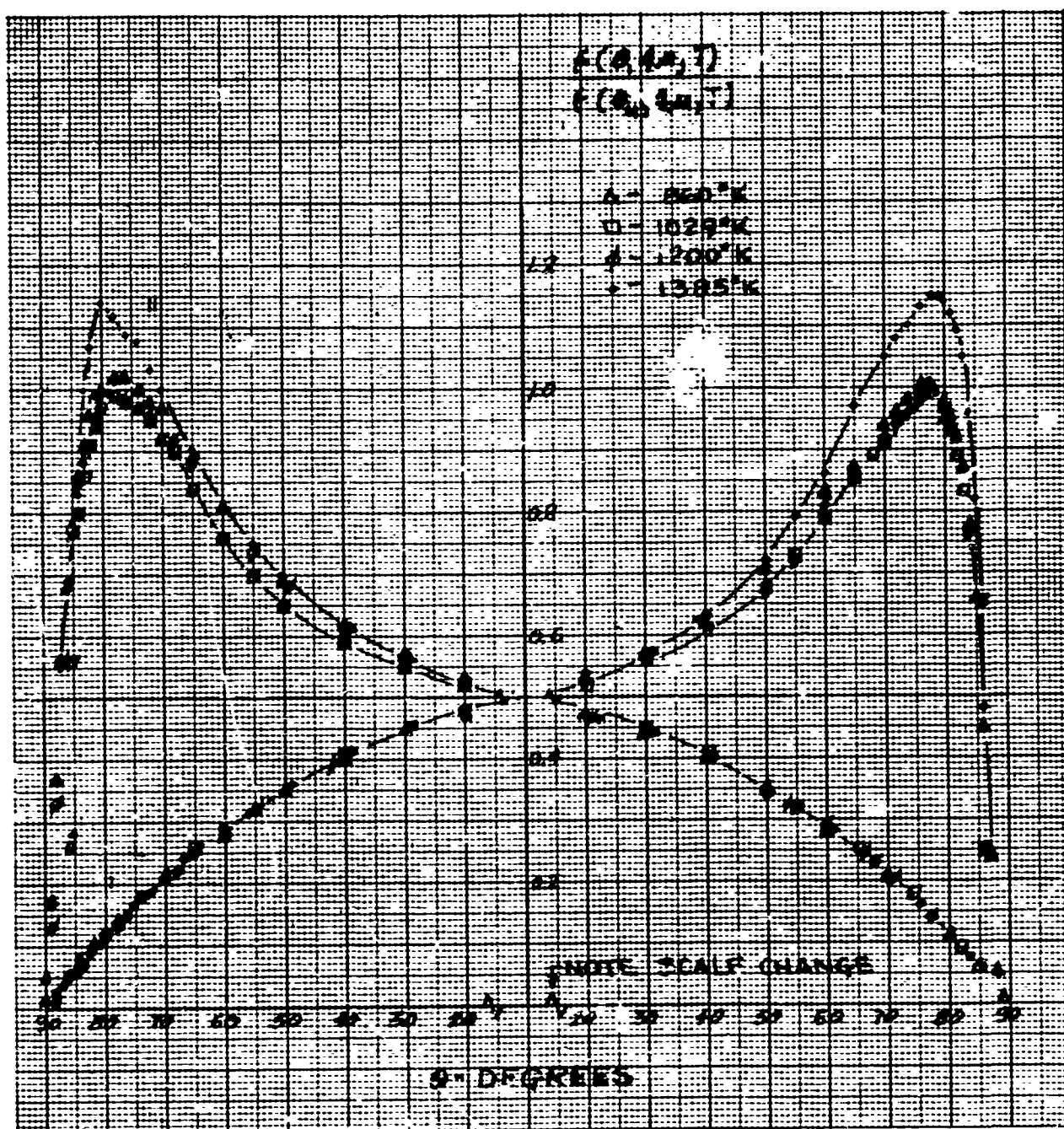


Figure 59 Relative Spectral Directional Emittance, $\lambda = 4 \mu$, Tungsten Sample 2

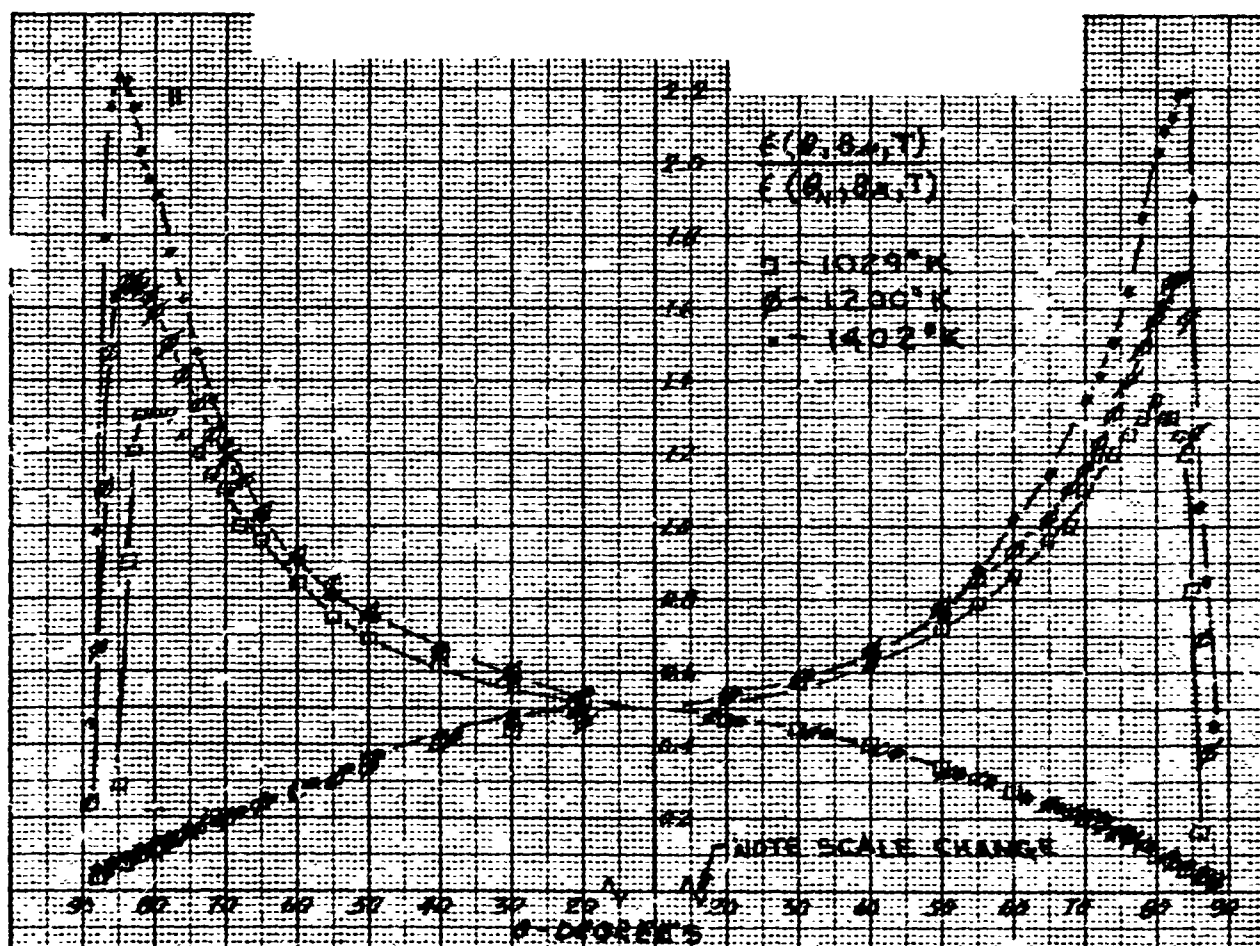


Figure 60 Relative Spectral Directional Emittance, $\lambda = 8 \mu$, Tungsten Sample 2

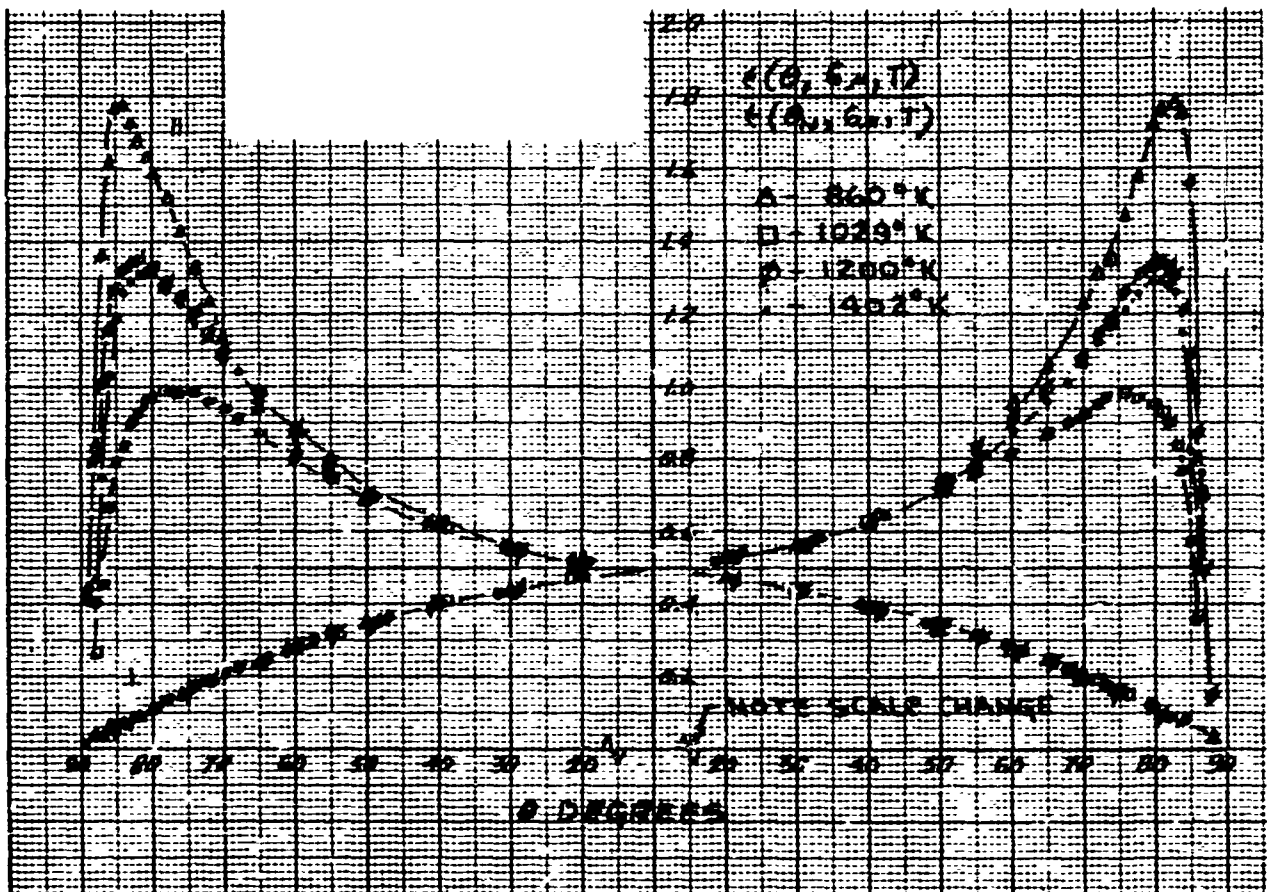


Figure 61 Relative Spectral Directional Emittance, $\lambda = 6 \mu$, Tungsten Sample 2

10.8 TUNGSTEN SAMPLE 3

1. Sample - Tungsten Sample 3.
2. Preparation - Grit Blasted, size 20 Mesh Silicon Carbide, 80 psi at 4 in.
3. RMS roughness - Before emittance tests, 110 μ in.; after, 38 μ in.
4. Test procedure - Sample was heated in vacuum at 1000°K for 1/2 hr before taking emittance data, after which absolute and relative directional emittance data were obtained at six temperatures from 542 to 1383°K. Absolute emittance data were rechecked at temperatures from 530 to 1358°K. Vacuum was maintained between 1 and 5×10^{-5} Torr throughout the tests. Total time at T_{\max} was 4.5 hr.
5. Emittance data - Absolute total and spectral normal emittance values are shown in Table 19.

Relative total directional emittance data are shown in Figure 65.

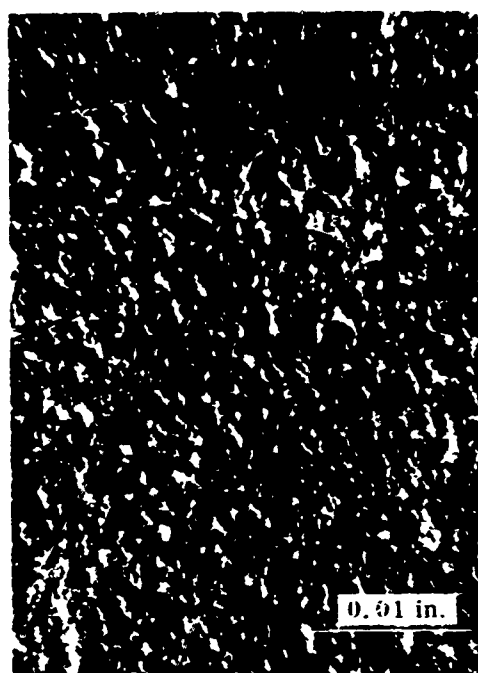
Relative spectral directional emittance data at 2, 4, 6 and 8 μ are shown in Figures 66 through 69.

6. Remarks - The absolute emittance data from this sample showed a significant drop in the total and spectral normal emittance values at temperatures above 1300°K. This behavior was the same as observed with tungsten sample 2 and is attributed to annealing relief of surface strain. Profile traces obtained after the emittance tests indicated the roughness of the sample to be considerably less than before, but no visual difference in surface texture was observed.

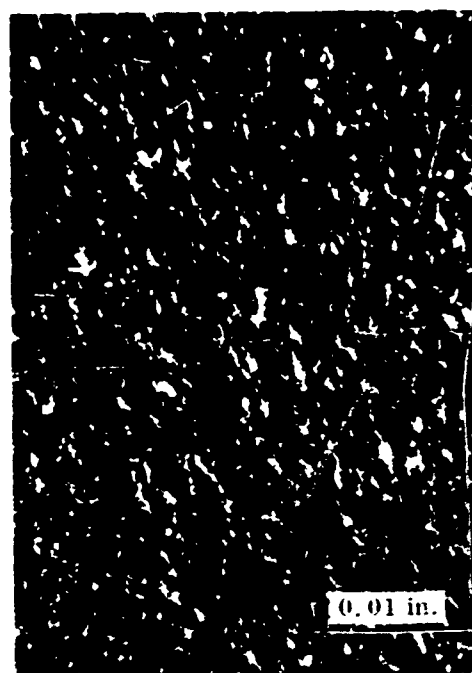
Surface and section photomicrographs indicating the surface condition of the sample before and after the emittance tests are shown in Figures 62 and 64. The photomicrographs indicate that recrystallization did not occur in this sample; however, a significant difference in the surface roughness is apparent, corresponding to the change indicated by the Proficorder traces.

The x-ray diffraction pattern from this sample contained three weak "d" lines in addition to the tungsten pattern. Positive identification of the lines was not made but they are presumably due to contamination of the surface by the silicon carbide grit. A significant amount of silicon was detected in the spark spectrographic analysis. No evidence of embedded grit was found in the microscopic examinations of the surface or section mounts.

The dissymmetry in the angular position of the relative directional emittance peaks on either side of normal indicates the sample alignment was off 2 or 3 deg.



Before



After

Oblique Illumination

Figure 62 Surface Photomicrographs of Tungsten Sample 3 Before and After Emittance Tests

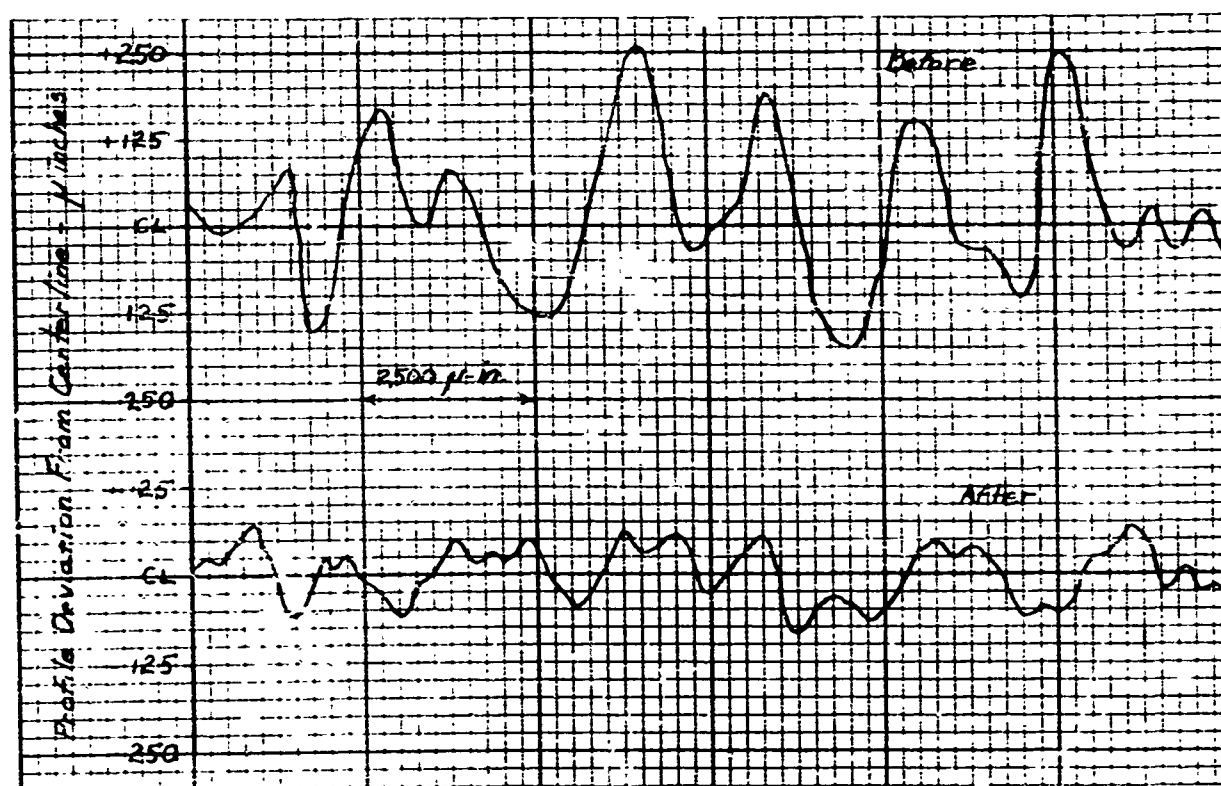


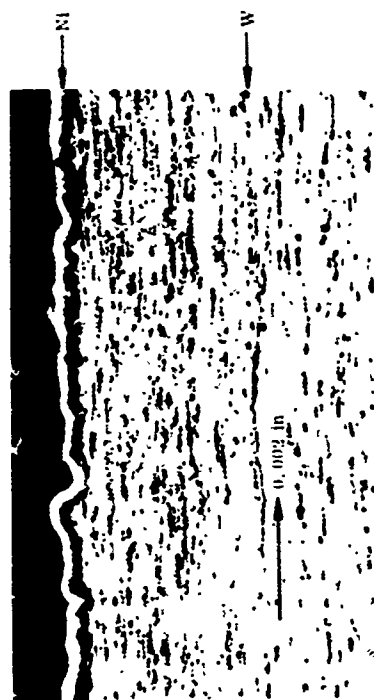
Figure 63 Typical Profile Traces for Tungsten Sample 3 Before and After Emittance Tests

Table 19

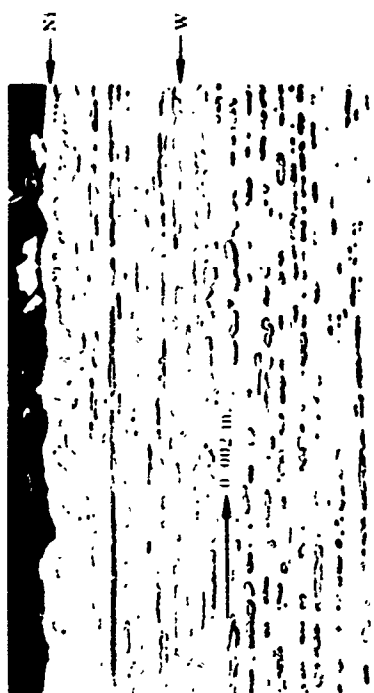
ABSOLUTE EMITTANCE DATA FOR TUNGSTEN SAMPLE 3

Temperature (°K)	Test	$\epsilon(\theta_N, T)$	$\epsilon(\theta_N, \lambda, T)$									
			0.65 μ (a)	1 μ	1.5 μ	2 μ	4 μ	6 μ	8 μ	10 μ	12 μ	
			First Temperature Cycle									
542	2	0.38				0.56	0.45	0.34	0.34	0.30		
692	4, 5	0.40			0.61	0.54	0.45	0.40	0.35	0.28	0.28	
863	7, 8	0.44			0.60	0.47	0.45	0.40	0.36	0.32	0.29	
1040	16, 17	0.45										
1214	29a, 30	0.51	0.59	0.70	0.61	0.55	0.46	0.41	0.37	0.34	0.30	
1383	42a, 43	0.44	0.52	0.56	0.48	0.45	0.40	0.36	0.32	0.30	0.27	
699	58, 59	0.35			0.46	0.41	0.36	0.32	0.29	0.26		
Second Temperature Cycle												
529	63	0.30										
700	64, 65	0.34			0.49	0.44	0.37	0.33	0.30	0.26		
858	66, 67	0.37			0.47	0.43	0.37	0.34	0.30	0.27	0.25	
1033	68, 69	0.39			0.53	0.45	0.39	0.35	0.31	0.28	0.27	
1198	71	0.42	0.60		0.54	0.48	0.40	0.36	0.33	0.30	0.27	
1358	72	0.46	0.56	0.60	0.52	0.49	0.44	0.40	0.36	0.33	0.31	

(a) Spectral emittance values at 0.65 μ were determined from optical pyrometer readings.



Cross Section Before



Cross Section After



Taper Section Before



Taper Section After

Figure 6-1 Cross and Taper Section Photomicrographs of Tungsten Sample 3 Before and After Etching Tests

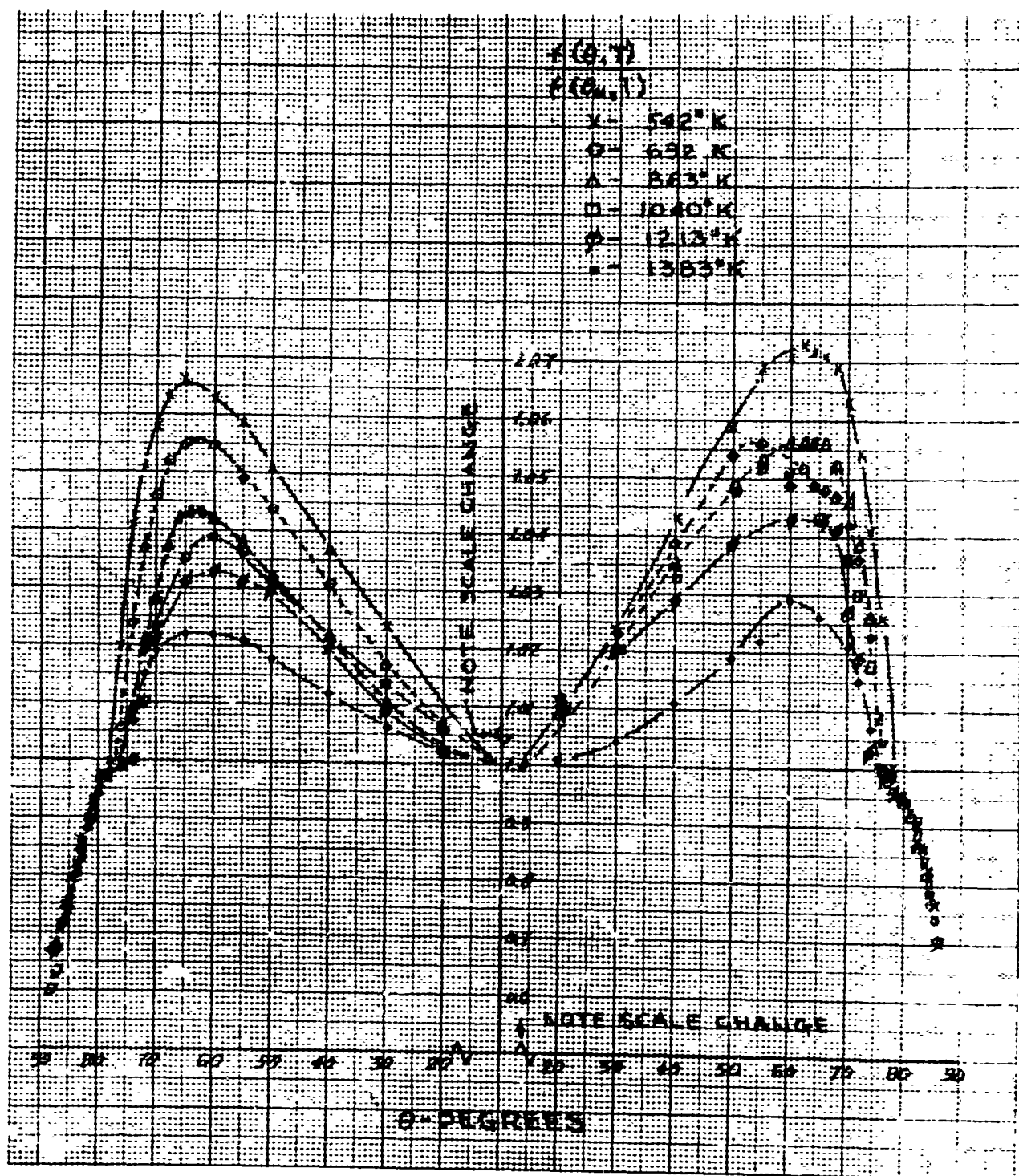


Figure 65 Relative Total Directional Emittance, Tungsten Sample 3

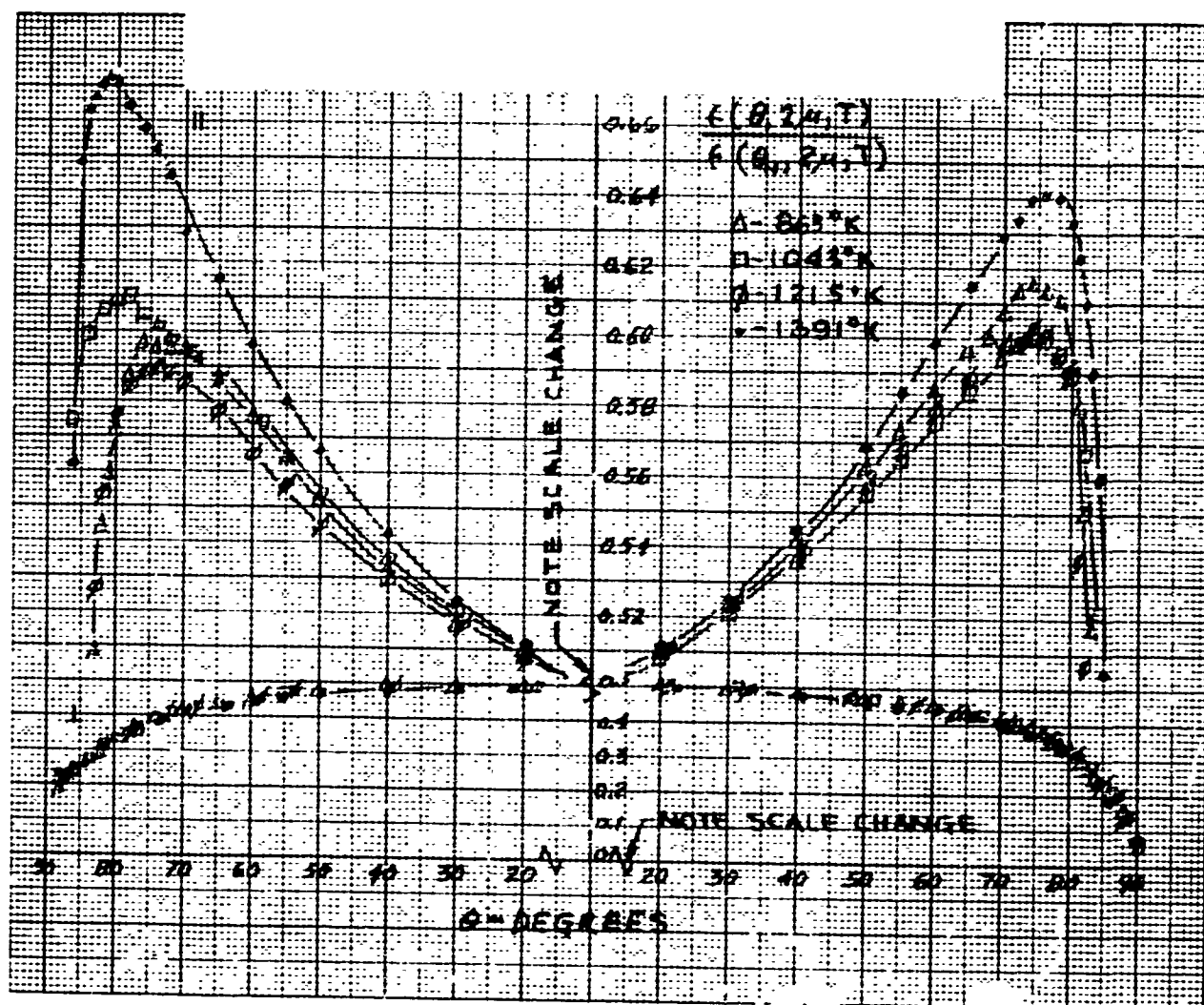


Figure 66 Relative Spectral Directional Emittance, $\lambda = 2 \mu$, Tungsten Sample 3

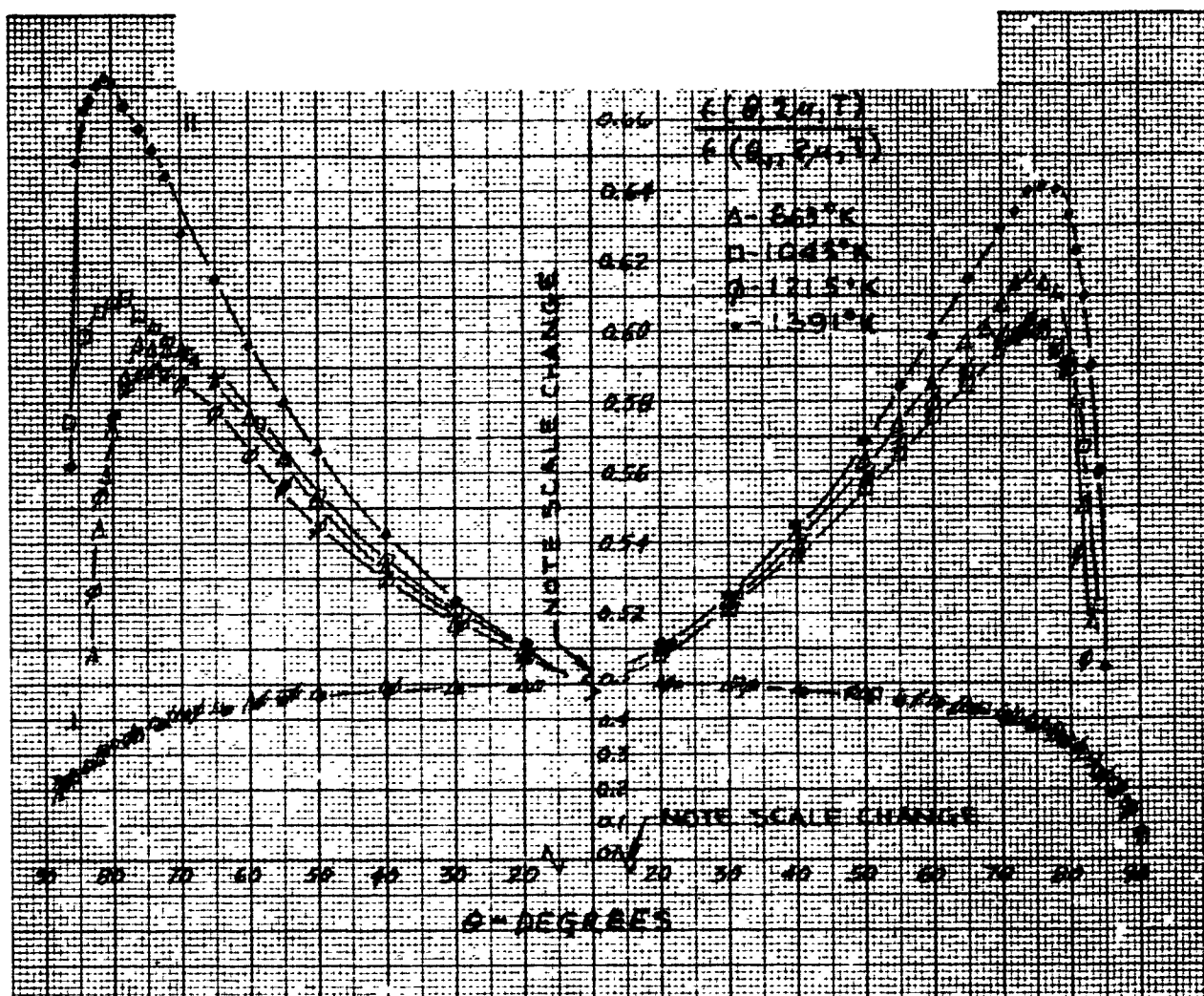


Figure 66 Relative Spectral Directional Emittance, $\lambda = 2 \mu$, Tungsten Sample 3

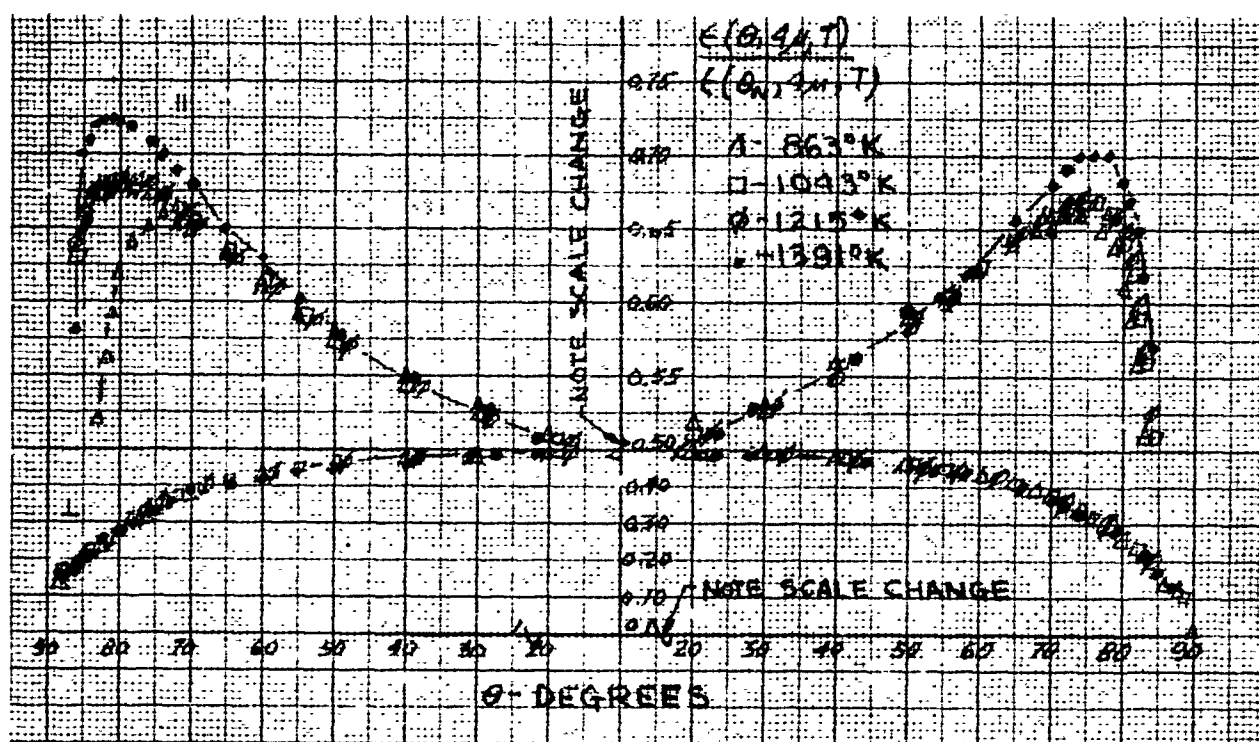


Figure 67 Relative Spectral Directional Emittance, $\lambda = 4 \mu$, Tungsten Sample 3

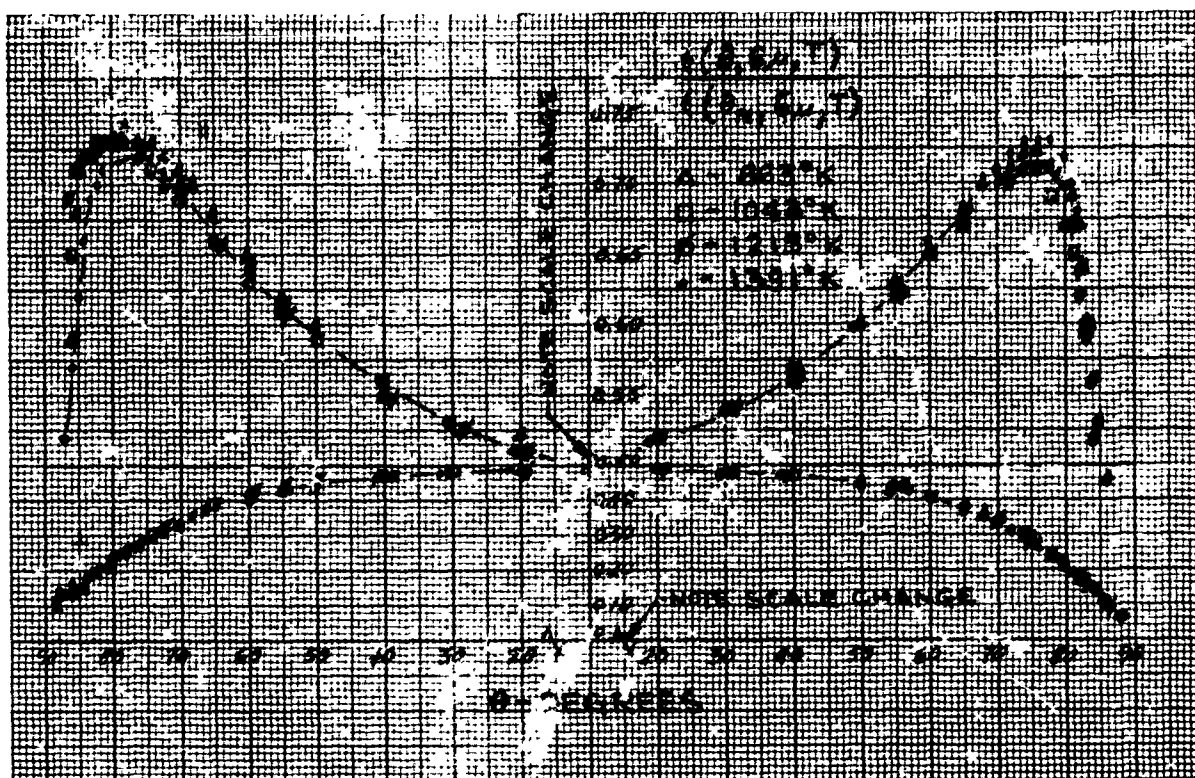


Figure 68 Relative Spectral Directional Emittance, $\lambda = 6 \mu$, Tungsten Sample 3

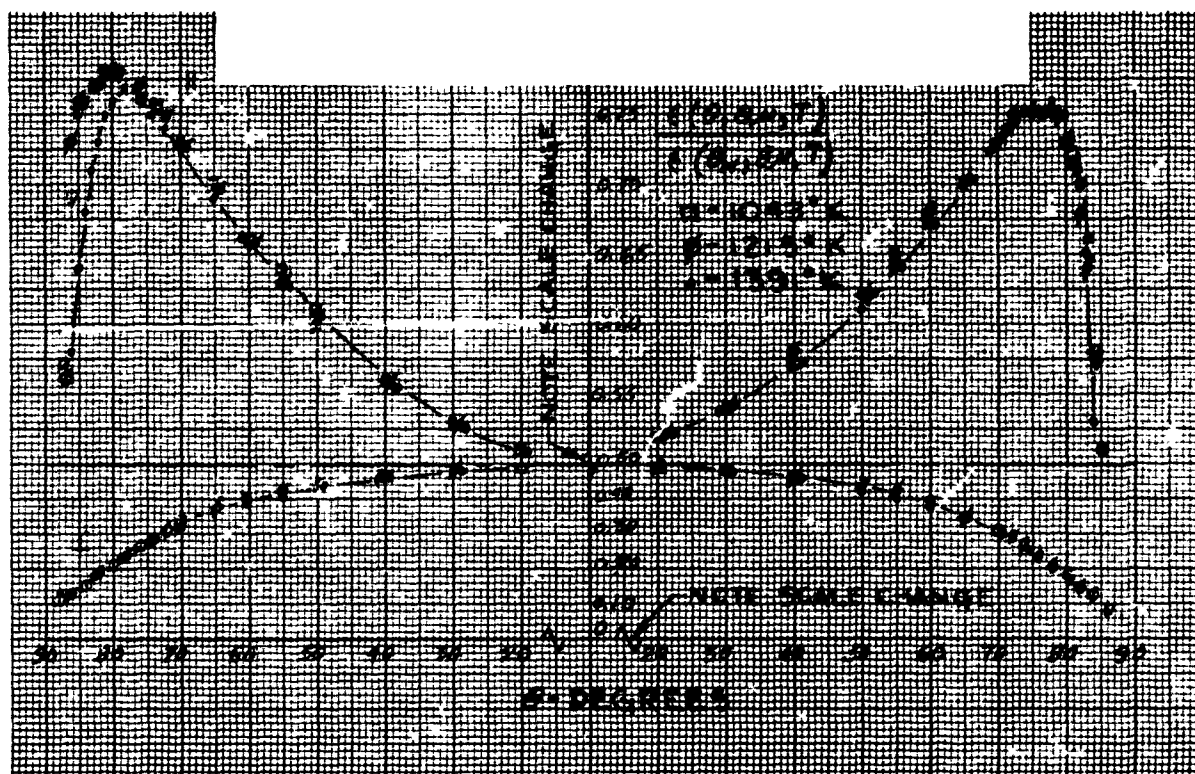


Figure 69 Relative Spectral Directional Emittance, $\lambda = 8 \mu$, Tungsten Sample 3

10.9 PLATINUM SAMPLE 1

1. Sample - Platinum Sample 1.
2. Preparation - None (tested as received)
3. RMS roughness - Before emittance tests (see subsection 8.1); after, $4.7 \mu\text{in}$.
4. Test procedure - Sample was heated in vacuum at 1300°K for 1 hr before taking emittance data after which absolute and relative directional emittance data were obtained at six temperatures from 697 to 1639°K . The absolute total normal emittance values were rechecked over the same range of temperatures to determine the effect of surface recrystallization on emittance. Vacuum, throughout the test was maintained between 1 and 7×10^{-5} Torr. Total time at T_{max} was 2 hr.
5. Emittance data - Absolute total and spectral normal emittance values are shown in Table 20.

Relative total directional emittance data are shown in Figure 73.

Relative spectral directional emittance data at 1 , 1.5 , 2 , 4 , and 6μ are shown in Figures 74 through 78.

6. Remarks - The absolute total normal emittance of this sample was observed to drop as the sample temperature was raised to 1640°K and then increased again during the time the relative directional emittance were measured. Surface recrystallization was visually observed at the end of the first test cycle, therefore total normal emittance values were rechecked. Emittance values obtained during the second temperature cycle were the same, or just slightly higher than the initial values until the temperature reached 1640°K . Recrystallization apparently does not greatly affect total emittance at temperatures below 1500°K . At 1640°K , the emittance of the sample was erratic. The change in total emittance appears to be caused by changes in the spectral emittance at wavelengths less than 4μ .

The appearance of the sample surface before and after the emission tests is shown in Figure 70. The interference photomicrographs in this figure indicate that the as received surface was considerably rougher than indicated by the Proficorder traces. After recrystallization, the peak-to-peak spacing appeared to be larger and the peak-to-valley depths more irregular. These characteristics were also detected by the Proficorder (Figure 71). These changes are probably the cause for the instability of the absolute emittance data at 1640°K . The cross and taper section photomicrographs of the sample in Figure 72 show roughness features in the after-test sections that were not present in the before-test sections.

X-ray diffraction and spark spectrographic analyses of the sample indicated no significant impurities. The diffraction pattern also indicated a strong preferred orientation of (200) and (220) crystal planes at the surface.

Dissymmetry in the angular position of the relative directional emittance peaks in Figures 73 through 78 indicate the sample may have been misaligned 2 or 3 deg.

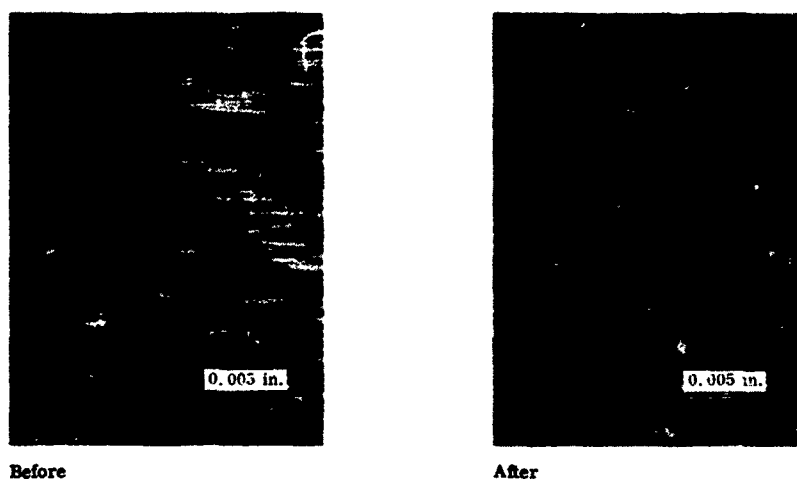
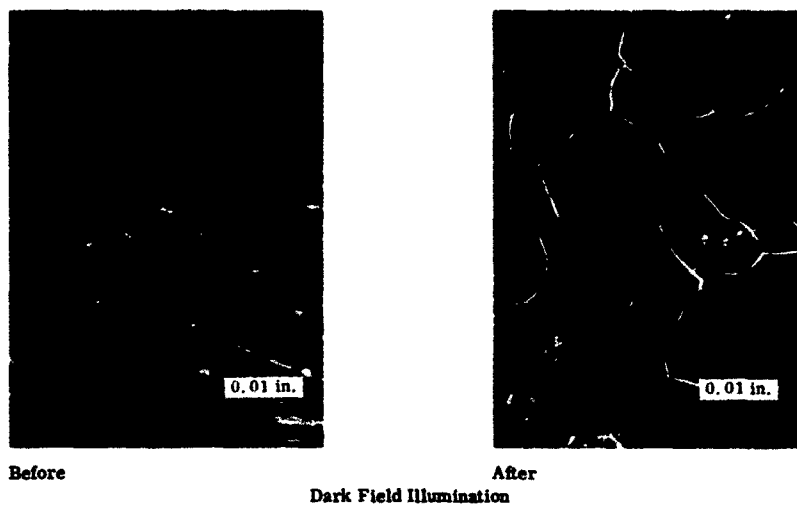


Figure 70 Surface and Surface Interference Photomicrographs of Platinum Sample 1 Before and After Emittance Tests

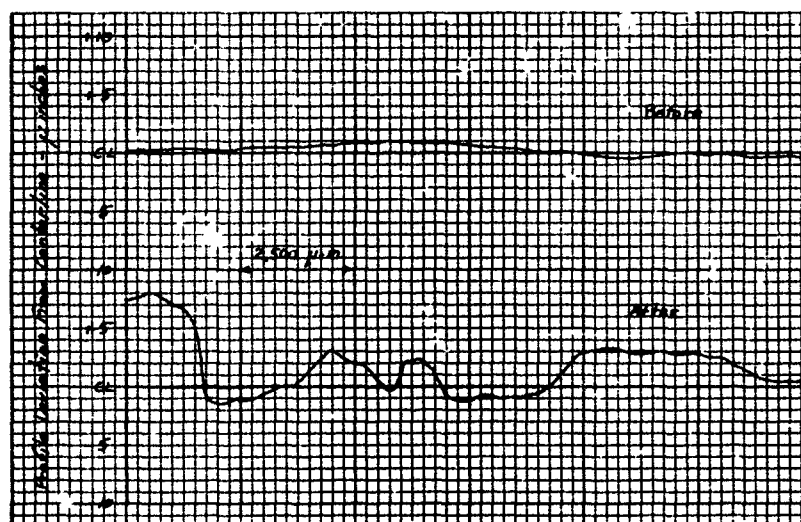
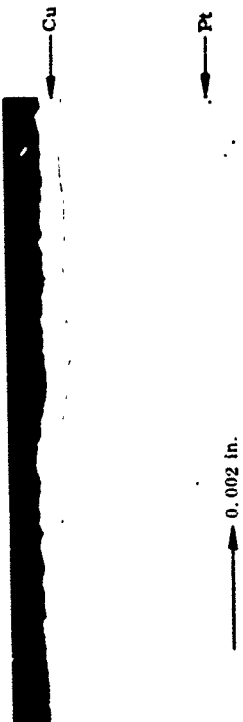


Figure 71 Typical Profile Traces for Platinum Sample 1 Before and After Emittance Tests

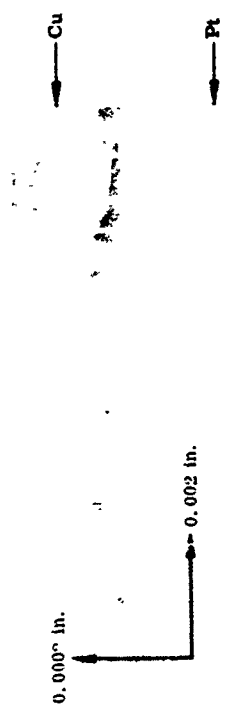
Table 20
ABSOLUTE EMITTANCE DATA FOR PLATINUM SAMPLE 1

Temperature (°K)	Test	$\epsilon(\theta_N, T)$	$\epsilon(\theta_N, \lambda, T)$								
			0.65 μ (a)	1 μ	1.5 μ	2 μ	4 μ	6 μ	8 μ	10 μ	12 μ
697	2, 4	0.074	0.220	0.296	0.220	0.163	0.093	0.070	0.066	0.056	
863	5, 7	0.098			0.220	0.163	0.105	0.084	0.077	0.068	
1033	12, 14	0.122			0.225	0.178	0.112	0.095	0.083	0.076	
1202	19, 21	0.200			0.230	0.187	0.125	0.098	0.081	0.079	
1369	34, 36	0.242			0.281	0.193	0.141	0.111	0.093	0.084	
1639	45, 47	0.212	0.29	0.245	0.167	0.156	0.141	0.128	0.112	0.104	0.109
1633	56	0.274	Second Temperature Cycle								
699	60	0.077									
871	61	0.102									
1032	62	0.125									
1200	63	0.213	0.33								
1362	64	0.242									
1497	64a	0.269									
1642	69	0.258									

(a) spectral emittance values at 0.65 μ were determined from optical pyrometer readings.



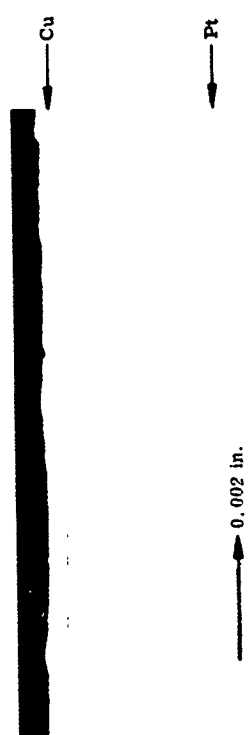
Cross Section After



Taper Section After (Unetched)



Taper Section After (Etched)



Cross Section Before



Taper Section Before (Unetched)



Taper Section Before (Etched)

Figure 72 Cross and Taper Section Photomicrographs of Platinum Sample 1 Before and After Emittance Test⁴

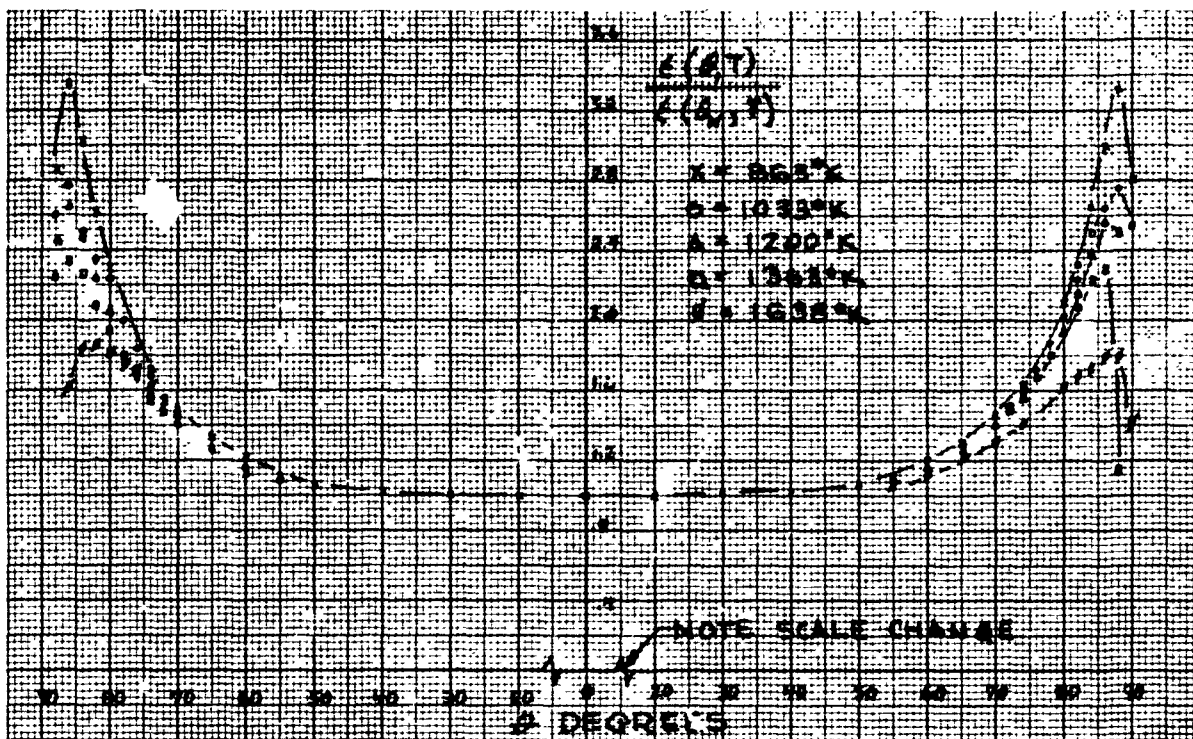


Figure 73 Relative Total Directional Emittance, Platinum Sample 1

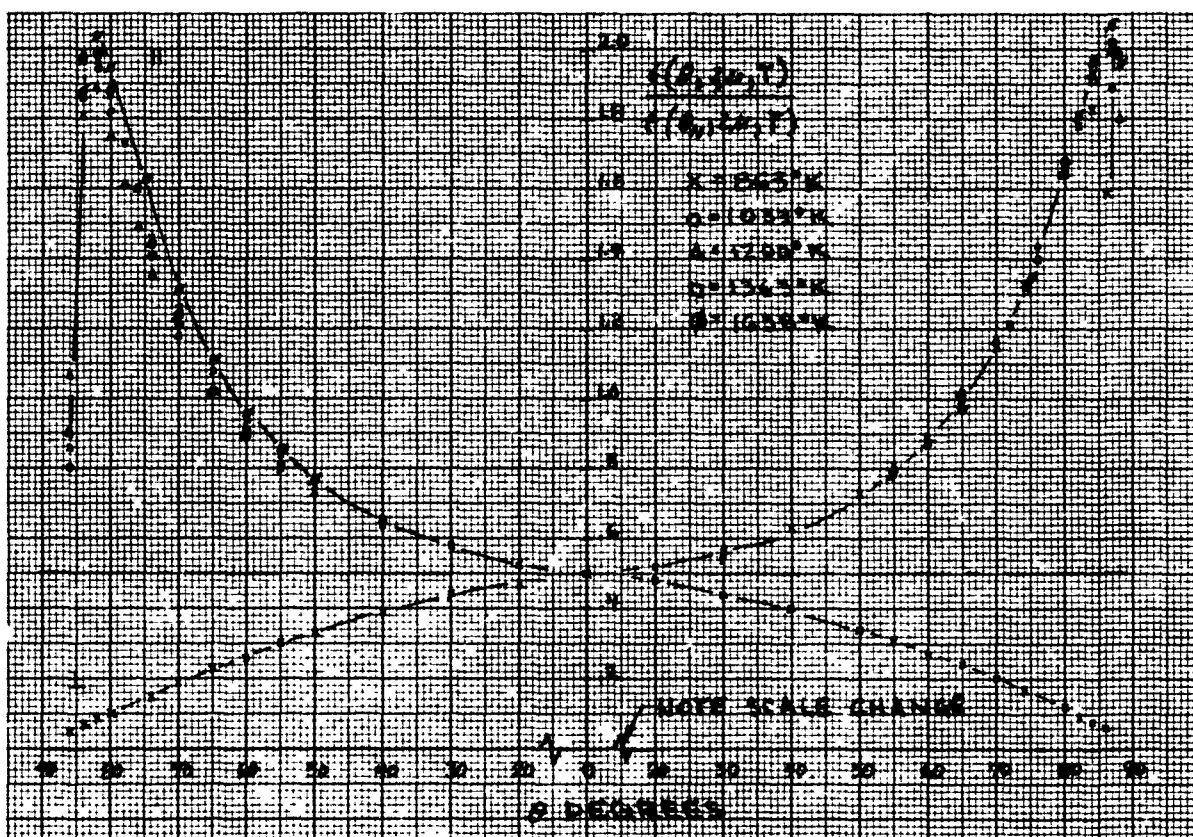


Figure 74 Relative Spectral Directional Emittance, $\lambda = 2 \mu$, Platinum Sample 1

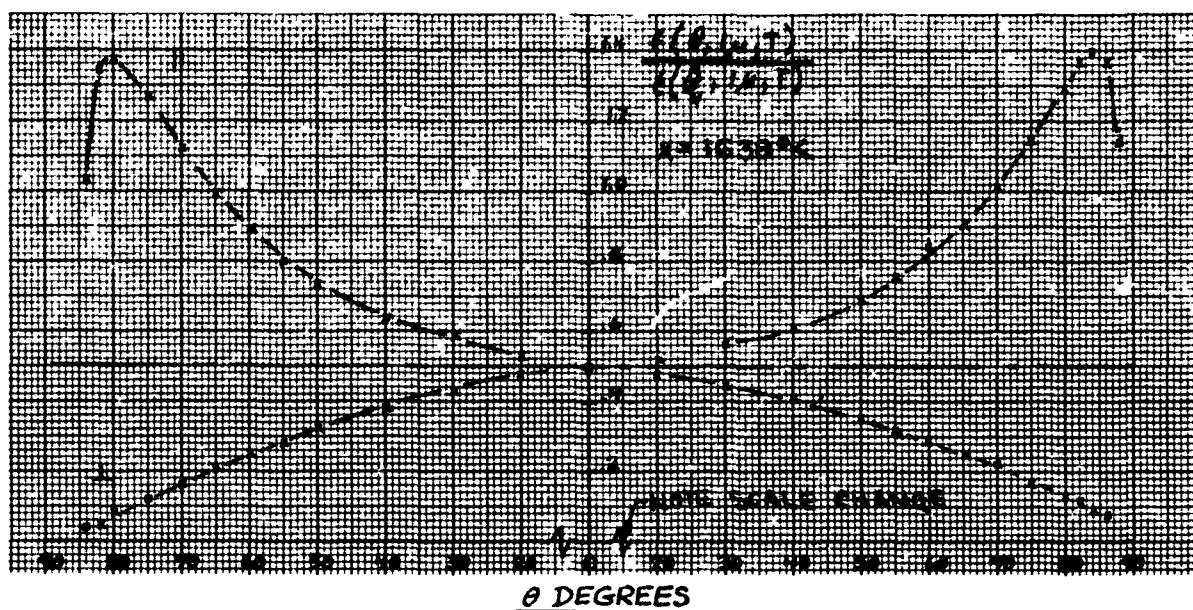


Figure 75 Relative Spectral Directional Emittance, $\lambda = 1 \mu$, Platinum Sample 1

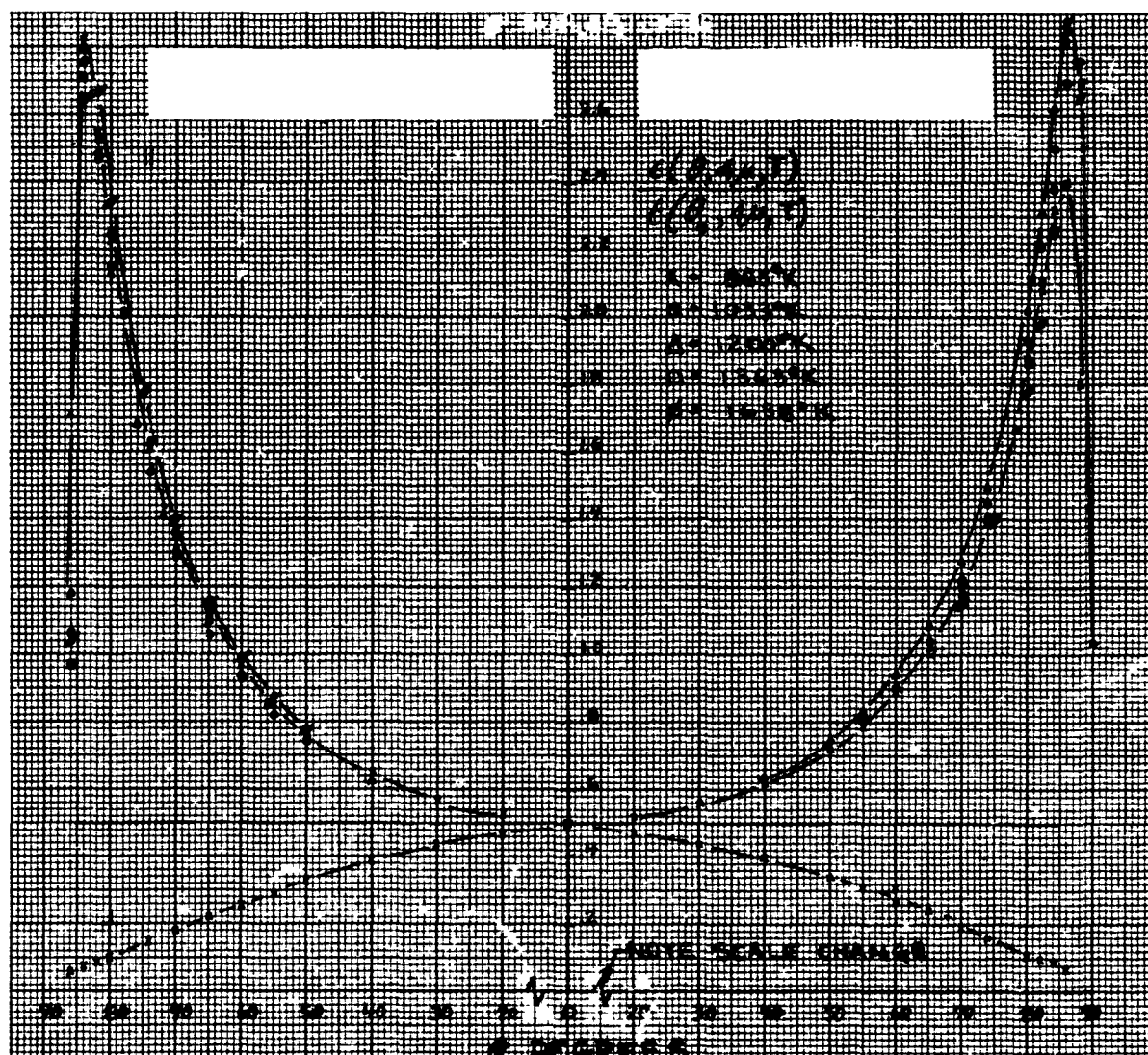


Figure 76 Relative Spectral Directional Emittance, $\lambda = 4 \mu$, Platinum Sample 1

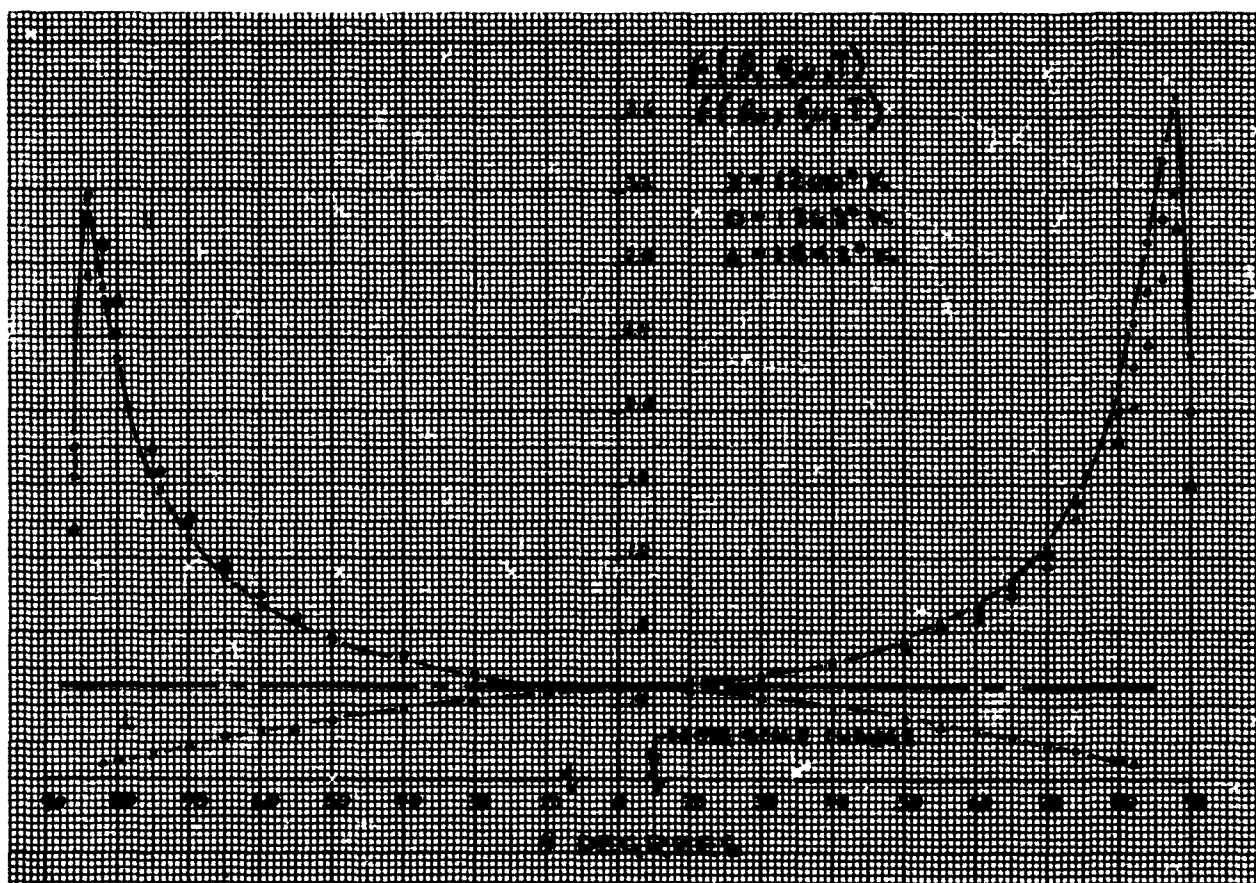


Figure 77 Relative Spectral Directional Emittance, $\lambda = 6 \mu$, Platinum Sample 1

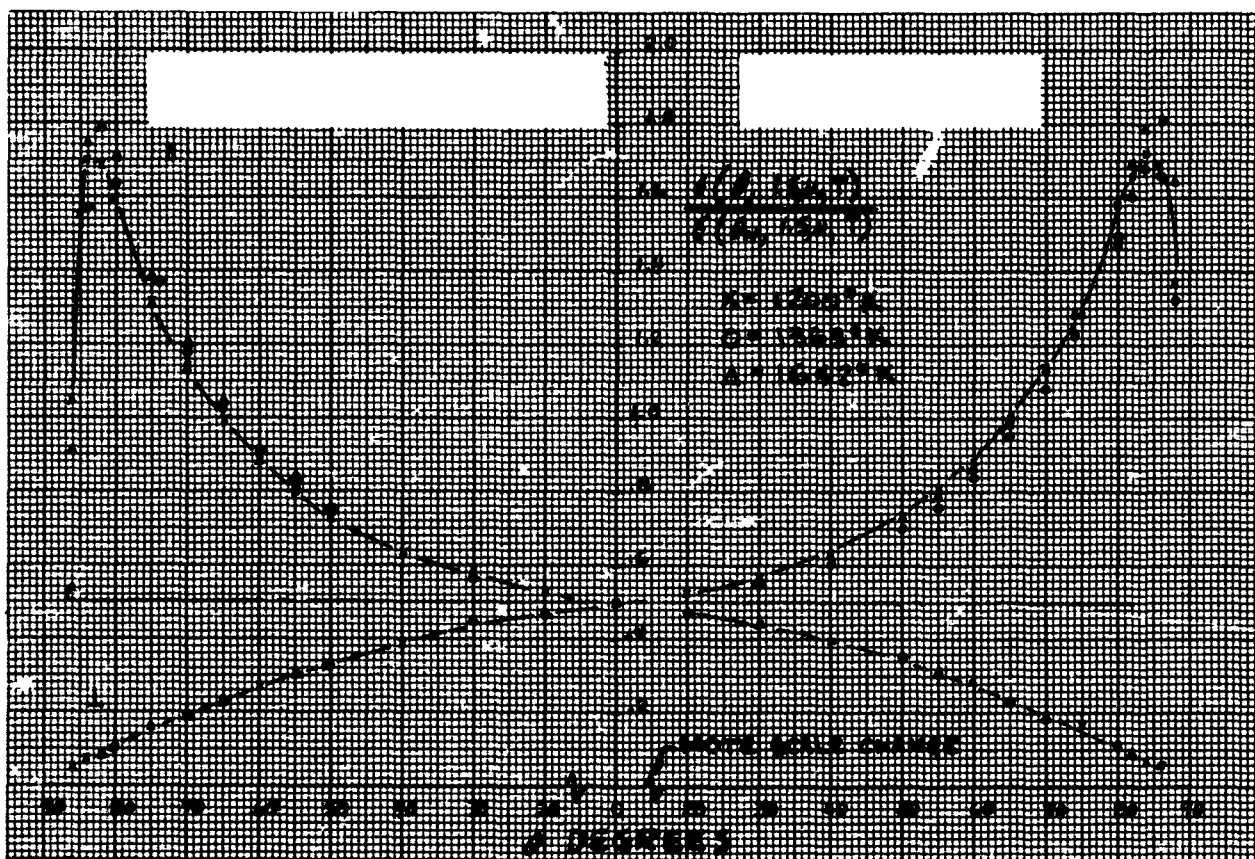


Figure 78 Relative Spectral Directional Emittance, $\lambda = 1.5 \mu$, Platinum Sample 1

10.10 PLATINUM SAMPLE 3

1. Sample - Platinum Sample 3.
2. Preparation - Glas-Shot blasted, Size MS-ML beads, 60 psi at 6 in.
3. RMS roughness - Before emittance tests, 169 $\mu\text{in.}$; after, 79 $\mu\text{in.}$
4. Test procedure - Sample was heated in vacuum to 1300°K for 1 hr before taking emittance data, after which absolute and relative directional emittance data were obtained at temperatures from 703 to 1625°K and rechecked at three of the lower temperatures. Vacuum throughout the tests was maintained between 1 and 6×10^{-5} Torr. Total time at T_{max} was 1.5 hr.
5. Emittance data - Absolute total and spectral normal emittance values are shown in Table 21.

Relative total directional emittance data are shown in Figure 82.

Relative spectral directional emittance data at 1.5, 2, 4, and 6 μ are shown in Figures 83 through 86.

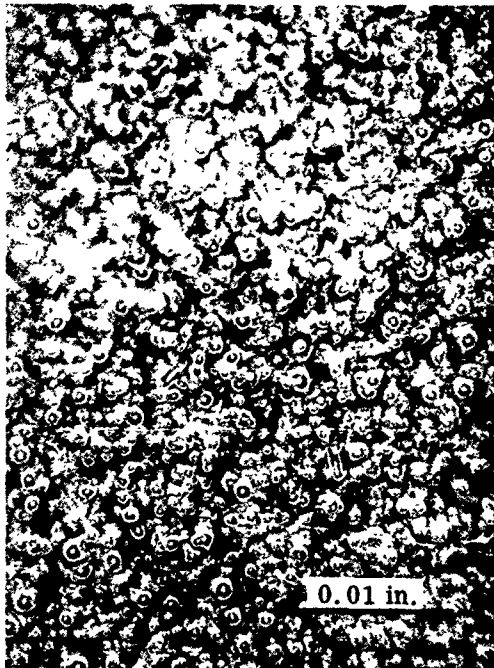
6. Remarks - As with platinum sample 1, the emittance of this sample also appeared to drop as the temperature was increased above 1600°K. Rechecks of the total normal emittance indicated only a slight drop in emittance at temperatures below 1600°K, however. From Proficorder traces obtained after the emittance tests, the RMS roughness of the sample was found to be less than 50% of the original value. The lower roughness is attributed to relief of surface strain and recrystallization of the sample, similar to the behaviour of the roughened copper samples.

Most of the drop in surface roughness is believed to have occurred during the initial annealing at 1300°K, prior to obtaining the emittance data.

Before and after photomicrographs of the sample surface are shown in Figure 79. Although grain boundaries were not visible through the roughness, the surface looked smoother to the eye at the conclusion of the emittance tests. Cross and taper section photomicrographs of the sample, after testing, are shown in Figure 81.

The x-ray diffraction pattern from this sample agreed with the pattern reported for platinum in Reference 30. This indicates that the preferred orientation of the as rolled surface was destroyed by the Glas-Shot blast treatment. A spectrographic analysis of this sample was not obtained; however, it is assumed that the results would have been similar to those for the copper samples. Contamination from the Glas Shot is suspected. No evidence of embedded glass was detected in the microscopic examinations of the surface and metallographic sections.

The dissymmetry in angular position of the relative directional emittance peaks in Figures 82 - 86 indicates the sample alignment was off approximately 1 deg.



Before



After

Bright Field Illumination

Figure 79 Surface Photomicrographs of Platinum Sample 3 Before and After Emittance Tests

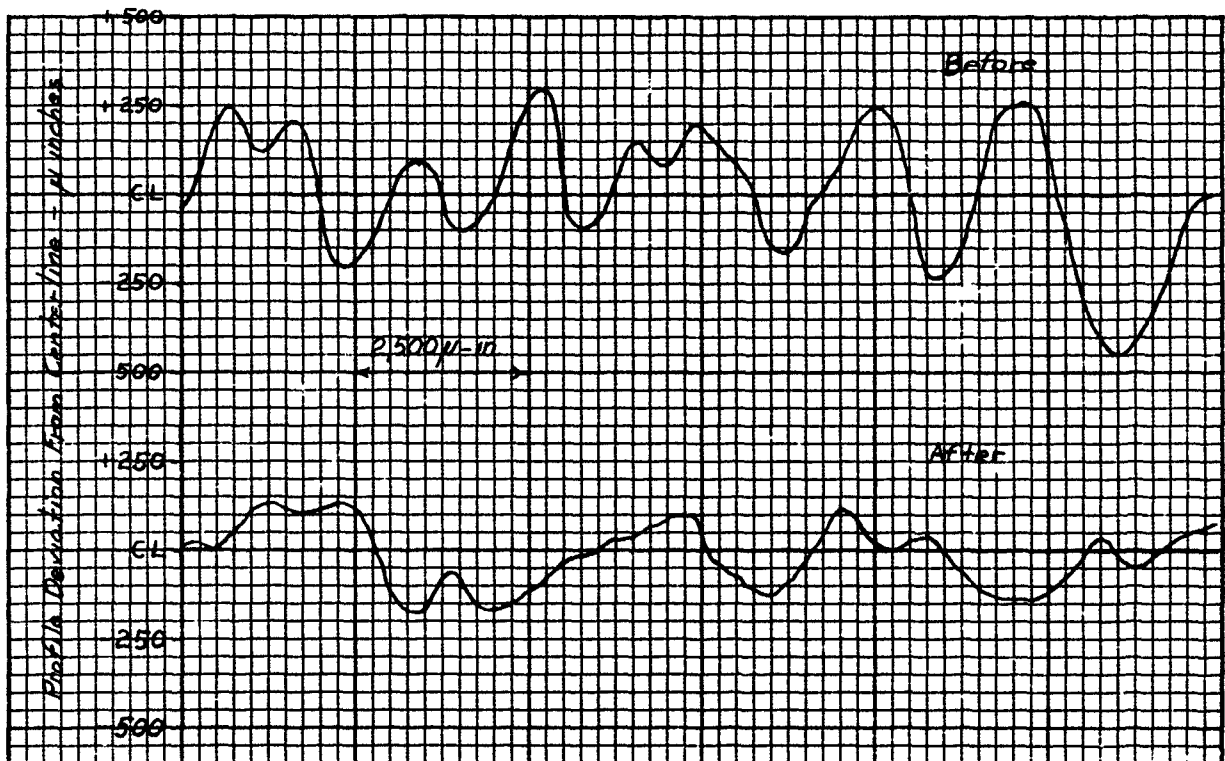
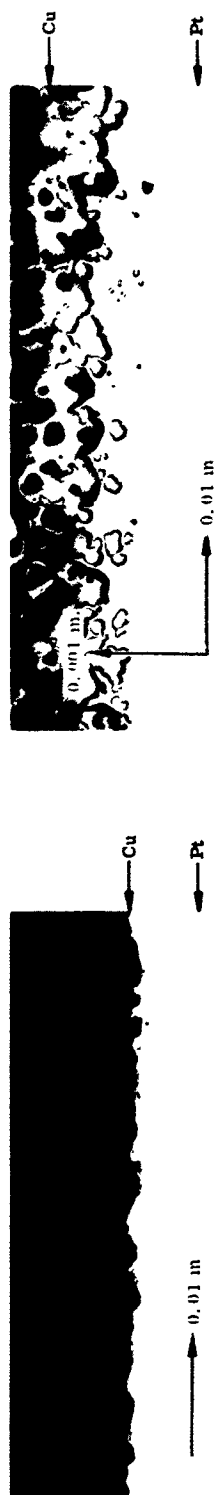


Figure 80 Typical Profile Traces of Platinum Sample 3 Before and After Emittance Tests

Table 21
ABSOLUTE EMITTANCE DATA FOR PLATINUM SAMPLE 3

Temperature (°K)	Test	$\epsilon(\theta_N, T)$	$\epsilon(\theta_N, \lambda, T)$							
			1 μ	1.5 μ	2 μ	4 μ	6 μ	8 μ	10 μ	12 μ
703	1, 3	0.105		0.300	0.214	0.121	0.101	0.100		
867	4, 6	0.122		0.269	0.203	0.133	0.118	0.107	0.097	
1034	11, 13	0.155	0.284	0.269	0.196	0.137	0.117	0.115	0.113	0.100
1202	18, 20	0.239	0.300	0.248	0.204	0.150	0.136	0.124	0.121	
1370	34, 36	0.279	0.283	0.224	0.189	0.149	0.135	0.129	0.127	0.114
1318	45, 47	0.296	0.280	0.206	0.186	0.159	0.138	0.126	0.118	0.115
1625	56	0.296								
1370	57	0.267								
1209	58	0.232								
989	59	0.129								



Taper Section After

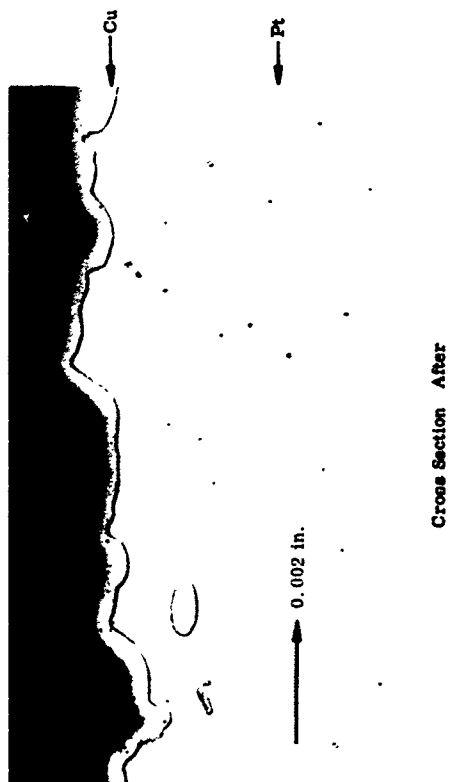
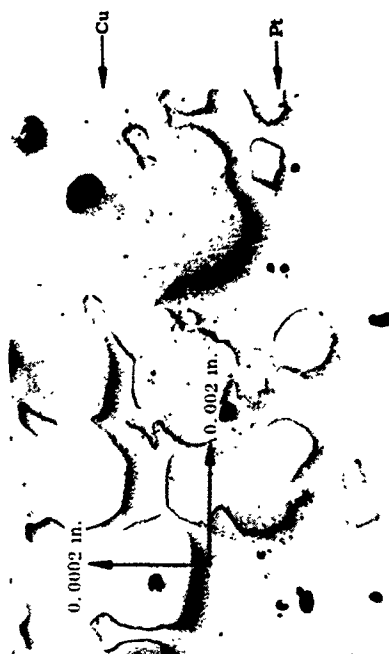


Figure 81 Cross and Taper Section Photomicrographs of Platinum Sample 3 After Emittance Tests

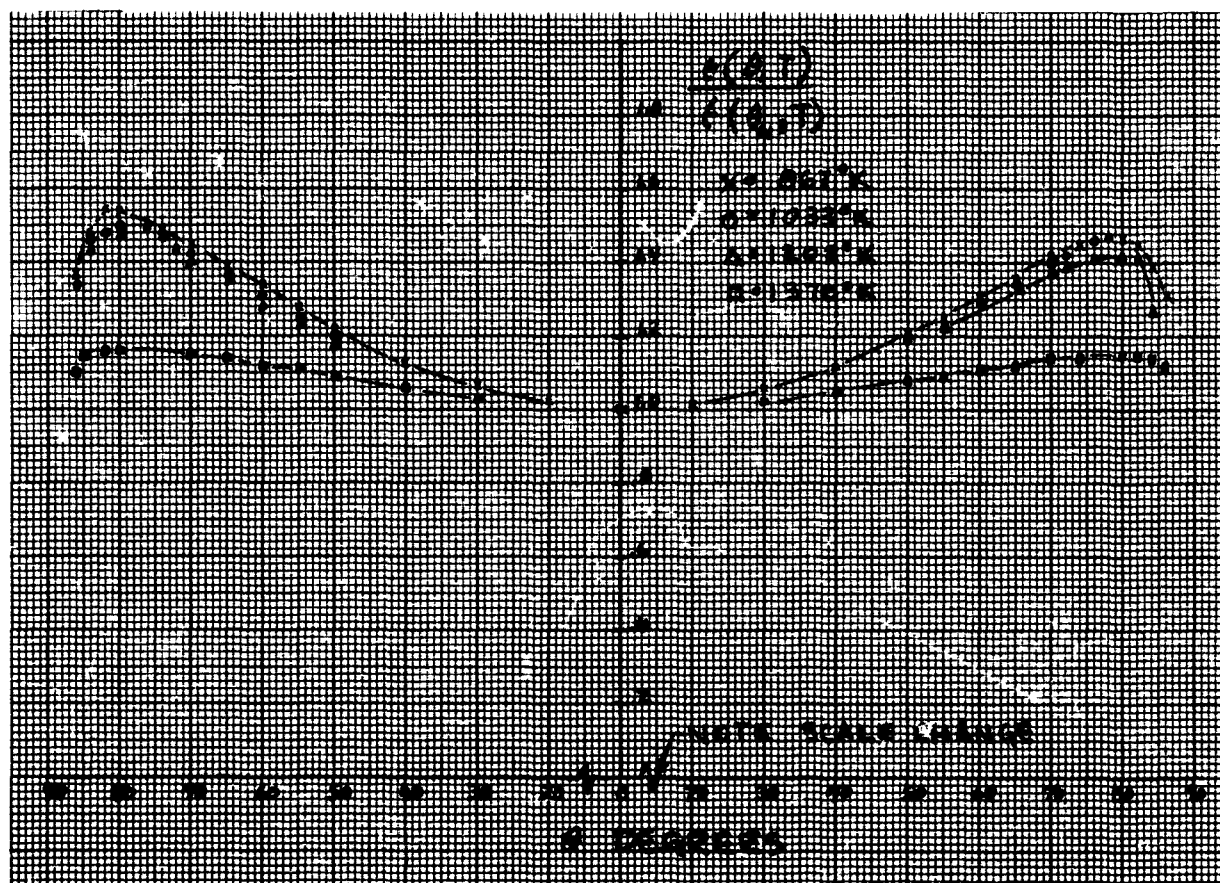


Figure 82 Relative Total Directional Emittance, Platinum Sample 3

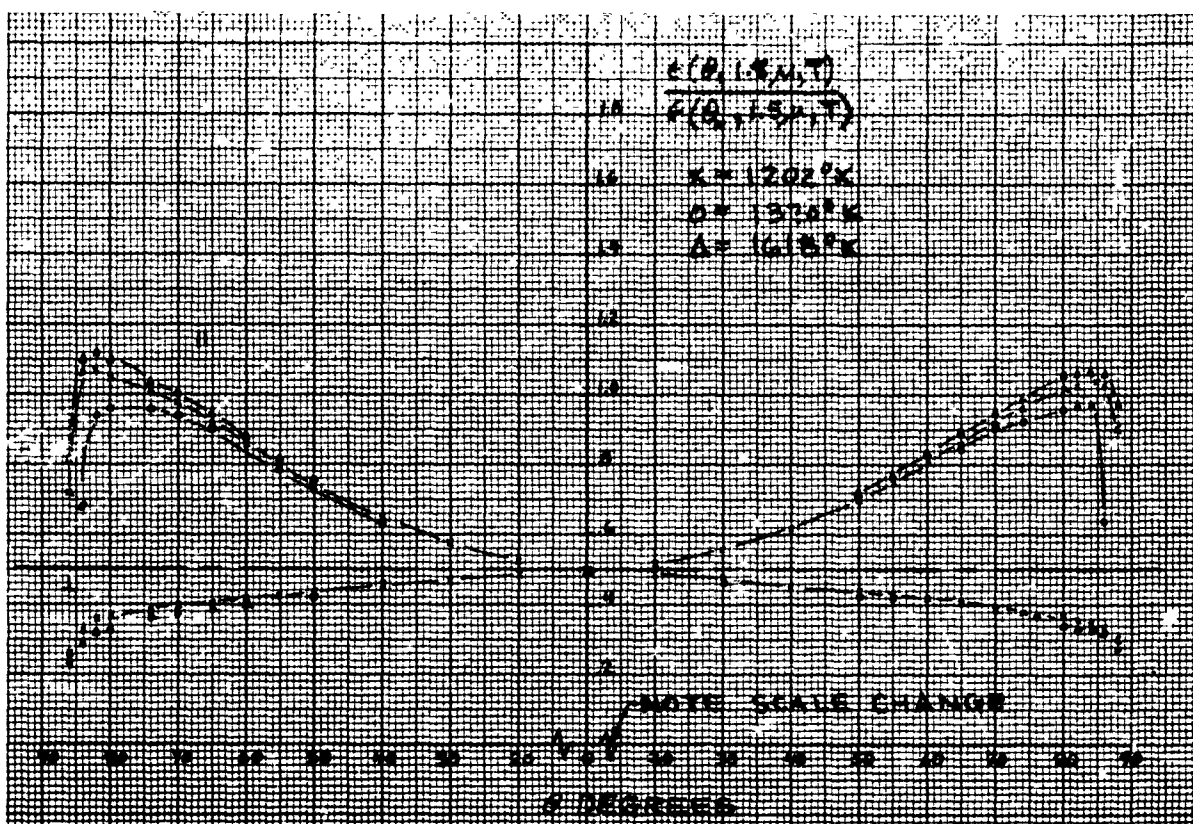


Figure 83 Relative Spectral Directional Emittance, $\lambda = 1.5 \mu$, Platinum Sample 3

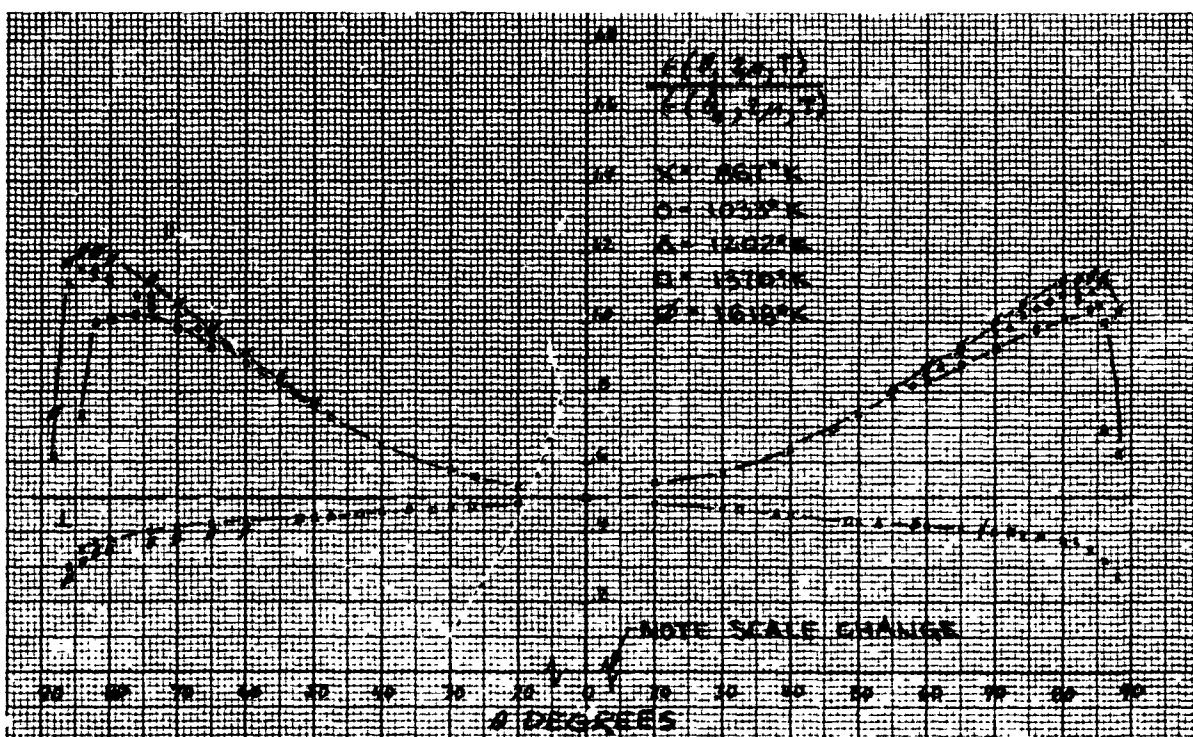


Figure 84 Relative Spectral Directional Emittance, $\lambda = 2 \mu$, Platinum Sample 3

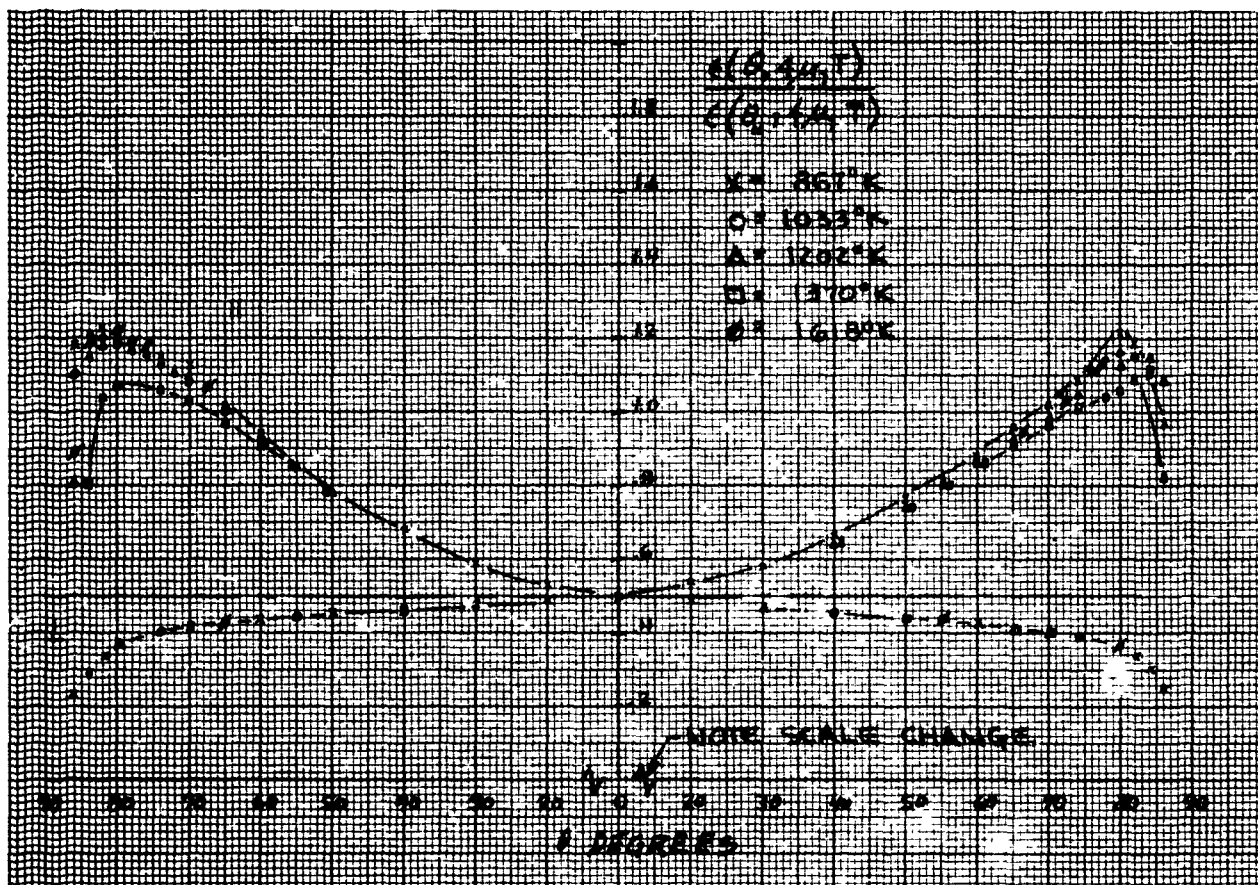


Figure 85 Relative Spectral Directional Emittance, $\lambda = 4 \mu$, Platinum Sample 3

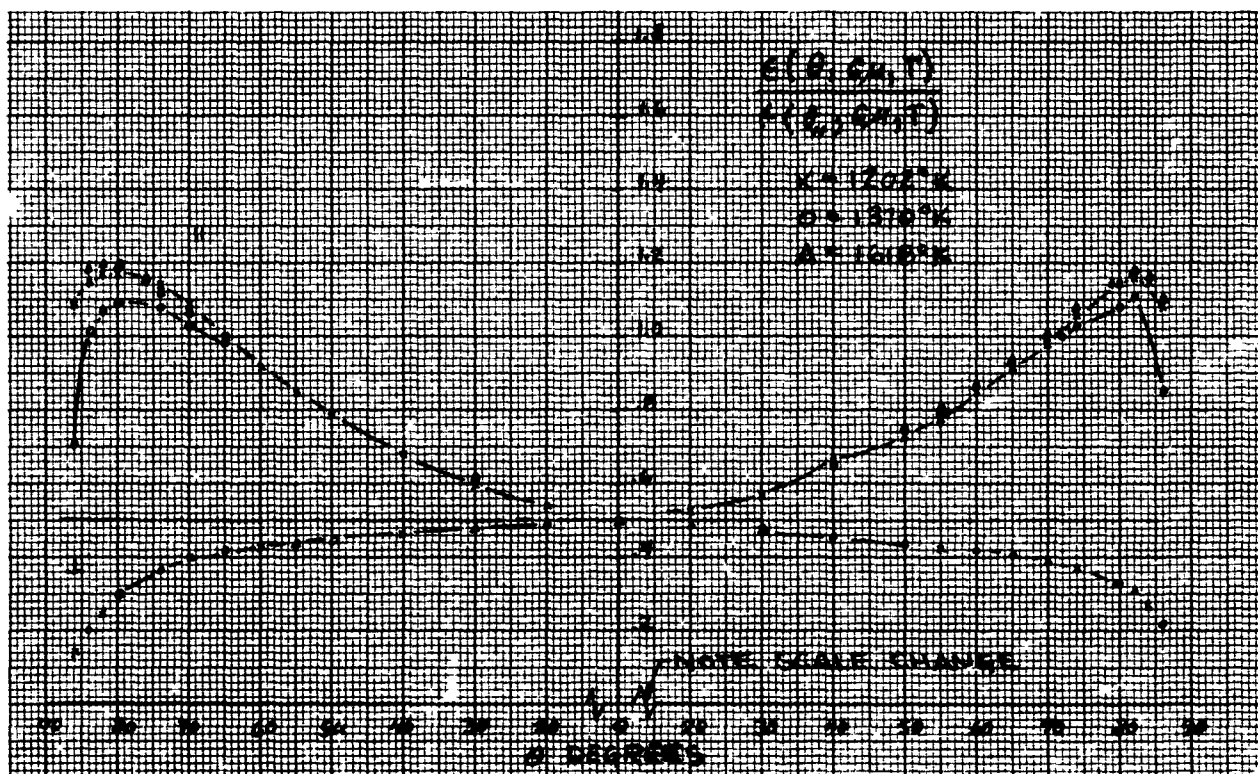


Figure 86 Relative Spectral Directional Emittance, $\lambda = 6 \mu$, Platinum Sample 3

10.11 PLATINUM SAMPLE 6

1. Sample -- Platinum Sample 6.
2. Preparation -- Glas-Shot, blasted, Size MS-XL, 40 psi at 6 in.
3. RMS roughness -- Before emittance tests, 91 μ in. ; after, 38 μ in.
4. Test procedure -- Sample was heated in vacuum to 1300°K for 1 hr before taking emittance data, after which absolute and relative directional emittance data were obtained at six temperatures from 697 to 1625°K and rechecked at two of the lower ones. Vacuum throughout the tests was maintained between 1 and 6×10^{-5} Torr. Total time at T_{\max} was 1.5 hr.
5. Emittance data -- Absolute total and spectral normal emittance values are shown in Table 22.

Relative total directional emittance data are shown in Figure 90.

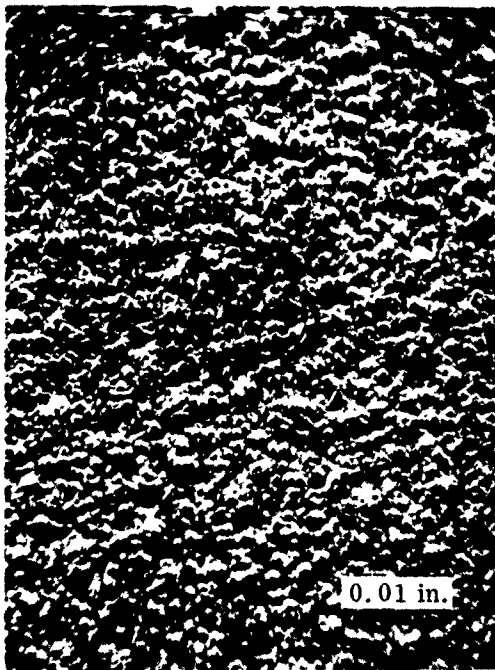
Relative spectral directional emittance data at 1.5, 2, 4, and 6 μ are shown in Figures 91 through 94.

6. Remarks -- As with platinum samples 1 and 3, the total and spectral normal emittance values appeared to drop as the sample temperature was increased above 1600°K. Rechecks of the total normal emittance values indicated only a slight drop in emittance at 1373 and 1193°K, however. Proficorder traces obtained after the emittance tests indicated a drop in rms roughness from 91 to 38 μ in. Most of this change is assumed to have occurred during the initial annealing treatment at 1300°K since no large change in the absolute emittance of the sample was observed.

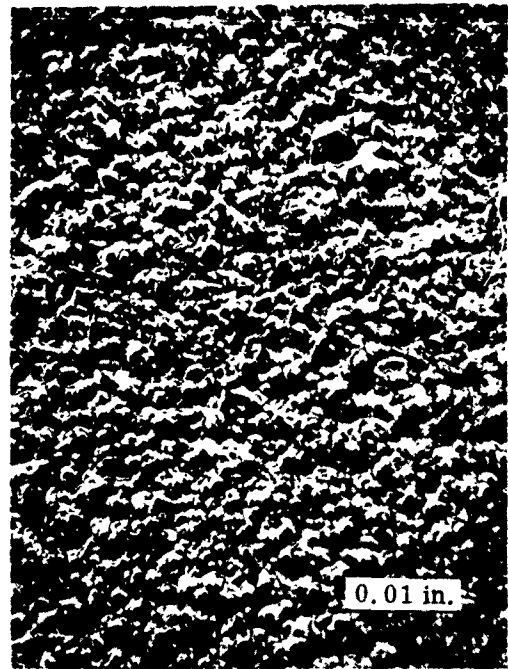
Before and after photomicrographs of the sample surface are shown in Figure 87. The nature of the surface profile before and after the emittance tests is shown in the section photomicrographs in Figure 89. The before test taper section mount was not suitable for examination. Because the section mounts were not etched, the grain structure of this sample was not observed; however, it is assumed to be similar to the before and after structure shown by the etched sections of platinum sample 1 (Figure 72).

The x-ray diffraction pattern from this sample indicated no detectable contamination of the surface. The relative intensities of the platinum "d" lines were observed to be intermediate to those observed from the patterns of platinum samples 1 and 3. This indicates that the preferred orientation of the as rolled surface had been modified by the Glas-Shot blast treatment, but not to the extent of complete randomization, as was indicated by the pattern from platinum sample 3. A spectrographic analysis of this sample was not obtained; however, it is assumed that the results would have been similar to those from the copper samples. Therefore, a slight amount of glass contamination is suspected. No evidence of embedded glass was detected in the microscopic examinations of the surface or in the metallographic sections.

Dissymmetry in the angular position of the relative directional emittance peaks in Figures 90 through 94 indicates the sample was misaligned approximately 2 deg.



Before



After

Dark Field Illumination

Figure 87 Surface Photomicrographs of Platinum Sample 6 Before and After Emittance Tests

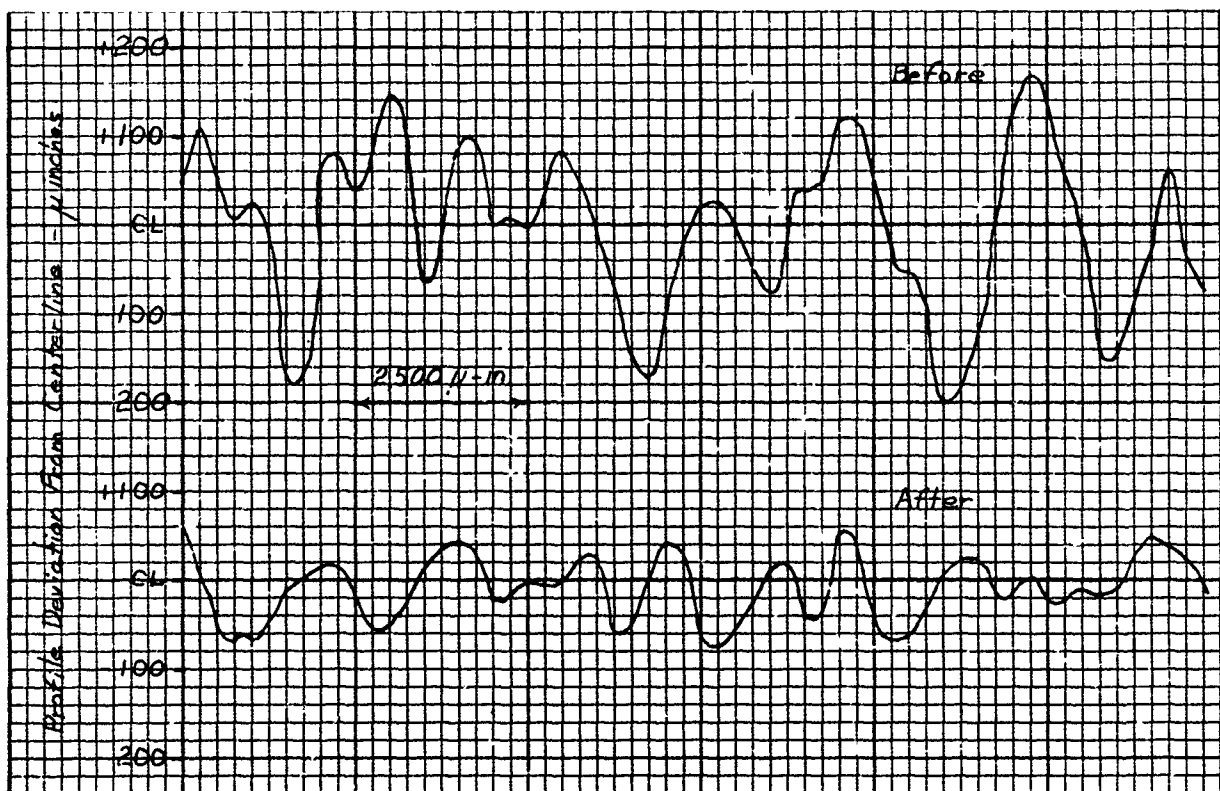
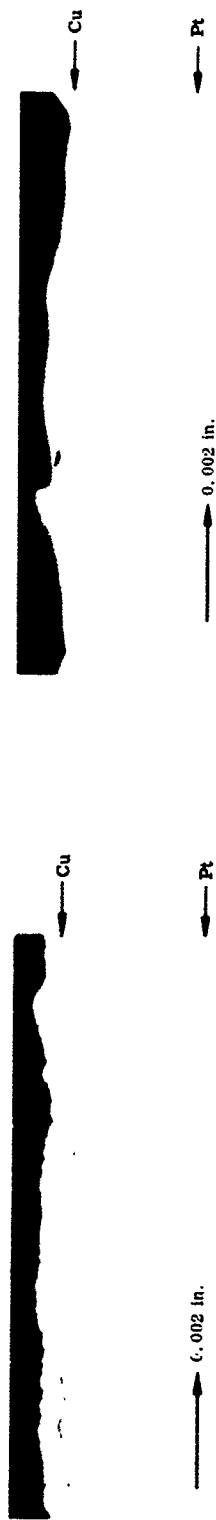


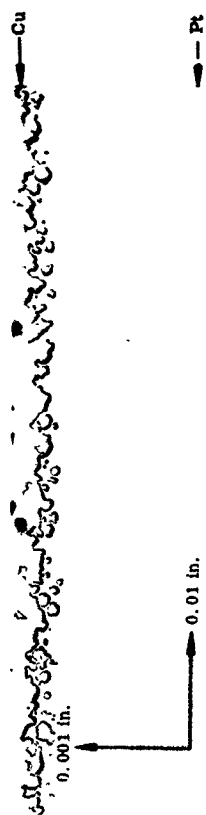
Figure 88 Typical Profile Traces of Platinum Sample 6 Before and After Emittance Tests

Table 22
ABSOLUTE EMITTANCE DATA FOR PLATINUM SAMPLE 6

Temperature (°K)	Test	$\epsilon(\theta_N, T)$	$\epsilon(\theta_N, \lambda, T)$							
			1 μ	1.5 μ	2 μ	4 μ	6 μ	8 μ	10 μ	12 μ
697	2, 4	0.090		0.275	0.197	0.107	0.089	0.081	0.071	
863	5, 7	0.114		0.264	0.190	0.118	0.099	0.089	0.084	
1025	12, 14	0.135		0.250	0.198	0.132	0.107	0.094	0.093	0.084
1194	19, 21	0.232	0.334	0.252	0.201	0.145	0.115	0.107	0.091	0.091
1369	30, 32	0.271	0.288	0.233	0.197	0.149	0.129	0.111	0.106	0.105
1618	41, 43	0.283	0.274	0.201	0.175	0.149	0.133	0.117	0.108	0.107
1625	51	0.278								
1373	52	0.253								
1193	53	0.216								



Cross Section Before



Cross Section After



Taper Section Before

Taper Section After

Figure 89 Cross and Taper Section Photomicrographs of Platinum Sample 6 Before and After Emittance Tests

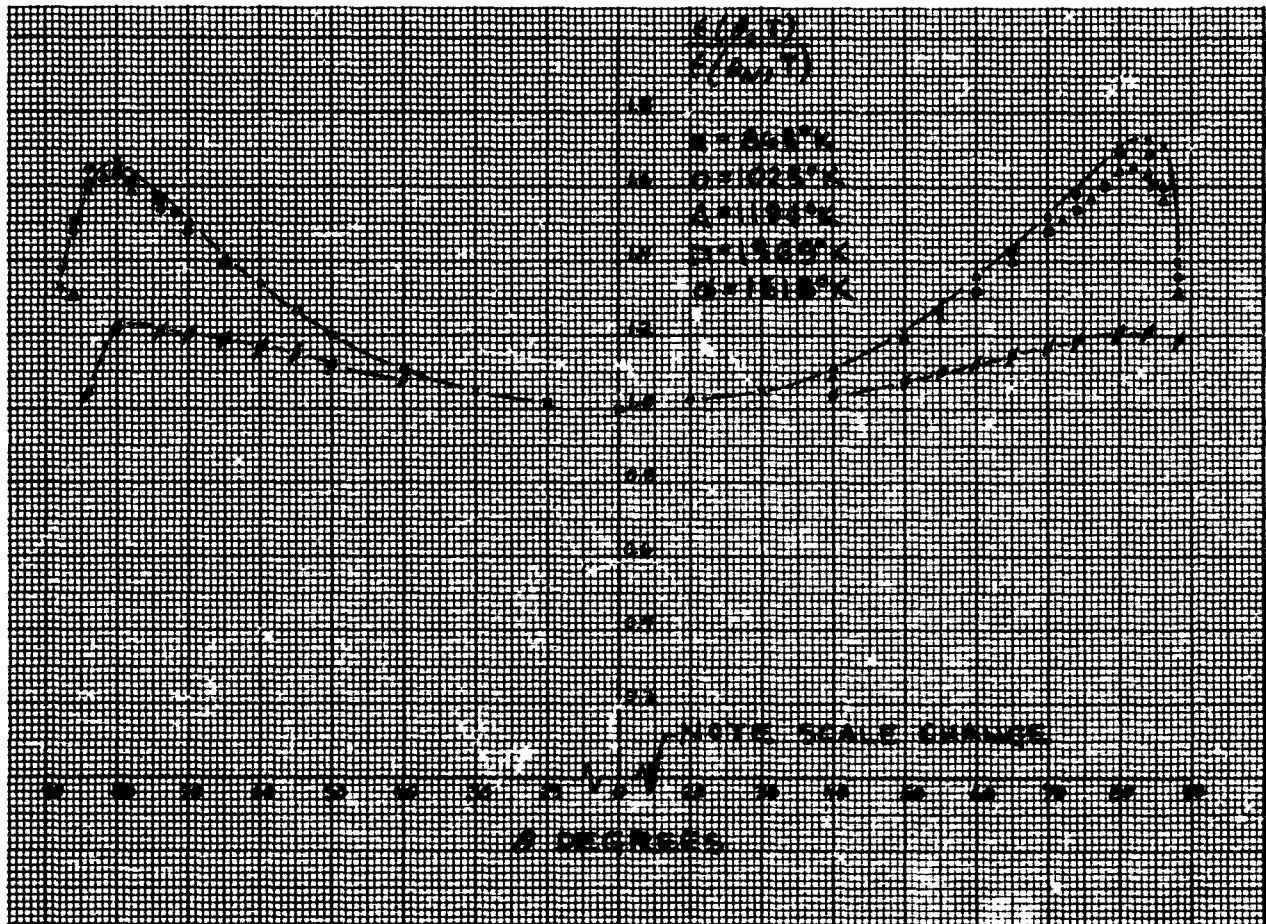


Figure 90 Relative Total Directional Emittance, Platinum Sample 6

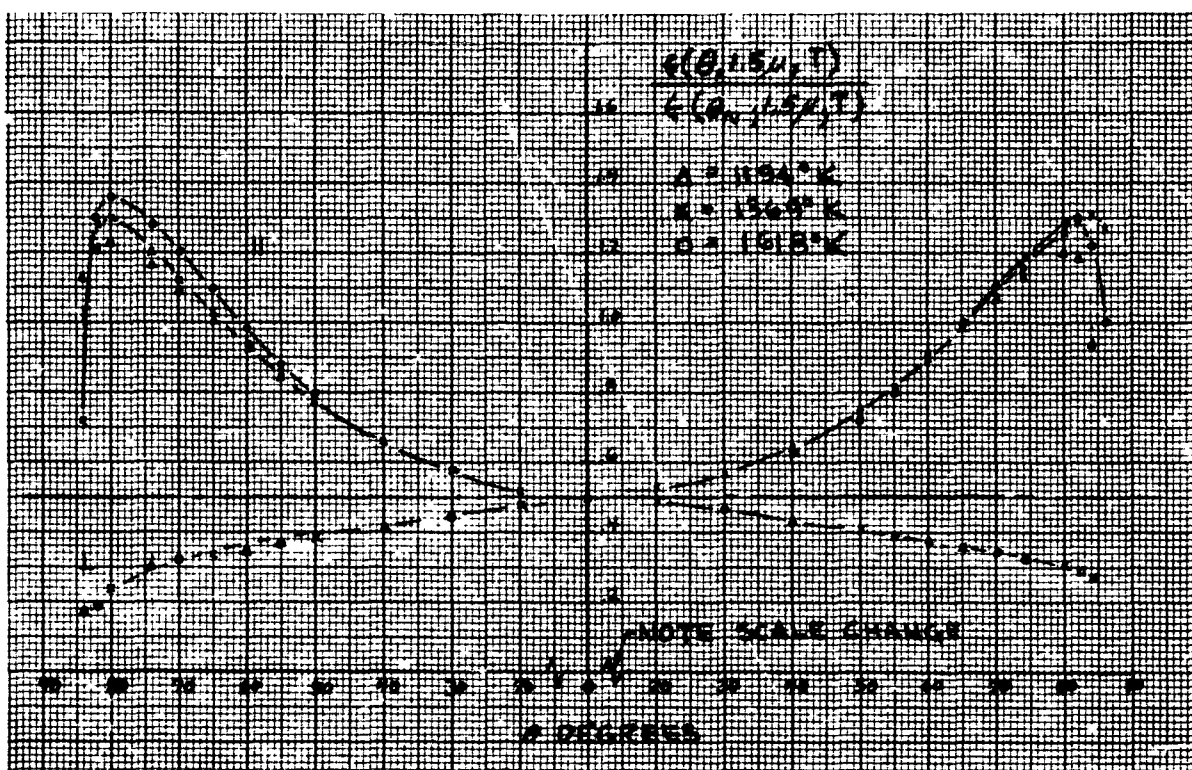


Figure 91 Relative Spectral Directional Emittance, $\lambda = 1.5 \mu$, Platinum Sample 6

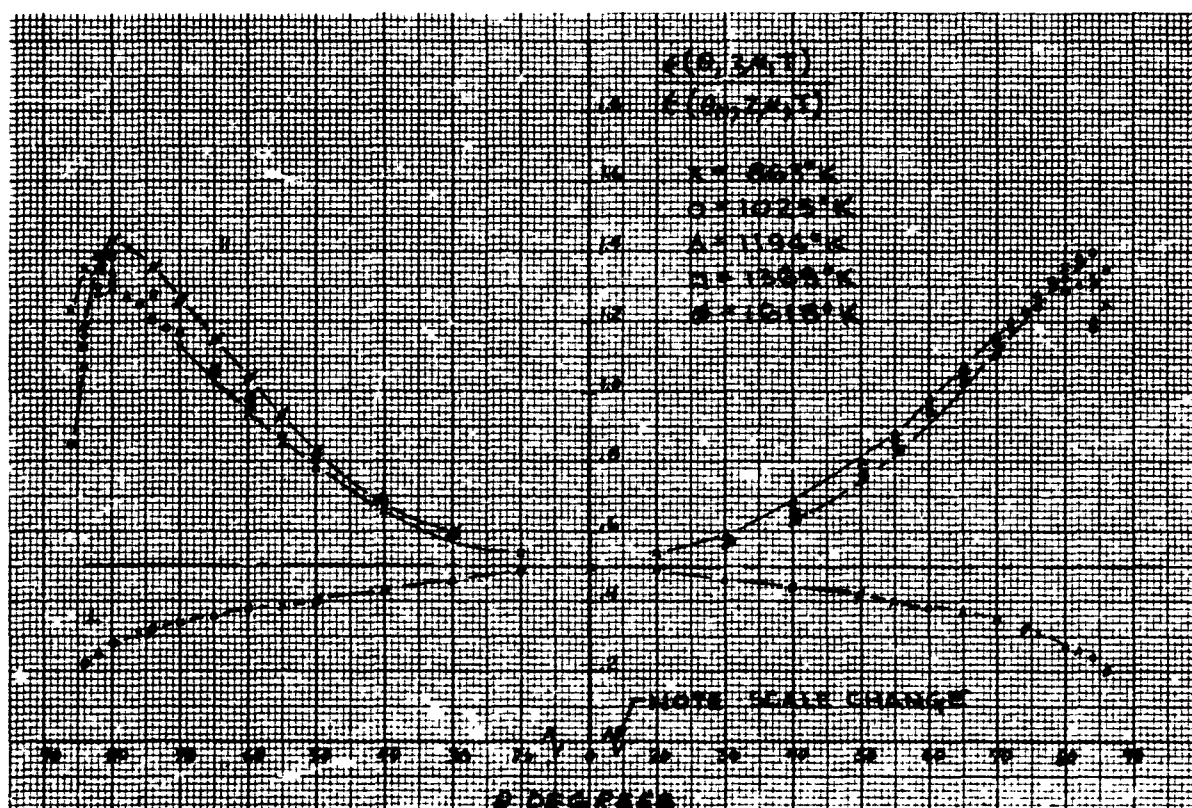


Figure 92 Relative Spectral Directional Emittance, $\lambda = 2 \mu$, Platinum Sample 6

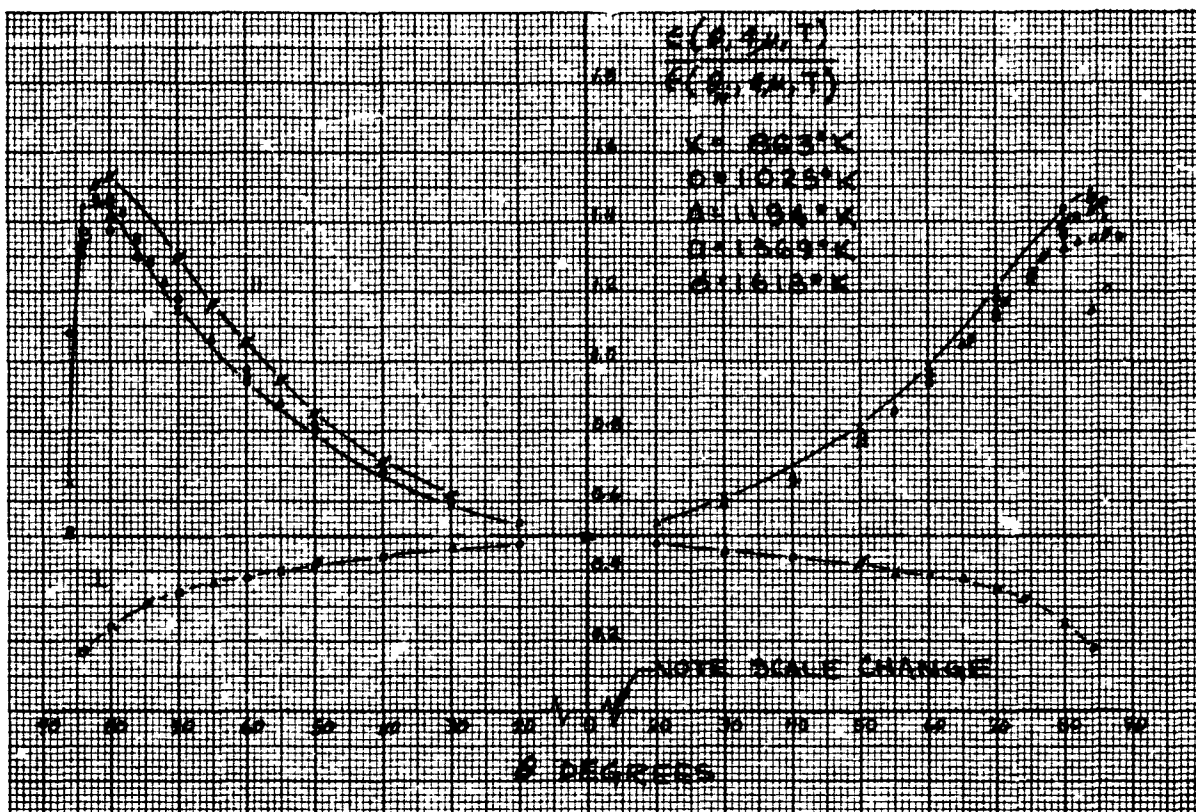


Figure 93 Relative Spectral Directional Emittance, $\lambda = 4 \mu$, Platinum Sample 6

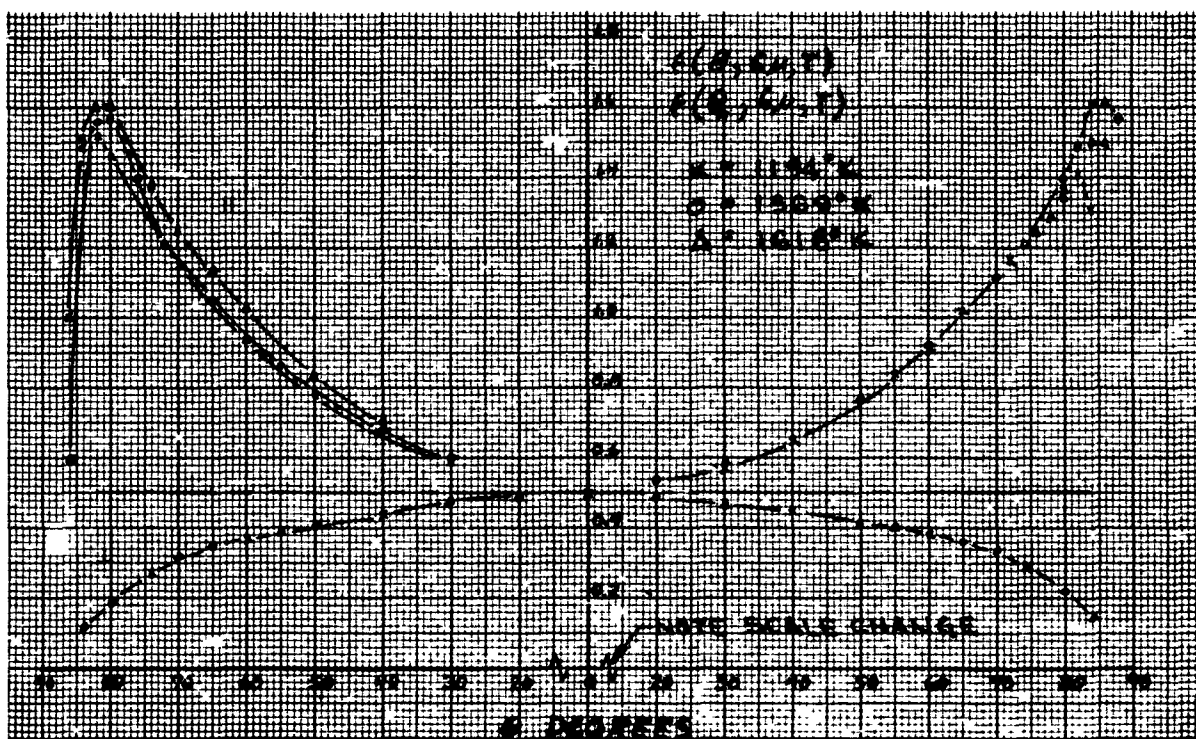


Figure 94 Relative Spectral Directional Emittance, $\lambda = 6 \mu$, Platinum Sample 6

Section 11

REFERENCES

1. A. G. Worthing, "Temperature Radiation Emissivities and Emittances," in Temperature, Its Measurement and Control in Science and Industry, American Institute of Physics, Reinhold, New York, 1941
2. Wright Air Development Center, Standardization of Thermal Emittance Measurements, by W. N. Harrison et al., WADC Technical Report 59-510, Wright-Patterson AFB, Ohio, Aug 1959
3. Born and Wolf, Principles of Optics, New York, Pergamon Press, 1959
4. W. S. Martin, "Optical Constants and Spectral Emissivities at High Temperatures," in Radiative Transfer From Solid Materials, edited by H. H. Blau, Jr., and H. Fischer, Macmillan Co., New York, 1962
5. S. Roberts, "Optical Properties of Nickel and Tungsten and Their Interpretations According to Drude's Formula," Phys. Rev., Vol. 114, No. 1, Apr 1959
6. H. Davies, "The Reflection of Electromagnetic Waves From a Rough Surface," Proc. Inst. Elec. Engr., Vol. 101, 1954, pp. 209-214
7. P. Beckmann and A. Spizzichino, "The Scattering of Electromagnetic Waves From Rough Surfaces," Macmillan Co., New York, 1963
8. S. O. Rice, "Reflection of Electromagnetic Waves From Slightly Rough Surfaces," Pure Appl. Math., Vol. 4, 1951, pp. 351-378
9. H. E. Bennett and J. O. Porteus, "Relation Between Surface Roughness and Specular Reflectance at Normal Incidence," J. Opt. Soc. Am., Vol. 51, 1961, pp. 123-129
10. H. E. Bennett, "Specular Reflectance of Aluminized Ground Glass and the Height Distribution of Surface Irregularities," J. Opt. Soc. Am., Vol. 53, 1963, pp. 1389-1394
11. J. O. Porteus, "Relation Between the Height Distribution of a Rough Surface and the Reflectance at Normal Incidence," J. Opt. Soc. Am., Vol. 53, 1963, pp. 1394-1402
12. R. C. Birkebak et al., "Effect of Surface Roughness on the Total Hemispherical and Specular Reflectance of Metallic Surfaces," J. Heat Transfer, Trans. ASME, Series C, Vol. 86, 1964, pp. 193-199
13. R. W. Ditchburn, Light, Interscience Publishers, New York, 1953, pp. 448-452
14. R. C. Birkebak and E. R. G. Eckert, "Effects of Roughness of Metal Surfaces on Angular Distribution of Monochromatic Reflected Energy," Trans. ASME, Paper 64-HT-26, May 1964

15. Yu. P. Lysanov, "On the Problem of Scattering of Electromagnetic Waves From a Rough Surface," Dokl. Akad. Nauk SSSR, Vol. 87, 1952, pp. 719-722 (in Russian)
16. V. A. Fok, "The Field of a Plane Wave Near the Surface of a Reflecting Body," Izv. Akad. Nauk SSSR, Ser. Fiz., Vol. 10, 1946, pp. 171-186 (in Russian)
17. American Metal Climax, Inc., "OFHC Brand Copper - Technical Survey," 1963, p. 3
18. S. Roberts, "Optical Properties of Copper," Phys. Rev., Vol. 118, No. 6, Jun 1960
19. J. J. Bikerman, "Surface Roughness," Surface Chemistry, Academic Press, 1958, pp. 181-197
20. B. Piper and W. P. Callis, "Surface-Finish Measurement on Non-Ferrous Materials," American Machinist, Special Report 476, 10 Aug 1959, pp. 105-120
21. J. F. Hagen and E. Lindberg, General Motors Corporation, Mechanical Dev. Dept., Res. Lab. Div., "Specification and Measurement of Surface Finish," Dec 1953
22. S. Tolansky, Surface Microtopography, Interscience Publishers, Inc., New York, 1960
23. A. G. Strang and F. Ogburn, "Measurement of Surface Roughness of Electrodeposited and Electropolished Surfaces by Means of the Microinterferometer," NBS Handbook 77, Vol. III, Precision Measurement and Calibration - Optics, Meteorology, and Radiation, pp. 324/1-335/12, 1 Feb 1961
24. D. B. Spangenberg, A. G. Strang, and J. L. Chamberlain, "Surface Texture Measurements of Metal Surfaces," Part B of "Effect of Surface Texture on Diffuse Spectral Reflectance," Paper 9 presented at Symposium on Thermal Radiation of Solids, San Francisco, 4-6 Mar 1964
25. F. A. Mohrnhelm and A. E. R. Westman, "Taper Sectioning of Basic Metal Surfaces and Electrodeposits," Plating, Sep 1954, pp. 1043-1047
26. A. J. Moore, "A Refined Metallographic Technique for the Examination of Surface Contours and Surface Structure of Metals (Taper Sectioning)," Metallurgia, Vol. 38, No. 22, Jun 1948, pp. 71-84
27. R. Newman and R. S. Halford, "An Efficient, Convenient Polarizer for Infrared Radiation," Rev. Sci. Inst., Vol. 19, No. 4, Apr 1948, pp. 270-271
28. I. Simon, "Spectroscopy in Infrared by Reflection and Its Use for Highly Absorbing Substances," J. Opt. Soc. Am., Vol. 41, No. 5, May 1951
29. H. H. Blau, Jr., et al., "Infrared Spectral Emittance Properties of Solid Materials," AFCRL-TR-60-416, Oct 1960

30. "Standard X-Ray Diffraction Powder Patterns," NBS Circular 539, Vol. 1, p. 31, 15 Jun 1953
31. Eaton and Conn, Handbook of Chemistry and Physics, 38th ed., Chemical Rubber Publishing Co., 1956

Appendix

REFLECTANCE OF A RANDOM ROUGH SURFACE OF FINITE CONDUCTIVITY FROM EXACT THEORY

C. L. Tien

A.1 INTRODUCTION

Existing theoretical treatments on the reflectance of a rough surface (Reference 7) can be classified as either approximate (Kirchhoff diffraction theory) or exact (the Rayleigh method). This appendix presents solutions available from the exact method as previously discussed by Rice (Reference 8). In its general form, the exact solution includes the effects of finite electrical conductivity, surface shadowing, and multiple reflections on the reflectance of a randomly roughened surface. However, the calculation is so cumbersome, because of the series solution obtained, that only the second-order result, which applies to a slightly rough surface, has been reported. This result is of interest only to the extent that it agrees precisely with the approximate diffraction theory solution (Reference 6). Therefore, the second-order result fails to include those real surface effects which cause significant changes in the spectral and spatial distribution of reflected energy. It is apparent that higher order solutions of the Rice theory should be sought in order to reveal basic information on the effects of shadowing, multiple reflections, and finite surface conductivity.

The purpose of this appendix is to present the exact approach in such a manner that the basic formulation is properly outlined with an indication of the difficulties involved in calculation of the third-order result. In contrast to the original formulation of Rice, this solution will be wholly on the case of finite surface conductivity, which is necessary for direct computation of the emittance or absorptance of a real surface. The second-order solution is described in detail and is used to obtain an approximate expression for the normal specular spectral reflectance of a slightly rough ($\sigma_m/\lambda \ll 1$) surface. Although the solution is approximate, it represents a result obtained from exact theory which has not been previously reported. Its agreement with diffraction theory results indicates that for slightly rough surfaces the shadowing and multiple reflection effects are negligible. More elaborate calculations involving higher order terms are required in order to study the effects of these surface characteristics.

A.2 DESCRIPTION OF A RANDOM ROUGH SURFACE

The three-dimensional random surface is represented by the equation $z = f(x, y)$, where z is the height measured from the mean plane surface placed on the x - y plane. The random behavior is characterized by expanding the function $f(x, y)$ in double Fourier series with random Fourier coefficients,

$$z \equiv f(x, y) = \sum_{m, n = -\infty}^{\infty} P(m, n) \exp \{-ia(mx + ny)\} \quad (\text{A. 1})$$

where $a \equiv (2\pi/L)$ and L is the period (or wavelength) of the surface and is assumed to be arbitrarily large. The random coefficients $P(m, n)$ are, in general, complex quantities and are subject to the condition

$$P(-m, -n) = P^*(m, n) \quad (A.2)$$

in order to make $f(x, y)$ real, where the asterisk denotes the complex conjugate. It is further assumed that (1) the four random variables formed by the real and imaginary parts of $P(m, n)$ and $P(-m, -n)$ are independent, i. e.,

$$\langle P(m, n)P(u, v) \rangle = 0, \quad (u, v) \neq (-m, -n) \quad (A.3)$$

where $\langle \rangle$ denotes the ensemble average over the universes of the real and imaginary parts of the $P(m, n)$'s; (2) that they are distributed normally about zero, i. e.

$$\langle P(m, n) \rangle = \langle P(-m, -n) \rangle = 0; \quad (A.4)$$

and (3) that all have the same mean square value so that

$$\langle P(m, n)P^*(m, n) \rangle = \langle P(m, n)P(-m, -n) \rangle \equiv \pi^2 W(p, q)/L^2 \quad (A.5)$$

where $W(p, q) \equiv W(|p|, |q|)$, $p \equiv am$, and $q \equiv an$, with p and q in dimensions of radians per length. The introduction of (π^2/L^2) in the definition of $W(p, q)$ and the physical meaning of $W(p, q)$, which will be called the roughness spectrum for the random surface, will become clear later.

The roughness of the surface is often characterized by the roughness parameter σ_m , which is defined as the root-mean-square value of the random height $f(x, y)$. From Equation A. 1 it follows that

$$\sigma_m^2 \equiv \langle f^2(x, y) \rangle = \sum_{m, n, u, v=-\infty}^{\infty} \langle P(m, n)P(u, v) \rangle \exp\{-iax(m+u) - iay(n+v)\}$$

In view of Equation A. 3,

$$\langle f^2(x, y) \rangle = \sum_{m, n} \langle P(m, n)P(-m, -n) \rangle$$

By letting L approach infinity, the above double summation can be replaced by a double integral, and from Equation A. 5

$$\langle f^2(x, y) \rangle = \iint_{-\infty}^{\infty} \frac{\pi^2 W(p, q)}{L^2} dm dn = \iint_{-\infty}^{\infty} \frac{1}{4} W(p, q) dp dq$$

or

$$\langle f^2(x, y) \rangle = \iint_0^{\infty} W(p, q) dp dq \quad (A.6)$$

The above equations clearly indicate that $(1/4)W(p,q)dpdq$ represents the contribution to the mean-square roughness, σ_m^2 or $\langle f^2(x,y) \rangle$, of those components in Equation A.1 between p and $p+dp$ (for the x-direction) and q and $q+dq$ (for the y-direction).

If \vec{N} denotes the unit vector normal to the surface, the components of \vec{N} are

$$N_x = -f_x N_z, \quad N_y = -f_y N_z, \quad N_z = \left(1 + f_x^2 + f_y^2\right)^{-1/2} \quad (\text{A. 7})$$

For slightly rough surfaces, the slopes f_x and f_y are all small and the above relations in Equation A.7 can be expanded in series,

$$\begin{aligned} N_x &= -f_x + \frac{1}{2}f_x^3 + \frac{1}{2}f_x f_y^2 + O(f^4) \\ N_y &= -f_y + \frac{1}{2}f_y f_x^2 + \frac{1}{2}f_y^3 + O(f^4) \\ N_z &= 1 - \frac{1}{2}f_x^2 - \frac{1}{2}f_y^2 + O(f^4) \end{aligned} \quad (\text{A. 8})$$

where $O(f^4)$ denotes the fourth and the higher orders of smallness. Note that the expressions in Equation A.8 represent the third-order approximation as compared with the second-order one:

$$N_x = -f_x + O(f^3), \quad N_y = -f_y + O(f^3), \quad N_z = 1 + O(f^3) \quad (\text{A. 9})$$

These approximations (Equations A.8 or A.9) will be used later to simplify the boundary conditions on the rough surface.

A.3 BASIC FORMULATION

Here, in this section, basic consideration will be given to the reflection of electromagnetic waves from a random wavy interface between two media. The upper medium is non-conducting, while the lower medium is of a finite conductivity. The magnetic permeability of these media will be assumed to be the same. The basic mathematical formulation, which is based on the Maxwell equations and the boundary conditions under the assumption of a slightly random wavy interface, will be described in this section; detailed calculation of the second-order results will be discussed later.

For propagation of electromagnetic waves in an isotropic, non-conducting medium (i.e., the upper medium), the electric intensity \vec{E} must obey the wave equation

$$\nabla^2 \vec{E} = -\frac{1}{v_0^2} \frac{\partial^2 \vec{E}}{\partial t^2}, \quad \nabla \cdot \vec{E} = 0 \quad (\text{A. 10})$$

where the wave velocity v_0 equals $(c_0/n_0) = (c_0/\sqrt{\mu\epsilon_0})$; c_0 is the speed of light in vacuum; n_0 is the refractive index; μ is the magnetic permeability; and ϵ_0 is the dielectric constant. For a horizontally polarized wave, the solution is expressed as

$$E_x = E_z = 0, \quad E_y = \exp\{i\omega t - i\beta(\alpha x - \gamma z)\} \quad (\text{A. 11})$$

where ω is the angular frequency; $\beta \equiv (2\pi/\lambda) = (\mu\epsilon_0)^{1/2}(\omega/c_0)$; λ is the wavelength; $\omega\lambda \equiv 2\pi v_0$; $\alpha \equiv \sin \theta$; $\gamma \equiv \cos \theta$; and θ is the angle of incidence.

For propagation in an absorbing medium (i. e., of finite conductivity), it is well known that the wave expression is the same as in the case of a non-conducting medium except that the material constant $n_0 = (\mu\epsilon_0)^{1/2}$ should be replaced by the complex refractive index

$$\bar{n} = \left[\mu\epsilon \left(1 + \frac{g}{i\omega\epsilon} \right) \right]^{1/2} \quad (\text{A. 12})$$

where g is the electric conductivity. The corresponding wave expression is

$$E_x = E_z = 0, \quad E_y = \exp\{i\omega t - \sigma'\alpha x + \tau\gamma'z\} \quad (\text{A. 13})$$

where $\sigma' = i\beta$, $\tau = (i\beta\bar{n}/n_0)$ and the absorption takes place in the z -direction.

For reflection of electromagnetic waves from a smooth interface between a non-conducting and a finite-conducting medium, the electric intensity for horizontal polarization would be

$$E_y^+ = E^+ \equiv \exp\{-\sigma'\alpha x\} \{ \exp(\sigma'\gamma z) + R \exp(-\sigma'\gamma z) \} \quad (z > 0) \quad (\text{A. 14a})$$

$$E_y^- = E^- \equiv T \exp\{-\sigma'\alpha x + \tau\gamma'z\} \quad (z < 0) \quad (\text{A. 14b})$$

where the time factor $\exp\{i\omega t\}$ is omitted for the convenience of writing

$$\gamma' \equiv (1 - \alpha'^2)^{1/2} \quad \tau\alpha' \equiv \sigma'\alpha \quad (\text{A. 15})$$

and

$$R \equiv \frac{\sigma'\gamma - \tau\gamma'}{\sigma'\gamma + \tau\gamma'}, \quad T \equiv 1 + R = \frac{2}{\sigma'\gamma + \tau\gamma'} \quad (\text{A. 16})$$

In Equation A. 14a, the intensity consists of the incident and reflected component, while Equation A. 14b represents the transmitted component.

Because of the random wavy interface, which results in a change of boundary conditions, the electric intensity is assumed to be in series form:

$$\begin{cases} E_x^+ = \sum A_{mn} E(m, n, z) \\ E_x^- = \sum G_{mn} F(m, n, z) \\ E_y^+ = E^+ + \sum B_{mn} E(m, n, z) \\ E_y^- = E^- + \sum H_{mn} F(m, n, z) \\ E_z^+ = \sum C_{mn} E(m, n, z) \\ E_z^- = \sum I_{mn} F(m, n, z) \end{cases} \quad (\text{A. 17})$$

where superscripts + and - refer to $z > f$ and $z < f$, respectively, and

$$\begin{aligned} E(m, n, z) &\equiv \exp \{-ia(mx + ny) - ib(m, n)z\} \\ F(m, n, z) &\equiv \exp \{-ia(mx + ny) + ic(m, n)z\} \\ ib(m, n) &\equiv [(\sigma')^2 + a^2(m^2 + n^2)]^{1/2} \\ ic(m, n) &\equiv [\tau^2 + a^2(m^2 + n^2)]^{1/2} \end{aligned} \quad (\text{A. 18})$$

The functions $E(m, n, z)$ and $F(m, n, z)$ which satisfy the wave equation, Equation A. 10, are due to the corresponding harmonic term in the expression of random surface, Equation A. 1. Expressions in Equation A. 17 thus represent the solution of the wave equation with the coefficients such as A_{mn} 's to be determined by boundary conditions. It is obvious that the coefficients are of the order $O(f)$ and higher.

The boundary conditions are established from the well-known fact that the tangential component of electric and magnetic vectors must be continuous at the interface. The normal component of electric intensity is $\bar{N}(\bar{E} \cdot \bar{N})$ where \bar{N} is the unit vector normal to the surface. The remaining portion of \bar{E} , the tangential component, is $\bar{E} - \bar{N}(\bar{E} \cdot \bar{N})$. The continuity of tangential component of electric intensity requires that

$$\begin{aligned} E_x^+ - N_x(N_x E_x^+ + N_y E_y^+ + N_z E_z^+) &= E_x^- - N_x(N_x E_x^- + N_y E_y^- + N_z E_z^-) \\ E_y^+ - N_y(N_x E_x^+ + N_y E_y^+ + N_z E_z^+) &= E_y^- - N_y(N_x E_x^- + N_y E_y^- + N_z E_z^-) \end{aligned} \quad (\text{A. 19})$$

The continuity of the z-component is satisfied also if the above two conditions are satisfied. This may be realized by multiplying the first by N_x and the second by N_y and

then adding. Noting that E_x and E_z are $O(f)$ but E_y is $O(1)$, Equation A. 19 under the third-order approximation of Equation A. 8 becomes

$$\begin{aligned} E_x^+ - f_x^2 E_x^+ - f_x f_y E_y^+ + f_x E_z^+ &= E_x^- - f_x^2 E_x^- - f_x f_y E_y^- + f_x E_z^- \\ E_y^+ - f_x f_y E_x^+ - f_y^2 E_y^+ + f_y E_z^+ &= E_y^- - f_x f_y E_x^- - f_y^2 E_y^- + f_y E_z^- \end{aligned} \quad (\text{A. 20})$$

For the second-order approximation of Equation A. 9, it reduces to

$$\begin{aligned} E_x^+ - f_x f_y E_y^+ + f_x E_z^+ &= E_x^- - f_x f_y E_y^- + f_x E_z^- \\ (1 - f_y^2) E_y^+ + f_y E_z^+ &= (1 - f_y^2) E_y^- + f_y E_z^- \end{aligned} \quad (\text{A. 21})$$

as indicated in the Rice paper.

The boundary conditions on the magnetic intensity \vec{H} can be directly obtained by substituting \vec{H} for \vec{E} in Equation A. 19. Since, according to one of the Maxwell equations, $\vec{H} = -(c_0/\mu) \nabla \times \vec{E}$, there follows on each side of two equations corresponding to those in Equation A. 19,

$$\begin{aligned} \left(\frac{\partial E_z}{\partial y} \right) - \left(\frac{\partial E_y}{\partial z} \right) - N_x^2 \left[\left(\frac{\partial E_z}{\partial y} \right) - \left(\frac{\partial E_y}{\partial z} \right) \right] - N_x N_y \left[\left(\frac{\partial E_x}{\partial z} \right) - \left(\frac{\partial E_z}{\partial x} \right) \right] - N_x N_z \left[\left(\frac{\partial E_y}{\partial x} \right) - \left(\frac{\partial E_x}{\partial y} \right) \right] \\ \left(\frac{\partial E_x}{\partial z} \right) - \left(\frac{\partial E_z}{\partial x} \right) - N_y N_x \left[\left(\frac{\partial E_z}{\partial y} \right) - \left(\frac{\partial E_y}{\partial z} \right) \right] - N_y^2 \left[\left(\frac{\partial E_x}{\partial z} \right) - \left(\frac{\partial E_z}{\partial x} \right) \right] - N_y N_z \left[\left(\frac{\partial E_y}{\partial x} \right) - \left(\frac{\partial E_x}{\partial y} \right) \right] \end{aligned} \quad (\text{A. 22})$$

Again noting that E_x , E_y , and their derivatives are $O(f)$, the third-order approximation shows Equation A. 22 becoming

$$\begin{aligned} \left(\frac{\partial E_z}{\partial y} \right) - (1 - f_x^2) \left(\frac{\partial E_y}{\partial z} \right) - f_x^2 \left(\frac{\partial E_z}{\partial y} \right) - f_x f_y \left[\left(\frac{\partial E_x}{\partial z} \right) - \left(\frac{\partial E_z}{\partial x} \right) \right] + f_x (1 - f_x^2 - f_y^2) \left(\frac{\partial E_y}{\partial x} \right) - f_x \left(\frac{\partial E_x}{\partial y} \right) \\ \left(\frac{\partial E_x}{\partial z} \right) - \left(\frac{\partial E_z}{\partial x} \right) (1 - f_y^2) - f_x f_y \left[\left(\frac{\partial E_z}{\partial y} \right) - \left(\frac{\partial E_y}{\partial z} \right) \right] - f_y^2 \left(\frac{\partial E_x}{\partial z} \right) - f_y (1 - f_x^2 - f_y^2) \left(\frac{\partial E_y}{\partial x} \right) - f_y \left(\frac{\partial E_x}{\partial y} \right) \end{aligned} \quad (\text{A. 23})$$

which reduces in the second-order approximation to

$$\begin{aligned} \left(\frac{\partial E_z}{\partial y} \right) - (1 - f_x^2) \left(\frac{\partial E_y}{\partial z} \right) + f_x \left[\left(\frac{\partial E_y}{\partial x} \right) - \left(\frac{\partial E_x}{\partial y} \right) \right] \\ \left(\frac{\partial E_x}{\partial z} \right) - \left(\frac{\partial E_z}{\partial x} \right) + f_x f_y \left(\frac{\partial E_y}{\partial z} \right) + f_y \left[\left(\frac{\partial E_y}{\partial x} \right) - \left(\frac{\partial E_x}{\partial y} \right) \right] \end{aligned} \quad (\text{A. 24})$$

The second-order boundary conditions in Equations A. 21 and A. 24 could be further simplified. The two relations

$$\sigma'\gamma(1 - R) = T\tau\gamma' \quad (\text{A. 25})$$

$$1 + R = T$$

ensure the continuity [up to $O(f^2)$] of the terms $f_x f_y E_y$ and $f_y^2 E_y$ in Equation A. 21 and $f_x^2 (\partial E_y / \partial z)$ and $f_x f_y (\partial E_y / \partial z)$ in Equation A. 24. This can be realized by substituting E_y in Equation A. 17 and noting $z = f$. Thus the second-order boundary conditions become

$$\begin{aligned} E_x^+ + f_x E_z^+ &= E_x^- + f_x E_z^- \\ E_y^+ + f_y E_z^+ &= E_y^- + f_y E_z^- \\ \left(\frac{\partial E^+}{\partial y}\right) - \left(\frac{\partial E^+}{\partial z}\right) + f_x \left[\left(\frac{\partial E^+}{\partial x}\right) - \left(\frac{\partial E^+}{\partial y}\right)\right] &= \left(\frac{\partial E^-}{\partial y}\right) - \left(\frac{\partial E^-}{\partial z}\right) + f_x \left[\left(\frac{\partial E^-}{\partial x}\right) - \left(\frac{\partial E^-}{\partial y}\right)\right] \\ \left(\frac{\partial E^+}{\partial z}\right) - \left(\frac{\partial E^+}{\partial x}\right) + f_y \left[\left(\frac{\partial E^+}{\partial x}\right) - \left(\frac{\partial E^+}{\partial y}\right)\right] &= \left(\frac{\partial E^-}{\partial z}\right) - \left(\frac{\partial E^-}{\partial x}\right) + f_y \left[\left(\frac{\partial E^-}{\partial x}\right) - \left(\frac{\partial E^-}{\partial y}\right)\right] \end{aligned} \quad (\text{A. 26})$$

No such simplification can be made in the third-order approximation, however, and thus the boundary conditions in Equations A. 20 and A. 23 must be used.

Substituting the assumed expression, Equation A. 17, into the boundary conditions, Equations A. 20, A. 23, or A. 21, Equation A. 24 would yield a set of relations for the coefficients A_{mn} , etc. The solution of the problem is completed once the coefficients A_{mn} are determined. In the following section, the second-order solution based on Equation A. 17 with boundary condition Equations A. 21 and A. 24 is presented. The third-order result is highly complicated, but its approach will be the same except for the use of boundary condition Equations A. 20 and A. 23 instead of Equations A. 21 and A. 24.

A. 4 SECOND-ORDER SOLUTION

The algebra involved in establishing the second-order relations among the coefficients is long but straightforward by substituting the assumed expression of

electric intensity, Equation A. 17, into boundary condition Equations A. 21 and A. 24 and neglecting terms of the order $O(f^3)$ and higher. They are

$$\begin{aligned}
 & \sum \{ [A_{mn} + f_x C_{mn}] E(m, n, f) - [G_{mn} + f_x I_{mn}] F(m, n, f) \} = 0 \\
 & \exp \{ -\sigma' \alpha x \} f^2 U + \sum \{ [B_{mn} + f_y C_{mn}] E(m, n, f) - [H_{mn} + f_y I_{mn}] F(m, n, f) \} = 0 \\
 & - \exp \{ -\sigma' \alpha x \} U [2f + \tau \gamma' f^2] + i \sum \{ [-a n C_{mn} + b(m, n) B_{mn} - f_x a m B_{mn} \\
 & + f_x a n A_{mn}] E(m, n, f) - [-a n I_{mn} - c(m, n) H_{mn} - f_x a m H_{mn} + f_x a n G_{mn}] F(m, n, f) \} = 0 \\
 & \sum \{ [-b(m, n) A_{mn} + a m C_{mn} - f_y a m B_{mn} + f_y a n A_{mn}] E(m, n, f) - [c(m, n) G_{mn} \\
 & + a m I_{mn} - f_y a m H_{mn} + f_y a n G_{mn}] F(m, n, f) \} = 0
 \end{aligned} \tag{A. 28}$$

where

$$U \equiv T[(\sigma')^2 - \tau^2]/2 \tag{A. 29}$$

The above equations, however, are still not of the form that will enable the determination of the coefficients A_{mn} , etc. This could only be accomplished by use of the relations

$$A_{mn} = A_{mn}^{(1)} + A_{mn}^{(2)} + \dots \tag{A. 30}$$

and similar expansions for B_{mn} , etc., where superscripts denote the corresponding order terms in the coefficients;

$$\begin{aligned}
 E(m, n, f) &= \exp \{ -ib(m, n)f \} E(m, n, 0) = [1 - ib(m, n)f] E(m, n, 0) \\
 F(m, n, f) &= \exp \{ ic(m, n)f \} F(m, n, 0) = [1 + ic(m, n)f] F(m, n, 0)
 \end{aligned} \tag{A. 31}$$

where the terms of $O(f^2)$ and higher in the square bracket are neglected because these terms will yield terms of $O(f^3)$ or higher in Equation A. 28;

$$\begin{aligned}
 f &= \sum_{u,v} P(u, v) E(u, v, 0) \\
 f_x &= \sum (-iau) P(u, v) E(u, v, 0) \\
 f_y &= \sum (-iav) P(u, v) E(u, v, 0)
 \end{aligned} \tag{A. 32}$$

and

$$f \exp \{-ia\nu x\} = \sum_{u,v} P(u,v)E(u + \nu, v, o) = \sum_{m,n} P(m - \nu, n)E(m, n, o) \quad (A.33)$$

Substituting Equations A.30 to A.33 into Equation A.28 and collecting the first-order terms lead to

$$\begin{aligned} A_{mn}^{(1)} &= G_{mn}^{(1)}, \quad B_{mn}^{(1)} = H_{mn}^{(1)} \\ id(m, n)B_{mn}^{(1)} - ian[C_{mn}^{(1)} - I_{mn}^{(1)}] &= 2UP(m - \nu, n) \\ -d(m, n)A_{mn}^{(1)} + am[C_{mn}^{(1)} - I_{mn}^{(1)}] &= 0 \end{aligned} \quad (A.34)$$

where

$$d(m, n) = b(m, n) + c(m, n) \quad (A.35)$$

In dealing with the second-order terms, the following relations will help to simplify the results:

$$\begin{aligned} \sum_{m,n} fJ_{mn}E(m, n, o) &= \sum_{m,n,k,l} J_{kl}P(m - k, n - l)E(m, n, o) \\ \sum_{m,n} f_x J_{mn}E(m, n, o) &= \sum_{m,n,k,l} [-ia(m - k)]J_{kl}P(m - k, n - l)E(m, n, o) \\ \sum_{m,n} f_y J_{mn}E(m, n, o) &= \sum_{m,n,k,l} [-ia(n - l)]J_{kl}P(m - k, n - l)E(m, n, o) \end{aligned} \quad (A.36)$$

where J_{mn} represents an arbitrary function of m and n ;

$$f^2 \exp\{-ia\nu x\} = \sum_{m,n,k,l} P(k - \nu, l)P(n - k, n - l)E(m, n, o) \quad (A.37)$$

and

$$c^2(m, n) - b^2(m, n) = (\sigma')^2 - \tau^2, \quad (A.38a)$$

$$b(m, n)C_{mn}^{(1)} + c(m, n)I_{mn}^{(1)} = 0, \quad (A.38b)$$

where Equation A.38a follows directly from the definitions of $c(m, n)$ and $b(m, n)$ and Equation A.38b from subtraction of the first-order terms in the two $\nabla \cdot \vec{E} = 0$ equations:

$$\begin{aligned} amA_{mn} + anB_{mn} + b(m, n)C_{mn} &= 0, \\ amG_{mn} + anH_{mn} - c(m, n)I_{mn} &= 0. \end{aligned} \quad (A.39)$$

The results for the second-order terms are

$$\begin{aligned} A_{mn}^{(2)} - G_{mn}^{(2)} &= h_1, \quad B_{mn}^{(2)} - H_{mn}^{(2)} = h_2, \\ an[C_{mn}^{(2)} - I_{mn}^{(2)}] - b(m, n)B_{mn}^{(2)} - c(m, n)H_{mn}^{(2)} &= h_3, \\ am[C_{mn}^{(2)} - I_{mn}^{(2)}] - b(m, n)A_{mn}^{(2)} - c(m, n)G_{mn}^{(2)} &= h_4, \end{aligned} \quad (A.40)$$

where

$$\begin{aligned} h_1 &= iam \sum_{k, \ell} [C_{k\ell}^{(1)} - I_{k\ell}^{(1)}] P(m - k, n - \ell) \\ h_2 &= \sum_{k, \ell} \{UP(k - \nu, \ell) + iam [C_{k\ell}^{(1)} - I_{k\ell}^{(1)}]\} P(m - k, n - \ell) \\ h_3 &= i \sum_{k, \ell} \{U\gamma'P(k - \nu, \ell) + [(\sigma')^2 + \tau^2]B_{k\ell}^{(1)}\} P(m - k, n - \ell) \\ h_4 &= i[(\sigma')^2 - \tau^2] \sum_{k, \ell} A_{k\ell}^{(1)} P(m - k, n - \ell) \end{aligned} \quad (A.41)$$

The six equations A.34 and A.39 suffice to determine the six first-order coefficients, which turn out to be

$$\begin{aligned} A_{mn}^{(1)} &= G_{mn}^{(1)} = \frac{2iUa^2_{mn}P(m - \nu, n)}{d(m, n)D_{mn}} \\ B_{mn}^{(1)} &= H_{mn}^{(1)} = \frac{2iUP(m - \nu, n)}{d(m, n)} \left[\frac{a^2_{mn}}{D_{mn}} - 1 \right] \\ C_{mn}^{(1)} &= \frac{i2Uanc(m, n)P(m - \nu, n)}{d(m, n)D_{mn}} \\ I_{mn}^{(1)} &= C_{mn}^{(1)} - \frac{i2UanP(m - \nu, n)}{D_{mn}} \end{aligned} \quad (A.42)$$

where

$$D_{mn} = a^2(m^2 + n^2) + b(m, n)c(m, n) \quad (A.43)$$

Similarly, the six equations A.39 and A.40 lead to

$$\begin{aligned} (dD_{mn})A_{mn}^{(2)} &= a^2 m^2 b h_1 + (D_{mn} - a^2 m^2)(ch_1 - h_4) + a^2 mn(bh_2 - ch_2 + h_3) \\ (dD_{mn})B_{mn}^{(2)} &= a^2 n^2 b h_2 + (D_{mn} - a^2 n^2)(ch_2 - h_3) + a^2 mn(bh_1 - ch_1 + h_4) \\ (dD_{mn})C_{mn}^{(2)} &= \tau^2 a(mh_1 - nh_2) + ca(mh_4 + nh_3) \end{aligned} \quad (A.44)$$

and $G_{mn}^{(2)}$, $H_{mn}^{(2)}$ and $I_{mn}^{(2)}$ can be obtained easily from Equation A.40. The expressions given in Equations A.42 and A.44 represent the second-order solution for the reflection of horizontally polarized electromagnetic waves from random wavy interfaces between two media, one being non-conducting and the other of a finite conductivity. A similar analysis could be performed for the vertically polarized waves.

A.5 SECOND-ORDER RESULTS FOR NORMAL SPECULAR REFLECTANCE

Recent experimental investigations on the effect of surface roughness on thermal radiative properties have often encountered the difficult problem of surface characterization, especially for surfaces of relatively fine finishes. The geometrical characterization of rough surfaces is often achieved by means of a mechanical instrument, the profilometer. The profilometer, however, causes certain inaccuracies in the measurements of surface roughness because the diameter of the tracing stylus is often comparable to the roughness to be measured. In order to provide a simple but precise method of determining surface roughness, Bennett and Porteus (Reference 9) suggested the use of specular reflectance measurements at nearly normal incidence. The reflectance method is to obtain the root-mean-square roughness from the measured specular reflectance by use of the theoretical relation established by Davies (Reference 6) based on diffraction theory. In the present section, the second-order solution based on the exact theory will be used to obtain the expression for the normal specular reflectance. It is found that the approximate result from diffraction theory does agree with the exact solution up to the second-order terms. This strengthens somewhat the theoretical basis of the reflectance method in determining the surface roughness.

For the horizontally polarized incident waves, the electric intensity field for a smooth surface is

$$E^+ = \exp\{-\sigma' \alpha x\} \{\exp(\sigma' \gamma z) + R \exp(-\sigma' \gamma z)\} \quad (A.45)$$

while for a rough surface it becomes

$$E^+ + B_{\nu 0}^{(2)} E(\nu, 0, z) = \exp\{-\sigma' \alpha x\} \left\{ \exp(\sigma' \gamma z) + \left[R + B_{\nu 0}^{(2)} \right] \exp(-\sigma' \gamma z) \right\} \quad (A.46)$$

By definition of specular reflectance, which represents the ratio of the energy reflected specularly to that incident,

$$\text{reflectance} \equiv \frac{\langle (E^+ - \exp\{-\sigma'\alpha x\} \exp\{\sigma'\gamma z\}) \rangle^2}{(\exp\{-\sigma'\alpha x\} \exp\{\sigma'\gamma z\})^2} \quad (\text{A. 47})$$

it follows that

$$R_o = R^2 \quad (\text{A. 48})$$

$$R_s = \left[R + \langle B_{\nu o}^{(2)} \rangle \right]^2$$

and

$$\frac{R_s}{R_o} = \left[1 + \frac{\langle B_{\nu o}^{(2)} \rangle}{R} \right]^2 \quad (\text{A. 49})$$

where R_o and R_s denote reflectance of the smooth and rough surfaces respectively. From Equation A.44, the average value of $B_{\nu o}^{(2)}$ can be expressed as

$$\langle B_{\nu o}^{(2)} \rangle = \frac{2U}{d(\nu, o)} \sum_{k, l} \left\{ \frac{[(\sigma')^2 - \tau^2]}{d(k, l)} \left[\frac{a_{kl}^2}{D_{kl}} - 1 \right] - i\tau\gamma \right\} \frac{\pi^2 W(r - \alpha\beta, s)}{L^2} \quad (\text{A. 50})$$

where the following relations have been used:

$$ic(\nu, o) = \tau\gamma' \quad , \quad a\nu = \beta\alpha = -i\sigma'\alpha \quad (\text{A. 51})$$

$$r \equiv ak = 2\pi k/L \quad , \quad s \equiv al \quad .$$

Letting L approach infinity so that the summation in Equation A.50 may be replaced by an integral, $\langle B_{\nu o}^{(2)} \rangle$ becomes

$$\langle B_{\nu o}^{(2)} \rangle = \frac{2i\sigma'\gamma[(\sigma')^2 - \tau^2]}{(\tau\gamma' + \sigma'\gamma)^2} \iint_{-\infty}^{\infty} \frac{1}{4} W(r - \beta\alpha, s) \left[-i\tau\gamma' + \frac{[(\sigma')^2 - \tau^2]}{c_1 + b_1} \left(\frac{s^2}{r^2 + s^2 + b_1 c_1} - 1 \right) \right] dr ds \quad (\text{A. 52})$$

where

$$ic_1 \equiv (\tau^2 + r^2 + s^2)^{1/2}$$

and

$$ib_1 \equiv [(\sigma')^2 + r^2 + s^2]^{1/2} = i(\beta^2 - r^2 - s^2)^{1/2} \quad (\text{A. 53})$$

For a slightly rough surface such as implied in the second-order calculations, the average distance between the hills of the surface is large compared with the wavelength of incident waves, i.e. the root-mean-square slope is small. Therefore, the roughness spectrum $W(p, q)$ is zero except for a small region around $p = 0$, $q = 0$. Consequently, under the integral in Equation A. 52 the following approximations can be made

$$\begin{aligned} b_1 &= \beta\gamma, & c_1 &= (\tau^2 + \beta\alpha^2)^{1/2} \\ s &= 0, & r - \beta\alpha &= 0 \end{aligned} \quad (\text{A. 54})$$

With these approximations it is found that

$$\langle B_{\nu 0}^{(2)} \rangle = -2\beta^2 \sigma_m^2 \gamma^2 \left(\frac{\sigma'\gamma - \tau\gamma'}{\sigma'\gamma + \tau\gamma} \right) \quad (\text{A. 55})$$

From Equations A. 49 and A. 55, the reflectance ratio is

$$\frac{R_s}{R_o} = (1 - 2\beta^2 \sigma_m^2 \gamma^2)^2 = 1 - (16\pi^2 \sigma_m^2 \cos^2 \theta / \lambda^2) \quad (\text{A. 56})$$

The limitation of horizontal polarization in the above result can be removed in the case of normally incident waves, and

$$\frac{R_s}{R_o} = 1 - (16\pi^2 \sigma_m^2 / \lambda^2) \quad (\text{A. 57})$$

which is identical to the diffraction-theory result (References 6 and 9) up to the second-order terms.

A. 6 CONCLUDING REMARKS

The exact approach to the calculation of reflectance of a rough surface is described and its second-order solution is given in detail. The normal specular reflectance based on the second-order calculation is found to agree with the diffraction-theory result of the same order. This probably implies that the effect of shadowing and multiple reflections is negligible in the second-order theory. In other words, the second-order calculation from the exact approach does not seem to yield any information on the important effect of shadowing and multiple reflections, which is essential in predicting the emittance or absorptances of a rough surface.

The second-order calculation as outlined here, however, is still incomplete in that the reflection of vertically polarized waves has not been given and the results of

the diffuse component have not yet been calculated. The former might shed some light on the depolarization effect while the latter is certainly important in determining total absorptance. These calculations, however, are relatively simple extensions of those that have been presented. Whether these second-order calculations would yield any new information is subject to confirmation.

Possible extension of the theory to include higher order terms – in particular, the third-order – has been clearly indicated in the above discussions. The mathematical manipulation would be very tedious and lengthy, but the result would probably be very valuable if certain indications of the effects of shadowing and multiple reflections were found. These effects have been totally unknown to date. It should also be pointed out that these calculations would require more information on the description of rough surface than just roughness. The full expression of roughness spectrum is definitely needed. This is equivalent to knowledge of the auto-correlation function of the random height as it is the Fourier transform of the roughness spectrum and vice versa. Therefore, for a higher order theory or for very rough surfaces, the surface geometrical characterization requires both the surface roughness (rms height) and the auto-correlation function of the random height.

NOMENCLATURE

A_{mn}	coefficient defined in Equation A. 17
a	$(2\pi/L)$
B_{mn}	coefficient defined in Equation A. 17
b	function defined in Equation A. 18
b_1	parameter defined in Equation A. 53
C_{mn}	coefficient defined in Equation A. 17
c	function defined in Equation A. 18
c_0	speed of light in vacuum
c_1	parameter defined in Equation A. 53
D_{mn}	coefficient defined in Equation A. 17
d	function defined in Equation A. 35
\vec{E}	electric intensity
E	function defined in Equation A. 18
F	function defined in Equation A. 18
f	z , height measured from the mean plane surface, Equation A. 1
G_{mn}	coefficient defined in Equation A. 17
g	electric conductivity of lower (absorbing) medium
\vec{H}	magnetic intensity
H_{mn}	coefficient defined in Equation A. 17
h_1, h_2, h_3, h_4	functions defined in Equation A. 41
I_{mn}	coefficient defined in Equation A. 17
L	period of the rough surface

m, n	integers denoting various harmonics, Equation A. 1
\vec{N}	unit normal vector to the surface
n_o	refractive index of upper (non-conducting) medium
\bar{n}	refractive index of lower (absorbing) medium
P	function defined in Equation A. 1
p, q	parameters defined in Equation A. 5
R	function defined in Equation A. 16
R_o	specular reflectance of a smooth surface
R_s	specular reflectance of a rough surface
r, s	parameters defined in Equation A. 51
T	function defined in Equation A. 16
U	parameter defined in Equation A. 29
u, v	integers denoting various harmonics like m, n
v_o	wave velocity in Equation A. 10
W	roughness spectrum of the surface, Equation A. 5
x, y, z	rectangular coordinates
α	$\sin \theta$
α'	$\sigma' \alpha / \tau$
β	$2\pi / \lambda$
γ	$\cos \theta$
γ'	$(1 - \alpha'^2)^{1/2}$
ϵ_o	dielectric constant of upper (non-conducting) medium
ϵ	dielectric constant of lower (absorbing) medium
θ	incident angle to the normal of the mean plane surface
λ	wavelength
μ	magnetic permeability
ν	$\beta \alpha / a$
σ_m	rms roughness
σ'	$i\omega(\mu\epsilon_o)^{1/2} = i\beta$
τ	$i\beta\bar{n}/n_o$
ω	angular frequency

Subscript

x, y, z denoting components in x, y , and z directions, respectively

Superscript

$+, -$ denoting upper (non-conducting) and lower (absorbing) media, respectively
 (n) denoting coefficients of n th-order contribution